Phosphorescent Organic Light Emitting Diodes Implementing Platinum Complexes

By

Jeremy David Ecton

A Dissertation Presented in Partial Fulfillment
of the Requirements for the Degree
Doctor of Philosophy

Approved May 2014 by the
Graduate Supervisory Committee:

Jian Li, Chair
James Adams
Terry Alford

ARIZONA STATE UNIVERSITY

August 2014

ABSTRACT

Organic light emitting diodes (OLEDs) are a promising approach for display and solid state lighting applications. However, further work is needed in establishing the availability of efficient and stable materials for OLEDs with high external quantum efficiency's (EQE) and high operational lifetimes. Recently, significant improvements in the internal quantum efficiency or ratio of generated photons to injected electrons have been achieved with the advent of phosphorescent complexes with the ability to harvest both singlet and triplet excitons. Since then, a variety of phosphorescent complexes containing heavy metal centers including Os, Ni, Ir, Pd, and Pt have been developed. Thus far, the majority of the work in the field has focused on iridium based complexes. Platinum based complexes, however, have received considerably less attention despite demonstrating efficiency's equal to or better than their iridium analogs. In this study, a series of OLEDs implementing newly developed platinum based complexes were demonstrated with efficiency's or operational lifetimes equal to or better than their iridium analogs for select cases.

In addition to demonstrating excellent device performance in OLEDs, platinum based complexes exhibit unique photophysical properties including the ability to form excimer emission capable of generating broad white light emission from a single emitter and the ability to form narrow band emission from a rigid, tetradentate molecular structure for select cases. These unique photophysical properties were exploited and their optical and electrical properties in a device setting were elucidated.

Utilizing the unique properties of a tridentate Pt complex, Pt-16, a highly efficient white device employing a single emissive layer exhibited a peak EQE of

over 20% and high color quality with a CRI of 80 and color coordinates CIE(x=0.33, y=0.33). Furthermore, by employing a rigid, tetradentate platinum complex, PtN1N, with a narrow band emission into a microcavity organic light emitting diode (MOLED), significant enhancement in the external quantum efficiency was achieved. The optimized MOLED structure achieved a light out-coupling enhancement of 1.35 compared to the non-cavity structure with a peak EQE of 34.2%. In addition to demonstrating a high light out-coupling enhancement, the microcavity effect of a narrow band emitter in a MOLED was elucidated.

ACKNOWLEDGMENTS

My thanks are due firstly to my advisor, Jian Li, who has instructed me in the scientific method throughout my graduate work and who taught me the value of an old Chinese proverb, “Dumb birds fly first.” More so, I thank him for imparting his expertise in the field and for the many critical discussions, for which this thesis is a product. Nathan Bakken for setting up the equipment used for device fabrication. Eric Turner and Guijie Li for imparting their knowledge on the photophysical processes in organic semiconductor materials and for the synthesis of many of the materials used in this thesis. Tyler Fleetham for imparting his wisdom and experience in the device fabrication process and for the many critical discussions of the work in this thesis. Barry O’Brien for sharing his wealth of knowledge and experience in the semiconductor field. This work would not have been possible without the financial support provided by the National Science Foundation, Universal Display Corporation, and the Department of Energy.

Of course I thank my friends and family for their love and support throughout. Most especially I thank my parents who made all of this possible. Without them, I would not have had the opportunities afforded to me throughout my life. For them, I hope that the fruition of my Ph.D work has made them proud and has rewarded them with the knowledge that that their many efforts and sacrifices in my behalf were not wasted.

Most of all, I would like to thank my beautiful wife. Her love and patience throughout has been critical to my success. To her I dedicate my love and this thesis.

TABLE OF CONTENTS

CHAPTER Page

CHAPTER Page

LIST OF TABLES

Table Page

LIST OF FIGURES

Figure Page

Figure Page

Figure Page

Figure Page

Figure Page

Figure Page

Figure Page

Figure Page

Figure Page

Figure Page

Figure Page

Figure Page

Figure Page

Figure Page

1 INTRODUCTION

1.1 Overview of Organic Electronics

1.1.1 The Electronic Age

We live in an electronic world. The number of internet connected electronic devices alone far exceeds the number of people on the planet with 10 billion connected devices as of 2012 and a forecasted 28 billion connected devices by the end of 2020 according to an IMS report.[1] The average American household has ~24 electronic products,[2] which combined can require up to 150 embedded microprocessors fabricated from various semiconductor chip manufacturing facilities to operate.[3] In addition to household products, as many as 40 embedded microprocessors are required to run the various electrical components of the average automobile. Thus, given the typical household has on average 2.3 vehicles according to an estimate in 2008, the average household relies on several hundred microprocessors to function.[3] In the health field, electronic devices have become an essential component in acquiring, processing, and interpreting data to assist in medical decisions. In short, our economic, health, and national security, rely on and are positively impacted by this world of electronics that we have created.

While electronics have solved many problems and is, in large, responsible for the progression of mankind, they have also been the cause of serious negative environmental impacts as well as some societal impacts in regards to their manufacturing, use, and disposal. Disposal of electronic devices in particular has become a serious concern in recent years.

According to the US Environmental Protection Agency (EPS), approximately 142,000 computers and 416,000 mobile devices are recycled or thrown away every day[2] and up to 2.4 million tons of electronic waste hit US landfills each year.[2] Harmful contaminants such as arsenic, barium, beryllium, cadmium, chromium VI , lead, lithium, mercury, nickel, selenium, americium, among others are basic materials used to fabricate these electronic devices and have been known to cause serious medical problems including diseases of the skin, decrease nerve conduction velocity and cause lung cancer, damage to heart, liver, kidney, spleen, and other physiological damages to the human body. Unfortunately these electronic devices often are not disposed of properly and enter garbage disposal sites that are unfit to safely contain these hazardous elements and prevent them from entering into the environment.[4] In addition to environmental concerns, the demand for rare minerals to fabricate electronic devices has become the driving force for financing civil violence by armed groups in the Democratic Republic of the Congo (DRC) or adjoining countries. These minerals mined under conditions of human right abuses, properly termed conflict minerals, are purchased by semiconductor corporations. While companies are aware of the problems associated with conflict minerals, such as Intel Corporation which has recently published a paper outlining their goal to achieve a Conflict-free supply chain, conflict minerals are still being purchased and used to fabricate electronic devices.

1.1.2 A New Era of Electronics

Organic semiconducting materials are a promising solution to many of the issues surrounding traditional materials used to fabricate electronic devices and may offer a more eco-friendly and affordable approach to growing our electronic

world. Organic materials exhibit an immense variation in structure and properties creating untold potential and novel functionality. Additionally, organic materials can be synthesized or processed with relative ease and have the ability to be deposited on a variety of low cost substrates such as glass, plastic or metal foil by organic chemical vapor deposition, organic thermal evaporation, or spin coating.[5] These favorable properties make the fabrication of electronic devices based on organic materials much simpler and potentially more cost effective compared to crystalline, inorganic semiconductor devices.

1.1.3 Mechanical, Optical and Electrical Properties of Organics

Solids based on organic semiconducting compounds are typically soft and fragile whereas inorganic semiconducting compounds are typically hard and brittle. These properties are strongly related to the intermolecular interactions. While organic compounds are typically bonded together by weak van der Waals forces that decrease as $1/R^6$, where R is the intermolecular spacing, inorganic semiconductors are bonded by strong covalent bonds whose strength falls off as $1/R^2$. Although, the soft and fragile nature of organic semiconducting compounds are less robust when exposed to adverse environmental agents such as moisture and corrosive agents compared to inorganic semiconductors, the mechanical properties of organic semiconductors has also opened the door to an array of innovative fabrication methods impossible with inorganic semiconductors. In particular, many processes can be directly printed through use of contact with stamps or by ink-jets and other solution based methods. Such ability allows for continuous roll-roll processing which is an attractive feature for large scale manufacturing.

Among the most attractive properties of organic materials for electronic devices is the ability to be tailored to optimize a particular function, including luminescent properties, absorption characteristics, charge mobility, energy level position, etc. This also leads to a large variety in the electrical and optical properties of organic semiconductor materials with potentially more flexibility in electronic device design. These properties depend strongly on the atomic structure and bonding properties of the material which can be broadly classified into three categories: small molecules, polymers, and biological materials. Small molecules refer to compounds with a well-defined molecular weight and further broken down into classification as monomers, dendrimers, and oligomers. By comparison, polymers are long-chain molecules containing an indeterminate number of molecular repeat units. Biological materials are complex, consisting of proteins and strands of DNA. Currently, there are no clear demonstrations of electronic applications based on biological materials, however reports of some applications such as DNA-based computing which uses the tendency of nucleotide bases to bind (hybridize) in preferred combinations to do computation are beginning to emerge. [6] Although, the properties of small-molecules and polymer organic thin films in organic electronics differ in regards to thin-film deposition and device preparations, there are in general more similarities than differences in both their electronic and optical properties. The excitonic state dominates the optical properties in both small molecules and polymers.[7] An exciton is a molecular excited state for which an electron/hole pair can recombine to generate either light (a radiative process) or heat (a non-radiative process). An exciton is "mobile" within the solid organic film and migrates in the film via a hopping mechanism; from molecule to molecule for small molecule films or along the polymer backbone for polymeric films. The most common exciton species in organic

electronics is the tightly bound Frenkel exciton with a binding energy of ~1eV that is generally localized on a single molecule at a time.[8] In special cases such as highly ordered molecular crystals, more weakly bound charge-transfer (CT) excitons are found in the optical spectra. These CT excitons are typically spread over one or more neighboring molecules with a binding energy of ~10-100meV (much lower than Frenkel states). By comparison, inorganic semiconductors form Wannier-Mott type excitons with yet smaller binding energies of typically only a few meV and therefore are rarely observed.

Similar to the exciton, the mobility of charge carriers (electrons or holes) in solid amorphous organic films typically occurs via a hopping mechanism between molecular sites or from chain to chain for small molecules and polymers, respectively. More specifically, holes hop along the highest occupied molecular orbital (HOMO) of the molecules and electrons hop along the lowest occupied molecular orbital (LUMO) of the molecules, which can be considered the organic analogs of the valence band and conduction band found in inorganic semiconductors, respectively. As a consequence of a hopping mechanism found in the charge carrier transport of organic semiconductors compared to band carrier transport found in inorganic semiconductors, carrier mobility's (μ) of organic semiconductors tend to be low compared with inorganic semiconductors. Typical room temperature carrier transport mobility values for organic semiconductors are between 10^{-6} to 1 $cm^2V^{-1}s^{-1}$ compared with 10^2-10^4 $cm^2V^{-1}s^{-1}$ for inorganic semiconductors.[9,10] In organic materials with a high degree of order, such as molecular crystals, carriers hop between closely spaced molecules (crystalline stacks) as opposed to hopping across individual molecular sites, and consequently tend to have higher mobility's than the

typical amorphous organic films. Mobility's of molecular crystals as high as 1 $cm^2V^{-1}s^{-1}$ has been reported at room temperature.[10-12] One approach to achieving a high degree of order in organic thin films and improve mobility is by the deposition (generally by spinning) of polymers onto substrates prepared by rubbing or other 'direction-inducing' processes, which can lead to alignment of chains, thus increasing the charge mobility relative to random disordered films.[13] Another approach to reducing disorder in organic films is by templating ordered epitaxy-like growth from crystalline substrates that impose their lattice order onto the adsorbed organic films.[14] However, this approach is limited to special cases involving only a few organic materials and substrates that may not necessarily be ideal for use in the given application.

More recently, advances in organic materials with long range order have been made. In particular, graphene, which contains carbon atoms densely packed in a regular sp^2-bonded atomic-scale hexagonal honey comb lattice, represents a whole new class of organic materials for use in organic electronics. The strong covalent bonds and highly ordered crystal like structure make graphene an excellent electrical conductor with mobility's as high as 200,000 $cm^2V^{-1}s^{-1}$. [15] Additionally, graphene has an unusual band structure and its experimental realization presents tantalizing opportunities to study phenomena ranging from exotic quantum Hall states to the Klein paradox or tunneling of relativistic particles. [15] The full benefits of graphene in organic electronics have yet to be realized, but offers a taste of the novelty and potential organic materials may offer our future world of electronics.

1.1.4 The Rise of a New Era

While the field of organic electronics has been actively studied by physicists and chemists for the past 50 years, only recently has organic electronics transitioned from the domain of "pure research" into practical application. For many years, organic semiconductor based devices fell far short of the stability and performance of devices based on "conventional" inorganic semiconductors such as silicon or gallium arsenide. A significant discovery in the mid-1980s changed the situation dramatically with the demonstration of an efficient, low voltage, thin film organic light emitting diode (OLED) by Ching Tang and Steven van Slyke. [16] By fabricating an organic heterostructure light emitting device composed of thin, amorphous organic materials, Tang and van Slyke achieved an increase in the luminescence quantum efficiency by approximately two order of magnitude compared to existing light emitting devices based on organic materials at the time with an efficiency of 1% at an operating voltage less than 10V (Figure 1a).[16] The electroluminescence occurs as a result of injecting charges (i.e. holes and electrons) into the organic semiconductor materials, Alq_3 and Diamine, where they meet and recombine to form photons. By comparison, state of the art OLEDs today consists of complex multilayer systems. Figure 1b shows a schematic of a common multilayer OLED architecture. In this configuration, holes are injected from a conductive anode into the highest occupied molecular orbital (HOMO) of the hole-transport layer (HTL) and electrons are injected from a conductive cathode into the lowest unoccupied molecular orbital (LUMO) of the electron-transport layer (ETL) where they migrate towards the center and into the emissive layer (EML). Typically a thin hole injection layer (HIL) and electron injection layer (EIL) is implemented into the device to improve charge

injection from the metallic anode and cathode, respectively, into the organic layers.[16] An electron blocking layer (EBL) and hole blocking layer (HBL) are typically used to confine charge carriers and excitons in the EML. For example, by inserting a material with a shallow LUMO energy level between the HTL and EML an energy barrier for electron transfer is formed, preventing leakage of electrons into the HTL. By comparison, by inserting a material with a deep HOMO energy level between the ETL and EML an energy barrier for hole transfer is formed, preventing leakage of holes into the ETL. In the event the triplet energies of the EBL and HBL materials are higher than the triplet energies of the EML material, an energy barrier for exciton transfer is formed.

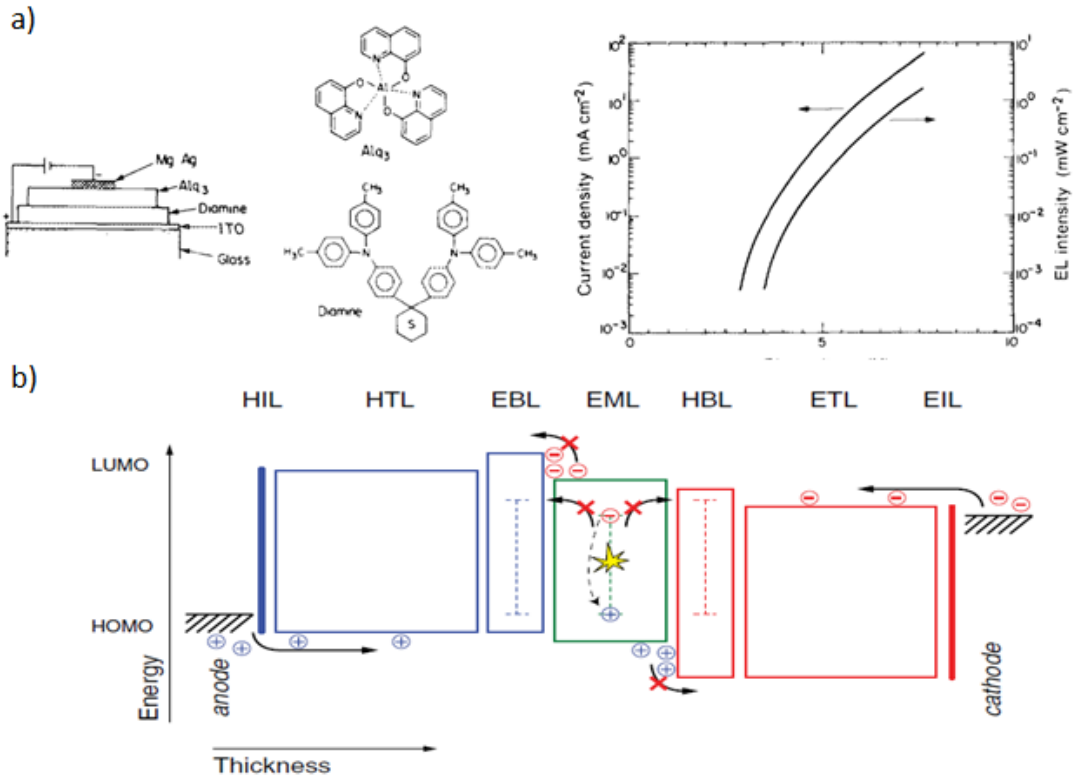

Figure 1. (a) The first thin film organic light emitting diode (OLED) based on a hetrostructure device architecture. The OLED was built on a glass substrate coated

with a transparent and conducting anode of indium tin oxide. The diamine and Alq_3 organic layers were capped with an opaque, reflective metal cathode composed of a Mg:Ag alloy. In this structure, holes are injected from the anode into the diamine layer and electrons are injected from the cathode into the Alq_3 layer. The diamine was selected as the so called hole transporting layer based on earlier studies of photoconductors which found this class of materials to have stable conductivity properties. In this hetrostructure device the electrons and holes can effectively recombine at the diamine/Alq_3 interface with minimal electron injection into the diamine layer and some hole penetration into the first 100 Angstroms of Alq_3.[16] (b) Energy diagram of a common multilayer OLED. The multilayer OLED typically consists of an hole injection layer (HIL), a hole-transport layer (HTL), an electron-blocking layer (EBL), an emissive layer (EML), a hole-blocking layer (HBL), an electron-transport layer (ETL), and the electron-injection layer (EIL) between a conductive anode and cathode. The top of the boxes for each layer indicate the energy level of the highest occupied molecular orbital (HOMO) and the bottom of the boxes for each layer indicate the energy level of the lowest unoccupied molecular orbital (LUMO). The dashed lines represent the triplet energy states of the organic materials in the case of phosphorescent materials.[16]

Although, this particular demonstration by Tang and VanSlyke was still insufficient to compete with the existing technologies at the time, it nevertheless demonstrated the potential of organic materials for solid state electronic devices and laid the foundation for a new generation of optoelectronic devices. Since then a wave of organic optoelectronic devices have been reported. In particular, the organic solar cell or organic photovoltaic (OPV) has received great attention from the scientific community in recent decades. Since the report of a two-layer organic solar cell with a 1% power conversion efficiency from Tang and VanSlyke,[1,7] OPVs consisting of small molecules, polymers, and dye-sensitized solar cells have experienced significant improvements in performance. In particular, the dye-sensitized solar cell has achieved power conversion efficiencies as high as 11%. [18] Although the efficiency, stability, and strength of OPVs remain far below their inorganic counterparts, OPVs are a promising prospect for a renewable energy source due to their low cost, light weight, and mechanical flexibility. According to authorities in the field, if the OPV power efficiency can be raised be a factor of 2-3, then OPVs will become the

mainstay of solar energy harvesting. The thin film transistor (TFTs) based on organic materials has also been heavily studied in recent years.[19, 20] The growing interest in organic thin film transistors is largely attributed to the ability to deposit on a room temperature surface which enables inexpensive, lightweight, flexible, and mechanically rugged plastic substrates for uses such as simple circuits on plastic cards or flexible displays. Other organic optoelectronic devices such as organic lasers, [21, 22] organic sensors, [23-25] and organic memories, [26, 27], have also begun to emerge.

1.2 A Bright Future for Display with OLEDs

Thus far, the most successful optoelectronic device in the realm of organic electronics is the organic light emitting diode (OLED). In particular, OLEDs have proven to be successful in high quality passive and active matrix displays. Several major international corporations such as Samsung Mobile Display, LG Display, Novaled Phillips, and General Electric are participating in the OLED display technical contest.

Figure 2. A selective history of OLED products from Samsung between 2010 to 2013. The images, from left to right, include the Samsung Ice Touch, the Samsung s8500 Phone (top) with the Samsung Galaxy Note Phone (bottom) with touch functionality based on super AMOLED technology, a comparison of OLED (Samsung Wave) and liquid crystal display (LCD) technology (Nokia X6), the Samsung Galaxy Tab 1 with

a 7" display, the Samsung Galaxy S3 with a 4.8" display, the Samsung 55" OLED TV (top) with the curved Samsung 55" OLED TV (bottom), and a "sneak peak" at the future of OLED display with a flexible smartphone prototype from Samsung. [28]

Samsung has been the leader in bringing OLED technology into commercial displays. In 2010, Samsung released the Samsung IceTouch with a 2" full-color transparent OLED display. Later that year, they released several products, including the s8500 Wave Phone with a 3.3" display, the Galaxy Note Phone with a 5.3" display and HD resolution (1280x800), and the Galaxy-Tab with a 7" display, based on their new Super AMOLED displays which included an integrated touch function with sensors just 0.001mm resulting in better images and greater visibility in direct sunlight. In 2012 they launched the Galaxy S3 with a 4.8" display along with their first OLED TV with a 55" display. Since that release over 50 million Galaxy S3 phones have been sold.[29] In 2013, they pushed the limits further by creating a prototype curved OLED TV with a 55" display which they demonstrated during their CES presentation. According to Samsung, the curved design provides more depth to the image for a more life-like viewing experience. Samsung is planning to bring this flexible display technology to the mobile market as well with an expected delivery date at the end of 2014. Figure 2 summarizes the aforementioned OLED based products released by Samsung the past 3 years. From the first 2" color display for mobile devices to the 55" flexed display for an OLED TV, significant progress has been made in a short span of time demonstrating the potential of organic electronics. Though impressive OLED technologies have come to fruition in recent years, the field is still in its infancy and has only begun to mature.

Several key features have made the organic light emitting diode an attractive alternative to other display technologies on the market. These key features include

(1) emissive pixels, (2) thickness, (3) weight, (4) flexibility, (5) response time, (6) efficiency, and (7) color gamut. Liquid crystal displays (LCDs), which have traditionally dominated the display market, contain an inherent source of inefficiency as they rely on selectively filtering a backlight to produce red, green, and blue light for display. By comparison, OLED pixels can emit directly blue, green, and red colors resulting in effective utilization of emitted light. In addition to effective utilization of light emission, excellent viewing characteristics including a higher viewing solid angle with approximately a lambertian emission pattern (constant luminance over all viewing angles in the forward direction) can be achieved with an OLED display. Since OLEDs are fabricated from organic thin films typically no more than 100nm thick, the display thickness is approximately only limited by the substrate thickness. Although displays are easier to fabricate on rigid substrates such as glass, advances in the fabrication of OLEDs on plastic substrates is progressing which will not only make for a thinner display but a more rugged and robust display as well that is less sensitive to cracking from mechanical stresses. Additionally, displays built on a plastic substrate will be considerably lighter resulting in untold possibilities such as mounting displays as large as 200 inches to walls with ease or even wearable displays built into clothing. Another attractive feature is the quick response time attributed to the short radiative lifetime of organic phosphors ranging between couple of nanoseconds for fluorescent materials to ~500 nanoseconds for phosphorescent materials. [30] One of the most attractive features of OLED technology is their potential for high efficiency. Low power displays are most important in mobile device applications where an extended battery life is highly desired. Organic phosphors are also capable of producing a large range of colors for displays with a high color gamut. A high color gamut is most

critical in photography. Thus, naturally, on-camera monitors with an OLED display have gained popularity in recent years. In particular, the AC7-OLED on-camera monitor exhibits a much larger color gamut than traditional LCD displays used in many of the common mobile displays as in the iPhone 5.[31]

Although significant improvements in display utilizing OLEDs have been achieved, continued effort in reducing the power consumption of OLEDs is needed. With the increased sales of smart phones and other mobile devices, a long battery life is desired, which can be extended to a great extent by reducing the power consumption of the display. Thus, further improvements in the device efficiency are desired and possible with continued research and development in organic materials and device architectures for OLEDs.

1.3 Efficient Lighting with Unique Design Potential

1.3.1 OLEDs for Lighting

While organic light emitting diodes have been widely developed for flat-panel displays, only recently has the efficiency and stability of white OLEDs risen to the point that they can be considered for solid state lighting applications. Considering white organic light emitting diodes (WOLEDs) have the potential of being ecofriendly, affordable, and efficient with low power consumption and high color quality, WOLEDs may someday replace existing lighting solutions and become the dominant source of solid state lighting.

1.3.2 The Need for Efficient Lighting

Solid state lighting (SSL) occupies a large portion of the world's energy demand which can be relieved to some extent by improving the power efficiency of SSL sources. This energy demand is particularly high in the United States. According to a 2010 DOE report, the U.S. consumes 700 TWh of electricity annually on lighting, constituting approximately 19% of the total U.S. electricity use.[32] A breakdown of the average daily operating hours and annual electricity usage for the residential, commercial, industrial, and outdoor sectors is summarized in Table 1.

Table 1. Summary of Lighting Market Characterization in 2010[32]

	Lamps	Average Daily Operating Hours	Wattage per Lamp	Annual Electricity Use (TWh)
Residential	5,811,769,000	1.8	46	175
Commercial	2,069,306,000	11.1	42	349
Industrial	144,251,000	13	75	58
Outdoor	178,374,000	11.7	151	118

A summary of the various lighting technologies and their electrical consumption is outlined in Table 2. Approximately 22% of the current lighting market relies on incandescent lamps to produce light.[32] Incandescence is a very old (>100 years) and inefficient technology (<5% of the electrons are converted to photons). While in recent years, many of the incandescent lighting sources have been replaced by the more efficient fluorescent lamps, fluorescent lamps contain harmful components such as mercury. Thus, SSL technologies that are eco-friendly, affordable, and efficient are desired and are needed in order to compete with the

incandescent bulb and the fluorescent lamp. In particular, inorganic light emitting diodes and organic light emitting diodes have drawn attention in recent years as they have the potential to be as efficient as fluorescent lamps without containing harmful pollutants such as mercury.

Table 2: U.S. Lighting consumption by sector and Lamp type in 2010 [32]

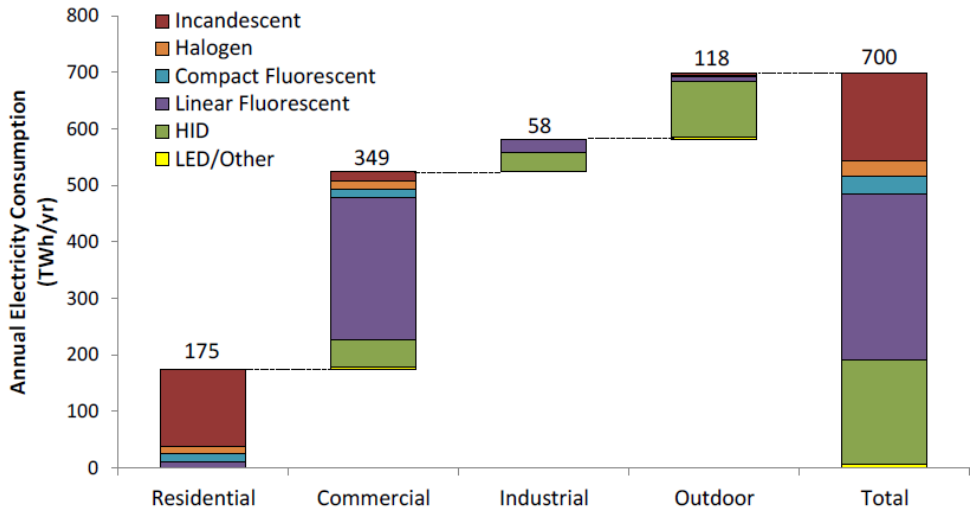

1.3.2 Requirements for Lighting and Current Trends in Lighting Technology

General illumination requires high quality light and can be described by 3 parameters: (1) The lumen output or luminous flux (lm), (2) the color rendering index (CRI), and (3) the correlated color temperature (CCT).

The lumen is a measurement of the brightness of a source or the power emitted from a source as interpreted by the human eye. The typical lumen output for

a 100-W incandescent lamp is ~1,500 lm or for a standard office fixture containing four fluorescent lamps behind a diffuser is ~5,000 lm.[33] CRI is an arbitrary unit of measurement that compares the ability of a light source to reproduce the true color of objects being lit by the source. Incandescent lamps have CRI values close to 100, whereas monochromatic sources such as low-pressure sodium lamps have CRI values close to 0. A source with a CRI of <70 is considered unacceptable for interior illumination applications. The CCT is the temperature of a blackbody spectrum closest to the color of the light source. The CCT for incandescent light bulbs is ~2700 K and is often referred to as "warm light". Sources such as LEDs with a down converting phosphor or fluorescent lamps often exhibit a higher CCT, so called "cool light", as it contains more high energy blue emission. Typically, warm light is more desirable to the consumer than cool light even if cool light sources can achieve a higher CRI. More on the metrics used to quantify solid state lighting will be discussed in Chapter 2.

Table 3 provides a summary of the efficiency, lifetime and color quality of existing light technologies and represents the best data found in literature as of 2008. Based on the data outlined in table 3, organic light emitting diodes can clearly achieve sufficient lighting quality for general illumination with CRI values greater than 90 and moderate power efficiency. However, affordability might be a more challenging goal for organic SSL. Two factors must be considered when comparing affordability of various SSL technologies: (1) purchasing cost and (2) operating cost. In some cases, the purchasing cost may be high, but the reduction in power usage and higher operational lifetime may suede consumers to pay more up front to save cost in the long-term. For example, inorganic LEDs are gaining increased popularity

in recent years in spite of a higher purchasing cost compared with incandescent bulbs. Significant improvements in luminous efficacy of inorganic LEDs over the past four decades has reduced the cost from $20/lm to about 0.01$/lm as of 2008.[33] Although, a 1,500-lm (100-W) incandescent bulb can be purchased for less than $0.50, representing a cost per lumen of <$0.03, the higher efficiency and operational lifetime already make inorganic LEDs more competitive than their purchasing price would suggest.[33]

Table 3. A Summary of Lighting Technologies[33]

Light Source	Efficiency (lm/W)	CRI	Lifetime (h)
Incandescent Lamp	10-15	>90	1000
Fluorescent Lamp	40-80	70	10,000
High-Pressure Sodium Lamp	140	<10	10,000
Light Emitting Device (LED)	>80	80	>10,000
Organic Light-Emitting Device (OLED)	65	>90	10,000

Compared to inorganic LEDs for SSL, OLEDs are far behind in terms of affordability. Assuming a WOLED with a power efficiency of 64 lm/W[34] was manufactured into a 1-ft^2 panel operating at a brightness of 4,000 cd/m^2, then the luminous flux would be ~1,200 lm (assuming lambertian emission). Thus, a reasonable cost point for organic SSL to compete in the current market is ~ $10.[33] Based on existing organic SSL materials and designs, such a cost point is not feasible. Among the most costly aspects of organic SSL technology is the substrate. Typically high quality glass with little impurity defects and a high surface quality is needed to grow efficient devices and minimize impurity diffusion into the device resulting in reduced operational lifetimes. While such high quality of glass is not an

issue for use in OLED displays to remain cost competitive, organic SSL cannot accommodate such a costly substrate and remain cost competitive with existing efficiencies and operational stabilities. Very low-cost float glass might be an option; however, methods that address the aforementioned issues need to be considered. Similarly, plastic is too expensive considering it also must be high quality; including dimensional stability, a glass transition temperature, and extremely low moisture permeability. Additionally, innovations in manufacturing are needed for organic SSL to become affordable. Batch coating techniques including vacuum sublimation or solution-based methodologies are unlikely to achieve the high through-put needed to be cost effective. Roll-roll coating which is a continuous and fast coating process, may lead to the high through-put needed, however, high purity devices free of contaminants necessary to yield high operational lifetimes are difficult to achieve without a vacuum system based fabrication process. Thus, if OLEDs are to compete with growing SSL technologies such as inorganic LEDs, either improvements in efficiency or reductions in manufacturing costs will be needed.

1.3.3 White Lighting Architectures in Organic SSL

One common approach to achieving organic white-light devices with a broad, white-light spectrum is by using multiple dopants; namely a combination of single-color sub-elements typically of either (1) red, green, and blue or (2) blue and orange (Figure 3). This can be achieved either by combining multiple dopants in a single layer or by doping a single dopant in multiple layers. While this approach is capable of achieving high quality white light, it requires a either additional layers or complicated co-depositions, resulting in a potentially higher manufacturing cost. Thus, simpler designs with fewer layers are desired. An alternative to combining

several sub-elemental colors to achieve a broad, white-light spectrum is by using a blue or ultraviolet device in conjunction with a down converting phosphor (Figure 3). While a blue device with a down converting phosphor design is simple with a potentially more cost effective manufacturing process than WOLEDs containing several sub-elemental colors, it has an inherent limitation in efficiency as the stokes shift in the down-converting process is a source of energy loss. In this thesis a novel architecture for generating high quality white light will be discussed (Chapter 3), which does not exhibit the inherent limitations of the traditional approaches of generating white light.

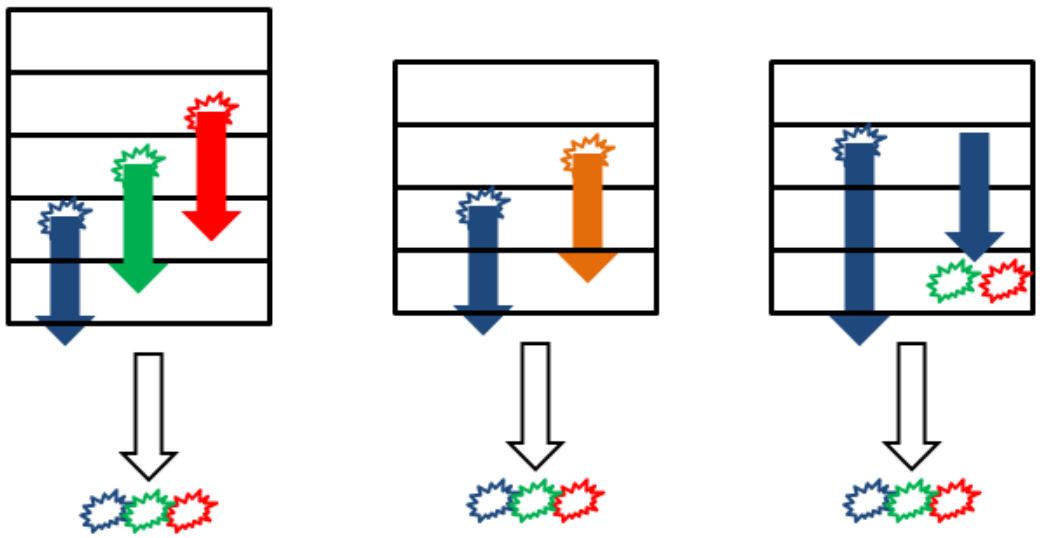

Figure 3. Some common WOLED architectures including combining multiple dopants in a single layer or by doping a single dopant in multiple layers composed of (1) red, green, and blue dopants (left) or (2) blue and orange dopants (middle) as well as (3) a blue device with a down-converting phosphor (right).

1.3.4 Current Challenges in Materials and Device Architectures of Organic SSL

As mentioned in the forgoing sections, organic semiconducting materials are in need of further development to achieve the efficiency required for organic SSL to

become a competitive choice for general illumination. More specifically, materials that enable devices with close to 100% internal quantum efficiency, wherein one photon is generated for every one electron injected with no barriers or losses to charge injection and transport, are desired. Thus, the field currently depends heavily on materials scientists and chemists to develop and synthesize new organic semiconducting materials to meet these high efficiency standards. In addition to high efficiency, electrochemically stable materials with high device operational lifetimes are needed.

Since the report of Tang and VanSlyke, with an estimated 1 photon generated for every ~25 electrons using an organic bilayer sandwiched between an anode and cathode, significant improvements in this ratio of generated photons to injected electrons has been achieved with a development in materials. One of the most influential factors for reducing this ratio is the advent of phosphorescent organic semiconductor materials.[35] As discussed in earlier sections, the optical properties of organic semiconductors are dominated by strongly bound excitons. The total spin of the exciton can form either a zero net spin (singlet excitons) or a non-zero net spin (triplet excitons) depending on the spin states of the constituent electron and hole. Only excitons with a net spin of zero can radiatively recombine without violating quantum mechanical spin conservation rules. Random optical or electrical stimulation yields only 25% of excitons with opposite spin and thus only 25% of the generated excitons can recombine to form light, known as fluorescence. The remaining 75% of the excitons are in high-spin "triplet" states, and direct recombination to the ground state is forbidden by quantum mechanical conservation rules. Thus, such materials, known as fluorescent materials, significantly limit the

device efficiency. Recently, it has been realized that by incorporating a heavy metal ion into an organic small molecule,[36] the metallic character can couple with organic ligands,[37] resulting in a metal-ligand charge-transfer state. Excited states in these cases retain enough metallic characteristics to remove the spin-forbidden nature of the radiative relaxation of the triplet state, resulting in nearly 100% radiative recombination of generated excitons. Such materials, known as phosphorescent materials, have the ability to harvest both singlet and triplet excitons in OLEDs compared to fluorescent materials, which have the ability to only harvest singlet excitons. The advent of phosphorescence was a giant leap forward towards highly efficient OLEDs approaching 100% internal quantum efficiency.

Since the advent of phosphorescent organometallic complexes with the ability to harvest triplet excitons, highly efficient WOLEDs with >20% have been reported.[34] However, further work is needed in developing semiconducting materials for white light electroluminescence. In particular, highly efficient phosphorescent emitters that are electrochemically stable with long device operational lifetimes and high color purity are desired. With regards to phosphorescent emitters for white OLEDs, blue emitters have been a major focus of the field in recent years as blue OLEDs typically have lower efficiencies and device operational lifetimes than red and green. Consequently, the efficacy of RGB WOLEDs as well as WOLEDs implementing a down-converting phosphor depends strongly on the properties of the blue emitter contained therein and is typically the bottle neck in either or both the efficiency and stability of WOLEDs based on those architectures (Figure 3). While stable blue fluorescent emitters can be used to fabricate WOLEDs with high operational lifetimes, the device efficiencies remain low.[38] Conversely, while

WOLEDs with high device efficiencies have been fabricated implementing blue PhOLED, the operational lifetime remains low.[39] Thus, the development of phosphorescent blue emitters that are both electrochemically stable and highly efficient are of paramount importance.

In addition to the need for improvements in the availability of efficient and stable phosphorescent emitters in OLEDs, improvements in device architectures are also needed. Although high device efficiency has been realized with the development of efficient charge transporting and charge injecting materials[40-42] combined with the advent of the aforementioned phosphorescent heavy metal complexes, which are capable of harvesting 100% of electrogenerated excitons, [36] the external quantum device efficiency remains limited to 20-30%, [34] as most of the photons generated do not contribute to the out-coupled power as a result of optical losses inside of the device. These optical losses include surface plasmon polaritions (SPPs),[43, 44] absorption at the metal electrode surface,[45] and modes trapped by total internal reflection due to the mismatch of the refractive indices between the organic layers (n~1.6-1.8)/ITO anode (n~1.9) and glass (n~1.5) (waveguide modes) and the mismatch of refractive indices between glass and air (n~1) (substrate modes).[46-49] Thus, device architectures that improve out-coupling efficiency are highly desired and provide the greatest potential for improvements in OLED efficiency and methods that improve the light out-coupling efficiency, or fraction of light emitted from the device to total generated light, need to be considered. There have been a number of methods reported that enhance the external quantum efficiency (EQE) of OLEDs and overcome the light out-coupling limitation. In particular, methods that release light trapped by total internal reflection include implementing a high

refractive-index (n≥1.8) substrate, creating surface roughness on the top of the substrate to allow more light to scatter out of the substrate,[50] implementing an ordered microlens array at the top of the substrate to eliminate the critical angle condition at the substrate/air interface,[51] growing a periodic two-dimensional (2D) photonic crystal to couple the guided waves to the radiation mode in the direction normal to the device surface,[52] or through the design of a microcavity OLED (MOLED).[53, 54] Thus, the development of the aforementioned methods combined with the development of novel materials and emitters for highly efficient devices may provide a route towards affordable and ecofriendly SSL sources.

1.3.5 Designer Lighting with OLEDs

Although, Organic SSL remains more costly at the present, the market for unique designer lighting with unique features may offer organic SSL a competitive edge in spite of higher cost. These unique features include emission over a large area with the potential for dual-sided emission from either straight or curved surfaces allowing for novel lighting designs difficult and often impossible to achieve based on current SSL technologies. Additionally, organic SSL is compact, light, and consequently more rugged than typical SSL technologies. Such unique properties provide designers untold possibility for lighting including lighting that is color-tunable, transparent, ultrathin, flexible, and wearable, just to name a few, resulting in an array of new niche lighting markets with far reaching applications. Thus, the market for such niche lighting may provide organic SSL the momentum needed to bring volumes up and subsequently bring cost down possibly to the point wherein OLEDs become competitive for general illumination.

1.4 Thesis Outline

The foregoing sections outlined the need of further development and improvements in device efficiency and stability of OLEDs for applications in both display and solid state lighting. This thesis endeavors to demonstrate improvements in device efficiency and stability by using novel device architectures and/or novel organic materials. More specifically, the ensuing chapters will focus on the use of platinum based complexes for efficient and stable phosphorescent OLEDs. Chapter 2 will describe the materials characterization methods and equipment as well as detail the device fabrication tools and methods. Chapter 3 will explore some highly efficient excimer based WOLEDs. Chapter 4 will explore a possible route towards both stable and efficient blue and white excimer based OLEDs. Chapter 5 will discuss a stable red OLED based on a phosphorescent platinum complex with high operational lifetimes. Chapter 6 will discuss the light out-coupling limit based on conventional OLED architectures and a possible route towards improved light out-coupling efficiency with a microcavity OLED (MOLED) design. Chapter 6 will also develop an optical model designed to assess microcavity effects in a MOLED. Based on the optical model developed, a design of experiment (DOE) will also be outlined with the intent of optimizing the light out-coupling efficiency with respect to light out-coupling reflectivity and organic thickness in a DBR/metal microcavity structure. Chapter 7 will compare the theoretical and experimental light out-coupling enhancement of MOLEDs utilizing the optimized structure developed in the DOE of chapter 6 with a highly efficient Pt-based green-emitting complex exhibiting narrow band emission (FWHM=18nm in solution of DCM). This thesis will conclude with a full summary and outlook on the work demonstrated.

2 METHODS AND CHARACTERIZATION

2.1 Lighting Standards and Definitions

In physics light is often quantified in terms of radiant energy (radiant flux, radiant intensity, radiance, etc.). In the field of organic electroluminescence from organic light emitting diodes, light is typically quantified in terms of luminous energy (luminance flux, luminous intensity, luminance, etc.). These definitions will now be defined.

The luminance flux, Φ, is the flow of radiant energy as perceived by the human eye. The eye responds in a characteristic way to radiant energy and depends strongly on the wavelength of the emitted light. The Luminance flux is typically evaluated in terms of the eye's photopic or scotopic response according to the following equation

Equation 1

$$\Phi = k_m \int \phi V(\lambda) d\lambda$$

Here, Φ is in lumens (lm), φ is the radiant power in W/nm, λ is the wavelength in nm, V(λ) is the photopic or scotopic response, and K_m is the maximum spectral luminous efficacy, which is 683 lm/W and 1754 lm/W for photopic and scotopic vision, respectively.

The luminous intensity, I, is the luminance flux per solid angle. The luminous intensity is described by the following equation

Equation 2

$$I_L = \frac{d\Phi}{d\Omega}$$

Here, I_L is in candela (cd), and Ω is the solid angle in steradian. The candela is equal to the luminous intensity (for a given direction) of a source that emits monochromatic radiation of frequency 540x10^{12} Hz (555 nm) and that has a radiant intensity in that direction of 1/683 W/sr.

The luminance, L_v, is defined by the derivative

Equation 3

$$L_v = \frac{d^2\Phi}{dAd\Omega\cos\theta}$$

Here, L_v is in cd/m^2 and is typically referred to as nits, θ is the angle between the surface normal and the specified direction in radians, and A is the surface area in m^2. A diagram of the luminance is shown in Figure 4.

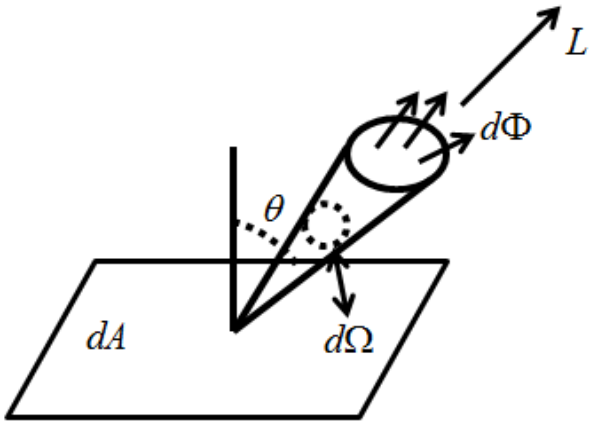

Figure 4. Diagram of the luminous intensity parameters

A source is considered lambertian when the luminous intensity in any direction varies as the cosine of the angle between that direction and the perpendicular to the surface element of the source according to the equation

Equation 4

$$I_L = I_{L,0} \cos\theta$$

Here $I_{L,0}$ is defined as the luminous intensity at the surface normal.

As a consequence Equation 4, a lambertian source therefore has the same luminance regardless of viewing angle, and the total luminous flux per unit area is π times the luminance. Typically, organic light emitting devices are assumed to have a lambertian intensity profile, however, special cases, as in the case of microcavity OLEDs, the lambertian assumption typically does not hold true. More on this topic will be discussed in the ensuing sections.

2.2 The Human Response

As alluded to in the previous section, the standard for lighting and display must account for the response of the human eye. The human response to light is a psychological phenomenon which, at the present, is poorly understood. Consequently, standards for quantifying color are based on mean values for a representative group of people. The most commonly used metric for quantifying color are based on the organization Commission Internationale de l'Eclariage (CIE). The CIE coordinate system will be described in more detail in the foregoing sections.

The human eye detects light by focusing light rays into the retina wherein light energy is converted into electrical energy. The human eye has a spectral

response that depends strongly on wavelength. This spectral response depends on the particular eye as well as the age of the person. Wavelengths below 380nm are filtered out by the cornea and crystalline lens and wavelengths between 380nm and 950nm propagate through with little attenuation. Wavelengths greater than 950nm, however, experience significant attenuation by the infrared water bands and the infrared radiation transmittance above 1400 nm is negligible. The absorbance of wavelengths in the visible region has been shown to increase with age. According to one report as much as a fourfold reduction in transmittance of shorter wavelengths compared to longer wavelengths is common.[55]

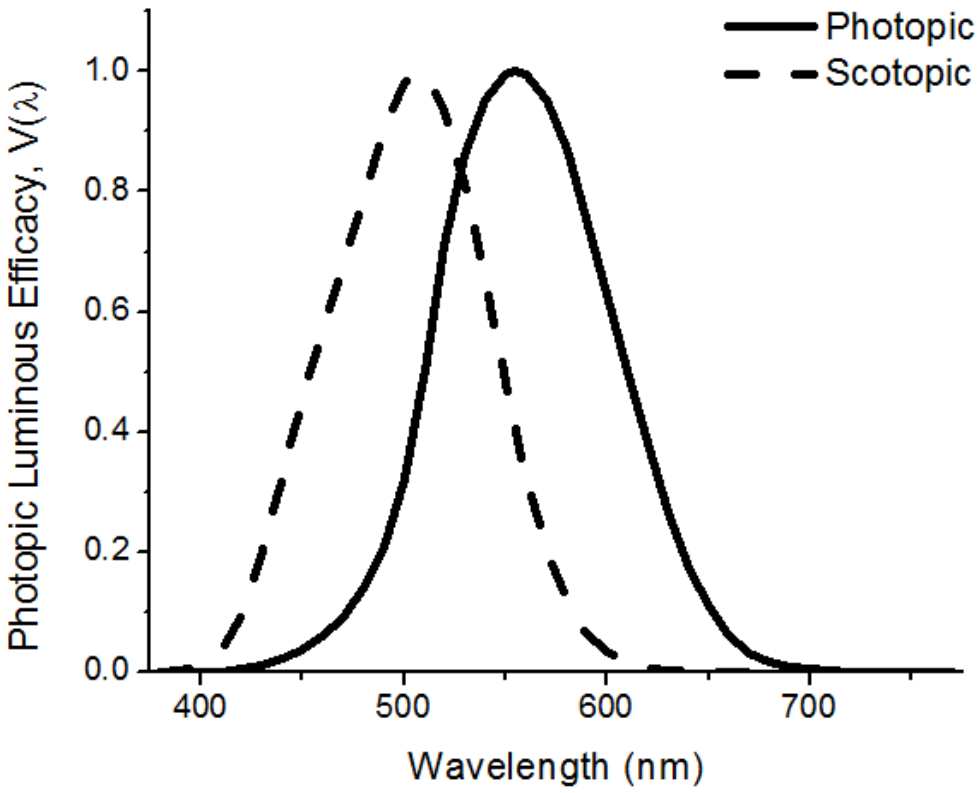

Figure 5. Photopic and Scotopic luminous effieciency versus wavelength

The eye consists of two main classes of photodetectors; rods and cones. Rods are responsible for our scotopic response or night vision and are extremely sensitive to light. Cones are responsible for our photopic or day vision and are responsible for our ability to discriminate color. The normalized scotopic and photopic responsivities are shown in Figure 5. The quantification of OLEDs in terms of the photopic response will be explored in the next sections.

2.3 Light Characterization

The best standard for high quality white light is, naturally, the sun. The solar spectrum can be described by Plank's blackbody spectrum equation which relates the spectral properties of the body to temperature:

Equation 5

$$\rho(\omega) = \frac{h\omega^3}{\pi^2 c^3 (e^{h\omega/k_B T} - 1)}$$

Here, ρ is the energy density per unit frequency, h is Plank's constant, c is the velocity of light, k_B is the Boltzmann constant, ω is the angular frequency, and T is the temperature in Kelvin.

Although actual sunlight as perceived on earth deviates slightly from Equation 5 due to scattering and absorptive effects of the atmosphere, it closely resembles the spectral characteristics of the sunlight and can therefore be used for defining the standards for lighting. Some of these standards will now be discussed.

The color temperature of a blackbody is defined as the color perceived at a certain temperature. For example, a blackbody radiator with a high color

temperature (i.e. 10,000 K) appears blue. For a non-blackbody radiator or source of light for which Equation 5 does not hold, the correlated color temperature (CCT) is the temperature of a blackbody radiator which has a color that most closely resembles that of the light source. The CCT, therefore, only specifies chromaticity and gives no information about the spectral power distribution.

In addition to being used as a measure of chromaticity, the correlated color temperature is also used to specify the color rendering index of a light source. This is an important metric for quantifying the capacity of a source to illuminate all colors in the visible spectrum. For example, the color of two light sources may appear identical, metameric, when viewed directly and will therefore have the same color temperature; however, the color of the reflected light from an object illuminated by these two sources may be significantly different. Thus, a method for distinguishing between two metameric sources such as the color rendering index (CRI) is needed.

The color rendering index (CRI) is a comparison between an object of a light source of a particular correlated color temperature to the reflection from the same object under illumination from a blackbody radiator of the same color temperature. The similarity of the two sources is ranked on a scale from 0 to 100, wherein a rating of 100 is a perfect match to a black body radiator. Sources with a rating above 80 are considered high quality lighting sources. Values below 70 are considered undesirable for natural lighting requirements.

Although CRI and CCT reflect the chromaticity and spectral output of a light source, a more comprehensive chromaticity measure is needed. There are several methods to define the chromaticity of a light source, however, the most common

chromaticity coordinate system used in display and lighting industries and the one that will be used throughout this thesis is the C.I.E. chromaticity coordinates. The method was originally developed in 1931 by CIE which defines all metameric pairs by giving the amounts X, Y, and Z of three imaginary primary colors required by a standard observer to match the color being specified. These amounts are calculated as a summation of the spectral compositions of the radiant power of the source times the spectral tristimulus values, or color matching functions[56] for an equal power source and expressed as

Equation 6

$$X = \int S(\lambda)\bar{x}(\lambda)d\lambda$$
$$Y = \int S(\lambda)\bar{y}(\lambda)d\lambda$$
$$Z = \int S(\lambda)\bar{z}(\lambda)d\lambda$$

Here, s(λ) is the spectral irradiance of the source, and $\bar{x}(\lambda)$, $\bar{y}(\lambda)$, and $\bar{z}(\lambda)$ are the spectral tristimulus values plotted in Figure 6. Chromaticity coordinates (x,y,z) are then calculated according to the following equations

Equation 7

$$x = \frac{X}{X + Y + Z}$$
$$y = \frac{Y}{X + Y + Z}$$
$$z = \frac{Z}{X + Y + Z}$$

By convention, CIE chromaticity coordinates are stated in terms of x and y only (x + y + z = 1) and plotted in a rectangular coordinate system.

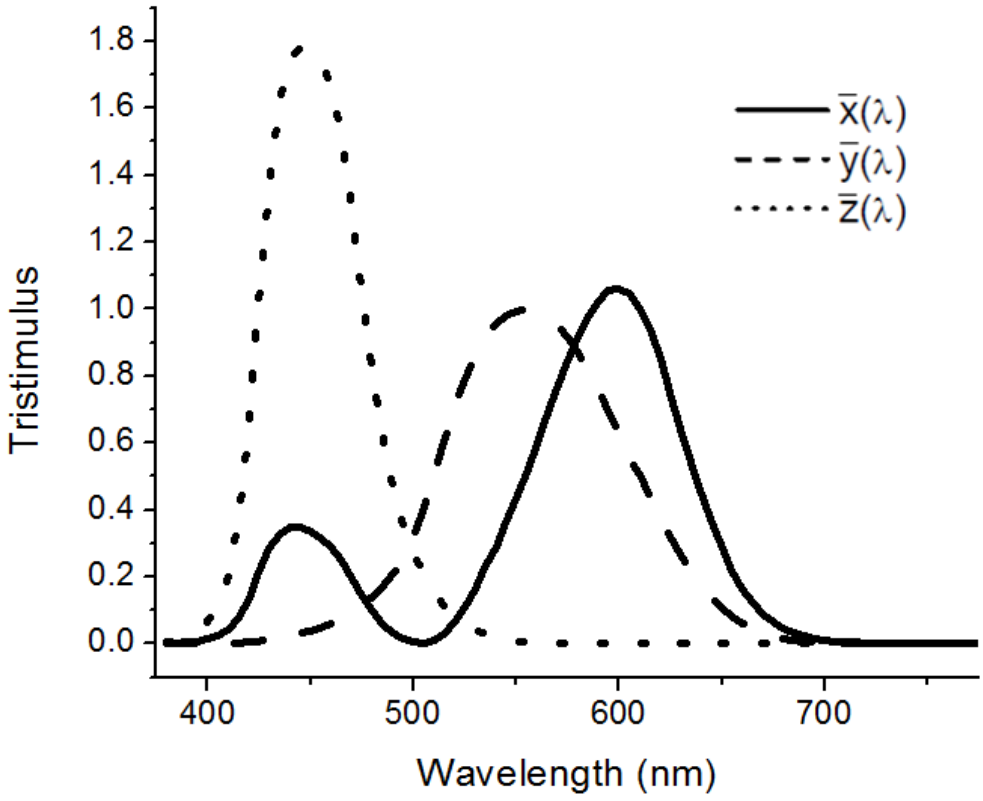

Figure 6. Spectral tristimulus values.

2.4 Experimental Methods and Equipment

2.4.1 Device Physics

An understanding of the basic device physics of OLEDs is necessary to understand the characterization methods in the next sections. This will now be discussed. Organic Light Emitting Diodes are composed of a series of thin, organic layers sandwiched between two conducting electrodes (Figure 7). When a positive

bias is applied to the anode, positive charges (holes) are ejected from the anode and negative charges (electrons) are ejected from the cathode. The charges migrate to the emission zone whereby they localize and relax on an electroluminescent (EL) emitting material resulting in the generation of a photon with a wavelength characteristic of the emitting material (Figure 7).

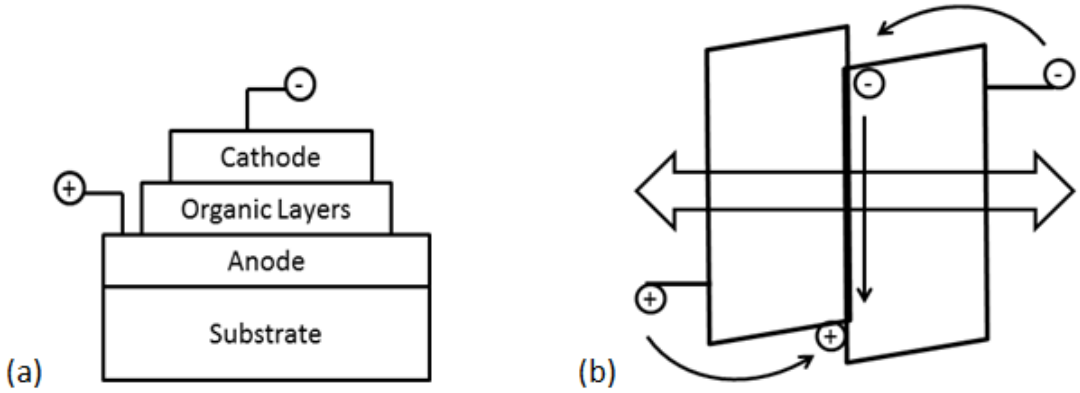

Figure 7. (a) Simplified OLED structure. (b) Energy Diagram of a typical hetrostructure OLED.

The efficiency of an OLED can be defined as the ratio of photons emitted from the device to the number of electrons injected into the molecular layers, known as External Quantum Efficiency (EQE).[57, 58] The EQE depends on 4 parameters and can be expressed as[59, 60]

Equation 8

$$\eta = \gamma \bullet \chi \bullet \eta_r \bullet \eta_{out} = \eta_{\text{int}} \bullet \eta_{out}$$

The charge balance factor (γ) is the ratio of excitons formed to total holes/electrons injected into the molecular layers. Charge imbalance exists due to differing mobility's of the organic carriers. When there is large differential in charge mobility between the hole transporting layer and electron transporting layer, for

example, there is a high probability of holes or electrons traveling though the device without forming an exciton resulting in significant leakage current and consequently low IQE.

The exciton spin factor (χ) is the ratio of photons generated to excitons formed and accounts for the spin statistics of the formed excitons.[35, 37] When holes and electrons combine to form an exciton, the spin states can add to give a total spin of 0 or 1, singlet exciton and triplet exciton respectively. A singlet exciton is antisymmetric under particle exchange with a total spin of 0. A triplet exciton is symmetric under particle exchange with a total spin of 1. Singlet excitons may recombine to form light, a process known as fluorescence. A triplet exciton, however, cannot recombine as recombination is forbidden per the Pauli Exclusion Principle. In the case of small molecules, 25% of the formed excitons are singlets and 75% of the formed excitons are triplets.[38, 46, 49] In the case of polymers, 50% of the formed excitons are singlets and the remaining 50% of the formed excitons are triplets. Thus, the IQE is severely limited by the exciton spin factor for many emissive molecules. However, when heavy metal ions, such as Ir, Pt, and Os, are introduced into the emitter molecules, the strong spin-orbit coupling mixes the excited singlet states and triplet state. Under these conditions, the previously forbidden triplet excitons are able to recombine in a process known as phosphorescence resulting in an exciton factor ~1.

The photoluminescence quantum efficiency (η_r) is the ratio of the number of emitted photons to the number of generated excitons and is intrinsic to the emissive material. The photoluminescence quantum efficiency can be expressed as[61]

Equation 9

$$\eta_r = \frac{\kappa_r}{\kappa_r + \kappa_{nr}}$$

Here κ_r and κ_{nr} denote the rate constants of the radiative and non-radiative decay of excitons. A photoluminescence quantum efficiency of 1 can be obtained with proper molecular design and high purity materials.[62, 63]

The light out-coupling efficiency (η_{out}) is the ratio of photons that exit the device to total photons generated. This efficiency is limited by various optical losses in the device to values of 20-30% typically.[64]

2.4.2 Device Fabrication

All devices in this thesis were processed on a 1 inch by 1 inch glass substrate pre-patterned with Indium Tin Oxide (ITO). The Organic layers and metallic cathode were grown by thermal evaporation in a Travato deposition chamber under high vacuum (~1e-8 Torr) through a shadow mask. The deposition chamber consists of 10 source positions and 4 substrate positions wherein individual control over the material composition and thickness for a given substrate is possible by changing the mask positions on the stage. Each substrate contained 4 emissive pixels with an active area of ~4 mm^2. The organic layers were deposited by passing DC current through a tantalum boat loaded with the given organic material. The electron injection layer, LiF, was deposited by passing a DC current through a tantalum spoon, loaded with a LiF crystal. The aluminum cathode was deposited by passing a DC current through a tungsten filament attached to a Boron Nitride crucible loaded with aluminum pellets. The thickness and deposition rate was controlled and

monitored using a 3 quartz crystal monitors at a deposition rate between 0.1A/sec to 1A/sec.

2.4.3 Photoluminescence

The photoluminescent spectra of the organic semiconducting materials in this thesis were measured on a Horiba Jobin Yvon Fluoro-Log-FL4-1057 spectrometer. The solution spectra were dissolved in a solution of DCM and excited with UV light. Thin film photoluminescent spectra was measured by depositing a thin film on glass under high vacuum by thermal evaporation and exciting with UV light.

2.4.4 Electroluminescence

The electroluminescent spectra of the devices in this thesis were collected on a Horiba Jobin Yvon Fluoro-Log-FL4-1057 spectrometer. The devices were driven at a low current density using a Keithley 2400 source meter to reduce degradation during measurement. The angular dependence on the electroluminescent spectra was measured using a rotating stage.

2.4.5 Photocurrent Measurements

The current-voltage-luminance measurements were conducted using two separate methods. For OLEDs in conventional structures, wherein the lambertian assumption is valid, current-voltage data was collected while the device was voltage driven from 0V to 8V using a Keithley 2400 source meter. The light emitted from the device was connected to a fiber optic cable wherein the emitted light propagated through the cable into a calibrated silicon photodiode and the photocurrent signal from the detector was collected. To account for light lost on account of absorbance in

the fiber optic cable and the gap between the device/fiber optic cable and between the fiber optic cable/silicon photodiode, a geometric factor was incorporated into the efficiency calculations to be discussed in the next section. The geometric factor (ratio of light detected to total light emitted) was determined by using a reference structure with a known efficiency and matching brightness with voltage, which was determined to be 0.20. The low geometric factor is a result of the large separation distance between the device surface and fiber optic cable and the between the fiber optic cable and silicon photodiode. The second method, wherein the lambertian assumption is not valid employs a large aperture light collection technique. Similar to the first method, current-voltage data was collected while the device was voltage driven from 0V to 8V using a Keithley 2400 source meter. The light emitted from the device was collected into an OSI optoelectronic photodiode, 220-DP, with a large active area (~200 mm^2) to cover the active device area entirely. The photodiode was in intimate contact with the device such that the majority of the emitted light was collected. As a consequence of the protective glass window casing on the large area photodiode, some of the light emitted from the device is reflected at the protective window surface and a geometric factor is required in the calculation to account for this loss. The geometric factor for the calibrated large area photodiode was determined following the same approach as the first method and was determined to be 0.85.

2.4.6 Characterization

When calculating the efficiency of OLEDs from J-V-L data it is important to

account for the wavelength dependent spectral response of the photodetector in the external quantum efficiency equation. Typically the spectral emission of OLEDs are broad and can introduce large errors in measurement if the wavelength dependence of the photodiode responsivity is not taken into account. A general equation for the external quantum efficiency that accounts for the wavelength dependent photodiode responsivity can be expressed as[57]

Equation 10

$$\eta_{ext} = \frac{q\int \lambda I_{\det}(\lambda)d\lambda}{hcfI_{OLED}\int R(\lambda)d\lambda}$$

Here h is Plank's constant, c is the speed of light in vacuum, f is the geometric factor or fraction of light emitted to that coupled into the detector, q is the electronic charge, I_{OLED} is the current, I_{det} is the incremental photocurrent generated in the photodetector by the OLED power ($P_{OLED}(\lambda)$) emitted at the center wavelength, λ, and R(λ) is the incremental photodiode responsivity between wavelengths λ and λ +dλ ($R(\lambda)=I_{det}(\lambda)/f(\lambda)P_{OLED}(\lambda)$). When the emission pattern is not lambertian, as in the case of microcavity OLEDs, then the geometric factor depends strongly on wavelength. In this case, the best experimental set up employs large aperture light collection optics such that the wavelength dependence of *f* is small (see section 2.4.5). Often times the detector sensitivity is expressed in terms of its own external quantum efficiency ($\eta_{det}=hcR(\lambda)/q\lambda$). Rearranging Equation 10 the external quantum efficiency can be expressed as[57]

Equation 11

$$\eta_{ext} = \frac{q\int \lambda I_{\det}(\lambda)d\lambda}{fI_{OLED}\int \lambda \eta_{\det}(\lambda)d\lambda}$$

In display, the luminous efficiency (η_L), in candelas per amp (cd/A) is typically used to quantify the properties of an OLED. This definition is similar to the external quantum efficiency; however, η_L weights all incident photons according to the photopic response of the eye. With this definition the luminous efficiency can be expressed as[57]

Equation 12

$$\eta_L = AL / I_{OLED}$$

Here L is the luminance of the OLED and A is the active area.

Another common metric used in display is the luminous power efficiency, or luminosity (η_p), in lumens per watt (lm/W). The luminous power efficiency is the ratio of luminous power emitted in the forward direction, L_p, to the total electrical power required to drive the OLED at a particular voltage. In terms of the spectrally resolved efficiencies previously discussed, the luminous power efficiency can be written as[57]

Equation 13

$$\eta_P = \frac{\phi_0\int g(\lambda)I_{\det}(\lambda)/R(\lambda)d\lambda}{fI_{OLED}V}$$

Here V is the voltage (V), g(λ) is the photopic response with a peak value of φ_0=683lm/W at λ=555nm where g(λ=555nm)=1.[65]

As can be seen in Equation 12 and 13, both the luminous efficiency and the luminous power efficiency depend strongly on the visible wavelength content of the OLED spectrum. Consequently, the external quantum efficiency tends to be a more useful metric for comparing the fundamental physical mechanisms responsible for light emission within an OLED. However, in lighting and display the luminous power efficiency is useful for comparing the power dissipated by the device. These terms will be used frequently throughout the remainder of this thesis.

3 SINGLE DOPED WHITE ORGANIC LIGHT EMITTING DIODES

3.1 Introduction

The typical approach to achieving white light is through the simultaneous emission of multiple emissive materials, which need to be employed in either a single emissive layer with multiple molecular emitters or multiple emissive layers.[42, 66, 67] However, the use of these multi-layered or multi-dopant device architectures, not only results in increased fabrication difficulty and costs but also yields several possible operational problems making them a less attractive approach for generating white light. Among these are voltage-dependent emission and color aging issues due to differing electrical properties or different degradation processes for each emissive dopant or emissive layer.[68] Therefore, in order to greatly simplify the device structure and eliminate many of these concerns, it will be ideal to develop an efficient and stable white OLED using a single emitter.

One possible route to achieving white light generation from a single emitter is through an excimer emitting complex, which has the potential of generating broad emission from a combination of red-shifted “aggregate” or excimer emission with the parent monomer emission.[69] With an appropriate molecular design, emission over the entire visible range is possible and high quality white light can be achieved with an appropriate balance of monomer and excimer contributions. Recently, there has been a growing interest in Pt(II) compounds for applications in excimer-based WOLEDs due to their square-planar geometries which offer the possibility of strong intermolecular interactions via intimate Pt-Pt contacts and their potential to form excimers at moderate concentrations with significantly low energy aggregate

emission with respect to the monomer emission.[70] Based on this approach, efficient excimer based WOLEDs utilizing square planar Pt complexes have been reported.[71-73]

Although the phenomenon of excimer formation has been widely observed,[74, 75] the photophysical properties of excimers remain poorly understood. For this reason, progress on phosphorescent excimers has depended almost entirely on the materials development. The first successful example of phosphorescent emitters for excimer-based white OLEDs is platinum (II) [2-(4',6'-difluorophenyl)pyridinato-N, $C^{2'}$)](2,4-pentanedionato) (FPt).[71] In contrast to many organic emitters, FPt can form a broadly emitting excimer. Thus, white light can be generated by coupling blue-green like emission from single FPt molecules and orange like emission from FPt aggregates. Maximizing the device efficiency and achieving high quality white illumination are keys to the success of excimer-based WOLEDs for lighting applications. The highest quality white illumination requires sources with CIE coordinates close to (0.33, 0.33) and a CRI value over 80.[74] As illustrated in Figure 8, previously reported excimer based WOLEDS using FPt and platinum(II) 1,3-difluoro-4,6-di(2-pyridinyl)benzene chloride (Pt-4) cannot produce a satisfactory white EL spectra due to either inefficient monomer emission (FPt)[71, 72] or unsuitable excimer emission color (Pt-4)[73]. Thus, further development in highly efficient excimer emitting platinum based complexes with monomer and excimer contributions that span the entire visible spectrum are desired. In the ensuing sections, a summary of a highly efficient excimer based WOLED implementing the complex platinum(II) bis(N-methyl-imidazolyl)-*benzene* chloride (Pt-16) with superior color quality and device efficiency's compared with FPt and Pt-4 will be

outlined. WOLEDs implementing Pt-16 exhibited a maximum external quantum efficiency (EQE) of 20.1% with a peak power efficiency of over 50 lm/W on a planar glass substrate and color coordinates of CIE(x=0.33, y=0.33) and a CRI of 80 as outlined if Figure 8.

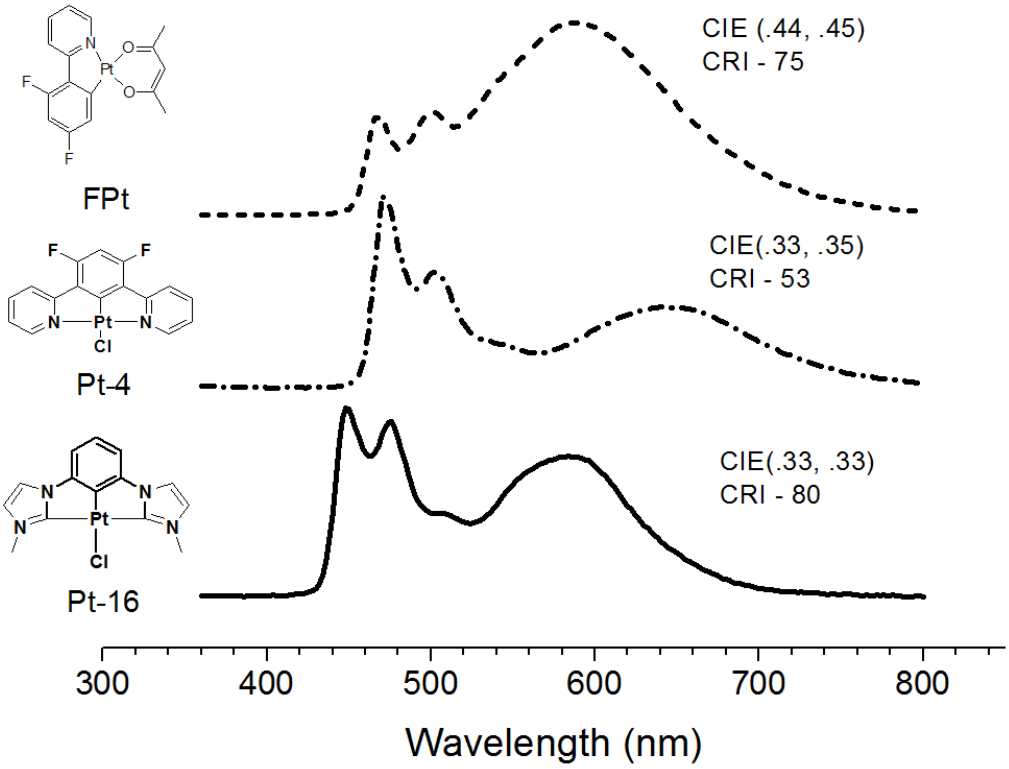

Figure 8. Molecular structure and emission spectra of FPt (dashed), Pt-4 (dash-dot), and Pt-16 (solid) in optimized device architectures with their reported CIE and CRI.

In addition to demonstrating highly efficient WOLEDs with excellent color quality, the ensuing sections will highlight some excimer behaviors found during our study. Unlike monochromic OLEDs, the EQE of which depends on the photoluminescent (PL) efficiency of emitters, the EQE of excimer-based WOLEDs hinges on the combined factors of PL efficiency from both monomers and excimers.[76] There is a lack of understanding of what determines the PL efficiency of excimers

which can be affected by many factors such as: the excited properties of monomers, the variation in the intermolecular force between monomers due to different molecular packing, host materials, or processing conditions, and quenching processes for either excitons or excimers. [77] Based on our experience, even a small molecular structural modification between platinum (II) bis(N-methyl-imidazolyl)-*benzene* chloride[9] (Pt-16) and platinum(II) bis(N-methyl-imidazolyl)-*toluene* chloride (Pt-17) (Figure 9), could significantly alter electroluminescent (EL) properties of their corresponding phosphorescent excimers. The ensuing sections will highlight some of these differences with a comprehensive comparative summary of the device performance of Pt-16 and Pt-17 excimer based WOLEDs.

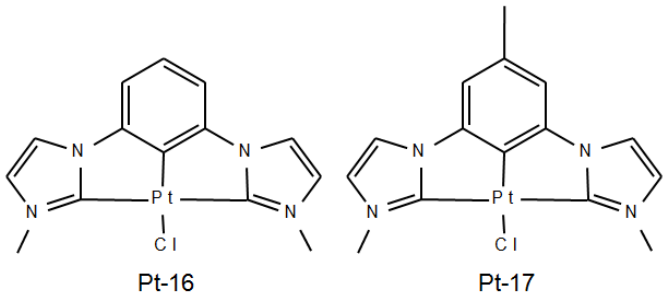

Figure 9. Molecular structure of Pt-16 (left) and Pt-17 (right).

3.2 Experimental

Room temperature photoluminescent spectra were measured in a solution of dichloromethane in a Horiba Jobin Yvon Fluoro-log-FL4_1057 spectrometer. Devices were fabricated on ITO coated glass substrates. PEDOT:PSS was filtered through a 0.2 μm filter and spin-coated on the pre-cleaned substrates, giving a 40-50 nm thick film. All other materials were deposited in a glove-box hosted vacuum deposition

system at a pressure of 10^{-7}torr. The EML was evaporated by a co-deposition of the emitter and 26mCPy to form a 25 nm-thick blend film.

The absolute PL quantum efficiency measurements of doped thin films were carried out on a Hamamatsu C9920 system equipped with a xenon lamp, integrating sphere and a model C10027 photonic multi-channel analyzer. EL spectra were measured with an Ocean Optics HR-4000 spectrometer and I-V-L characteristics were taken with a Keithley 2400 Source Meter and a Newport 818 Si photodiode. All device operation and measurement were carried out inside a nitrogen-filled glove-box. Individual devices had areas of 0.04 cm^2. Agreement between luminance, optical power and EL spectra was verified with a calibrated Photo Research PR-670 Spectroradiometer with all devices assumed to be Lambertian emitters.

The materials used have acronyms as follows: NPD: N,N′-diphenyl-N,N′-bis(1-naphthyl)-1,1′-biphenyl-4,4″-diamine. TAPC: di-(4-N,N-ditolyl-amino-phenyl) cyclohexane. PO15: 2,8-bis(diphenylphosphoryl)-dibenzothiophene. 26mCPy: 2,6-bis(N-carbazolyl) pyridine. BmPyPB: 1,3-bis(3,5-dipyrid-3-yl-phenyl)benzene.

A series of devices implementing Pt-16 and Pt-17 were fabricated according to the following layer sequence: Glass/Patterned ITO/40nm-50nm PEDOT:PSS/30nm NPD as a hole-transporting layer/10nm TAPC as an electron-blocking layer/25 nm emissive layer/40nm electron transporting layer and hole-blocking layer/1nm LiF/90nm Al cathode. The emissive layer consists of either 26mCPy as a host or TAPC:PO15(1:1) (Structures A and B) as co-host materials with Pt-16 and Pt-17 as a phosphorescent emitters. The exciton blocking layer and electron transporting layers are either a combined HBL/ETL of 40nm PO15 (structure A) or a separated HBL of 10nm PO15 and ETL of 30nm BmPyPB (structure B). A summary of the various

device architectures and molecular structures of the aforementioned materials are shown in Figure 10.

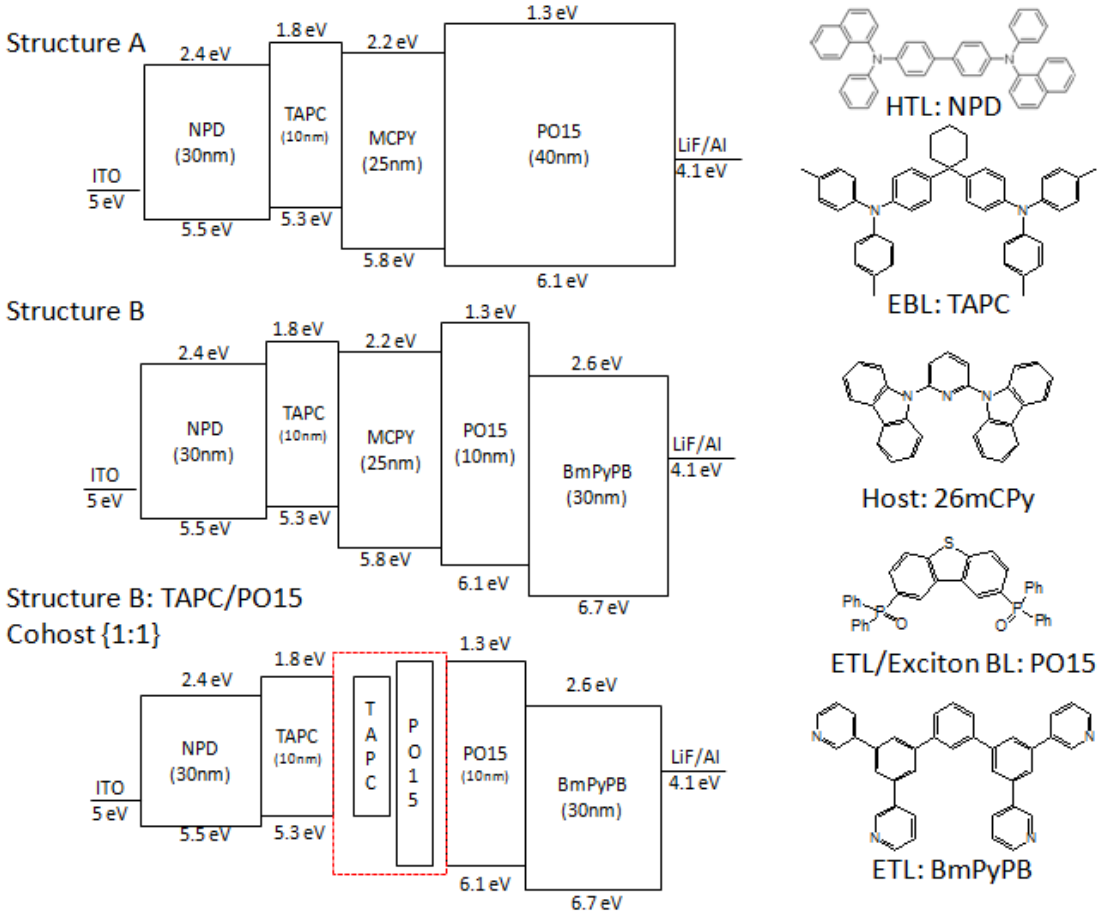

Figure 10. The energy level diagram of the device structures in this study. The molecular structure of the materials used in device structure A (top), structure B (middle), and the cohost structure B (bottom) are shown on the right.

3.3 Results and Discussion

The photoluminescent spectra of Pt-16 and Pt-17 in a solution of DCM are shown in Figure 11. Both Pt-16 and Pt-17 share similar photoluminescent characteristics with a monomer emission peak of 450nm and 460nm for the Pt-16

complex and Pt-17 complex, respectively. Additionally, the emitter, Pt-16, has a slightly narrower emission band compared with Pt-17 with a FWHM of 46nm compared to 51nm for Pt-17.

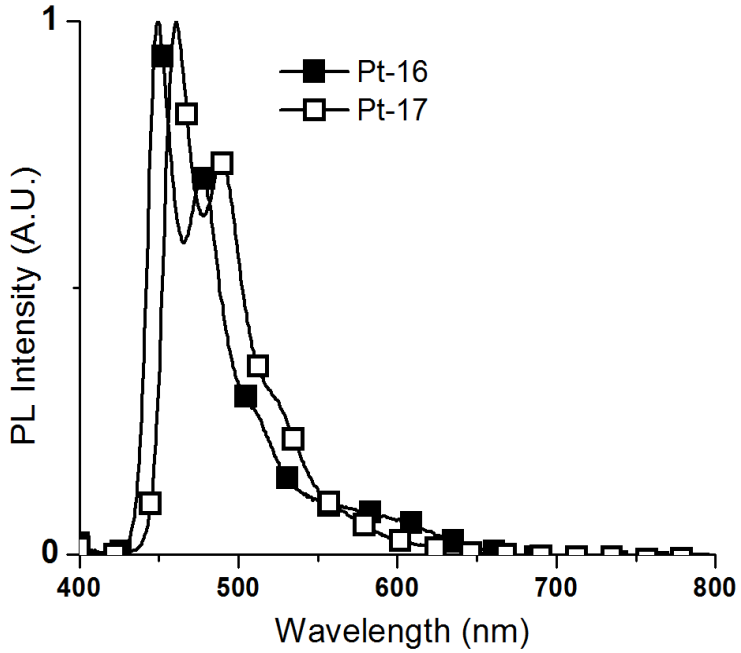

Figure 11. The photoluminescent spectra of Pt-16 and Pt-17 in a solution of DCM.

Despite containing similar monomer emission energy and similar molecular structures, the device characteristics of Pt-16 and Pt-17 based OLEDs are drastically different. With a similar device structure of ITO/PEDOT:PSS/NPD(30 nm)/TAPC(10 nm)/x%emitter:26mCPy(25 nm)/PO15(40 nm)/LiF/Al, Pt-16 and Pt-17 based OLEDs demonstrate different trends in the dependence of device efficiency on dopant concentration. A summary of Pt-16 and Pt-17 devices are illustrated in Figure 12.

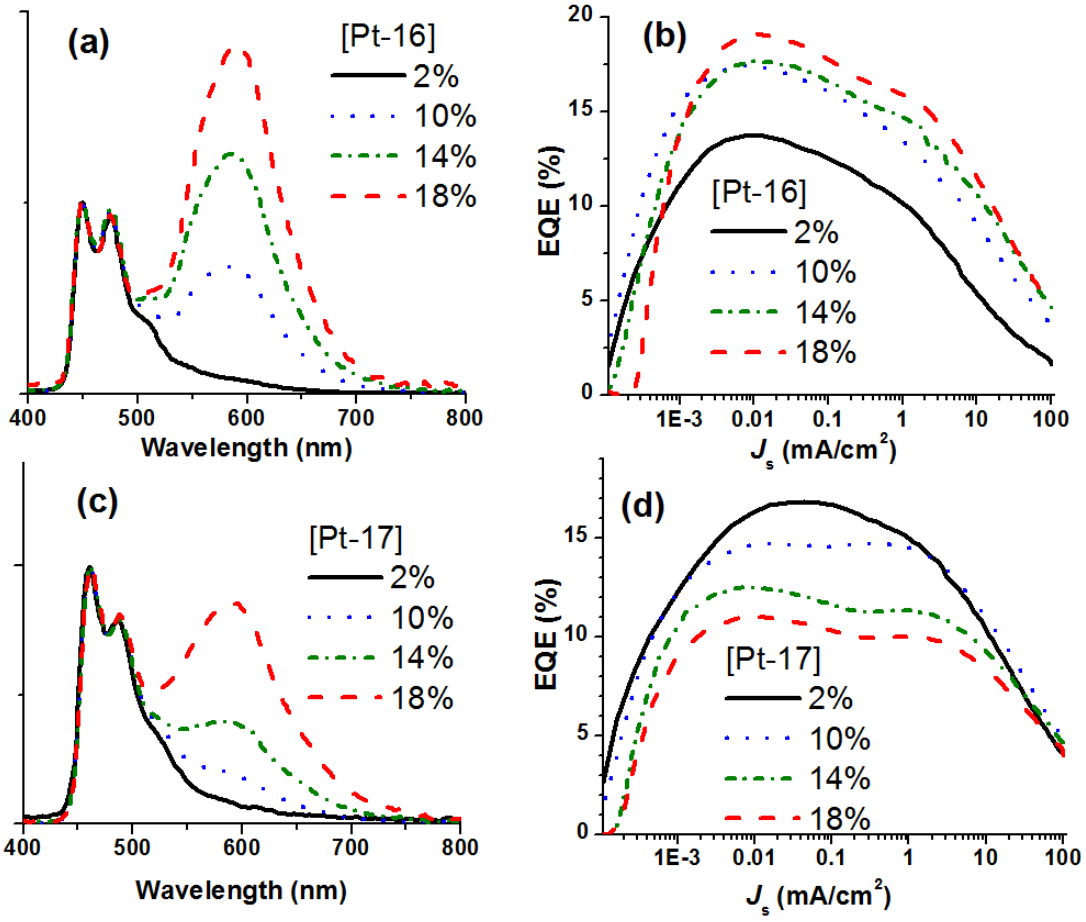

Figure 12. Electroluminescent emission spectra (a), Forward-viewing external quantum efficiency vs. current density (b) for Pt-16 and electroluminescent emission spectra (c), Forward-viewing external quantum efficiency vs. current density (d) for Pt-17 with concentrations of 2% (solid line), 10% (dotted line), 14% (dash-dotted line), and 18% (dashed line) in the device structure of : ITO/PEDOT:PSS/30nm NPD/10nm TAPC/25nm x% emitter in 26mCPy/40nm PO15/LiF/Al.

With increasing dopant concentrations, both Pt-16 and Pt-17 based OLEDs observe the general trend of having a more pronounced red-shifted emission peak (Figure 12) that is attributed to excimer emission rather than dimer emission on the basis of no observable red-shifted absorption band for Pt-16:26mCPy at high dopant concentrations.[71-73] However, the device efficiencies of Pt-16 based OLEDs (Figure 12, top) are much higher at high dopant concentrations and a slightly lower at low dopant concentration than those reported in Pt-17 based devices (Figure 12, bottom).

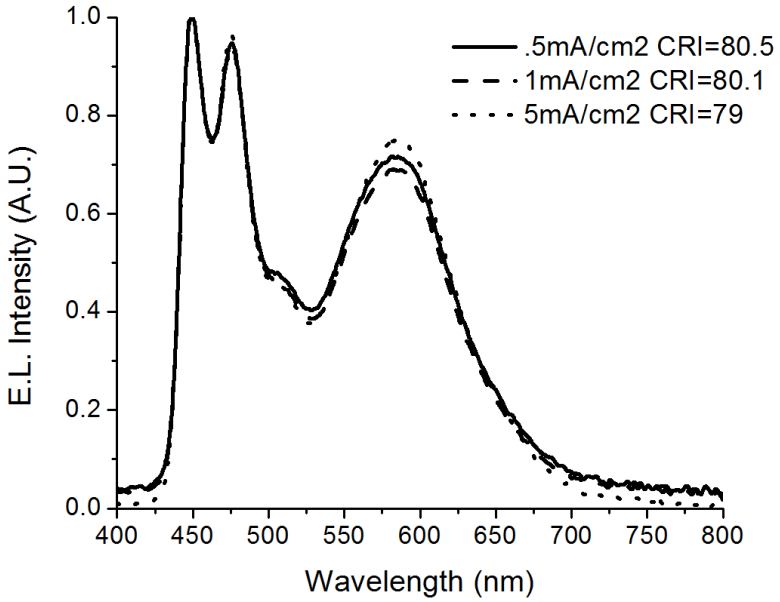

Figure 13. The electroluminescent spectra at a drive current of 0.5 mA/cm^2, 1 mA/cm^2,, and 5 mA/cm^2, for Pt-16 in the device structure: ITO/PEDOT:PSS/30nm NPD/10nm TAPC/25nm 10% Pt-16 in 26mCPy/40nm PO15/LiF/Al.

With respect to the electroluminescent characteristics, as the dopant concentration for Pt-17 based OLEDs increases, the ratio of excimer emission vs. monomer emission increases and yields a white light emission with appropriate CIE coordinates and desirable CRI values only at concentrations as high as 18%. However, this increased excimer contribution at high concentrations is accompanied by a dramatic drop-off in maximum EQE from 16.9% for the 2%-doped Pt-17 device to 11.0% for the 18%-doped Pt-17 device. On the other hand, the peak EQE of Pt-16 devices increases with higher dopant concentration from 13.7% for the 2%-doped Pt-16 device to 19.2% for the 18%-doped Pt-16 device despite showing similar resistances in the current-voltage characteristics for devices with the same high dopant concentration. Moreover, for 10%-doped Pt-16 device (versus 18%-doped Pt-17 device), the excimer emission is strong enough to yield a white emission with CIE coordinates of (0.32, 0.32) and a CRI of 80. This high color quality emission spectrum

showed minimal dependence on current density (and driving voltage) within the typical operating range of 100-500 cd/m^2 (Figure 13) as has been previously demonstrated for excimer based devices. This independence of electroluminescent spectral characteristics on the driving current make excimer based WOLEDs an attractive solution for lighting and display enabling consistent color characteristics independent of drive current and brightness. It has been shown in a previous reporting that Pt-17 based excimer WOLEDs also exhibit this independence of electroluminescent spectral characteristics on the driving current.[73]

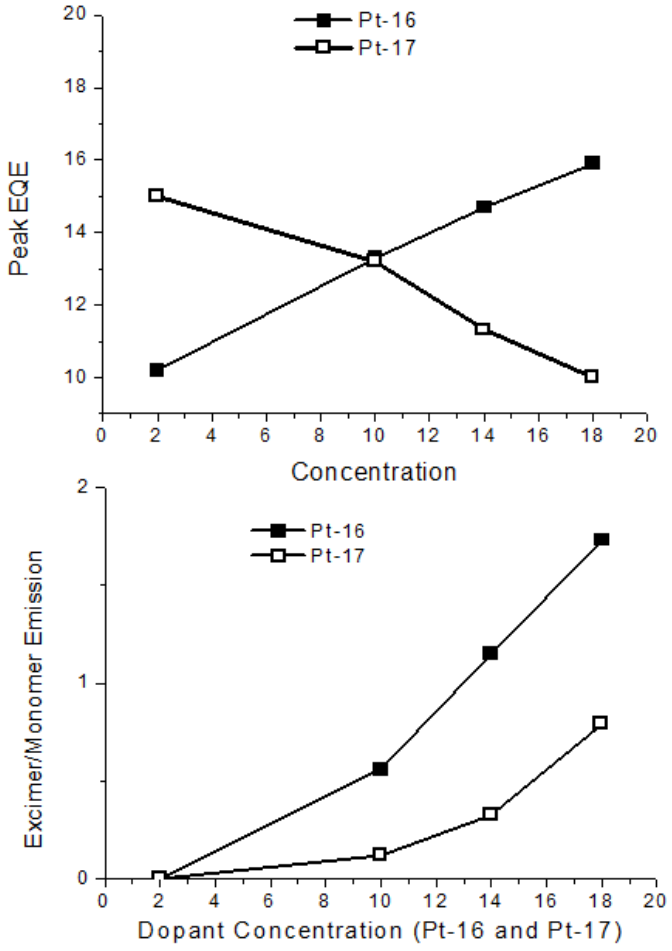

Figure 14. Peak EQE versus dopant concentration (left) and Excimer/Monomer emission intensity ratio versus dopant concentration of Pt-16 (solid squares) and Pt-

17 (open squares) in the device structure of: ITO/PEDOT:PSS/30nm NPD/10nm TAPC/25nm x% emitter in 26mCPy/40nm PO15/LiF/Al.

A summary of the peak EQE versus concentration for Pt-16 and Pt-17 based WOLEDs as well as the ratio of excimer/monomer emission ratio versus concentration of Pt-16 and Pt-17 are shown in Figure 14. WOLEDs implementing the complex Pt-16 form excimer more readily than WOLEDs implementing the complex Pt-17 with an excimer peak that exceeds the monomer peak at concentrations as low as 14% compared to >18% for WOLEDs implementing Pt-17.

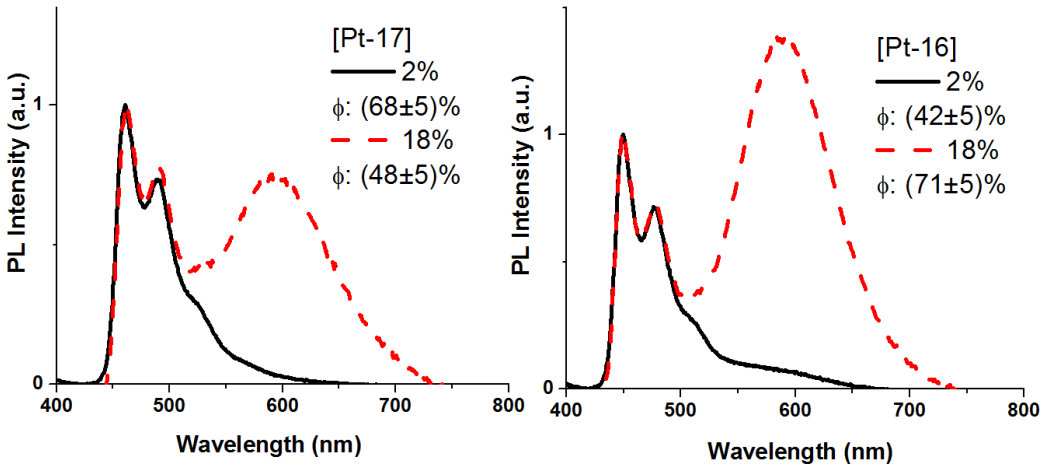

Figure 15. The thin film PL spectra of Pt-17 (left) and Pt-16 (right) and PL quantum efficiency's (inset) for a dopant concentration of 2% (monomer emission) and 18% (monomer plus excimer emission).

The PL quantum efficiencies of doped films at various concentrations were measured in order to uncover the cause for the different device characteristics of Pt-16 and Pt-17 based OLEDs (Figure 15). Although both Pt-16 and Pt-17 have similar molecular structures, the quantum efficiency of 2% Pt-16:26mCPy film (42±5%) is much lower than that of 2% Pt-17:26mCPy film (68±5%). This can be attributed to a faster non-radiative decay process for Pt-16 due to its higher emission energy, resulting in a smaller energy difference between the lowest excited

state and the metal-centered quenching state. A similar trend has also been observed for other blue-emitting Pt and Ir complexes.[78, 79] However, it is surprising that the quantum efficiency of 18% Pt-16:26mCPy film (71±5%) is much higher than that of 18% Pt-17:26mCPy film (48±5%) with both excimers demonstrating similar emission spectra and emission energies (Figure 15). Thus, the EQE decrease of the Pt-17 based OLEDs with higher dopant concentrations, can be associated with the drop-off in PL quantum efficiency of the Pt-17 doped thin films, in addition to considering possible polaron-quenching and other exciton-quenching mechanisms.[80, 81] Meanwhile, the significant increase in the PL quantum efficiency of Pt-16 doped thin films at high concentrations can explain the improvement in EQE for Pt-16 based OLEDs with larger dopant concentrations, which makes Pt-16 a perfect candidate for excimer based white OLEDs.

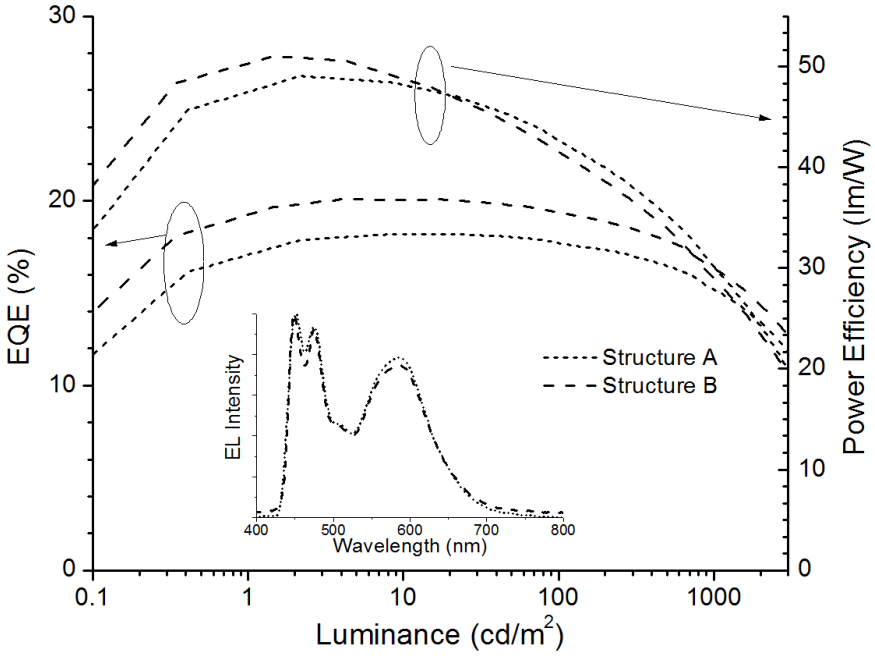

Figure 16. Forward-viewing external quantum efficiency (%) versus current density (mA/cm^2) of Pt-16 based WOLEDs of Structure A (dotted line) and Structure B cohost (dashed line). Electroluminescent spectra (inset) of the devices at 1 mA/cm^2.

Structure A is: ITO/PEDOT:PSS/30nm NPD/10nm TAPC/25nm 10:45:45 Pt-16:TAPC:PO15/40nm PO15/LiF/Al. Structure B cohost is: ITO/PEDOT:PSS/20nm TAPC/25nm 10:45:45 Pt-16:TAPC:PO15/10nm PO15/30nm BmPyPB/LiF/Al.

Utilizing the benefits of efficient Pt-16 excimer emission, devices were fabricated aimed at achieving high EQE at typical operating conditions of 100 to 1000cd/m^2. To reduce the high EQE "roll-off" at higher luminance, 26mCPy was replaced with a co-host of TAPC:PO15 (1:1) for 10%-doped Pt-16 device (labeled as Structure B cohost) following the previous literature report.[82] Additionally, a 30nm BmPyPB layer was used to replace 30nm of the PO15 layer (label as Structure B) in order to further improve charge balance and resulting device efficiency. Although, BmPyPB has been reported to have a higher electron mobility than PO15, a 10nm PO15 layer is still necessary as a hole blocking layer as the LUMO level of BmPyPB is too low and will potentially quench Pt-16 excitons.[83] As a result, the Pt-16 device with the Structure B cohost, exhibits the highest device efficiency (η_{EQE} = 20.1%) amongst all reported excimer-based WOLEDs. A summary of the Pt-16 in the aforementioned device structures are shown in Figure 16 and a summary of all devices fabricated in this study are shown in Table 4. The EL spectrum of this device also yields highly desirable CIE coordinates of (0.33, 0.33) and a CRI of 80, with EL characteristics independent of current density. A maximum forward power efficiency of η_P=51 lm/W was recorded at the brightness of 1 cd/m^2, which remains at a high η_P=41 lm/W at 100 cd/m^2 and η_P=29 lm/W at 1000 cd/m^2. The performance of this device is comparable to the best reported WOLEDs in literature that have achieved maximum η_{EQE}=20.1% and peak η_P=41.3 lm/W for white light with CIE (0.38, 0.45) and CRI of 85 but used 3 different dopants embedded in multiple emissive layers. Another report demonstrated a maximum η_{EQE}=26.6% and peak η_P=67.2 lm/W for a WOLED employing a blue fluorescent host material and a yellow

phosphorescent dopant but produced only a yellowish white light with CIE (0.46, 0.44), unsatisfactory CRI, and showed moderate voltage dependence in the emission color.[82]

Table 4. A summary of device characteristics at 1 mA/cm^2. The device structure is ITO(65nm)/PEDOT/NPD(30nm)/TAPC(10nm)/x%Emitter:26mCPy(25nm)/PO15(40nm)/LiF(1nm)/Al(90nm) unless otherwise noted (*†).

Emitter	Bias(V)	luminance (cd/m^2)	EQE (%)	CIEx	CIEy	CRI	P.E. (lm/W)
2%Pt-16	4.7	150	10.2	0.18	0.19	--	10.0
10%Pt-16	4.4	295	13.3	0.32	0.32	80	21.0
14%Pt-16	4.8	319	14.7	0.38	0.37	73	21.1
18%Pt-16	4.6	386	15.9	0.41	0.39	70	26.5
10%Pt-16*	3.3	371	16.8	0.32	0.33	80	35.2
10%Pt-16*†	3.5	396	18.2	0.33	0.33	80	35.2
2%Pt-17	4.8	249	15.0	0.18	0.25	--	16.3
10%Pt-17	5.2	285	14.5	0.23	0.30	64	17.2
14%Pt-17	4.6	236	11.3	0.29	0.33	76	16
18%Pt-17	4.5	226	10.0	0.37	0.38	80	15.9
18%Pt-17*	4.0	350	15.7	0.37	0.40	80	27.3

*A Cohost of TAPC:PO15 is used in the EML
†A 10nm PO15/30nm BmPyPB HBL/ETL is used

3.4 Conclusion

In this section, a possible alternative to generating broad white light emission from multiple sub-elemental colors was demonstrated and a highly efficient white light emission from a single dopant and single emissive layer was achieved. WOLEDs implementing the complex Pt-16 achieved a peak EQE over 20%, CIE coordinates of (0.33, 0.33) and a CRI value of 80, which are comparable or superior to state-of-the-art WOLEDs with multiple dopants. Moreover, excimer-based WOLEDs will have great potential to further improve the device efficiency if more efficient blue-emitting square planar Pt complexes can be developed. The record high power efficiency of Pt-16 based WOLEDs can be further improved by employing state-of-the-art charge-injection materials and out-coupling techniques, which will set a clear path for the potential of a single-doped WOLED with η_P of 100 lm/W. Overall, the demonstration of a single-doped WOLEDs with high efficiency and high illumination quality presents a unique opportunity to significantly simplify the device architecture and eliminate the problems of color aging and color instability for WOLEDs using multiple emitters. This will help to expedite the potential commercialization of WOLEDs for lighting applications.

4 A ROUTE TOWARDS STABLE BLUE PHOLEDS

4.1 Introduction

Organometallic phosphorescent complexes have become the mainstay of highly efficient OLEDs and significant progress has been made in recent years with respect to their quantum efficiency's.[41] Their ability to harvest 100% of electrogenerated excitons[36, 84] yielding high external quantum efficiencies[85] makes them an essential factor in highly efficient of OLEDs, however further development in the availability of phosphorescent complexes is needed. More specifically, phosphorescent complexes that are both highly efficient and electrochemically stable yielding high operational device stability are highly desired. Though, great strides have been made in recent years in this area, the realization of both highly efficient and highly stable phosphorescent complexes remains a challenge. Blue emitting phosphorescent complexes in particular, which typically exhibit lower operational lifetimes compared to red and green, are highly desired and essential if OLEDs are to compete with existing lighting and display technologies.[86]

Thus far, the approach to achieve efficient blue phosphorescent OLEDs has primarily focused on Ir-based complexes.[87, 88] In particular extremely efficient deep blue emitting devices have been achieved using fluorinated Ir complexes such as iridium(III) bis(3',5'-diflouro-4'-cyanophenyl-pyridinato-N,C^2) picolinate (FCNIrpic) which exhibited a maximum external quantum efficiency (EQE) of 24.2% and Commission Internationale de L'Éclairage (CIE) coordinates of (0.14,0.20).[89] More recently, Pt-based complexes have also received increasing attention as they have demonstrated external quantum efficiencies (EQE) approaching or equal to their

Iridium analogs.[90] One such example, platinum(II) 1,3-diflouro-4,6-di(2-pyridinyl)benzene chloride (Pt-4) exhibited a maximum EQE of 16% and CIE coordinates (0.16, 0.26).[91] Despite the high efficiencies exhibited by fluorinated Pt or Ir complexes, the large electro-negativity of fluorine may destabilize the molecule, leading to potentially short device operational lifetimes.[92] Thus blue phosphorescent emitters with fluorine-free cyclometalating ligands are desired.

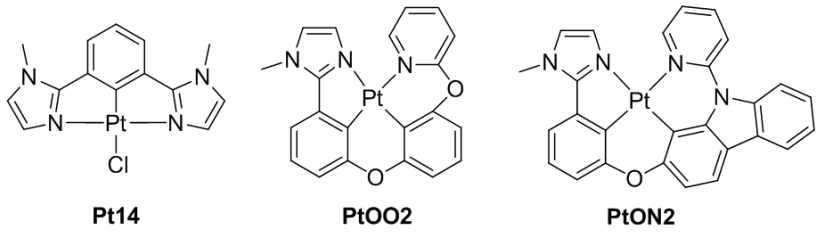

Figure 17. The molculcar structure of Pt14 (left), PtOO2 (middle), and PtON2 (right).

One investigation of a series of platinum complexes with a fluorine free blue phosphorescent emitter utilized a Pt(N^C^N)Cl cyclometalating ligand.[93] In the investigation, devices utilizing the complex Platinum m-di(methyl-imidazolyl)benzene Chloride (Pt-14) achieved impressive device efficiencies of over 18%. Nevertheless, N^C^N type compounds like Pt-14, typically still require monoanionic ligands such as a phenoxyl group or chloride to bond to the platinum ion, thus, a new molecular design motif with a more stable molecular structure will be highly desired.[94, 95] Recently, there has been demonstrated success in the utilization of tetradentate, cyclometalated platinum complexes which have the benefit of potentially being completely halogen free and have also demonstrated high photoluminescent quantum yields of close to 100%.[96] In this study, such tetradentated platinum complexes having blue-green emission and external

quantum efficiencies (EQE) exceeding 22% in a device setting are demonstrated. The molecular structures of the complexes investigated in this study (Pt-14, PtOO2 and PtON2) are shown in Figure 17.

4.2 Experimental

4.2.1 Experimental Conditions

The absorption spectra were recorded on an Agilent 8453 UV-visible Spectrometer. Steady state emission experiments at both room temperature and 77K were performed on a Horiba Jobin Yvon Fluoro-Log-FL4-1057 spectrometer. Photoluminescent quantum efficiency (Φ) measurements were carried out at room temperature in a solution of dichloromethane. Before the emission spectra were measured, the solutions were thoroughly bubbled by nitrogen inside of a glovebox with the content of oxygen less than 0.1 ppm. A solution of coumarin 47 (coumarin 1; Φ=0.73, excited at 360nm)[97] in ethanol was used as references for Pt complexes. The equation $\Phi_s = \Phi_r[(\eta_s^2 A_r I_s)/(\eta_r^2 A_s I_r)]$ was used to calculate quantum yield, where Φ_s is the quantum yield of the sample, Φ_r is the quantum yield of the reference, η is the refractive index of the solvent, A_s and A_r are the absorbances of the sample and reference at the wavelength of excitation, and I_s and I_r are the integrated areas of emission bands.[98] Phosphorescence lifetime (τ) were performed on the same spectrometer with a time correlated single photon counting method using a LED excitation source. The radiative decay rate constant (k_r) was estimated by $k_r=\Phi/\tau$ and the nonradiative decay rate (k_{nr}) was estimated by $k_{nr}=(1-\Phi)/\tau$. For low temperature (77 K) emission spectra, the solute was dissolved in 2-MeTHF and cooled to 77K with liquid nitrogen. ^{1}H spectrum was recorded at 400 MHz, ^{13}C NMR

spectrum was recorded at 400 MHz on Varian Liquid-State NMR spectrometer in DMSO-d_6 solutions using residual H_2O (δ = 3.33 ppm) as internal reference for ^1H NMR spectrum and DMSO-d_6 (δ = 39.52 ppm) as internal reference for ^{13}C NMR spectrum.

Cyclic voltammetry and differential pulse voltammetry were performed using a CH Instrument 610B electrochemical analyzer. Anhydrous DMF (J.T. Baker) was used as the solvent under a nitrogen atmosphere, and .1 M tetra(*n*-butyl)-ammonium hexaflourophosphate was used as the supporting electrolyte. A glassy carbon electrode was used as the working electrode. A silver wire was used as the *pseudo*-reference electrode. A Pt wire was used as the counter electrode. The redox potentials are based on the values measured from differential pulsed voltammetry and are reported relative to a ferrocenium/ferrocene (Fc^+/Fc) redox couple used as an internal reference (0.45 V vs SCE).[99]

4.2.2 Materials

Poly[3,4-ethylenedioxy thiophene] doped with poly[styrene sulfonate] (PEDOT:PSS, Clevios PVP AI 4083) was purchased from H.C. Stark inc. and N,N'-diphyenyl-N,N'-bis(1-naphthyl)-1,1'-biphenyl-4,4"-diamine (NPD) was purchased from Aldrich and sublimed in a thermal gradient furnace prior to use. 2,8-bis(diphenylphosphoryl) dibenzothiophen (PO15)[71], di-[4-(N,N-di-toylyl-amino)-phyenyl]cyclohexane (TAPC)[71], 2,6-bis(N-carbazolyl)pyridine (26mCPy)[78], 1,3-bis(3,5-dipyrid-3-yl-phenyl)benzene (BmPyPB), Platinum phenyl-methylimidazole (PtOO2)[100] and Platinum m-di(methyl-imidazolyl)benzene Chloride (Pt-14)[93] were prepared following literature procedure.

4.2.3 Device Fabrication and Characterization

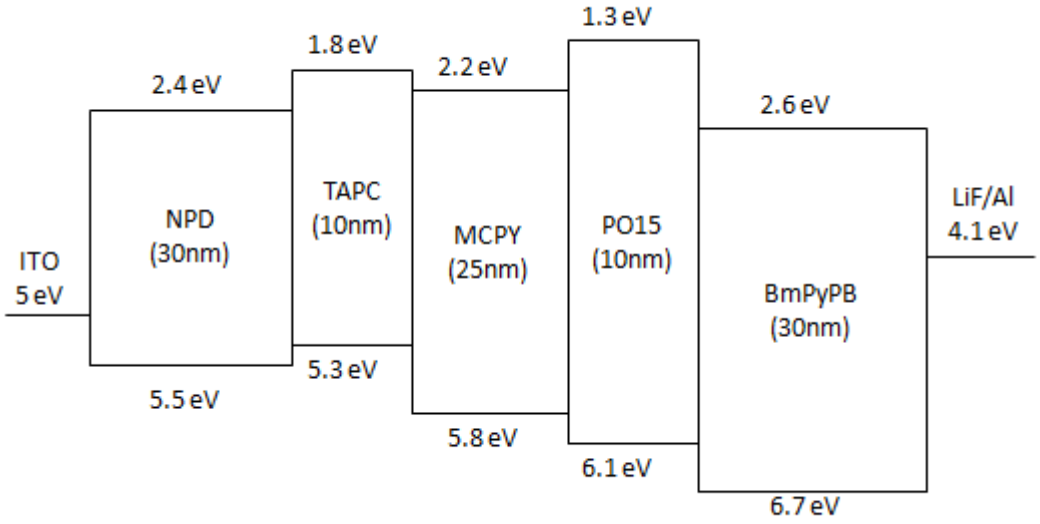

Figure 18. The energy level diagram of the device structures in this study of glass/ITO/NPD(30nm)/TAPC(10nm)/mCPy26:Dopant(25nm)/PO15(10nm)/BmPyPB(30nm)/LiF(1nm)/ Al(100nm).

The devices were fabricated on a glass substrate pre-coated with a patterned transparent indium tin oxide (ITO) anode using the structure of ITO/PEDOT:PSS/NPD(30nm)/TAPC(10nm)/8%Dopant:26mCPy(25nm)/PO15(10nm)/ BmPyPB(30nm)/LiF/Al. The energy level diagram including the HOMO and LUMO energies of the materials for the structure above is outlined in Figure 18. All small molecular materials were sublimed in a thermal gradient furnace prior to use. Prior to organic depositions, the ITO substrates were cleaned by sonication in water, acetone, and isopropanol followed by UV-ozone treatment for 15 minutes. PEDOT:PSS was filtered through a 0.2μm filter and spin-coated on the pre-cleaned substrates, giving a 40nm thick film. Organic materials were thermally evaporated at deposition rates of 0.5 to 1.5 Å/s at a working pressure of less than 10^{-7} Torr. The deposition rates and thicknesses were monitored by quartz crystal microbalances. A

thin 1 nm LiF layer was deposited at rates of <0.2 Å/s and aluminum cathodes were deposited at a rate of 1 Å/s through a shadow mask without breaking vacuum. Individual devices had areas of 0.04 cm^2. All device operation and measurement were done inside a nitrogen-filled glove-box. I-V-L characteristics were taken with a Keithley 2400 Source-Meter and a Newport 818 Si photodiode. EL spectra were taken using the Jobin Yvon Fluorolog spectrofluorometer. Agreement between luminance, optical power and EL spectra was verified with a calibrated Photo Research PR-670 Spectroradiometer with all devices assumed to be Lambertian emitters.

4.3 Results and Discussion

4.3.1 Electrochemical and Photophysical Properties

Table 5. Photophysical Properties of Pt14, PtOO2 and PtON2

	Emission at RT					Emission at 77K			
	λ_{max} [nm]	Φ	τ [μs]	k_r [10^5 s^{-1}]	k_{nr} [10^5 s^{-1}]	λ_{max} [nm]	τ [μs]	E_{ox} [V]	E_{red} [V]
Pt-14	470	0.56	11	0.51	0.4	465	12	0.31	-2.73
PtOO2	468	0.64	9	0.71	0.4	462	12	0.33	-2.62
PtON2	466	0.61	6.5	0.94	0.6	460	8.7	0.29	-2.57

Room temperature emission spectra were measured in a solution of dichloromethane. 77 K emission spectra were measured in a solution of 2-MeTHF. Coumarin 47 was used as a reference for quantum efficiency measurement in a dilute solution. The radiative decay rate constant (κ_r) was estimated by the lifetime (τ) and the quantum efficiency (Φ) of the samples where $\kappa_r=\Phi/\tau$ and $\kappa_{nr}=(1-\Phi)/\tau$. Redox measurements were carried out in anhydrous DMF solution using DPV. The redox values are reported relative to Fc/Fc^+.

The electrochemical properties of Pt-14, PtOO2 and PtON2 were examined using cyclic voltammetry, and the values of the redox potentials were determined using differential pulsed voltammetry (Table 5). The oxidation potential ($E_{ox}^{1/2}$) of PtOO2 and PtON2 are similar to the oxidation potential of Pt-14. Compared with Pt-14, PtOO2 and PtON2 have a lower reduction potential which is attributed to the addition of a pyridyl group into the complex system of PtOO2 and PtON2.

The absorption features of PtOO2 and PtON2 are shown in Figure 19. Both complexes exhibit very strong absorption bands below 300 nm ($\varepsilon > 1 \times 10^4$ L $mol^{-1}cm^{-1}$) due to $^1\pi$-π^* transitions localized on phenyl methyl imidazolyl ligands, together with a set of intense bands in the region 320-400 nm ($\varepsilon > 2 \times 10^4$ L $mol^{-1}cm^{-1}$) which are attributed to MLCT transitions involving both the cyclometalating ligands and platinum metal ions.[90] The weaker absorption bands in the region 400-500nm are attributed to triplet transitions (inset of Figure 19) and occur near the energy maximum emission at 77K (Figure 19). Both PtOO2 and PtON2 exhibit similar T_1 absorption transitions in energy, while PtON2 appears to have more pronounced T_1 absorption bands.

The room temperature emission spectra and low-temperature (77 K) emission spectra for PtOO2 and PtON2 are recorded in Figure 20. The low temperature photoluminescent characteristics of PtOO2 and PtON2 are similar with a peak intensity at 462 and 460nm, respectively. Additionally, both molecules have similar vibronic progressions indicating that the lowest excited states of the platinum complexes are mainly localized on the cyclometalated ligand. However, the vibronic progressions of PtOO2 is more pronounced. The room temperature peak wavelength of PtOO2 (468nm) is slightly higher than the room temperature peak wavelength of

PtON2 (466nm). Both PtOO2 and PtON2 exhibit a 6nm red shift in the peak wavelength and broadening in the room temperature emission spectrum relative to the low-temperature emission spectrum. Although PtOO2 and PtON2 have similar photoluminiscent quantum efficiencies, the radiative lifetime (τ) of PtOO2 is higher relative to PtON2 resulting in a smaller radiative decay rate (k_r) of PtOO2 relative to PtON2. Thus, the higher T_1 absorption, the smaller contribution of the vibronic sideband of the emission spectrum, and the faster radiative decay process for PtON2 indicates a more ^{1}MLCT/^{3}MLCT character mixed in the lowest excited state properties of platinum complexes due to the use of pyridyl carbazolyl ligand compared to the phenoxyl pyridyl ligand. A similar observation was reported in the phenyl carbine-based Platinum complexes in a previous publication.[101]

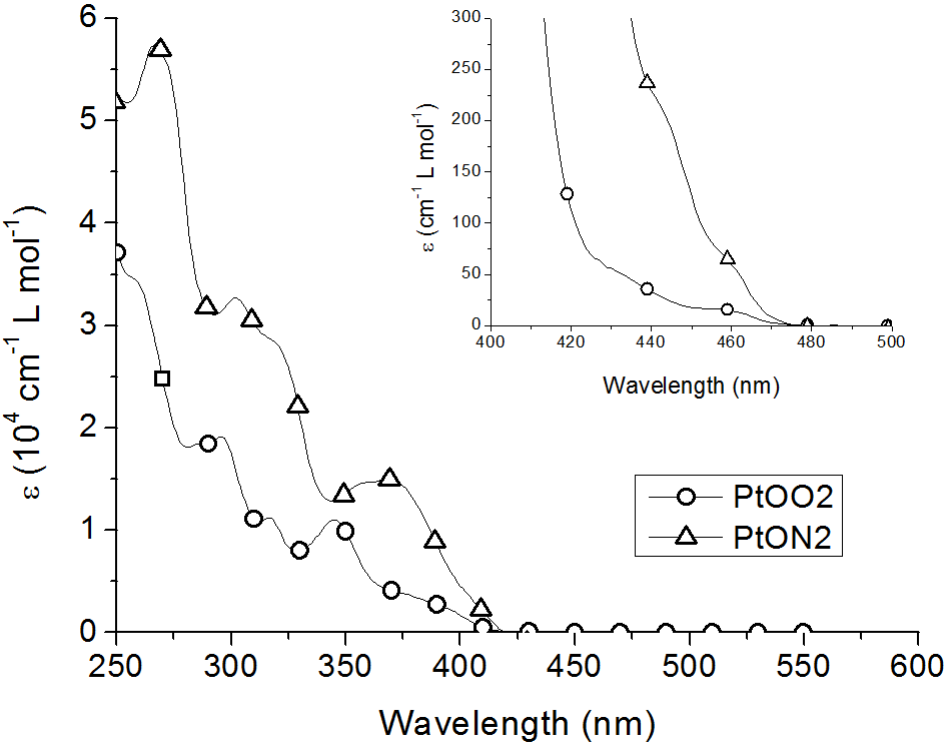

Figure 19. The absorption spectra of PtOO2 (Circles) and PtON2 (Triangles) in CH_2Cl_2 at room temperature. The T_1 absorption transitions are shown in the inset.

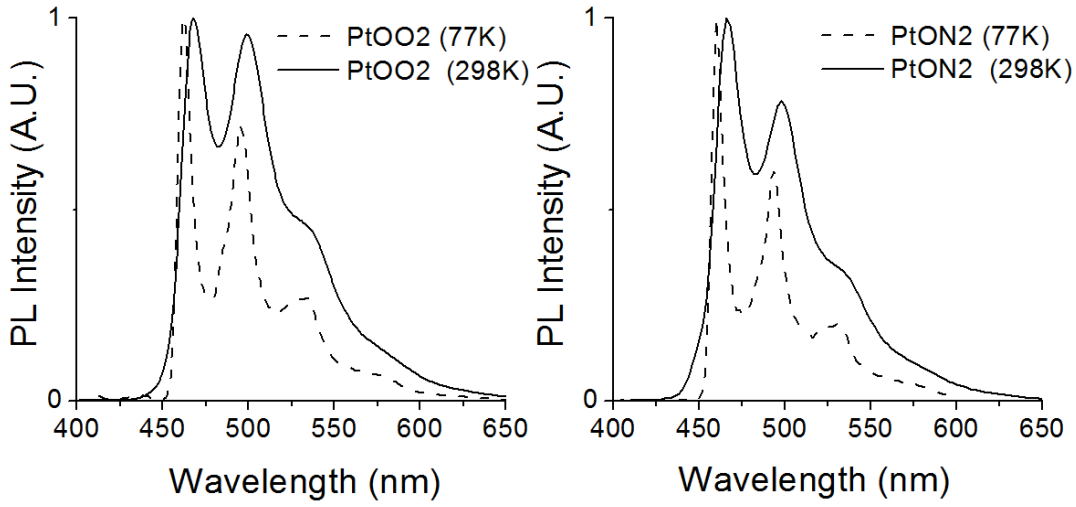

Figure 20. Room temperature (solid line) and 77K photoluminescent (dotted line) emission spectra of PtOO2 (Left) and PtON2 (Right). For room temperature measurements the solutes were dissolved in CH_2Cl_2. For low temperature (77K) 2-MeTHF was used as the solvent.

4.3.2 Device Performance

The EL spectra and CIE coordinates for devices employing PtOO2 and PtON2 in the structure of ITO/PEDOT:PSS/NPD(30nm)/TAPC(10nm)/8%Dopant: 26mCPy(25nm)/PO15(10nm)/BmPyPB(30nm)/LiF/Al are displayed in Figure 21. The structure chosen incorporates the hole blocking layer (PO15) and the electron blocking layer (TAPC) which results in good confinement of the excitons inside the emissive layer for reduced efficiency roll-off.[82] A 30nm NPD and BmPyPB layer were used due to their relatively high hole and electron mobility, respectively.[83] Additionally, the host material (26mCPy) was judiciously chosen per the suitable triplet energy for the emitters in this study resulting in good energy transfer and exclusive dopant emission.

Both PtOO2 and PtON2 have similar EL characteristics with a primary peak wavelength at 470nm and a secondary peak wavelength at 502nm. The intensity of the secondary peak wavelength of the PtOO2 device is slightly larger than the PtON2 device. Consequently, PtOO2 in a device has a slightly larger y-coordinate CIE (0.34) relative to PtON2 in a device (0.32).

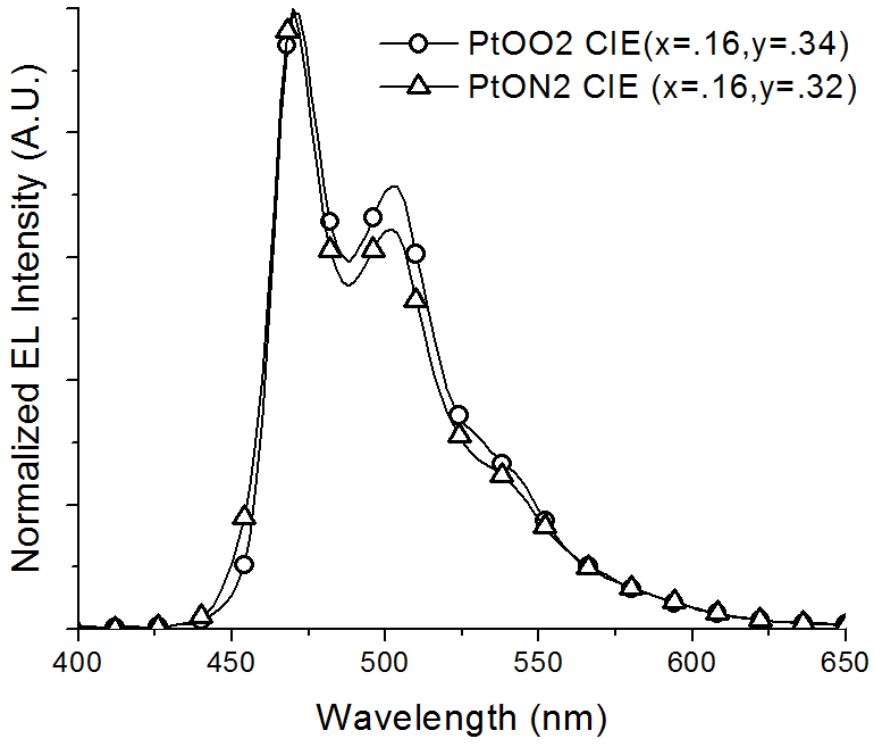

Figure 21. Normalized electroluminescent spectra, accompanied by CIE values at 1mA/cm2 for the dopants PtOO2 (Circles) and PtON2 (Triangles) in the device structure of ITO/PEDOT:PSS/NPD(30nm)/TAPC(10nm)/ 8% Dopant:26mCPy(25nm) /PO15(10nm)/ BmPyPB(30nm)/LiF/Al.

The device performance of PtOO2 and PtON2 are displayed in Figure 22. The complexes PtOO2 and PtON2 exhibit similar device efficiencies as they have similar photoluminiscent quantum efficiencies (0.64 and 0.61, respectively). The EQE of PtOO2 in a device is slightly higher than PtON2 in a device, with a maximum forward viewing EQE of 23.1% at a current density 0.02 mA/cm^2 compared to a

forward viewing EQE of 22.9% at a current density 0.03 mA/cm^2 for PtON2 in a device. Devices of PtON2 had reduced EQE roll off, dropping to only 20.1% at 100 cd/m^2 and 17.5% at 1000 cd/m^2 compared to 20.9% at 100 cd/m^2 and 15.7% at 1000 cd/m^2 for devices of PtOO2. The power efficiency of the PtOO2 based device has a peak value of 48.8 lm/W with only a slight drop to 37.3 lm/W at a practical operating brightness (100 cd/m^2). Devices of PtON2 have a peak value of 43.4 lm/W with only a slight drop to 36.5 lm/W at a practical operating brightness (100 cd/m^2).

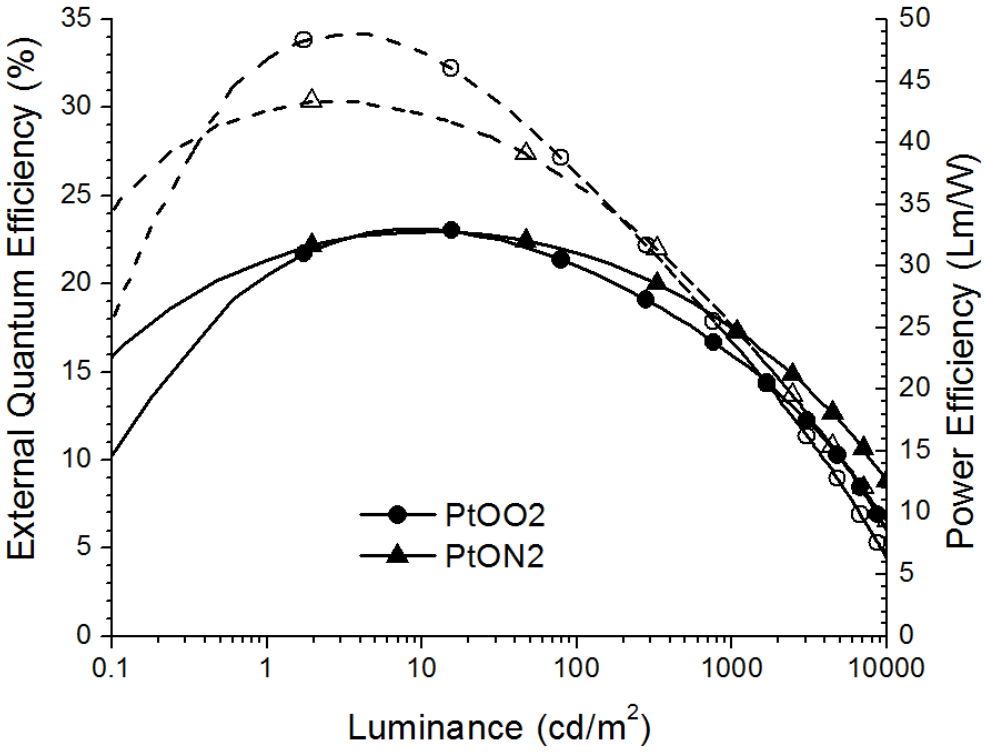

Figure 22. Power efficiency-luminance (open symbols) and external quantum efficiency-current density (closed symbols) characteristics for PtOO2 (circles) and PtON2 (Triangles) in the device structure of ITO/PEDOT:PSS/NPD(30nm)/ TAPC(10nm)/8%Dopant:26mCPy(25nm)/PO15(10nm)/BmPyPB(30nm)/LiF/Al.

4.4 Conclusion

In this section, highly efficient halogen free phosphorescent complexes with high external quantum efficiencies emitting in the blue-green region were demonstrated. Devices based on the halogen free platinum complex, PtOO2 and PtON2 yielded external quantum efficiencies over 20%. Elimination of halogens from the Pt-based phosphorescent emitters should provide a viable route to stable deep blue phosphorescent emitters for displays and lighting applications. Additionally, the development of halogen free Pt-based phosphorescent emitters may also provide a viable route towards stable and efficient white light as Pt-based complexes have the potential of excimer emission which enables broad emission covering the entire visible spectrum for white light emitting devices.

5 STABLE AND EFFICIENCT RED PHOLEDS

5.1 Introduction

The foregoing sections discussed the need for further developments in highly efficient phosphorescent OLEDs with high operational lifetimes and demonstrated a possible route towards a stable blue PhOLED. In this chapter, an efficient and stable red PhOLED will be discussed. Thus far, the approach to achieve efficient red phosphorescent OLEDs has primarily focused on Ir-based complexes.[87, 88, 102] In particular, highly efficient iridium based red PhOLEDs have been fabricated utilizing cyclometalating ligands such as phenylquinolines/phenylisoquinolines,[103-105] phenylquinazolines,[106] and phenylquinoxalines.[106] Among these, a highly efficient and stable device utilizing the tris(1-phenylisoquinoline) irdium(III) ($Ir(piq)_3$) complex exhibited a maximum EQE of 12.6%, color coordinates CIE (x=0.64, y=0.35) and an estimated operational lifetime at 50% of initial luminance, $T_{0.50}$, of 1×10^7 hours at an initial luminance of 100 cd/m^2.[107] Platinum based complexes, however, have received significantly less attention despite demonstrating external quantum efficiencies (EQE) approaching or equal to iridium analogs.[89, 90] While previous reports have suggested that platinum complexes may exhibit shorter operational lifetimes relative to their iridium analogs due to the square planar geometry of the Pt^{II} complex which typically exhibits irreversible oxidation due to rapid solvolysis of the Pt^{III} species,[76] great strides have recently been made in improving the stability of platinum based complexes utilizing a tetradentate cyclometalated design. In particular, a series of deep blue, tetradentate, Pt-based complexes have demonstrated high quantum efficiencies and moderate device operational lifetimes compared with their Ir analogs possessing similar emitting ligands.[101] Another

report demonstrated a highly efficient and stable symmetric tetradentate cyclometalated platinum complex, Pt7O7, capable of blue and white emission which exhibited high quantum efficiencies and highly stable white emission with a $T_{0.5}$ of over 10 000 h at 100 cd/m^2 further demonstrating the potential for highly efficient and stable tetradentate cyclometalated platinum complexes.[108] Here we report a novel red emitting phenyl-quinolone based tetradentate cyclometalated platinum complex, PtON11Me, with an operational stability close to or exceeding its iridium analog. Devices employing PtON11Me exhibited a maximum EQE of 8.3%, color coordinates CIE (x=0.61, y=0.36) and an estimated operational lifetime $T_{0.97}$ ~ 1560 h, higher than its iridium analog, tris(1-phenylquinoline) iridium(III) (PQIr), using a similar device architecture.[109] This demonstrates the potential for platinum based phosphorescent emitters with long operational lifetime and high quantum efficiencies in OLED displays.

5.2 Experimental

5.2.1 Materials

The materials used in this study were 1,4,5,8,9,11-hexaazatriphenylene-hexacarbonitrile (HATCN), N,N'-diphyenyl-N,N'-bis(1-naphthyl)-1,1'-biphenyl-4,4"-diamine (NPD), 4,4'-bix(N-carazolyl) biphenyl (CBP), di-[4-(N,N-di-toylyl-amino)-phyenyl]cyclohexane (TAPC), diphenyl-bis[4-(pyridine-3-yl)phenyl]silane (DPPS), 1,3-bis(3,5-dipyrid-3-yl-phenyl)benzene (BmPyPB), bis(2-methyl-8-quinolinolato) (biphenyl-4-olato)aluminum (BAlq), and tris-(8-hydroxyquinoline) aluminum (Alq).

5.2.2 Materials Characterization

The absorption spectra were recorded on an Agilent 8453 UV-visible Spectrometer. Phosphorescence lifetime (τ) determinations were performed on a Horiba Jobin Yvon Fluoro-log-FL4-1057 spectrometer with a time correlated single photon counting method using a LED excitation source. The radiative decay rate constant (k_r) was estimated by $k_r=\Phi/\tau$ and the nonradiative decay rate (k_{nr}) was estimated by $k_{nr}=(1-\Phi)/\tau$. Room temperature emission spectra was measured in a solution of dichloromethane. For low temperature (77 K) emission spectra, the solute was dissolved in 2-MeTHF and cooled to 77K with liquid nitrogen. ^{1}H spectra were recorded at 400 MHz, ^{13}C spectra were recorded at 100 MHz on Varian Liquid-State NMR instruments in DMSO-d_6 solutions and chemical shifts were referenced to residual protiated solvent. ^{1}H NMR spectra were recorded with residual H_2O (δ = 3.33 ppm) as internal reference; ^{13}C NMR spectra were recorded with DMSO-d_6 (δ = 39.52 ppm) as internal reference. The following abbreviations (or combinations thereof) were used to explain ^{1}H NMR multiplicities: s = singlet, d = doublet, t = triplet, q = quartet, m = multiplet. Shanghai Institute of Organic Chemistry performed the mass spectrum measurements.

5.2.3 Device Fabrication and Characterization

The devices were fabricated on a glass substrate pre-coated with a patterned transparent indium tin oxide (ITO) anode. All small molecule materials were sublimed in a thermal gradient furnace prior to use. Prior to organic depositions, the ITO substrates were cleaned by sonication in water, acetone, and isopropanol. Organic materials were thermally evaporated at deposition rates of 0.5 to 1.5 Å/s at

a working pressure of less than 10^{-7} Torr. The deposition rates and thicknesses were monitored by quartz crystal microbalances. A thin 1 nm LiF layer was deposited at rates of <0.2 Å/s and aluminum cathodes were deposited at a rate of 1 Å/s through a shadow mask without breaking vacuum. Individual devices had areas of 0.04 cm^2. All device operation and measurements were done inside a nitrogen-filled glove-box. I-V-L characteristics were taken with a Keithley 2400 source-meter and a Newport 818 Si photodiode. Electroluminescent (EL) spectra were measured with an Ocean Optics HR-4000 spectrometer. Agreement between luminance, optical power and EL spectra was verified with a calibrated Photo Research PR-670 Spectroradiometer with all devices assumed to be lambertian emitters. The luminance versus. time measurements were conducted at a constant dc current under accelerated conditions (20 mA/cm^2) and photocurrent measurements were recorded every 30 seconds for an ~80 hour time interval. All luminance versus time measurements were conducted in a nitrogen environment and uninterrupted throughout the duration of the test. To eliminate external light from compromising the measurement's, the set up was covered with a dark colored cloth and aluminum foil.

5.3 Results and Discussion

5.3.1 Photophysical Properties

The room temperature and low temperature (77 K) emission spectra for PtON11Me are shown in Figure 23. The low temperature photoluminescent peak occurs at 586nm and the room temperature emission spectrum exhibits a 28nm shift and broadening with a peak intensity of 614nm relative to the low-temperature emission spectrum.

The absorption features of PtON11Me are shown in the inset of Figure 23. The very strong absorption bands below 300nm are assigned to $^1\pi$-π^* ligand centered (LC) transitions, the strong bands between 320-450nm are attributed to metal-to-ligand-charge-transfer (MLCT) transitions. PtON11Me has a short phosphorescent lifetime of 3.6 microseconds in a solution of CH_2Cl_2 at room temperature and 6.8 microseconds in 2-MeTHF at low temperature (77K). Furthermore, the PL quantum efficiency of PtON11Me in a doped PMMA film at room temperature is experimentally determined to be 40±5%, indicating that PtON11Me is an efficient emitter and suitable for OLED applications, however, it is still under our investigation to uncover why PtON11Me has a much lower quantum efficiency than its blue-emitting and green-emitting analogs like PtON1, PtON7 and Pt7O7.[101]

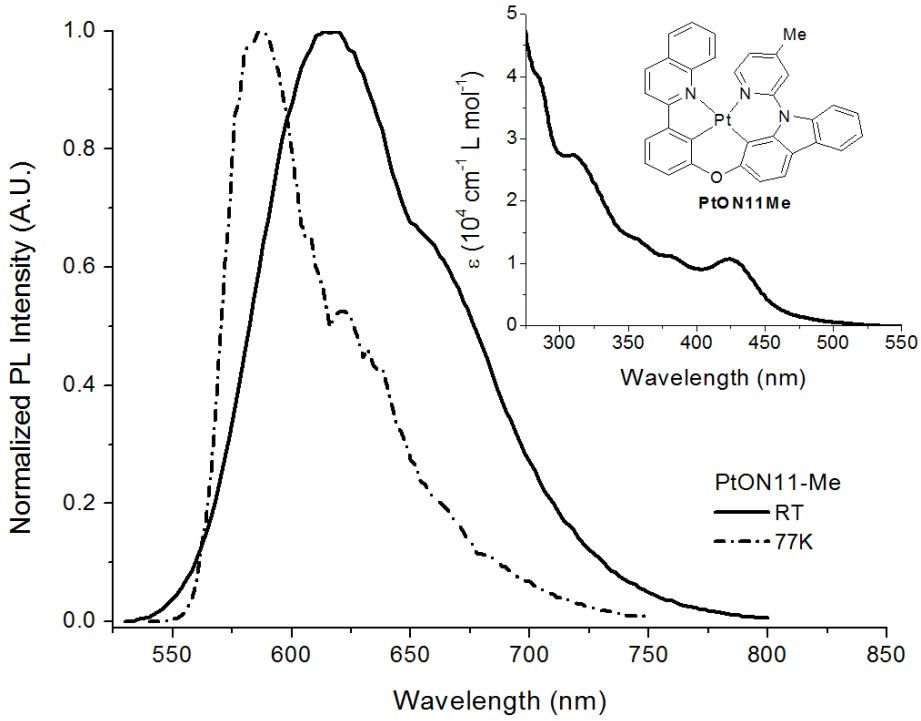

Figure 23. Room temperature (solid line) and 77K (dotted line) photoluminescent emission spectra of PtON11Me. For room temperature measurements the solutes were dissolved in CH_2Cl_2. For low temperature (77K) 2-MeTHF was used as the solvent. The absorption features and molecular structure of PtON11Me are shown in the inset.

The complex PtON11Me has a short phosphorescent lifetime of 3.6 microseconds at room temperature and 6.8 microseconds at low temperature (77K) due to the CbPy chelate in the ligand, which has significant ^{1}MLCT/^{3}MLCT character in its lowest excited state. The non-radiative decay rate is 12.2×10^4 s^{-1} and radiative decay rate is 2.5×10^4 s^{-1}, resulting in a quantum efficiency of 17%. The absorption coefficient in units of 10^4 cm^{-1} L mol^{-1} versus wavelength in nanometers of PtON11Me is shown in the inset of Figure 23. The molecular structure of the complex PtON11Me is also shown in the inset.

5.3.2 Device Performance and Operational Lifetime

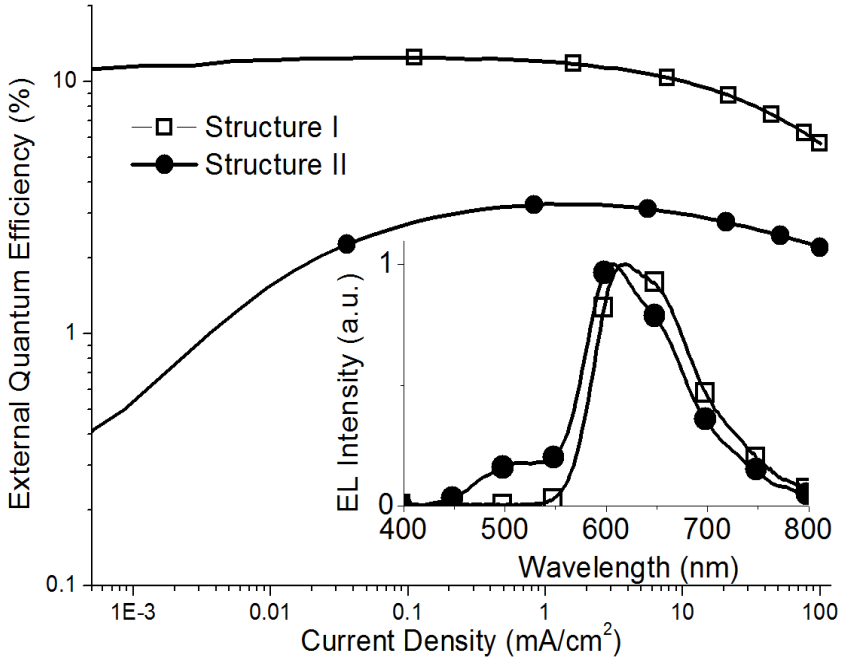

Figure 24. The normalized EL spectra (inset) and the external quantum efficiency-versus current density for PtON11Me in structure I (open squares): ITO/HATCN(10nm)/NPD(40nm)/TAPC(10nm)/2%PtON11Me:CBP(25nm)/DPPS(10 nm)/BmPyPB(40nm)/LiF(1nm)/Al(100nm) and structure II (closed circles): ITO/ HATCN(10nm)/NPD(40nm)/2%PtON11Me:CBP(25nm)/BAlq(10nm)/Alq(30nm)/LiF(1 nm)/Al(100nm).

Devices were fabricated in the structure of ITO/HATCN(10nm)/NPD(40nm)/ TAPC(10nm)/2%PtON11Me:CBP(25nm)/DPPS(10nm)/BmPyPB(40nm)/LiF(1nm)/ Al(100nm) (structure I). NPD and BmPyPB were chosen due to their relatively high hole and electron mobility, respectively.[83, 109] Both DPPS and TAPC have a high triplet energy of 2.87 and 2.7 eV, respectively, which effectively confines excitons inside the emissive layer (EML).[110] Additionally, DPPS has a deep HOMO level (6.5 eV), effectively confining holes inside the EML. In this exciton confining structure, exclusive PtON11Me emission is observed and moderate efficiency is achieved with a maximum forward viewing EQE of 12.4% as shown in Figure 24.

Although OLEDs implementing the materials DPPS, TAPC, and BmPyPB have yielded high external quantum efficiencies, the device operational lifetimes of devices implementing these materials remain low due to their poor electrochemical stability.[93] Thus, PtON11Me was also implemented in the device structure of ITO/HATCN(10nm)/NPD(40nm)/2%PtON11Me:CBP(25nm)/BAlq(10nm)/Alq(30nm)/ LiF(1nm)/ Al(100nm) (structure II) which has been shown to exhibit high operational lifetimes.[109] The 10nm TAPC layer was omitted and the 10nm DPPS layer was replaced by a 10nm BAlq layer which has proven to yield stable and efficient red phosphorescent OLEDs.[109] Additionally, the 40nm BmPyPB ETL was replaced by a thinner 30nm Alq layer. The EL spectra of devices in structure II showed non-exclusive emission from PtON11Me with observed peaks at ~525nm, suggesting poor confinement of excitons in the EML. Consequently, a reduction in the maximum forward viewing EQE to 3.3% is observed. The poor confinement of excitons in the case of structure II is attributed to the low triplet energy of BAlq (2.2eV),[111] which for a dopant concentration of only 2% leads to the possibility of

migration of triplet excitons out of the EML before being trapped on the dopant molecules.[112]

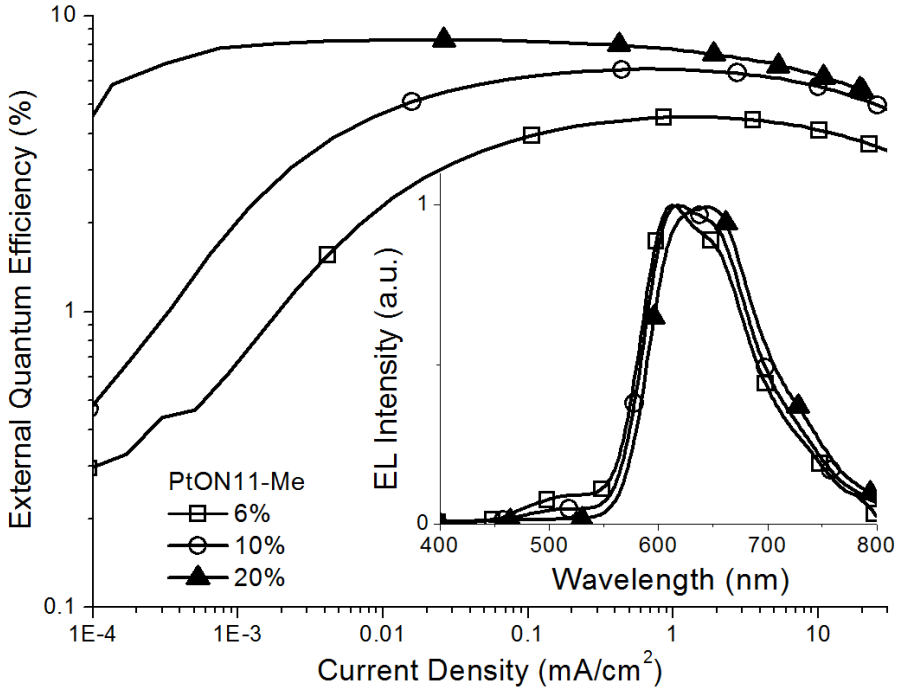

Figure 25. The normalized EL spectra (inset) and the external quantum efficiency-versus current density for PtON11Me in device structure II: ITO/HATCN(10nm)/NPD(40nm)/x%PtON11Me:CBP(25nm)/BAlq(10nm)/Alq(30nm)/ LiF(1nm)/Al(100nm) for 6% (open squares), 10% (open circles), and 20% (solid triangles) PtON11Me concentration in CBP.

In order to improve the charge balance and obtain exclusive PtON11Me emission in structure II, the dopant concentration of PtON11Me must be increased. This has been shown to improve device performance in PhOLEDs for select cases.[113] Thus, the influence of PtON11Me concentration on device performance was examined using the device structure of ITO/HATCN(10nm)/NPD(40nm)/x% PtON11Me: CBP(25nm)/BAlq(10nm)/Alq(30nm)/LiF(1nm)/Al(100nm). The electroluminescent spectra and device performance for 6%, 10%, and 20%

PtON11Me concentration in CBP is summarized in Figure 25. Increasing the concentration to 10% resulted in an emission primarily originating from PtON11Me. By increasing the PtON11Me concentration further to 20%, exclusive PtON11Me emission was achieved and a higher maximum forward viewing EQE of 8.3% was observed compared to a maximum forward viewing EQE of 4.5% and 6.1% for the 6% and 10% PtON11Me doped devices, respectively.

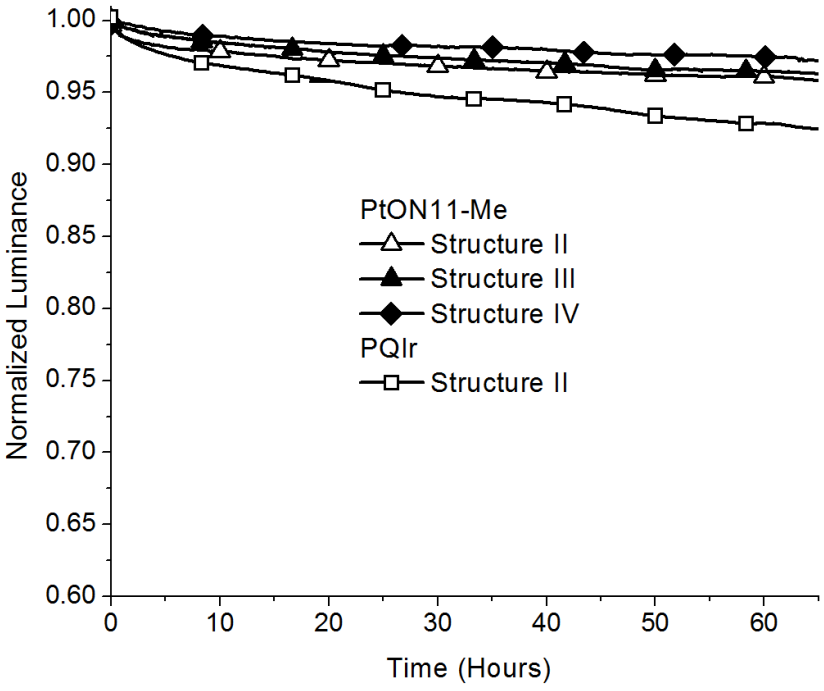

Figure 26. Normalized luminance versus time under constant direct current of 20 mA/cm^2 for devices of PtON11Me in structure II (open triangles), structure II (solid triangles), structure IV (solid diamonds). The normalized luminance versus time for devices of PQIr in structure II (open squares) is also shown.

The device operational lifetime of PtON11Me was examined in the optimized structure II configuration with a PtON11Me concentration of 20%. For a comparison, the phosphorescent complex PQIr, known for its high external quantum efficiency and operational lifetime ($T_{0.5}$ = 15 000 h normalized to 100 cd/m^2) was also fabricated in structure II.[109] The luminance versus time characteristics shown in

Figure 26 were assessed under accelerated conditions at a driving current of 20mA/cm^2. To correlate luminance decay against initial brightness, $T_{0.97}$, corresponding to the time for the luminance decay to reach $0.97L_0$ was measured for the various devices. At a constant drive current of 20mA/cm^2, the initial luminance (L_0) of PtON11Me in structure II was 1104cd/m^2 with a $T_{0.97}$ = 26.3 h compared to a 20% PQIr doped device in structure II with an initial luminance of 2400 cd/m^2 and a $T_{0.97}$ = 8.2 h. The lifetime, $T_{0.97}$, for both of the devices at an initial luminance of 100 cd/m^2 was determined using the relationship $T_{0.97}(L_1)= T_{0.97}(L_0)(L_0/L_1)^{1.7}$ yielding $T_{0.97}$ = 1560 h and $T_{0.97}$ = 1776 h for the PtON11Me and PQIr devices, respectively. The PtON11Me based device exhibited a luminance decay of $0.90L_0$ at 246 h at a drive current of 20mA/cm^2, which corresponds to a $T_{0.90}$ = 11 800 h at an initial luminance of 100 cd/m^2. In some cases, the operational lifetime can be improved using a cohost structure.[114] For this reason, PtON11Me was also implemented into the cohost structure of ITO/HATCN(10nm)/NPD(40nm)/x%PtON11Me:CBP:BAlq(25nm)/BAlq (10nm)/Alq(30nm)/LiF(1nm)/Al(100nm) (structure III) with a PtON11Me concentration of 20% PtON11Me and a 1:1 CBP:BAlq ratio. Structure III exhibited a $T_{0.97}$ = 42 h at an initial luminance of 1200 cd/m^2, corresponding to a $T_{0.97}$ = 2870 h at 100 cd/m^2. To improve the device operational lifetime further, PtON11Me was implemented into the structure of ITO/HATCN(10nm)/NPD(40nm) /x%PtON11Me:mCBP:BAlq(25nm)/BAlq(10nm)/Alq(30nm)/LiF(1nm)/Al(100nm) with a 6% PtON11Me concentration and a 1:1 mCBP:BAlq ratio. The new structure incorporating the host mCBP resulted in a higher estimated operational lifetime of $T_{0.97}$ = 3112 h at 100 cd/m^2. A summary of the operational lifetime values and the device characteristics for the devices in this study is given in Table 6. Further improvements in the device operational stability can be further expected with the

incorporation of state-of-the-art host and blocking materials that can decrease the turn-on voltage, improve the electron to photon conversion efficiency, and eliminate degradation mechanisms associated with the various host and blocking materials.

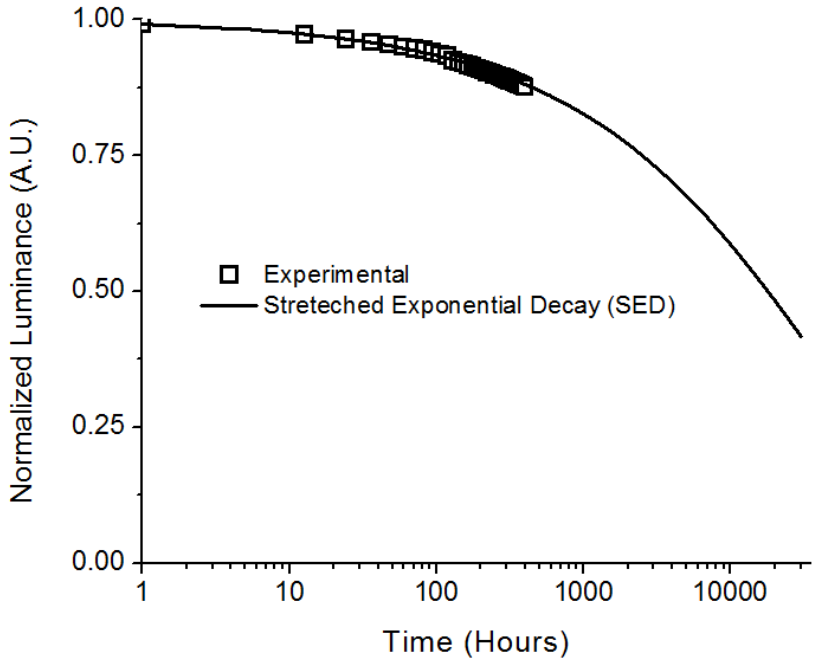

Figure 27. Normalized luminance versus time under constant direct current of 20 mA/cm^2 for 400 hours for devices of PtON11Me in structure II. The experimental data (black squares) was fitted with a stretched exponential decay (SED) function (solid line). The linear coordinate system also shown for clarity (inset).

To correlate luminance decay against initial brightness, $T_{1/2}$ ($0.5L_0$) is typically employed as a figure of merit.[107] However, since running to $0.5L_0$ is not practical for high device stabilities such as the ones in this investigation, we find it convenient to use $T_{0.90}$, corresponding to the time for the luminance decay to reach $0.90L_0$. Since the time dependent relative luminance L(t) most commonly shows an exponential decay behavior, the $T_{1/2}$ can be approximated by extrapolation. According to a report by Merheim et al., best results can be obtained by fitting the

whole data set with a stretched exponential decay function (SED).[107] The extrapolated Luminance decay curve using an SED function for PtON11Me in device structure II is shown in Figure 27. The $T_{0.90}$ with an initial luminance of 1104 cd/m^2 was 246 hours corresponding to a $T_{0.90}$ of 11,800 hours at an initial luminance of 100cd/m^2. Using the extrapolated SED function with ß=0.4475 and τ=40567.7, the $T_{1/2}$ at an initial luminance of 100 cd/m^2 is ~188,000 hours.

Table 6. A summary of device characteristics of PtON11-Me in the 4 different devices structures.

Type	Emitter	CIE_x	CIE_y	EQE Peak (%)	EQE at 100 cd/m^2	L0‡ (cd/m^2)	EQE‡ (%)	$T_{0.97}$‡	$T_{0.97}$* at 100 cd/m^2
I	PtON11Me 2%	0.63	0.36	12.5	12.1	1942	9.0	†	†
II	PtON11Me 2%	0.54	0.40	3.3	3.3	904	2.8	†	†
II	PtON11Me 6%	0.59	0.38	4.5	4.5	980	3.7	†	†
II	PtON11Me 10%	0.61	0.37	6.3	6.2	1150	5	†	†
II	PtON11Me 20%	0.61	0.36	8.3	7.5	1104	5.6	26.2	1560
III	PtON11Me 20%	0.61	0.36	8	7.4	1200	5.6	42	2870
IV	PtON11Me 6%	0.6	0.36	4.7	4.6	902	3.9	74	3112
II	PQIr 20%	0.66	0.34	7.7	7.4	2400	7.4	8.2	1776

†Operational lifetime was only determined for electrochemically stable device architectures and for devices which exhibited exclusive dopant emission.
‡Device characteristics at J=20mA/cm^2
*Device operational lifetime estimated using the relationship $T_{0.97}(L_1)= T_{0.97}(L_0)(L_0/L_1)^{1.7}$.

5.4 Conclusion

An efficient and stable red phosphorescent OLED was demonstrated utilizing the cyclometalated, tetradentate, quinolone based platinum complex, PtON11Me. Using the exciton confining structure I, a maximum forward viewing EQE of 12.5% with color coordinates CIE (x=0.63, y=0.36) was achieved. By implementing PtON11Me in the electrochemically stable structure II, a high operational lifetime was achieved with an estimated $T_{0.97}$ = 1560 h at 100 cd/m^2 and a maximum forward viewing EQE of 8.3%. The operational lifetime was improved further by implementing PtON11Me into the CBP:BAlq cohost structure III which exhibited an estimated $T_{0.97}$ = 2870 at 100 cd/m^2. The highest device operational lifetime was achieved incorporating PtON11Me into the mCBP:BAlq cohost structure IV with an estimated $T_{0.97}$ = 3112 at 100 cd/m^2. We found that platinum complexes can act as efficient and stable dopants with efficiencies and operational lifetimes close to or exceeding those of their iridium analogs.

6 MICROCAVITY ORGANIC LIGHT EMITTING DIODES FOR IMPROVED LIGHT EXTRACTION EFFICIENCY: A THEORETICAL APPROACH

6.1 The Light Out-Coupling Limit

The light out-coupling efficiency (η_{out}) is defined as the ratio of photons that are emitted from the device into air to the total number of photons generated. While significant improvements in the device efficiency of OLEDs has been realized in recent years with the development of efficient charge transporting and charge injecting materials combined with the advent of phosphorescent heavy metal complexes, which are capable of harvesting 100% of electrogenerated excitons,[36, 84, 115] resulting in near 100% total internal quantum efficiency in select devices,[35] the external quantum device efficiencies remains limited to 20-30% as most of the photons generated remain trapped as a result of total internal reflection (TIR) and other optical losses.[35, 116]

The light out-coupling losses are dominated by 4 primary mechanisms; surface Plasmon polaritions (SPPs), waveguide modes, substrate modes, and electrode absorption.[44, 117-119] For a typical bottom emitting OLED architecture (Figure 28) the SPPs account for 40% of the out-coupling losses, the waveguide modes account for 15% of the light loss, the substrate mode account for 23% of the light loss, and the metal losses due to absorption by the electrodes accounts for 4%. A summary of these mechanisms are outlined in Figure 28. Modes trapped by total internal reflection (waveguide and substrate modes) occur due to the mismatch of the refractive indices between the ITO anode (n~1.9) and glass substrate (n~1.5) as well as between the glass substrate and air (n~1).[47] As a result of the

aforementioned loss mechanisms, only 20% to 30% of the light emitted in the active region contributes to the farfield optical power of the OLED. Thus, in order to improve the efficiency of OLEDs, methods that improve the light out-coupling efficiency, or fraction of photons emitted from the device to total generated photons, need to be considered.

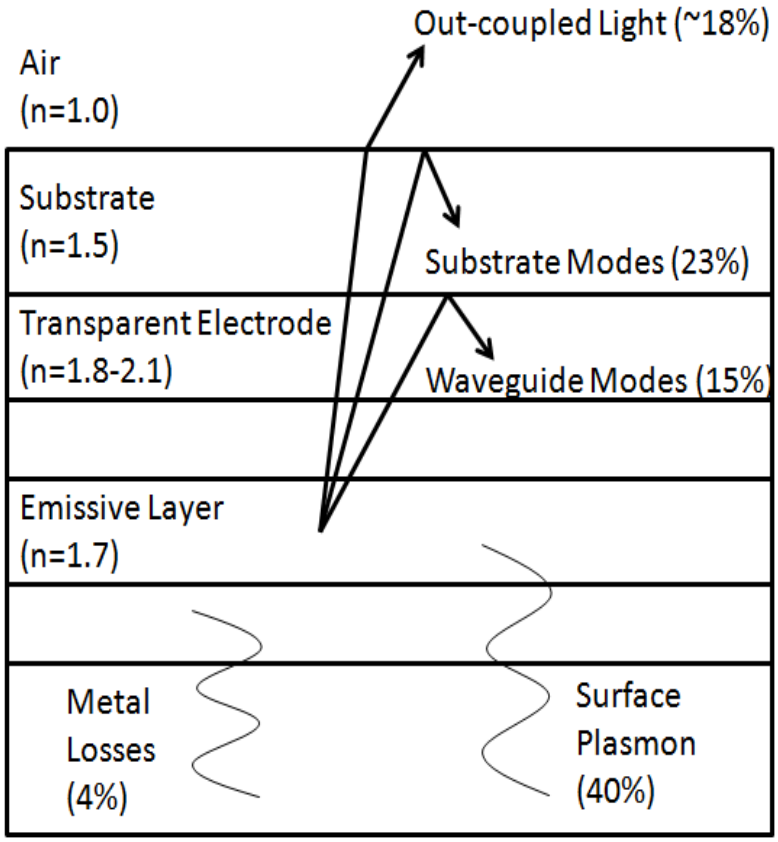

Figure 28. Schematic of a multilayer OLED and the various optical losses including absorption at metal surfaces, surface plasmon effects, and losses from total internal reflection (waveguide modes and sud substrate modes).

6.2 Light Extraction Methods

There have been a number of reported methods that enhance the external quantum efficiency (EQE) of OLEDs and overcome the light out-coupling limitation for typical OLEDs. Some of these methods include implementing a substrate with high index materials ($n \geq 1.8$) combined with backside substrate modification,[49] creating surface roughness at the glass/air interface of the substrate to allow more photons to scatter out of the substrate,[50, 121-123] implementing an ordered microlens array at the glass/air interface of the substrate to reduce the angle of incidence of the glass/air interface below the critical angle,[124] growing a periodic two-dimensional (2D) photonic crystal to couple the guided waves to the radiation mode in the direction normal to the device surface,[52, 125] or through the design of a microcavity OLED (MOLED). [53, 126-134] MOLEDs are of particular interest due to their simple fabrication and their ability to be used in conjunction with the other aforementioned strategies.[126, 135] The ensuing sections will focus on the design of microcavity OLEDs for enhancing the light out-coupling efficiency. To assist with MOLED design, optical models will now be developed.

6.3 The Microcavity Effect

A MOLED is formed by positioning the emissive layer (EML) in between a highly reflective cathode and semi-reflective out-coupling mirror separated by a distance on the order of the wavelength of light emitted creating an optical "micro" cavity. Interference effects caused by the cavity redistribute the internal power flow[126] and, in select cases, change the spontaneous emission of the source inside the cavity.[136] With an appropriate cavity design, a preferential propagation direction of

the photons can be forced from the total internal reflection regime toward the extraction cone, resulting in an increase in light out-coupling efficiency.[137] Following this approach, significant improvements in device performance can be achieved with, typically, only a slight modification to the original device structure.[126, 135]

6.3.1 Purcell Effect

As previously suggested, for select cases, the spontaneous emission of the source itself can experience significant changes in the presence of an optical cavity including a change in the total power radiated by the dipole and a change in radiative electron-hole recombination rate and hence lifetime. The change of the carrier lifetime due to the presence of a cavity, known as the Purcell effect,[138] has been studied in detail.[139-141] The change in lifetime is often expressed in terms of the Purcell factor:

Equation 14

$$F_p = \frac{\frac{1}{\tau}}{\frac{1}{\tau_0}} = \text{Emitted Dipole Power in Cavity / Emitted Dipole Power in bulk}$$

Here, F_p is the Purcell factor and τ and τ_0 are the radiative lifetimes with and without cavity, respectively. An analytical solution is possible for the case of a horizontal dipole in the middle of a cavity with perfect reflecting mirrors.[140] The results depend on the phase of the mirror. The Purcell factor is given as a function of cavity order for r=+1 and r=-1 in Figure 29.

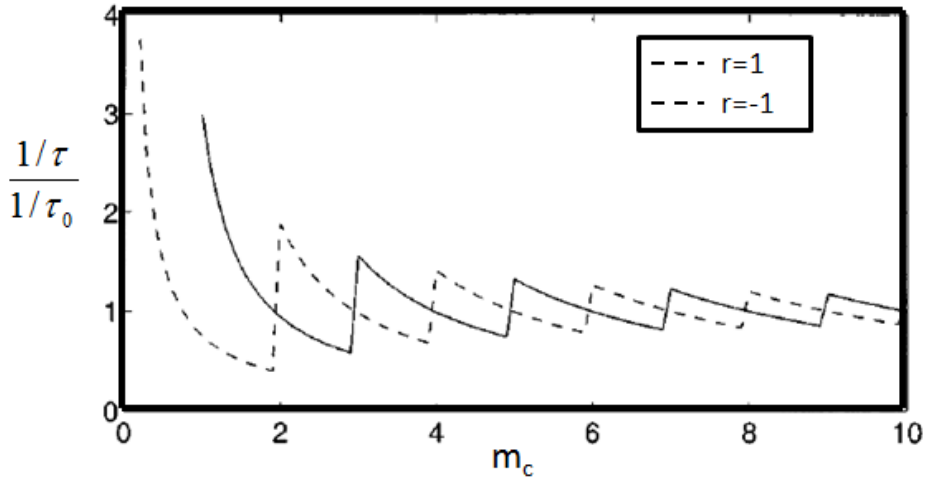

Figure 29. Horizontal dipole in the middle of a cavity[142].

Apart from the singular $1/m_c$ behavior for small cavity order (m_c) in the r=+1 case, for r=-1 (perfect metallic mirrors), the maximum Purcell-factor is 3 and is obtained in a half-wavelength thick cavity (order 1 cavity or λ/2 cavity, m_c=1). For higher order cavities (thick cavities), the Purcell factor converges to 1. In other words, high order cavities with many modes have a similar impact on the dipole as uniform space with a continuum of modes. Thus, for planar cavities with cavity lengths larger than λ/2 (m_c>1), the potential increase or decrease in the spontaneous emission rate is at most a factor of 3 or 2, respectively.[139-141] More significant changes in lifetime, however, can be expected in three dimensionally confined cavities. For example, enhancement factors greater than 15 have been observed for three-dimensionally confined cavities with a small volume, such as quantum dots in pillar micro-cavities (F_p=5) or micro-disks (F_p=15).[143]

In a micro-cavity bound by DBR mirrors the Purcell factor is generally close to 1[53, 144-149] due to the narrow angular range of reflectivity resulting in a large number of leaky modes.[150] With structures confined by metal mirrors, high Purcell

factors can be achieved via coupling to surface Plasmon modes.[151] The interaction between the free charges at the metal surface and electromagnetic radiation results in surface plasmons having greater momentum, or equivalently, a greater in-plane wave-vector k_{sp} compared to "free" photons in the semiconductor, i.e. $k_{sp}>nk_0$. This increased momentum (in-plane wave-vector) means that SP modes are non-radiative, they are bound to the interface between the metal and the dielectric.

The dipole emission has near-field and far-field components. The far-field component propagates as plane waves while the near-field is made up of evanescent waves which are quite intense. While the focus for improved extraction in MOLEDs is on the plane wave components, potential for improvement also resides in converting the evanescent waves into plane waves via coupling to surface Plasmon modes. This can be achieved by prism coupling or Bragg scattering.[118, 152, 153]

6.3.2 Low-finesse Microcavity's

Thus far, the majority of MOLED reporting's have concentrated on using structures with low to moderate Q-factors, wherein little to no change in the spontaneous lifetime is observed.[53, 144-149] Although, higher finesse cavities can result in large enhancement of both electroluminescence and photoluminescence in the forward direction for sharply directed forward emission, this enhancement is often accompanied by a large color change versus viewing angle and low total light extraction enhancement.[154-156] Theoretical work has suggested that low-finesse MOLEDs are a more promising structure for use in lighting and display applications as they combine the advantage of a small color shift and reasonable enhancement in total extraction efficiency.[131] This improvement in the light extraction efficiency of

low-finesse MOLEDs is achieved not by changing the spontaneous emission of the source itself, but by a redistribution of the power as a result of interference effects created by the optical cavity. With an appropriate cavity design, the preferential propagation direction of the photons can be changed from the total internal reflection regime toward the extraction cone resulting in an increase in light out-coupling efficiency (Figure 30). An optical model will now be developed beginning with a simple scalar approach to progressively more sophisticated models.

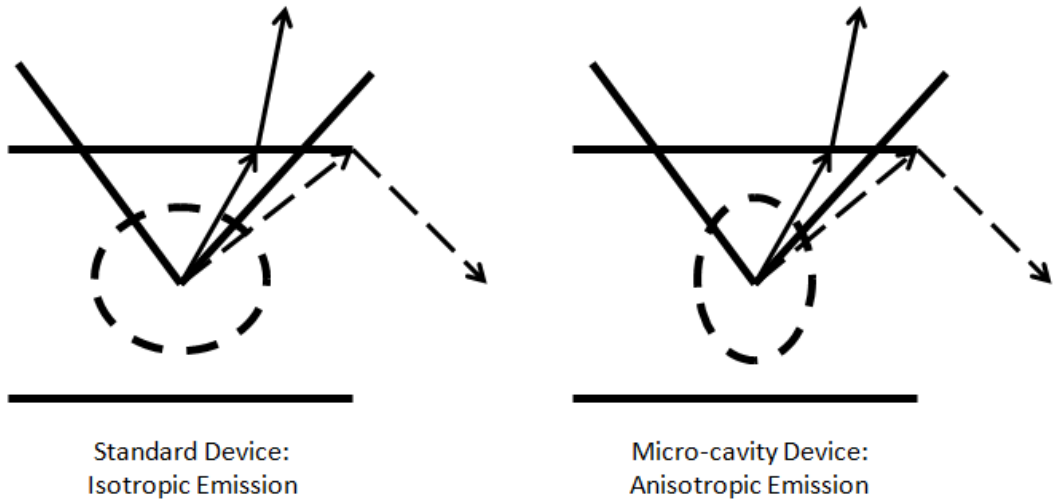

Figure 30. Typical organic phosphors in conventional OLED structures have isotropic emission wherein the emitted power is uniform in all directions for a given wavelength. Only light rays inside of the extraction cone (solid line) are permitted to escape due to total internal reflection caused by the mismatch in the index of refraction of the medium at which the source emits (n_i) with respect to the exit medium (n_o), where $n_i > n_o$. Consequently, light rays outside the extraction cone (dotted line) cannot escape. By implementing reflective mirrors (right) into the device architecture with a separation on the order of an integer value (m) of one-half of the emission wavelength (λ), the power can be shifted from the total internal reflection regime towards the extraction cone, such that more power propagates within the extraction cone.

6.4 The Scalar Model

6.4.1 Point Source Near a Single Mirror

A simple case will first be described to familiarize the reader with the concepts to be covered in this Chapter. Consider a point source distance, d, from a mirror with field reflection coefficient, r, defined as the ratio of the reflected electric field to incident electric field ($r=E_r/E_i$).

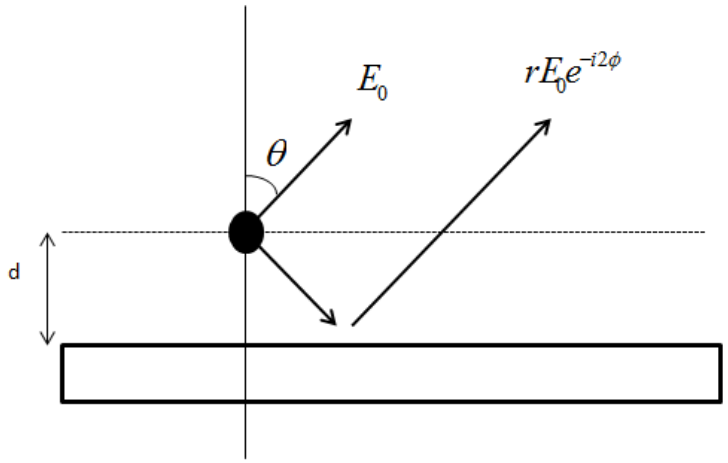

Figure 31. A point source near a single mirror, where d is the distance between the source and mirror, E_0 is the dipole farfield without a mirror, r is the ratio of reflected electric field to incident electric field, θ is the angle of incidence, and φ is the phase difference between the direct and reflected contribution of the field.

For the simplified scalar approach, the electric far field of a plane wave of monochromatic light incident on a single mirror is given by the sum of each wave as expressed in the following equation

Equation 15

$$E_t = E_0\left[1 + re^{-i2\phi}\right]$$

Here E_t is the total electric field, E_0 is the dipole far field without a mirror and is the phase difference between the direct and the reflected contribution of the field and is given by

Equation 16

$$\phi = k_0 nd\cos\theta$$

Here k_0 is the wave vector, n is the refractive index of the medium, θ is the angle of incidence, and d is the distance between the source and mirror.

For reflections whereby a change in phase occurs at the mirror, the total electric

Equation 17

$$E_t = E_0\left[1 + re^{-i(2\phi_{eff})}\right]$$

Equation 18

$$2\phi_{eff} = 2k_0 nd\cos\theta - \arg(r)$$

Here Arg(r) is the phase change of the wave upon reflection at the mirror surface.

6.4.2 Resonant Condition for a Single Mirror

Constructive interference between the two waves occurs when

Equation 19

$$2\phi_{eff} = 2m\pi$$

For normal incidence ($\theta=0$) and reflection of a wave incident on an ideal metal mirror ($\arg(r)=\pi$), the conditions for destructive and constructive interference are expressed as

Equation 20

$$\text{Optical Length, (nd)} = \frac{\lambda}{4}(2m+1) \quad \text{Constructive Interference condition}$$

Equation 21

$$\text{Optical Length, (nd)} = \frac{\lambda}{4}(2m) \qquad \text{Destructive Interference condition}$$

In this case, constructive interference occurs at the anti-nodal position and destructive interference occurs at the nodal position.

The maximum, minimum and average field intensity ($|E_t|^2$) over all angles is then given by

Equation 8a $\qquad$ Maximum = $(1+|r|)^2$

Equation 8b $\qquad$ Minimum = $(1-|r|)^2$

Equation 8c $\qquad$ Average = $1 + |r|^2$

Thus, for a perfect mirror ($|r|=1$), the resultant power of the source can be anywhere between 0 and 4 and is strongly dependent on the direction. This simple case demonstrates the profound influence the environment can have on the far field power distribution of the emitting source as a result of wave interference.

6.4.3 Transmission of a Fabry-Perot Cavity

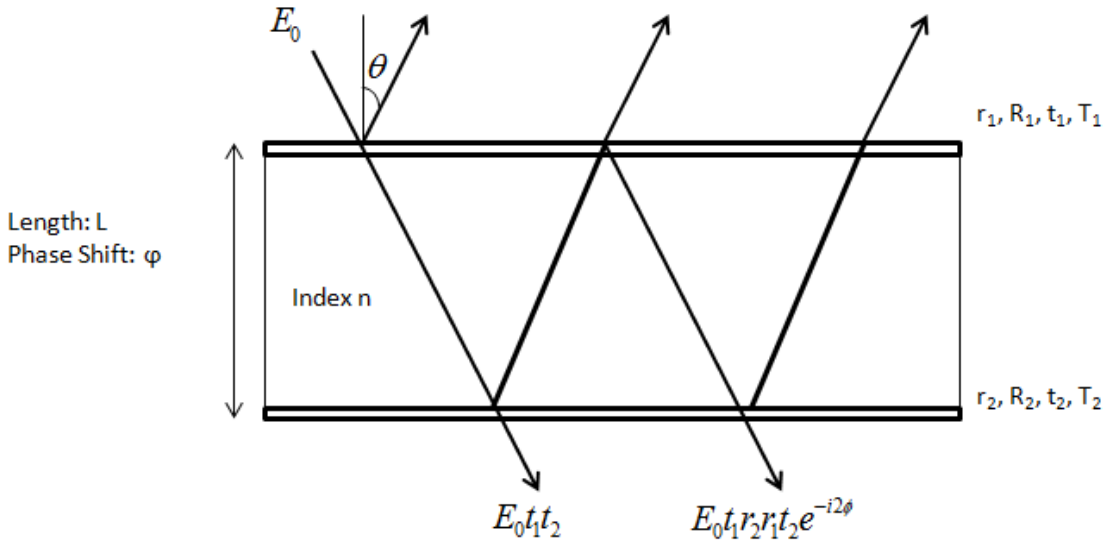

Figure 32. Transmission of a Fabry-Perot cavity, where E_0 is the dipole farfield without a mirror, r is the ratio of reflected electric field to incident electric field, t is the ratio of transmitted electric field to incident electric field, R is the reflectivity energy, T is the transmission energy, L is the cavity length, n is the index of refraction of the medium, θ is the angle of incidence, and φ is the phase difference between the direct and reflected contribution of the field.

Consider an electric field propagating wave incident on a Fabry-Perot cavity with index of refraction, n, at an angle, θ, from the normal plane of incidence. The transmitted electric far field of a plane wave of monochromatic light is given by the sum of the transmitted waves[157]:

Equation 22

$$E_t = E_0 t_1 t_2 \left[1 + r_1 r_2 e^{-i(2\phi_{eff})} + (r_1 r_2 e^{-i(2\phi_{eff})})^2 + \ldots + (r_1 r_2 e^{-i(2\phi_{eff})})^{2n}\right]$$

Equation 23

$$E_t = E_0 \frac{t_1 t_2}{1 - r_1 r_2 e^{-i(2\phi_{eff})}}$$

Equation 24

$$2\phi_{eff} = 2\phi - \arg(r_1) - \arg(r_2)$$

Here E_t is the transmitted electric field, E_0 is the dipole farfield without a cavity, and t_1/t_2 and r_1/r_2 are the field transmission and reflection coefficients, respectively. Arg(r1) and Arg(r2) are the phase changes at the mirror and 2φ corresponds to the cavity round-trip phase shift and is equal to

Equation 25

$$2\phi = 2k_0 nL\cos\theta$$

Here L is the cavity length, k is the amplitude of the wave vector ($k=2\pi/\lambda$) in the cavity with refractive index n, and θ is the angle of incidence.

The power transmission coefficient (T_{FP}) for a Fabry-Perot Cavity is given by:

Equation 26

$$T_{FP} = \frac{|E_t|^2}{|E_0|^2} = \frac{T_1 T_2}{1 + R_1 R_2 - 2\sqrt{R_1 R_2}\cos(2\phi_{eff})} = A(2\phi_{eff})T_2$$

Here T_1 , T_2 and R_1 , R_2 are the power transmission and reflection coefficients for the top and bottom mirror, respectively ($T_i=|t_i|^2$, $R_i=|r_i|^2$). The power transmission coefficient (T_{FP}) is related to the Airy Factor ($A(2\varphi_{eff})= T_{FP}/T_2$). The Airy factor (A) or cavity enhancement factor defines the resonant modes of the cavity. The resonant modes represent cases of optimum constructive interference (peaks in transmission)

and are strongly dependent on the cavity length. The Airy factor and resonance will be discussed in more detail in later sections.

6.4.4 Point Source in a Fabry-Perot Cavity

Consider now a source inside of a Fabry-Perot Cavity as shown in Figure 33.

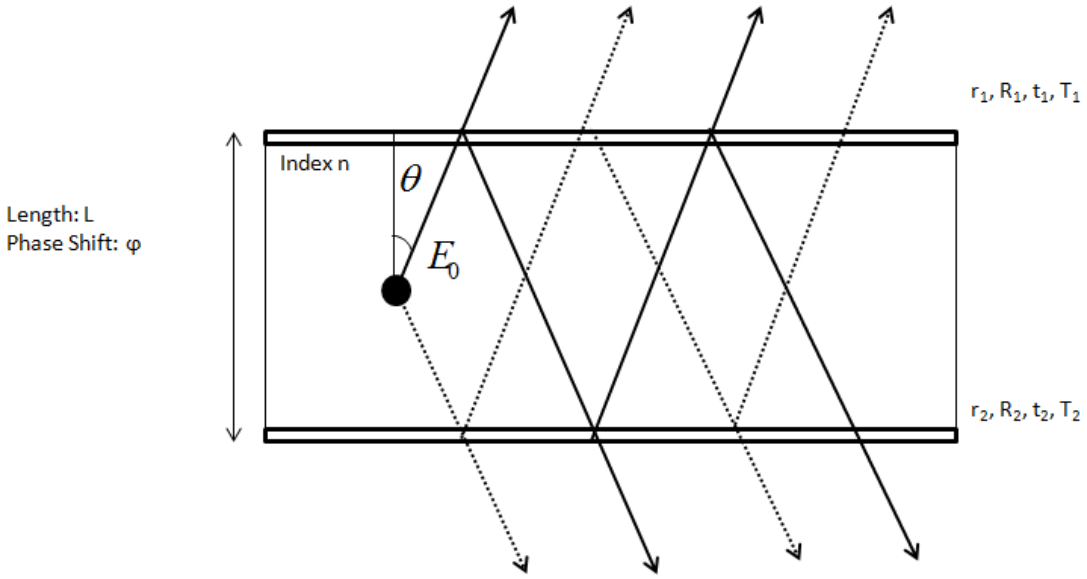

Figure 33. Point source inside a Fabry-Perot cavity, where E_0 is the dipole farfield without a mirror, r is the ratio of reflected electric field to incident electric field, t is the ratio of transmitted electric field to incident electric field, R is the reflectivity energy, T is the transmission energy, L is the cavity length, n is the index of refraction of the medium, θ is the angle of incidence, and φ is the phase difference between the direct and reflected contribution of the field.

For a source within a Fabry-Perot cavity, the result strongly resembles the case of transmission from an external source through a Fabry-Perot cavity with the exception that an additional term (ζ) must be added to account for the additional set of waves emitted downwards by the source (dotted line). This can be expressed as

Equation 27

$$T_{top} = A(2\phi_1^{eff}) \times \zeta(2\phi_2^{eff}) = \frac{T_{FP} \times \zeta}{T_2} = \frac{T_1(1 + R_2 + 2\sqrt{R_2}\cos(2\phi_2^{eff}))}{1 + R_1R_2 - 2\sqrt{R_1R_2}\cos(2\phi_1^{eff})}$$

Equation 28

$$2\phi_1^{eff} = 2\phi_1 - \arg(r_1) - \arg(r_2)$$

Equation 29

$$2\phi_2^{eff} = 2\phi_2 - \arg(r_2)$$

The first term, the Airy factor ($A(2\phi_1^{eff})$), given in Equation 27, is strongly dependent on the length of the cavity. The Airy factor is periodic with period π in φ_{1eff}. Its maxima define the resonant modes of the cavity and obey the phase condition $2\varphi_{1eff} = 2m\pi$ with m a positive or negative integer.

Equation 30

$$A(2\phi_1^{eff}) = \frac{1}{1 + R_1R_2 - 2\sqrt{R_1R_2}\cos(2\phi_1^{eff})}$$

The second term, the standing wave factor ($\zeta(2\phi_2^{eff})$), given in Equation 30, is strongly dependent on the position of the source within the cavity. According to the above equation, the transmission is high in a Fabry-Perot when the source is located at an antinode position of the standing wave.

Equation 31

$$\zeta(2\phi_2^{eff}) = 1 + R_2 + 2\sqrt{R_2}\cos(2\phi_2^{eff})$$

6.4.5 Resonance in a Fabry-Perot Cavity

A resonance or a resonant mode can be described as a condition for which the cavity enhancement factor or Airy factor goes through a maximum. In a given Fabry-Perot cavity, resonance will occur for a particular combination of wavelength and wave propagation direction or angle. As noted previously, a resonant condition occurs when $2\varphi_{1eff} = 2m\pi$ with m being a positive or negative integer. For simplicity and to demonstrate the concept of resonance, it will be assumed that the power transmission and reflection coefficients are independent of wavelength and angle of incidence and that no phase change occurs at the mirror surface (arg(r)=0). Under these conditions the resonant condition simplifies to

Equation 32

$$2\pi m = 2k_0 nL\cos\theta$$

As will be shown shortly, it is convenient to rewrite the resonant condition in terms of the z component of plane wave k-vector (k_z):

Equation 33

$$2\phi = 2k\ nL\cos\theta = 2k_z nL = 2m\pi$$

Rearranging Equation 33 yields

Equation 34

$$k_z = \frac{m\pi}{nL}$$

Thus, resonance occurs in intervals of π/nL with respect to the z component of the wave-vector. For perfect resonators ($|r_1 r_2|=1$), these resonant intervals form resonant planes in K-space.

The concept of resonance in a Fabry-Perot can be more conveniently expressed graphically in the K-space representation. In the K-space representation, a monochromatic source resembles a sphere satisfying the dispersion relation:

Equation 35

$$k_x^2 + k_y^2 + k_z^2 = k^2 = \left(\frac{2\pi}{\lambda}\right)^2 = \left(\frac{n\omega}{c}\right)^2$$

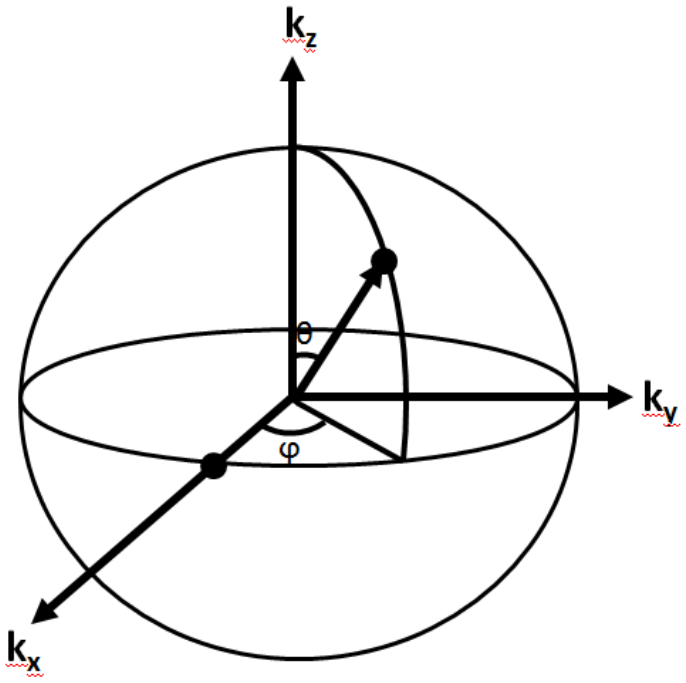

Figure 34. Dimensional K-Space representation of the wave-vector (red arrow).

As the emission properties of the Fabry-Perot cavity are independent on the azimuthal angle (φ), the k-space representation can be broken down into two dimensions and the dispersion relation can be simplified to:

Equation 36

$$k_{\parallel}^2 = k_x^2 + k_y^2$$

Equation 37

$$k_z^2 + k_{\parallel}^2 = k^2 = \left(\frac{2\pi}{\lambda}\right)^2 = \left(\frac{n\omega}{c}\right)^2$$

For perfect resonators wherein the optical cavity contains perfect mirrors (R=1), resonance for a given wave-vector, k, occurs only when there is a crossing of the K-vector sphere defined by the dispersion relation (solid line) with the resonance planes (dotted line).

As can be seen from the Figure 35, for a given wavelength the resonant modes form a discrete set as a function of θ and a continuous set as a function of φ (cones of resonance). One of these resonance cones are depicted in the Figure 36. The resonant plane spacing is inversely dependent on the length of the cavity. Thus, the number of resonant modes (or rather of resonant cones) will increase as the cavity thickness is increased. Vice versa, by decreasing the thickness the number of cones can be reduced to 1 (or even 0 in special cases). Figure 36 depicts an identical monochromatic source (same k-vector magnitude) in 2 different sized cavities. As can be seen for the smaller cavity (left), less resonant modes are present.

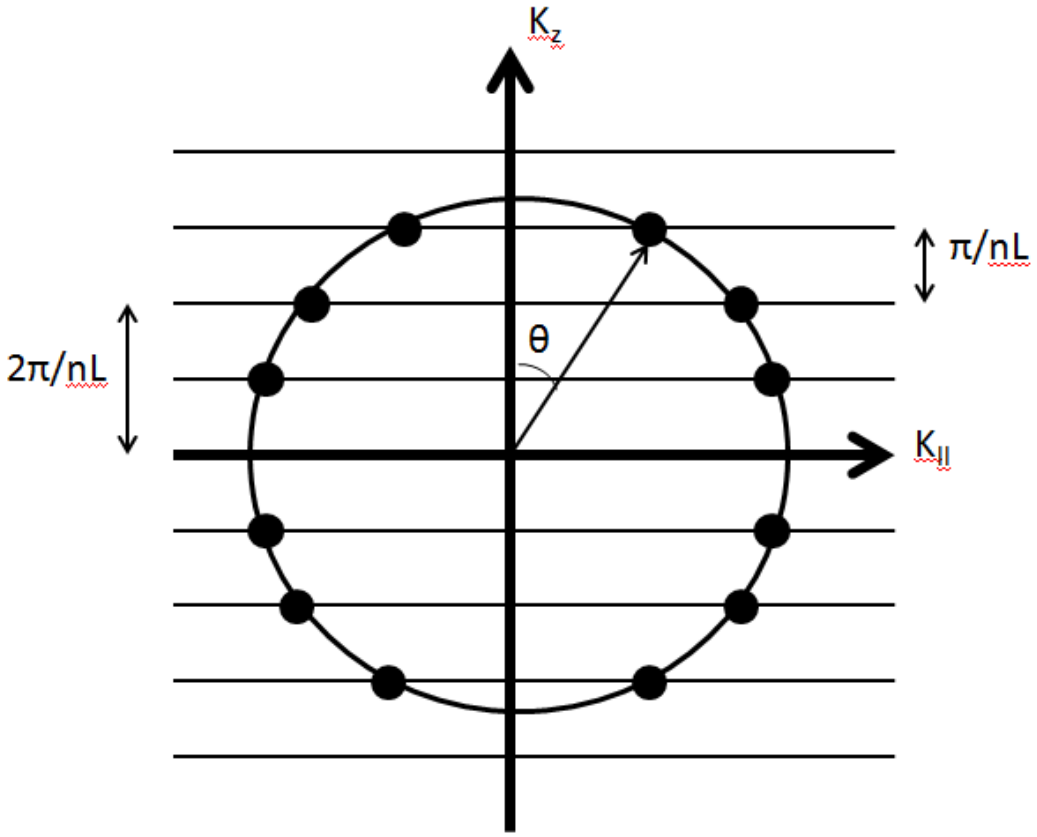

Figure 35. Dimensional projection of K-Space. Points of resonance (black dots) occur upon intersection of the k-sphere (black circle) with the resonant planes (black lines). The separation of resonances occurs in intervals of π/nL per the resonant condition given in equation 19.

When the Fabry-Perot medium has an index, n, greater than the external medium, then total internal reflection occurs whereby light greater than the critical angle (θ_c) of the cavity mirror's is reflected and trapped inside the cavity. Thus only those wavevectors within the critical angle can be extracted. These wave-vectors form a cone, known as the extraction cone (Figure 36).

An additional observation that can be made from Figure 36 is that as the number of resonant modes increase, the relative number of resonance modes in the extraction cone decreases and resonant modes outside of the extraction cone increases.

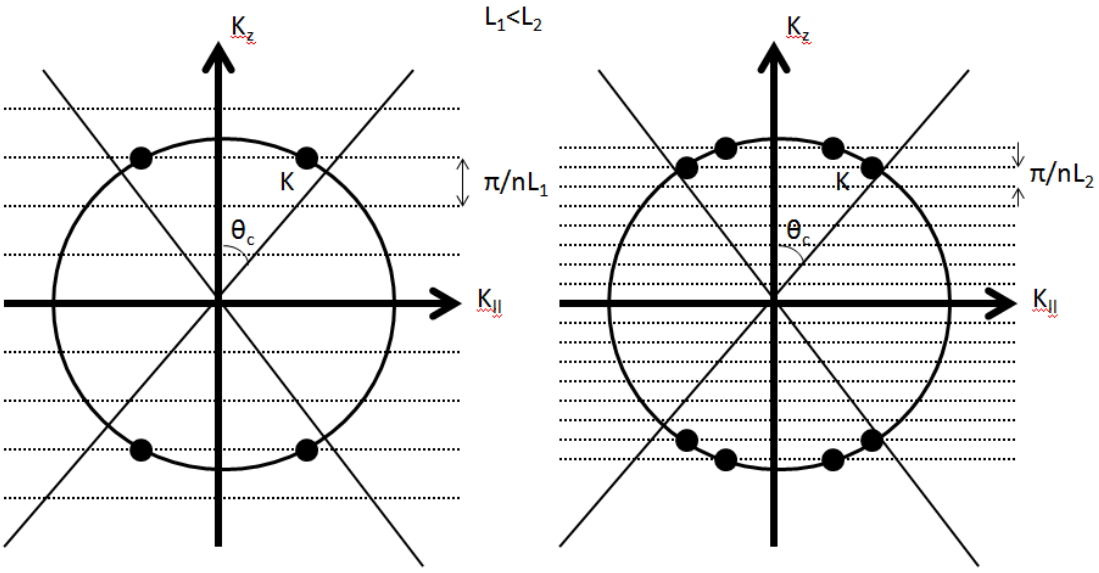

Figure 36. K-space representation of 2 different cavities with different cavity lengths. Cavity 1 (L_1) is smaller than cavity 2 (L_2) and has twice as many resonant conditions inside the extraction cone (diagonal lines).

6.4.5 The Airy Factor

For simplicity, let us consider again a source within a Fabry-Perot resonator with R1=R2=R and z=L/2 and ideal mirrors ($\varphi=\varphi_1=\varphi_{1eff}=\varphi_{2eff}$). Equation 27 reduces to:

Equation 38

$$T_{top} = \frac{T_1(1+R\ +2R\cos(2\phi\ ))}{1+R^2\ -2R\cos(2\phi\ )}$$

Equation 39

$$2\phi = knL\cos\theta$$

In the case of a perfect resonator ($|r_1r_2|=1$, R=1) as described previously, the transmittance approached infinity, and the resonant modes became singularities, which can be described by a Dirac distribution. For more realistic situations wherein $|r_1r_2|<1$, the optical mode density is no longer a Dirac distribution and the resonant peaks caused by the Airy factor have a finite width. The full width half

maximum (FWHM), defined as $\delta\varphi_{1eff}$, is inversely proportional to the cavity finesse (F) according to the following equation

Equation 40

$$F = \frac{\Delta\varphi}{\delta\varphi}$$

Here $\Delta\varphi$ is the separation between adjacent resonances and $\delta\varphi$ is the full-width half maximum of the resonance peak (Figure 37).

Thus, the higher the reflectivity of the optical cavity mirrors, the lower the FWHM, and the higher the finesse. As discussed previously, typically a low to moderate finesse optical cavity is implemented for optimizing the out-coupling efficiency of MOLEDs.

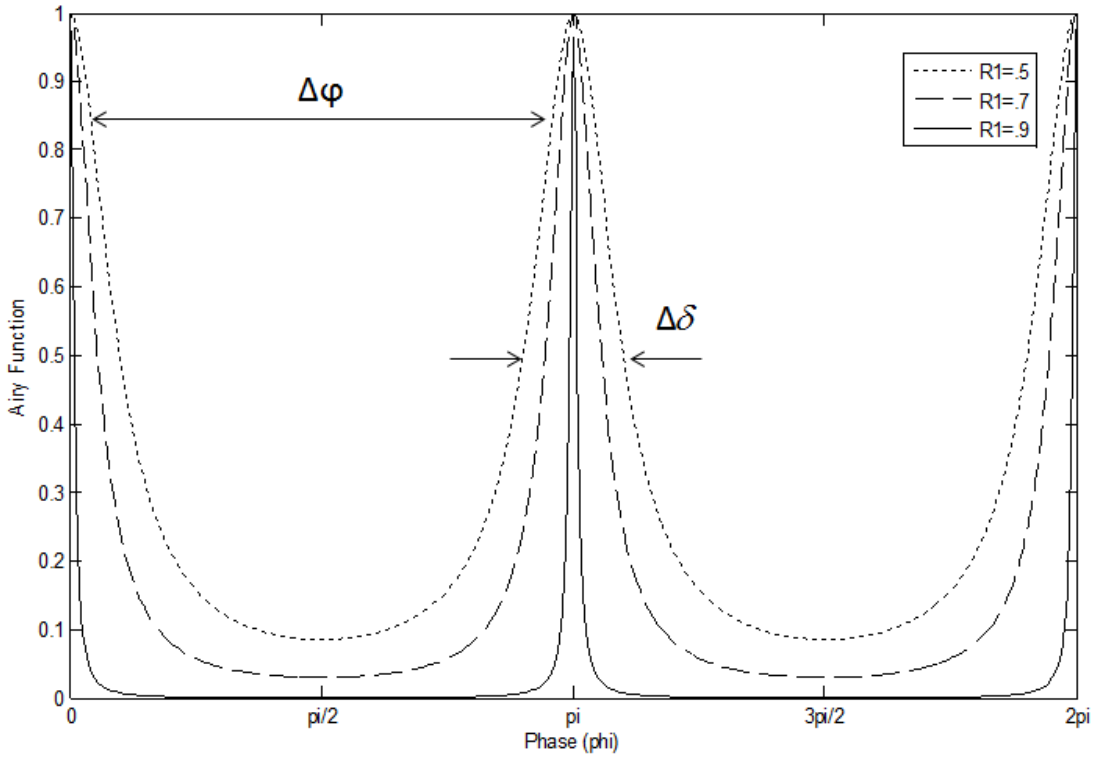

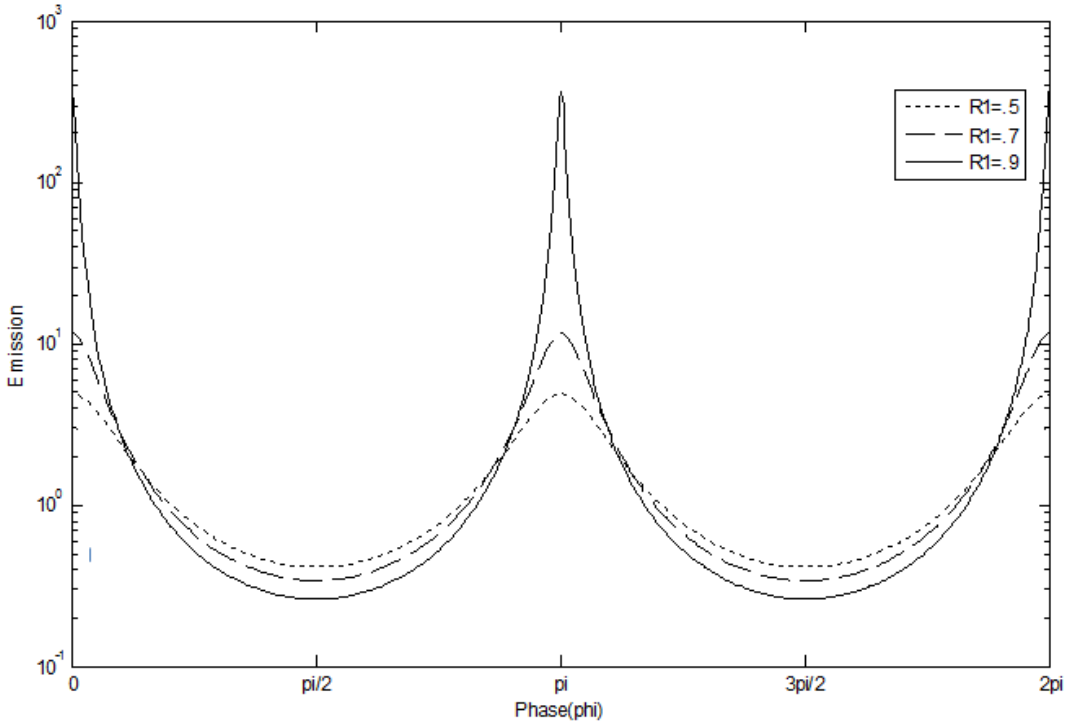

Figure 37. The Airy function (top) and Emission (bottom) vs phase for different out-coupling reflectivity's (R_1). Resonant peaks occur at integer values of π for this simplified case.

The Emission through the top of the cavity is strongly dependent on the phase of the cavity. Thus for wave-vectors out of phase with the cavity, the emission is significantly reduced. Additionally, the reflectance of the coupling mirror has a strong dependence on both the emission and the line width of the Airy resonant peak. Given the full-width half max (FWHM) is inversely proportional to the Finesse of the cavity, as the reflectance of the mirrors increases, the full width half maximum of the resonant peaks decreases and the drop in transmission for wavelengths out of phase with the cavity becomes more pronounced.

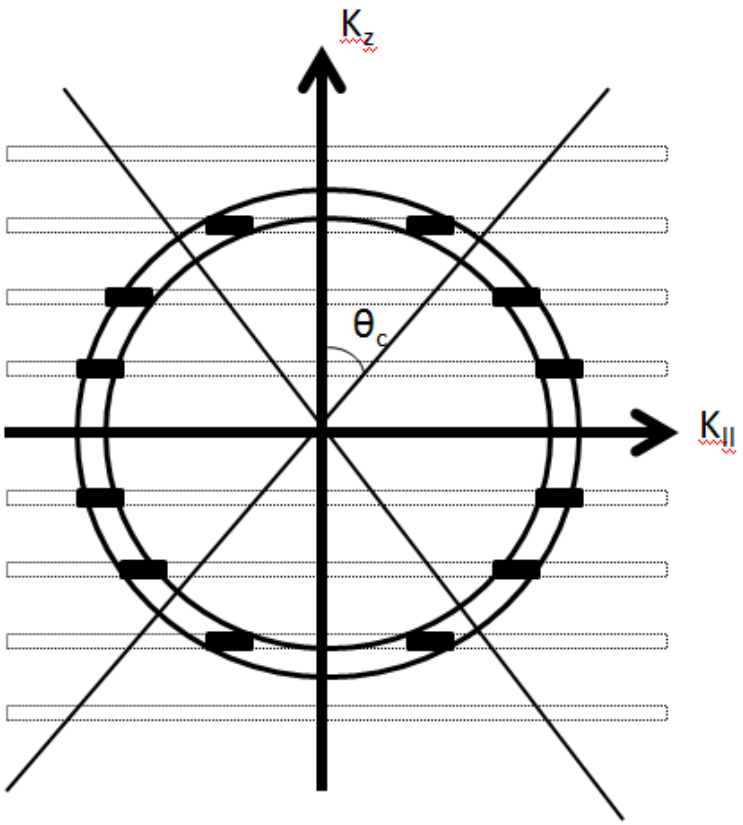

Figure 38. Resonant regions for imperfect resonators defined by dark shaded regions.

For imperfect resonators as in those described in Figure 37, the k-space picture described previously must be slightly modified. In this case, the resonances of the Airy factor are no longer discrete, but continuous with a spread defined by the Finnesse. Consequently, the resonant planes in K_z are no longer planes, but slabs. Additionally, if the point source is not monochromatic it has a non-zero spectral width (such is the case of spontaneous emission from an organic semiconductor) and the dispersion sphere should be broadened to a shell. Thus for imperfect resonators, volumetric overlap between the slabs and the shell define regions of resonance as shown in Figure 38.

The resonant angles larger than the critical angle correspond to leaky modes and guided modes and do not contribute to the light emission exiting the cavity.[47, 133, 158, 159] Only those resonances for which the angle of incidence is less than the critical angle (θ_c) can be extracted. In terms of the z component of the wave-vector, this corresponds to values between $k_z=k_0$ and $k_z=k_0\cos\theta_c$. As the light emission is proportional to the area under the Airy factor, the light extraction can be approximated as ratio of the area under the Airy factor within the extraction cone (from $k_z=k_0$ and $k_z=k_0\cos\theta_c$) to the total area under the Airy factor from $k_z=k_0$ and $k_z=0$.

6.4.6 Cavity Order

As shown previously, the resonant condition can be written in terms of k_z or in terms of the angle of incidence. An alternative way to express resonance is through the cavity order (m_c) which is the cavity thickness expressed in number of half wavelengths[142]:

Equation 41

$$m_c = \frac{d}{\lambda / 2n}$$

A cavity order of 1 ($m_c=1$) corresponds to an optical cavity length (given by the product of the index of refraction and the geometrical thickness {nL}) equal to $\lambda/2$. A cavity order of 2 ($m_c=2$) corresponds to an optical cavity length λ and so on. The resonance can then be written in terms of the optical cavity length[142]

Equation 42

$$m_c \cos\theta = m$$

From this equation it is clear that the number of resonances is limited to m_c. The cavity order will be discussed in more detail in the design rules section.

6.4.7 Cavity Tuning

Resonant conditions in a Fabry-Perot cavity outlined previously (Equation 33) can be rewritten as a function of wavelength ($k_0=2\pi/\lambda$):

Equation 43

$$nL = \frac{m\lambda}{2\cos\theta}$$

Equation 43 suggests that the resonant condition for a given optical cavity length (nL) depends on (1) the incident angle and (2) wavelength of the source emission. As shown in previous sections, when the incident angle and wavelength satisfy Equation 43, a resonant condition occurs. For clarity, when such conditions are met, the incident angle and wavelength will be referred to as the resonant angle and resonant wavelength, respectively. For a non-monochromatic source exhibiting a large dispersion of wavelengths, the optical length should be set such that majority of wavelengths satisfy a resonant condition within the extraction cone ($\theta < \theta_c$) to optimize the light enhancement emanating from the cavity. This is typically done by extending the spectral position of the optical mode beyond the peak intrinsic emission wavelength to form a so called over-tuned or detuned optical cavity compared to a tuned cavity for which the spectral location of the optical mode corresponds to the peak emission wavelength of the source. Such an approach is

based on the result in Equation 43 which suggests that the cavity length is directly proportional to the resonant wavelength and inversely proportional to the cosine of the resonant angle. Consequently, the resonant wavelength decreases with increasing resonant angle for a given cavity length and blue shifting of resonant peaks with increasing angle is observed. Thus, resonant conditions occur only for resonant wavelengths equal to or less than the cavity length for incident angles greater than 0°. For this reason, setting the optical cavity length equal to the resonant wavelength (tuned cavity) would limit the number of resonant contributions to wavelengths equal to or less than the peak emission wavelengths of the source and thus the overall power emanating from the cavity. More discussion on cavity tuning will be described in future sections.

6.5 Design Rules

The aforementioned sections, discussed a simplistic model to describe light out-coupling in a Fabry-Perot cavity or microcavity. While these approaches are insufficient to model an actual MOLED, they can be used to derive a number of approximate design rules for a simplified MOLED design, that can be used as guidelines for the first phase of design. In this section the basic design rules for MOLEDs are explained. For a more detailed discussion the reader is referred to work presented by Benisty et al.[131, 160]

6.5.1 Out-coupling Reflector

A typical MOLED consists of a fully reflective back mirror and a semi-reflective out-coupling mirror. The most important design parameter in a Fabry-Perot cavity is the semi-reflective out-coupling mirror. Various reflectors for Fabry-

Perot cavities have been studied including metallic reflectors, distributed Bragg reflectors (DBRs), and hybrid metal-DBR reflectors. Metal mirrors have the advantage of high reflectivity over a large spectral range including the near infrared and a large part of the visible range. Additionally, the reflectivity of metal mirrors does not depend on the angle of incidence. The disadvantage of metal mirrors is, except for cases of very thin films, the metallic reflectors are absorbing, resulting in a low transmittance making them unsuitable for out-coupling mirrors. Another disadvantage of metallic mirrors is a phase change occurs upon reflection at the metal surface. In order to compensate for this change in phase, an additional phase-matching layer with an appropriate thickness needs to be added.

DBRs consist of a series of high and low index material pairs. Typically the materials are dielectrics in which case they are properly termed dielectric distributed Bragg reflectors (DDBRs).[161] Unlike metallic mirrors, they are non-absorbing. Additionally, DBRs have a tunable Reflectance Energy, dependent upon the number of pairs and index of refraction difference of the materials. High reflectivity's (~100%) are possible given sufficient number of pairs. A disadvantage of DBRs is they have a narrow band of high reflectivity in the spectral and angular regime. Additionally, due to the partial penetration of the optical wave in the reflector the use of DBRs as Fabry-Perot mirrors results in a significantly increased effective cavity length and cavity order.[142, 162, 163] This thesis will focus on distributed Bragg reflectors as out-coupling mirrors in MOLEDs due to the minimal absorption losses and the large range of reflectance energies possible with a DBR configuration. The optical properties and design of DBRs will now be described.

DBRs are periodic structures with a unit cell of two layers, consisting of alternating layers of low (n_l) and high (n_h) refractive index material with an optical thickness of a quarter wave for the designed wavelength, defined as λ_{Bragg} [164, 165]

Equation 44

$$d_i = \frac{\lambda_{Bragg}}{4n_i}(i = h,l)$$

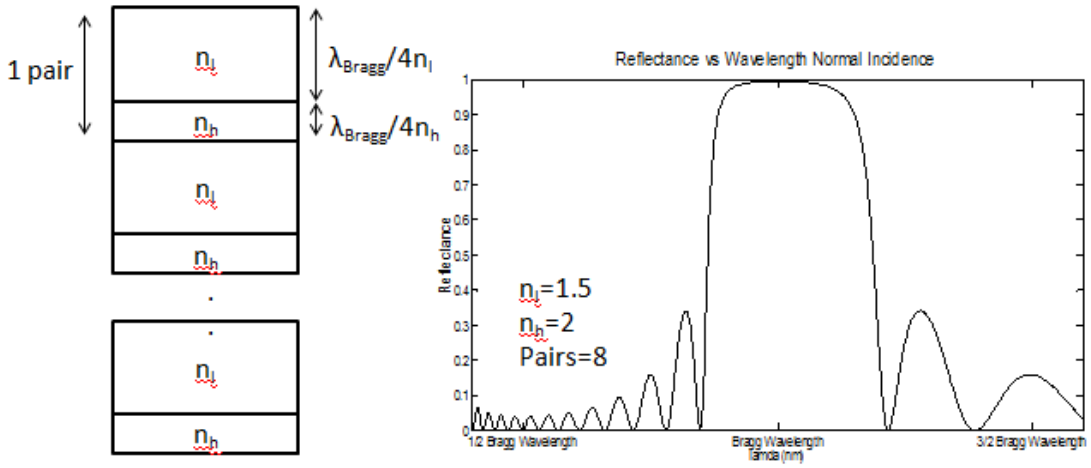

Figure 39. Distributed Bragg reflector structure with thickness $\lambda/4n_i$ where n_i is index of the low and high refractive index material (left). Reflectance spectra for a DBR with 8 pairs and Δn of 0.5. The reflectance peaks at the Bragg wavelength (right).

The reflectance properties are strongly dependent on the following parameters:

Equation 45

$$n_{eff} = 2\left(\frac{1}{n_l} + \frac{1}{n_h}\right)^{-1}$$

$$\Delta n = n_h - n_l$$

$$\frac{\Delta n}{n_{eff}}$$

The dependence on the reflectance energy as a function of number of pairs and refractive index difference can be calculated analytically. Consider a DBR consisting of "p" pairs sandwiched between two media of refractive index n_0 and n_s. Its reflectivity at its central wavelength λ_{Bragg} for normal incidence is given by[131, 166]

Equation 46

$$R_0 = R_0(p) = \left[\frac{1 - \frac{n_s}{n_0}\left(\frac{n_l}{n_h}\right)^{2p}}{1 + \frac{n_s}{n_0}\left(\frac{n_l}{n_h}\right)^{2p}} \right]^2$$

The high reflectivity band is called the stop-band. Beyond the stop-band, DBRs are no longer mirrors and allow propagative photon states called leaky modes. The width of the spectral stop-band scales with the refractive index difference $\Delta n / n_{eff}$ and is approximately given by[167]

Equation 47

$$\Delta\lambda_{stopband} = \frac{2\lambda_{Bragg}\Delta n}{\pi n_{eff}}$$

For a more general case with multiple layers with different refractive indices and different dispersion relationships the matrix method can be used to calculate the reflectance of a multi-layer stack.[166, 168] A matlab program implementing the

matrix method to calculate the reflectance of a multi-layer stack used throughout this thesis is included in the appendix (I).

6.5.2 MOLED structure and design

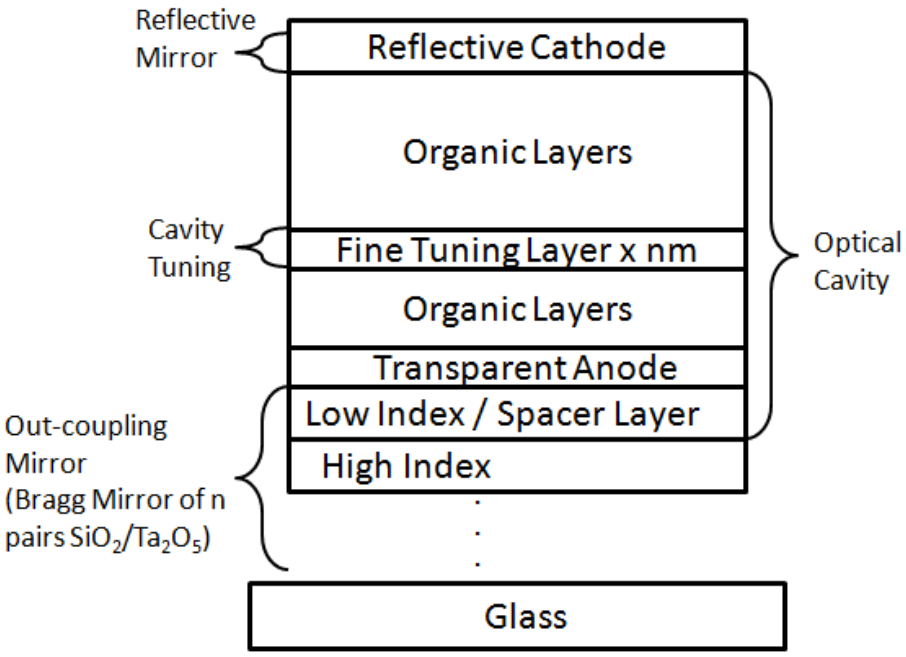

Figure 40. Schematic diagram of a common microcavity OLED. The optical cavity is defined between the reflective cathode mirror and the Bragg mirror, composed of alternating quarter-wavelength thick high index materials and low index materials. Cavity tuning is possible by varying the transporting layers. A spacer layer is inserted between the transparent anode and high index material to tune the cavity order without affecting the electrical performance of the MOLED.

Figure 40 shows a schematic diagram of a common MOLED configuration which consists of a highly reflective cathode and a semi-reflective distributed Bragg reflector (DBR) or quarter wave stack (QWS) out-coupling mirror. The DBR consists of λ/4 optically thick repeat pairs of a high index dielectric and a low index dielectric. Typically a low index material is inserted between the transparent anode and high

index dielectric material to tune the optical cavity. Such an approach can significantly extend the optical cavity without compromising the electrical performance of the device. Thus, high order cavities, as in the case of multimode resonance for white color tuning, is achievable using a low index spacer layer. In practice, fine-tuning of the cavity is also needed to achieve high external quantum efficiency's which is possible by varying the electron or hole transporting layers. The optical cavity is approximately equal to the optical length between the high index material and metallic cathode.

A microcavity OLED can be designed to optimize one or more of the following criteria:

(1) Optimization of overall external quantum efficiency

(2) Optimization of spectral width

(3) Optimization of brightness within a desired solid angle

Often time's one criterion optimization will affect another criterion optimization. For this reason, compromises between one criterion and another must be made. In this section, the design rules will focus only on optimization of the overall external quantum efficiency. The other criteria will be discussed further in later sections.

The basic design rules for enhancing light out-coupling in a MOLED based on the design outlined in Figure 40:

(1) Minimize the cavity order (m_c)

(2) Design the out-coupling reflectivity such that $R_1^{opt}=1-m_c/n^2$

(3) Position the Airy Factor inside of escape window $[k_0, k_0\cos\theta_c]$

(4) Implement a source with a narrow spectral width

(5) Maximize reflectivity of back mirror (R_2)

As a general rule the order of the cavity should be as low as possible.[142] As suggested in an earlier section, maxima in the Airy factor ($A(k_z)$) with respect to the z-component of the wave vector (K_z) define resonant modes of the cavity. With increasing cavity order the Airy factor peaks narrow which reduces the total area under the area curve inside of the extractable region (Appendix II).

Ideally, the Airy peak should be squeezed symmetrically inside of the escape window $[k_0, k_0\cos\theta_c]$ such that the majority of the Airy Peak is within the window. Increasing the out-coupling reflectivity results in a narrowed Airy peak inside of the window increasing the light extraction from the cavity but can also result in significant absorption losses due to the increased number of round trips. By setting the Airy factor at the escape window edges ($\theta=0$ and $\theta=\theta_c$) to a reasonable value (~10% of its peak value), the following condition can be found for the optimal out-coupling reflectivity (R_1^{opt}) in the case of a lossless cavity[131]

Equation 48

$$R_1^{opt} = 1 - \frac{m_c}{n^2}$$

According to Equation 48, the optimum out-coupling reflectivity, therefore, is on the order of ~40% for an order 2 cavity and an active region refractive index of 1.8. It will be shown in future sections that this value agrees very well with more sophisticated models designed to assess light out-coupling in MOLEDs.

In addition to optimizing the out-coupling mirror reflectivity, the cavity length should also be set such that the position of the Airy peak is centered inside of the escape window $[k_0, k_0\cos\theta_c]$ which can be achieved be over-tuning or detuning the cavity. For a source with a large spectral distribution, the cavity detuning design must consider many wavelength as not all wavelengths can be centered inside of the escape window for a given cavity length. Typically, the peak emission wavelength of the source should be centered inside of the escape window, however, this condition varies from case to case depending on the spectral shape of the source. This point leads to the next design rule which suggests that the MOLED should implement sources with intrinsically narrow band emission characteristics or a small full width half maximum (FWHM). Figure 41 effectively demonstrates this point in terms of a k-space coordinate system.

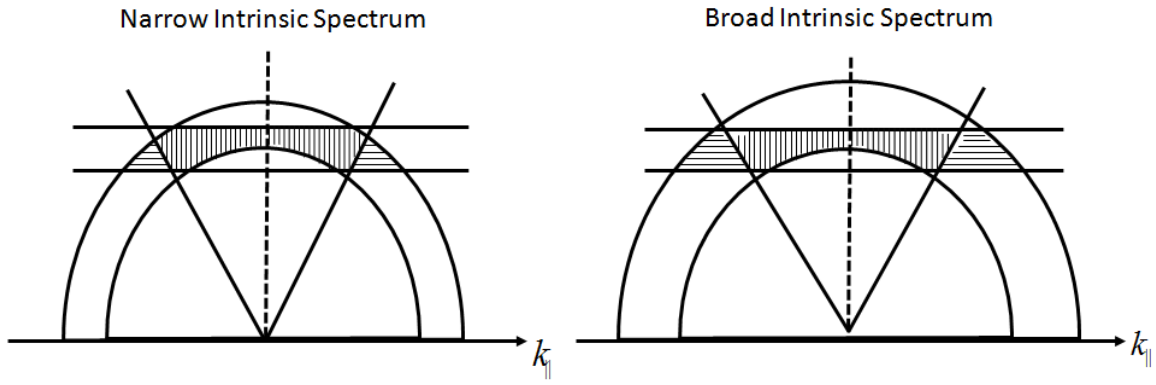

Figure 41. The blue band represents the 2D projection of a non-monochromatic k-sphere for a narrow (left) and broad (right) emission spectrum. The vertical lines represent resonant conditions within the extraction cone (contribute to farfield intensity). The horizontal lines represent resonant conditions outside of the extraction cone (do not contribute to the farfield intensity).

Finally rule 5 suggests that the back mirror reflectivity (R_2) should be as high as possible. Thus, cathode materials with high reflectivity's and small absorption coefficients should be implemented into MOLEDs.

6.6 Method of Source Terms: Transition to a vectorial electromagnetic problem with electrical dipole source terms

Design rules defined in the previous section can be used as a guideline in the first phase of design, however a quantitatively accurate design of a MOLED is only possible by numerical analysis. While the previous approaches have been used to develop general guidelines, in practice, specific details of MOLED performance including the light out-coupling efficiency, angular intensity profile, and spectral shape is needed. Thus, a more rigorous optical model will now be considered.

The scalar approach as outlined in previous sections implies not only that the fields are scalar, but that the point source was a scalar. In reality, we must consider vectorial fields and vectorial sources.

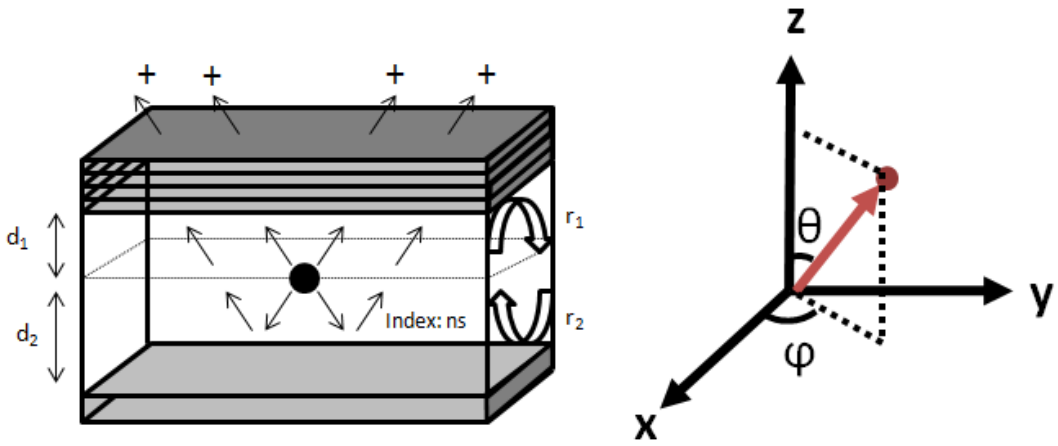

Figure 42. A schematic of a multilayer OLED (left) with an emitting medium (n_s). The dipole is located at a distance d_1 from the upper mirror and d_2 from the bottom mirror with a total mirror separation of d. The upper mirror has a reflection coefficient of r_1 and the bottom mirror has a reflection coefficient of r_2. The power is reflected at the mirror surfaces creating interference inside the cavity. The emission angle θ and φ are defined in a Cartesian coordinate system (right).

In the weak-coupling regime, the spontaneous emission process of a bulk semiconductor can be adequately represented by an electric dipole.[162] An electric dipole can be decomposed into a horizontal and vertical component. The horizontal component has a dipole moment in the (x-y)-plane and the vertical component has a dipole moment along the z-axis. Similar to the electric dipole, an electromagnetic wave can also be separated into two components; a Transverse Electric (TE or s) and Transverse Magnetic (TM or p). A TE is a plane wave that has its E-field in the (x-y)=plane and orthogonal to k and a TM is a plane wave that has its H-field transverse to the plane of incidence. A plane wave component A of the field resulting from an electric dipole has its electric field in the plane of the dipole moment and the wave-vector k, vanishing sinusoidally for emission in the direction of the dipole moment.[162] Decomposing an arbitrary linear polarization into TE and TM, averaging the field amplitude over the azimuthal angle φ, and normalizing the total emitted power results in plane wave amplitudes (expressed as density per unit solid angle) summarized below.[162]

Table 7. Source terms for horizontal and vertical dipoles[137]

	TE	TM
Horizontal	$A_{\uparrow\downarrow}^{h,s} = \sqrt{\frac{3}{16\pi}}$	$A_{\uparrow\downarrow}^{h,p} = \sqrt{\frac{3}{16\pi}}\frac{k_z}{k} = \sqrt{\frac{3}{16\pi}}\cos\theta$
Vertical	$A_{\uparrow\downarrow}^{v,s} = 0$	$A_{\uparrow\downarrow}^{v,p} = \sqrt{\frac{3}{16\pi}}\frac{k_\parallel}{k} = \sqrt{\frac{3}{16\pi}}\sin\theta$

Thus, the complete vectorial problem can be decomposed into three simple scalar problems; a TE generated by a parallel dipole, a TM generated by a parallel dipole, and a TM generated by a perpendicular dipole.[131, 160, 162]

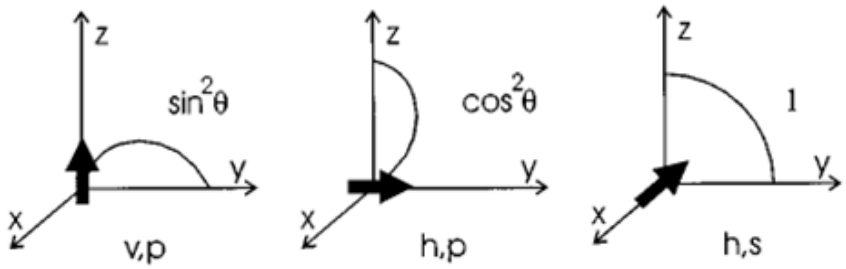

Figure 43. Emission patterns for a vertical dipole emitting TM (left), a horizontal dipole emitting TM (middle) and a horizontal dipole emitting TE (right).

The emitted intensity $I^{or,pol}(\theta)$ (pol=s,p, or=horizontal, vertical) for an internal emission angle, θ, caused by the source's downwards and upwards propagating plane wave component $A^{or,pol}_{\downarrow}$ and $A^{or,pol}_{\uparrow}$ can be calculated letting the plane propagative and evanescent waves propagate in the multilayer. The different contributions in the outside medium give rise to a field distribution, a power distribution and an extraction efficiency given by[137]:

Equation 49

$$E^{or,pol}(\theta) = \left|A^{or,pol}_{\uparrow} + A^{or,pol}_{\downarrow} r_2 \exp(-i2\phi_2)\right| \ldots$$
$$\cdot t_1 \exp(-i\phi_1) \cdot \left|1 + r_1 r_2 \exp(-i2\phi) + r_1^2 r_2^2 \exp(-i4\phi) + \ldots\right|$$

Equation 50

$$I^{or,pol}(\theta) = T_1 \left|E^{or,pol}(\theta)\right|^2 = T_1 \frac{\left|A^{or,pol}_{\uparrow} + A^{or,pol}_{\downarrow} |r_2| \exp(-i2\phi_{2eff})\right|^2}{\left|1 - |r_1 r_2| \exp(-i2\phi_{eff})\right|^2}$$

Equation 51

$$\eta_{extr} = \frac{2\pi \int_0^{\theta_c} I^{or,pol}(\theta) \sin\theta d\theta}{\int_0^{\pi} I^{or,pol}(\theta) \sin\theta d\theta}$$

Here $|r1r2|<1$, r1 and r2 the upwards and downward amplitude reflection coefficients (Er/Ei), T1 the upwards power transmission coefficient $|E_t^2/ E_i^2|$ and:

Equation 52

$$\phi_i = k_0 n_s d_i \cos(\theta)$$

Equation 53

$$\phi = \phi_1 + \phi_2$$

Equation 54

$$2\phi_{eff}(\theta,\lambda) = 2\phi - \arg(r_1) - \arg(r_2)$$

Equation 55

$$2\phi_{ieff}(\theta,\lambda) = 2\phi_i - \arg(r_i)$$

Here d_1 and d_2 are the distances of the dipole from the interfaces of the first layer of the upper mirror and the first layer of the bottom mirror, respectively. R_1, r_2, and T_1 are polarization dependent and can be calculated using a transfer matrix method. Similar to the scalar approach outlined earlier, the numerator is called the standing wave factor and expresses the dependence of the emitted intensity on the position of the source. The inverse of the denominator is called the cavity enhancement factor

or Airy factor. The cavity enhancement factor peaks (resonance occurs) when the following condition is met:

Equation 56

$$2\phi - \arg(r1) - \arg(r2) = 2\phi_{eff}(\theta, \lambda) = 2m\pi$$

In bulk semiconductor materials, the emission is isotropic and the dipole can have any orientation. In this case, one third of the power generated by dipoles is generated by vertical dipoles and two thirds by horizontal dipoles and the intensity becomes[137]

Equation 57

$$I(\theta) = \frac{2}{3}(I^{h,s}(\theta) + I^{h,p}(\theta)) + \frac{1}{3}I^{v,p}(\theta)$$

6.7 The Finite Difference Time Domain Method

The previous approach assumes the cavity is composed of a single medium. However, OLEDs contain several layers with different refractive indices. Additionally, the previous model depends on knowledge of the exact location of the cavity, which may result in erroneous results when the reflection points are not defined accurately in the model. For a more accurate assessment of the light extraction efficiency in OLEDs, the finite difference time domain method should be used.

6.7.1 Theory

The finite difference time domain (FDTD) method was first proposed by Kane S. Yee in 1966 and consists of a time-dependent solution of Maxwell's equations

based on their differential form using central difference approximations of both the space and the time-derivatives.[169, 170] The formulation is based on discretizing the volume domain with a regular, structured, staggered, rectangular grid, solving Maxwell's equations discretely in both space and time, where the time step used is related to the mesh size through the speed of light. The technique is an exact representation of Maxwell's equations in the limit that the mesh cell size goes to zero.

Several commercially available software programs implement the Yee algorithm for solving Maxwell's equations for complex geometries. In particular, Lumerical FDTD Solutions has been common software used in the field for analysis of light extraction in OLEDs.[169, 170] The software gives both time and frequency domain information to the user and handles a wide variety of material properties including metals. Results obtained from the near field may be transformed to the far-field to obtain scattering patterns.

Figure 44 shows a schematic of a typical OLED structure. The OLED structure is modeled inside the FDTD computational domain. The metal cathode is modeled as a perfect electric conductor, allowing no energy to escape the simulation volume along the metal cathode boundary. The substrate and surrounding organic layers are defined by a perfectly matched layer (PML) boundary condition which allows electromagnetic waves to propagate out of the computational domain without being reflected back into the computational domain.

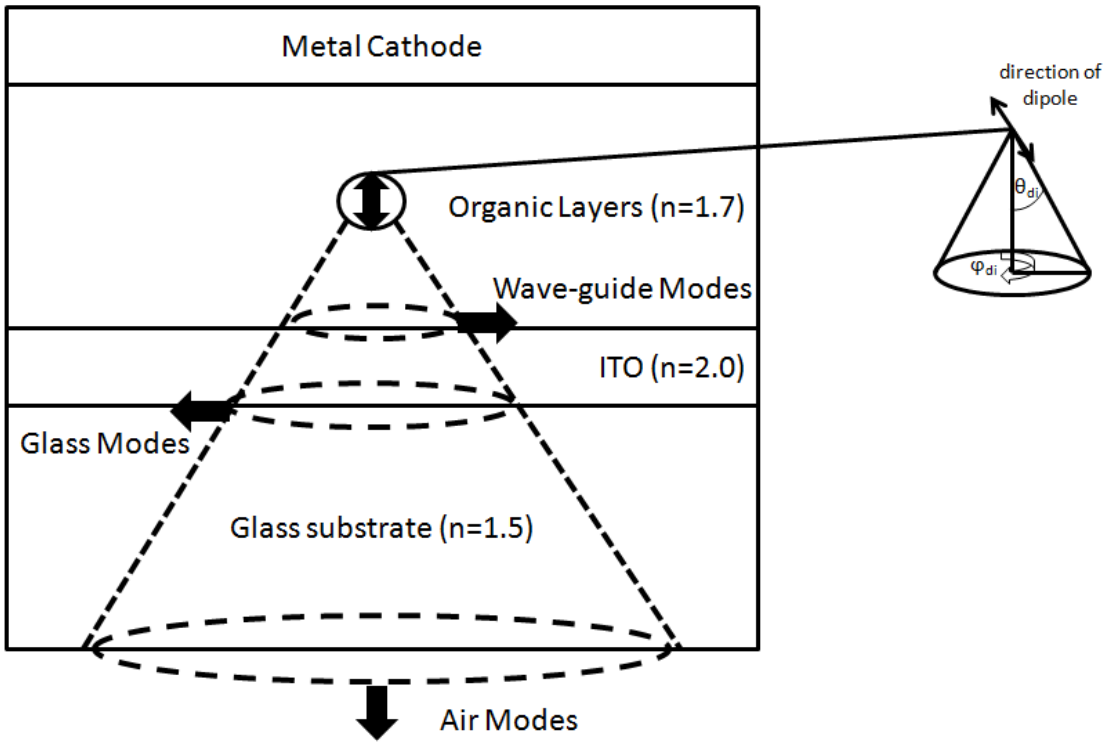

Figure 44. Schematic of a typical OLED structure.

FDTD is a time domain technique; consequently, the electromagnetic fields are solved as a function of time. As OLEDs are broadband emitters, the power equation (Equation 58) must be determined as a function of angular frequency (ω) or wavelength. This is done by putting the time domain data through a Fourier transform (Equation 59 and 60). For convenience, the frequency data is normalized by the source spectrum (Equation 61).

Equation 58

$$\vec{P}(\omega) = \frac{\vec{E}(\omega) \times \vec{H}(\omega)}{\left|s(\omega)\right|^2}$$

Equation 59

$$\vec{E}(\omega) = \frac{1}{s(\omega)} \int \exp(i\omega t)\vec{E}(t)dt$$

Equation 60

$$\vec{H}(\omega) = \frac{1}{s(\omega)} \int \exp(i\omega t)\vec{H}(t)dt$$

Equation 61

$$s(\omega) = \frac{1}{N} \sum_{sources} \exp(i\omega t) s_j(t)dt$$

E(t) and H(t) are the electric and magnetic fields as a function of time, respectively. $s_j(t)$ is the source time signal of the j^{th} source and N is the number of active sources in the simulation volume. The time signal of the dipole source, s(t), is described by a pulse (Equation 62).

Equation 62

$$s(t) = \sin(\omega_0(t - t_0)) \exp\left(- \frac{(t - t_0)^2}{2(\Delta t)^2} \right)$$

Ideally, s(t) would be a dirac delta function (in which case s(ω)=1), allowing for a response containing all frequencies from a single simulation. For a variety of reasons, it is more efficient and numerically accurate to excite the system with a short pulse such that the spectrum, $|s(\omega)|^2$, has a reasonably large value over all frequencies of interest.

In an OLED electrons and holes recombine to excitons in the emission zone. While in principle, the radiative decay of an exciton must be described quantum mechanically in terms of photons; in practice it is possible to treat the generated

light classically using electromagnetic point dipole sources.[171] The propagation of light is therefore given by the solution of Maxwell equations for an oscillating dipole in the layered structure and depends on its location and orientation. The total injected power of the oscillating dipole depends strongly on the dipoles local density of states as fields reflected by nearby structures re-interfere with the source, causing it to inject more or less power than in a homogenous environment.[172] In the 3D FDTD calculation, the total injected power is normalized to the power injected in a homogenous environment. To simulate a perfectly isotropic, incoherent source, 3 simulations of the same dipole orientated along the x/y/z axes are calculated and then summed up incoherently.[171] The energy flow in the structure and into the substrate is then derived from the electrical and magnetic fields. Since the direction of the dipole can be arbitrary, the results must be averaged over all dipole directions. This can be expressed by the Equation 63.

Equation 63

$$\bar{p} = \int_0^{\pi/2}\int_0^{2\pi} p(\theta_{di},\phi_{di})\sin(\theta_{di})\,d\theta_{di}\,d\phi_{di} \Big/ \int_0^{\pi/2}\int_0^{2\pi} \sin(\theta_{di})\,d\theta_{di}\,d\phi_{di}$$

The variable $p(\theta_{di},\phi_{di})$ is the power as a function of the dipole direction θ_{di} and ϕ_{di}.

Since the OLED structure is uniform in the in-plane direction the system contains azimuthal symmetry and the power equation becomes a function of θ_{di} only ($p(\theta_{di},\phi_{di})=p(\theta_{di})$). The dipole power for each mode for various θ_{di} is calculated in

three-dimensional space in the FDTD domain. According to Chen et al., the power can be perfectly described by Equation 64.

Equation 64

$$p(\theta_{di}) = p(0°)\cos^2(\theta_{di}) + p(90°)\sin^2(\theta_{di})$$

Substituting Equation 64 into Equation 63, we obtain:

Equation 65

$$\vec{p} = \frac{1}{3}p(0°) + \frac{2}{3}p(90°)$$

As shown in Figure 44, the power of the wave-guide is determined by simply calculating the power that flows along the Organic/ITO waveguide. The computational domain extends 400nm deep into the glass substrate. The total power at this domain is assessed and the transmission of power from glass to air is treated by ray optics,[173] i.e., the light that propagates inside the glass substrate with an angle less than the critical angle of the glass/air interface (41.8°) is considered as the air mode and the light that propagates inside the glass substrate at an angle larger than 41.8° is considered the glass mode. The light extraction efficiency of an OLED is defined as the fraction of optical power generated in the active layer over the power that is transmitted into air (air modes). The overall extraction efficiency of the OLED is the ratio of the transmission of power from glass to air over the total injected power.

6.7.2 Overview of Model Assumptions

It is now worth reviewing the main assumptions of the modeling framework described in the previous section in order to define the general limits of validity of this approach. We can summarize the assumptions used in the modeling framework as follows:

(i) The emitting medium, the substrate material, and the far-field medium in the OLED multilayer are assumed to be nonabsorbing.

(ii) The transition dipole of the phosphorescent molecular emitter is assumed to be isotropic.

(iii) OLED devices are operated at low excitation levels or, equivalently, at low exciton concentrations in the emitting layer.

(iv) The extension of the exciton generation is small compared to the cavity length. In particular, we consider the limit of a δ-distributed exciton generation profile.

(v) The source is monochromatic with an out-coupling efficiency equal to the ratio of total output power of the peak wavelength emission energy to total injected power of the dipole at the peak wavelength emission energy.

(vi) The multilayer stack consists of perfectly smooth layers and interfaces.

The first assumption is an intrinsic limitation of the electromagnetic model used in this work. For the systems we will analyze in the foregoing sections, it can be verified that the effect of self-absorption in the emitting layer could be safely neglected due to the generally weak overlap between absorption peak and luminescence spectrum of the materials in this study.

The second assumption in the list above, i.e., isotropic transition dipole moments, is present due to the lack of specific information with respect to the orientation of the emitting dipoles in molecular emitting systems. Recently, experimental evidence of non-isotropic emission with a ratio for parallel versus perpendicular emitting sites was reported to be equal to 2:0.67 in the phosphorescent system NPB:Ir(MDQ)$_2$(acac) , larger than the commonly considered isotropic portion 2:1.[174, 175] It is expected, however, for the system involved that the information about the emitter orientation to lie within the accuracy limits of our device fabrication process and characterization uncertainties.

The third and fourth assumption has been made necessary due to missing quantitative knowledge of various internal microscopic quantities and distributions, for which physical models are unavailable or still under development. Particular care, however, has been taken in the design of experiment and in the choice of the characterization conditions to ensure that these assumptions are satisfied, and thus experiment and theory can be meaningfully compared.

The fifth assumption is valid only for select cases wherein the source exhibits an intrinsically narrow band emission. The design of experiment to be described included optimization of a MOLED implementing the tetradentate, cyclometalated

platinum complex, PtN1N, with an intrinsically narrow emission spectral band (FWHM=18nm in solution of DCM). The specific emission properties of PtN1N will be discussed in more detail in the foregoing sections. We have found the fifth assumption to be valid for MOLEDs implementing PtN1N as theoretical calculated data are in good agreement with the experimental findings. For organic emitters with a large full width half maximum, the optical model developed must be modified to account for many wavelengths.

The sixth assumption assumes perfectly smooth layers and neglects the surface roughness of the layer interfaces as well as the glass/air transition, which may lead in some underestimation of the overall light out-coupling efficiency.

6.7.3 Simulation Accuracy Check

A three-dimensional multilayer OLED was modeled based on the device structure of Glass/ITO(60nm)/HATCN(10nm)/NPD(xnm)/TAPC(10nm)/8%PtN1N :26mCPy (25nm)/DPPS (10nm)/BmPyPB(45nm)/LiF(1nm)/Al(100nm), where x=30nm, 40nm, 50nm, and 60nm. Optical constants for the various layers were experimentally measured using an ellipsometer and were included as inputs in the optical model. The structure chosen incorporates the highly efficient phosphorescent emitter, PtN1N, with a radiative quantum efficiency close to unity. The structure also incorporates effective hole and electron blocking and transporting materials resulting in close to 100% internal quantum efficiency. Additionally, the phosphorescent emitter exhibits a narrow band emission (FWHM=18nm based on the thin film PL), making the emitter a suitable candidate for the monochromatic assumption suggested in the previous section. Thus, the external quantum efficiency

is approximately equal to the out-coupling efficiency calculated at the peak thin film photoluminescent emission wavelength of 496nm. The device structure as well as the photoluminscent characteristics of the phosphorescent emitter, PtN1N, in a thin film (25nm) of 8%PtN1N:26mCPy are shown in Figure 45.

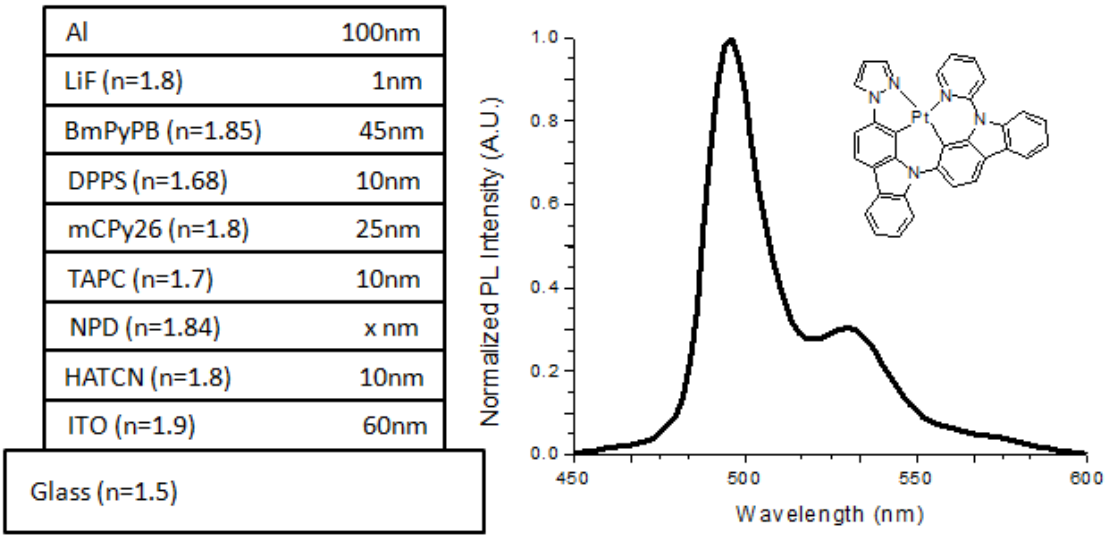

Figure 45. The device structure (left) and photoluminescent spectrum (right) of PtN1N in a thin film of 26mCPy including the molecular structure of PtN1N (inset).

The accuracy of the simulation depends on several factors including the size of the computational domain and the mesh size (Maxwell boundary condition domains). To assess the accuracy of the simulation, the afore–mentioned factors were investigated. In theory, the larger the computational domain and the smaller the mesh size, the nearer the finite difference time domain approximation approaches a solution to Maxwell's equations in continuum space. However, increasing the computational domain and reducing the mesh size also results in a higher number of computations and computational memory. For this reason, it is important to define the point at which reducing the computational effort will result in inaccuracies. Following this approach, the computational power necessary to

accurately simulate light propagation in OLED structures can be determined without utilizing excessive computational power. The limiting regime was found by individually varying the size of the computational domain (increasing the domain) as well as the mesh size (reducing the mesh size) until no further change was observed in simulation outputs. The extraction efficiency, outlined in a previous section, was used as metric to compare the outputs of the simulation under different mesh size and computational domain conditions. All calculations in this thesis followed this optimization process.

Based on the results, a mesh size of 10nm x 10nm x 8nm and a computational domain of 4um x 4um x 2um will result in a sufficiently accurate assessment of the extraction efficiency in OLEDs as further increases in the computational domain or further reductions in the mesh size results in negligible changes in the simulation output. The accuracy of the simulation was further investigated by comparing the calculated extraction efficiency with the external quantum efficiency of the OLED in this study. Since the OLED structure in consideration has near 100% internal quantum efficiency, the calculated light out-coupling efficiency is approximately equal to the external quantum efficiency. The spatial and temporal resolution of the FDTD calculation was 10nm and 0.019 fs, respectively. The size of the optimized computational domain is 4000x4000x2000 nm, where the last dimension refers to the direction perpendicular to the OLED layers. The comparison of the actual and theoretical external quantum efficiency as well as the measured electroluminescent spectra are shown in Figure 46.

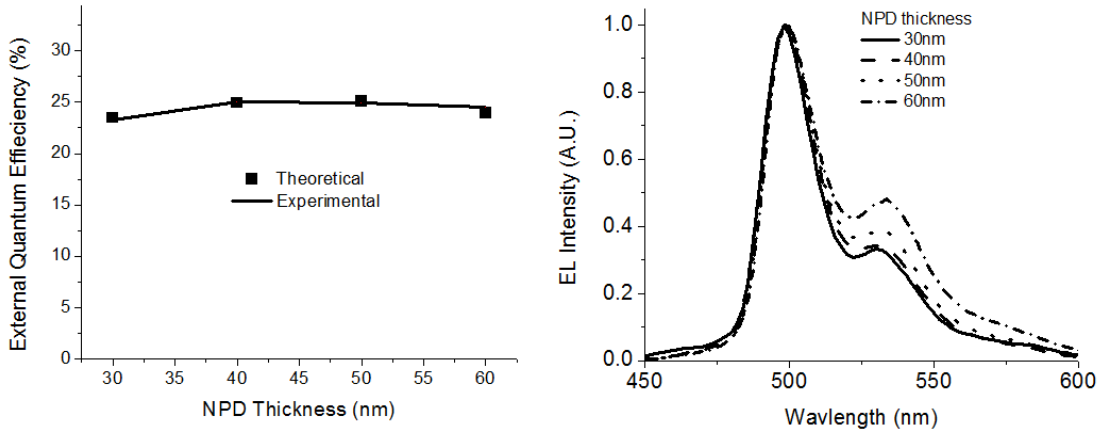

Figure 46. The theoretical extraction efficiency (black squares) at different NPD layer thicknesses versus the measured external quantum efficiency (black line) of the OLED (left). The measured electroluminescent spectra for a 30nm, 40nm, 50nm, and 60nm NPD layer.

The measured external quantum efficiency for OLEDs containing a 30nm, 40nm, 50nm, and 60nm NPD thick layer were 23.3%, 25.0%, 24.9%, 24.5%, respectively, compared to theoretical values of 23.5%, 24.9%, 25.1%, and 23.9%, respectively. The theoretical and experimental values agree well and exhibit a similar trend with an optimal NPD thickness of 40nm, likely as a result of microcavity effects. This is supported by a slight red-shifted spectrum with increasing NPD thickness, typical of cavity detuning.

6.8.1 Design of Experiment Description

A design of experiment will now be described wherein the light out-coupling efficiency of the platinum complex, PtN1N, in a MOLED architecture was optimized by varying the (1) cavity length and (2) the DBR configuration or out-coupling mirror reflectivity.

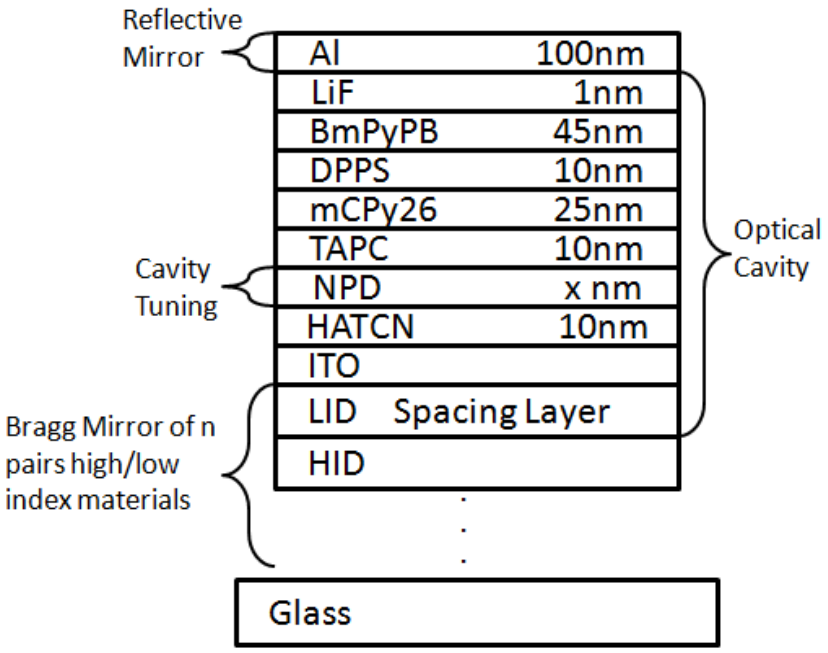

Figure 47. A schematic diagram of the MOLED design explored in this DOE. Cavity tuning is accomplished by varying the hole transported layer, NPD, and the out-coupling reflector is tuned by varying the material and the number of the high low index Bragg pairs.

A schematic of the proposed MOLED design is outlined in Figure 47. The cavity length was tuned by varying the thickness of the hole transport layer, NPD, which has a high hole mobility resulting in little change in the electrical properties of the device with a wide range of thicknesses, which will be shown in Chapter 7. In this design of experiment, the NPD thickness was varied from 30nm to 60nm. The out-coupling reflectivity was tuned by varying the high and low index material as well as the number of quarter wave stack (QWS) pairs of the DBR. In this design of experiment, two common low index dielectric materials (SiO_2 and MgF_2) and six common high low index dielectric materials (MgO, Y_2O_3, ZnO, ZrO_2, TeO_2, and TiO_2) were implemented in the MOLED described previously with 3 different configurations (1 DBR pair, 2 DBR pairs, and 3 DBR pairs) for a total of 36 DBR

structures. A summary of the DBR structures in this DOE are outlined in Table 8 which includes the quarter wave thickness ($\lambda/4n$) for the low index dielectric (t_{low}) and the high refractive index (t_{high}) based on the refractive index at 496nm. Each DBR structure was designed to optimize reflectivity at the peak thin film photoluminescent emission wavelength of 496nm. Each structure consisted of a 100nm optical spacer layer consisting of MgF_2 and SiO_2 for structures 1-6 and 7-12, respectively, outlined in Table 8. The measured dispersion relation is outlined in Appendix III.

Table 8. A summary of the Low/High index configurations investigated in this DOE

Configuration	Low/High Dielectric	n_{low} [496nm]	n_{high} [496nm]	t_{low} (nm)	t_{high} (nm)
1	MgF2/MgO	1.38	1.75	91	71
2	MgF2/Y2O3	1.38	1.95	91	64
3	MgF2/ZnO	1.38	2.05	91	61
4	MgF2/ZrO2	1.38	2.22	91	56
5	MgF2/TeO2	1.38	2.32	91	54
6	MgF2/TiO2	1.38	2.71	91	46
7	SiO2/MgO	1.49	1.75	84	71
8	SiO2/Y2O3	1.49	1.95	84	64
9	SiO2/ZnO	1.49	2.05	84	61
10	SiO2/ZrO2	1.49	2.22	84	56
11	SiO2/TeO2	1.49	2.32	84	54
12	SiO2/TiO2	1.49	2.71	84	46

The various combinations of each structure result in a large range of peak reflective energy's from 11% to 90%. A summary of the reflectance versus

wavelength and summary table for each DBR combination is outlined in the Appendix III.

6.8.2 Results and Discussion

A total of 144 runs (4 NPD thickness and 36 DBR structure combinations) were simulated using the FDTD method. The full run scheme is referenced in Appendix III. A summary of the light extraction efficiency or light out-coupling efficiency for the single DBR pair consisting of (1) the low index dielectric MgF_2 with a high index dielectric MgO, Y_2O_3, ZnO, ZrO_2, TeO_2, and TiO_2, and (2) the low index dielectric SiO2 with a high index dielectric MgO, Y_2O_3, ZnO, ZrO_2, TeO_2, and TiO_2 is summarized in Figure 48.

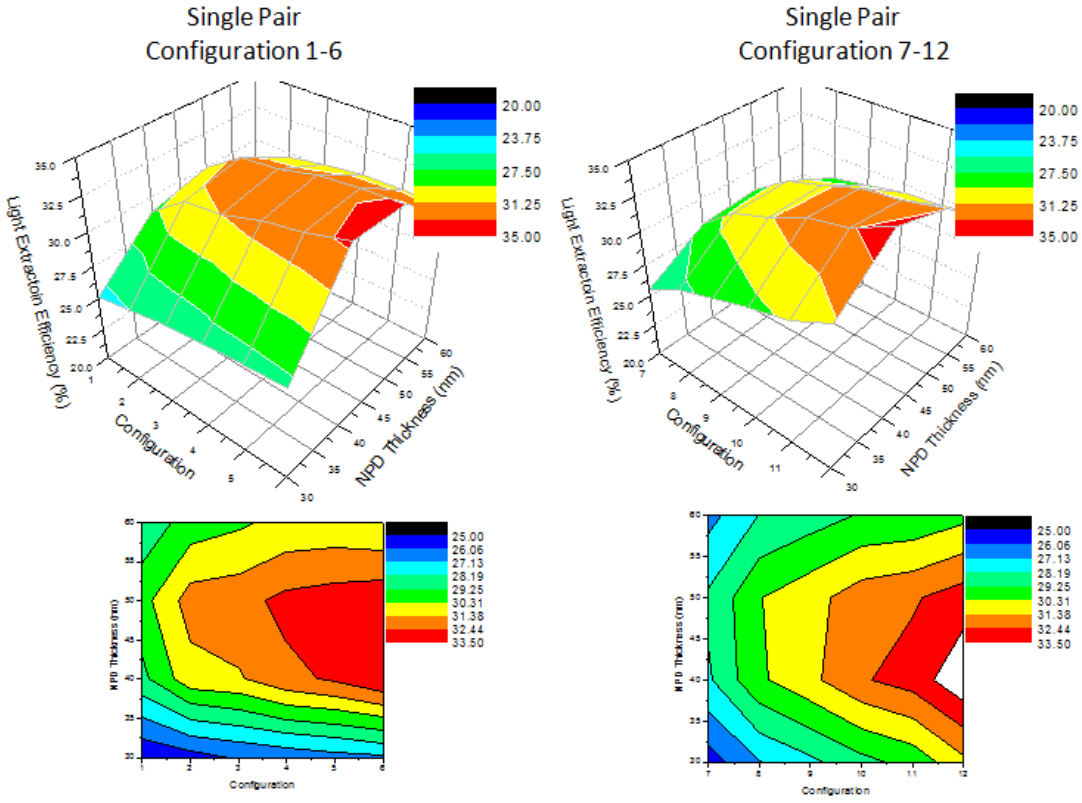

Figure 48. A summary of the light extraction efficiency or light out-coupling efficiency for a single DBR pair consisting of the low index dielectric MgF_2 with a high index dielectric MgO, Y_2O_3, ZnO, ZrO_2, TeO_2, and TiO_2 (left), and the low index dielectric SiO2 with a high index dielectric MgO, Y_2O_3, ZnO, ZrO_2, TeO_2, and TiO_2 (right) for NPD thickness 30nm, 40nm, 50nm, and 60nm.

Configuration 6 with the low index dielectric, MgF_2 and high index dielectric, TiO_2, exhibited an extraction efficiency of 26.72%, 33.45%, 33.21%, and 30.3% for a 30nm, 40nm, 50nm, and 60nm NPD thickness, respectively, compared to configuration 1 with the low index dielectric, MgF_2 and high index dielectric, MgO, which had an extraction efficiency of 25.13%, 28.95%, 29.92%, and 28.51% for a 30nm, 40nm, 50nm, and 60nm NPD thickness, respectively. For a given NPD thickness, the light extraction efficiency increased with increasing index of refraction of the high index dielectric. The index of refraction of the high index dielectric is directly related to the reflectance energy of the DBR stack. Thus, light extraction efficiency increased with increasing reflectance energy of the out-coupling mirror or DBR stack. Similar behavior was observed for configurations implementing the low index material SiO_2 (configuration 7-12). In particular, configuration 12 with the low index dielectric, SiO_2 and high index dielectric, TiO_2, exhibited a light extraction efficiency of 31.10%, 34.31%, 33.02%, and 30.03% for a 30nm, 40nm, 50nm, and 60nm NPD thickness, respectively, compared to configuration 7 with the low index dielectric, SiO_2 and high index dielectric, MgO, which had an extraction efficiency of 25.53%, 28.06%, 28.37%, and 26.77%. The highest extraction efficiency for the single DBR case was achieved with a 40nm NPD thickness and a low index dielectric, SiO_2, and high index, TiO_2, dielectric with an extraction efficiency of 34.3%.

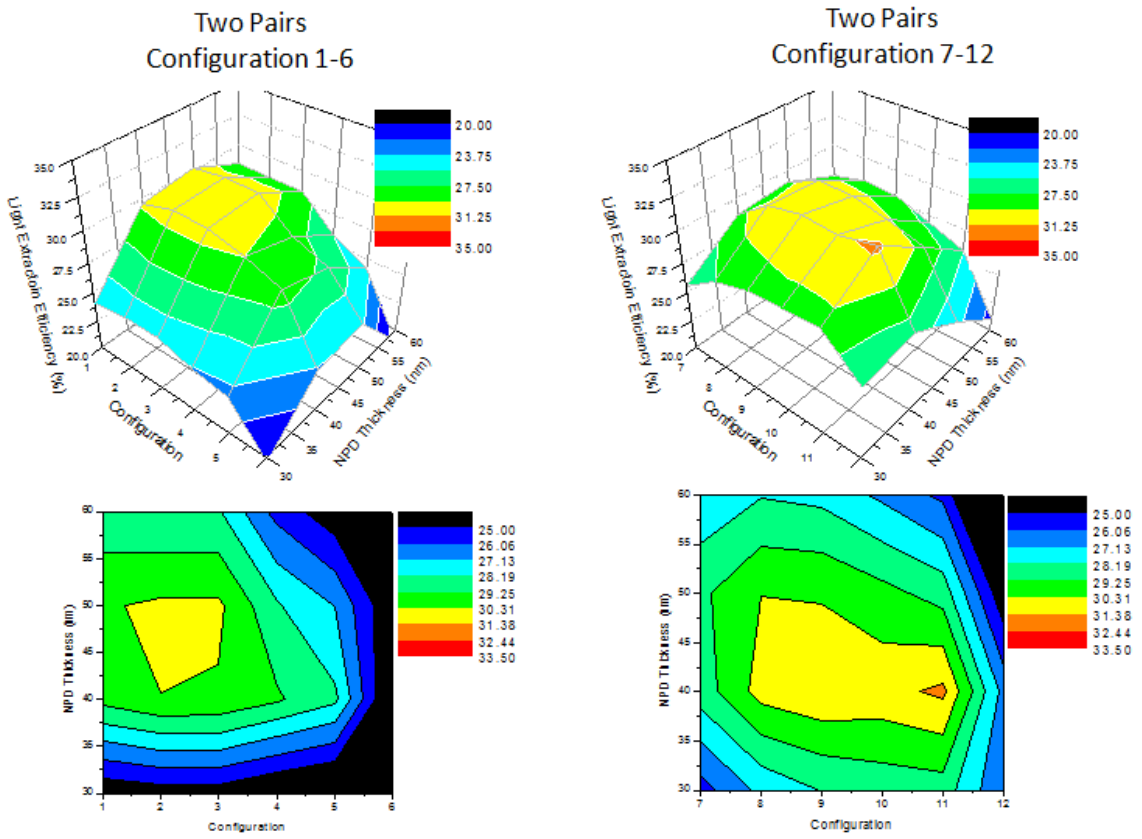

Figure 49. A summary of the light extraction efficiency or light out-coupling efficiency for a DBR stack of 2 DBR pairs consisting of the low index dielectric MgF_2 with a high index dielectric MgO, Y_2O_3, ZnO, ZrO_2, TeO_2, and TiO_2 (left), and the low index dielectric SiO2 with a high index dielectric MgO, Y_2O_3, ZnO, ZrO_2, TeO_2, and TiO_2 (right) for NPD thickness 30nm, 40nm, 50nm, and 60nm.

A summary of light extraction efficiency for configurations 1-6 and 7-12 for 2 DBR pairs is shown in Figure 49. In the case of 2 DBR pairs containing the low index dielectric, MgF2, the optimal extraction efficiency of 30.50% was achieved with a 50nm NPD thickness and high index dielectric, Y_2O_3, compared to the 2 DBR case containing the low index dielectric, SiO_2, with an optimal extraction efficiency of 31.60% with a 40nm NPD thickness and high index dielectric, TeO_2. Unlike the single DBR case wherein light extraction efficiency increases for a given a NPD thickness with increasing index of refraction of the high index dielectric, maxima in the light extraction efficiency occurs at moderate indices of refraction of the high

index dielectric for both MOLEDs containing the low index dielectric MgF_2 and SiO_2. These maxima in the extraction efficiency are directly related to the reflectance energy of the out-coupling mirror and supports the design rules outlined in section 6.5.2 (rule 2) which suggest that the highest extraction efficiency is achieved by balancing the extent at which the Airy peak is contained within the escape window and the absorption losses on account of increased number of round trips inside the cavity.

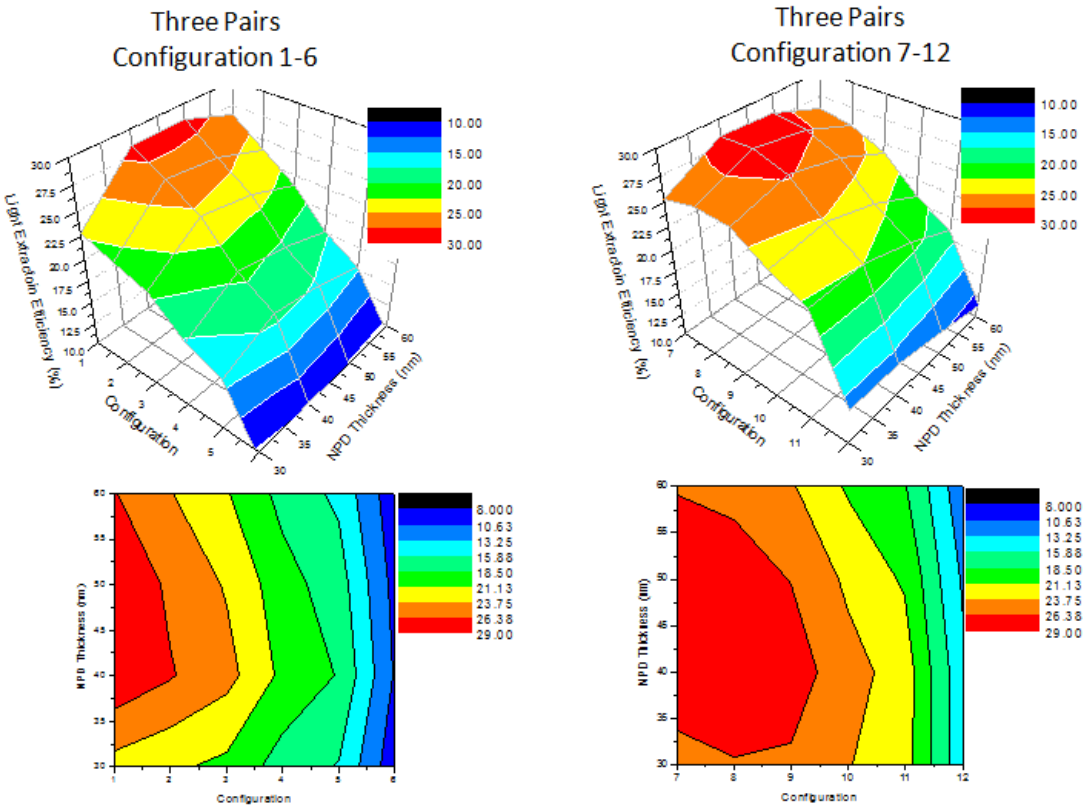

Figure 50. A summary of the light extraction efficiency or light out-coupling efficiency for a DBR stack of 3 DBR pairs consisting of the low index dielectric MgF_2 with a high index dielectric MgO, Y_2O_3, ZnO, ZrO_2, TeO_2, and TiO_2 (left), and the low index dielectric SiO2 with a high index dielectric MgO, Y_2O_3, ZnO, ZrO_2, TeO_2, and TiO_2 (right) for NPD thickness 30nm, 40nm, 50nm, and 60nm.

A summary of light extraction efficiency for configurations 1-6 and 7-12 for 3 DBR pairs is shown in Figure 50. In the case of 3 DBR pairs containing the low index dielectric, MgF2, the optimal extraction efficiency of 28.50% was achieved with a 40nm NPD thickness and high index dielectric, MgO, compared to the 3 DBR case containing the low index dielectric, SiO_2, with an optimal extraction efficiency of 28.4% with a 40nm NPD thickness and high index dielectric, MgO. In this particular case, increasing the index of refraction of the high index dielectric resulted in a reduction in the light extraction efficiency. This also is directly related to the reflectance energy of the out-coupling mirror. While increasing the reflectivity of the out-coupling mirror reflectance energy narrows the airy peak and confines the Airy peak more inside of the escape window, the increased round trips inside the cavity result in significant absorption losses and reduction in efficiency.

To determine the relationship between the out-coupling reflectivity and light extraction efficiency directly, a summary of the peak reflectance energy of select DBR structures and NPD thicknesses of 30nm, 40nm, 50nm, and 60nm versus light extraction efficiency were plotted in Figure 51. The optimum extraction efficiency is achieved with a ~40% out-coupling reflectance energy and a 40nm NPD thickness. Interestingly, the optimum out-coupling mirror reflectance energy based on a rigorous optical model agreed well with the optimum out-coupling reflectance energy based on the assumption in section 6.5.2 (rule 2) with an optimum reflectance energy of 38% ($R_1^{opt}=1-m_c/n^2$, $m_c=2$, $n\sim1.8$).

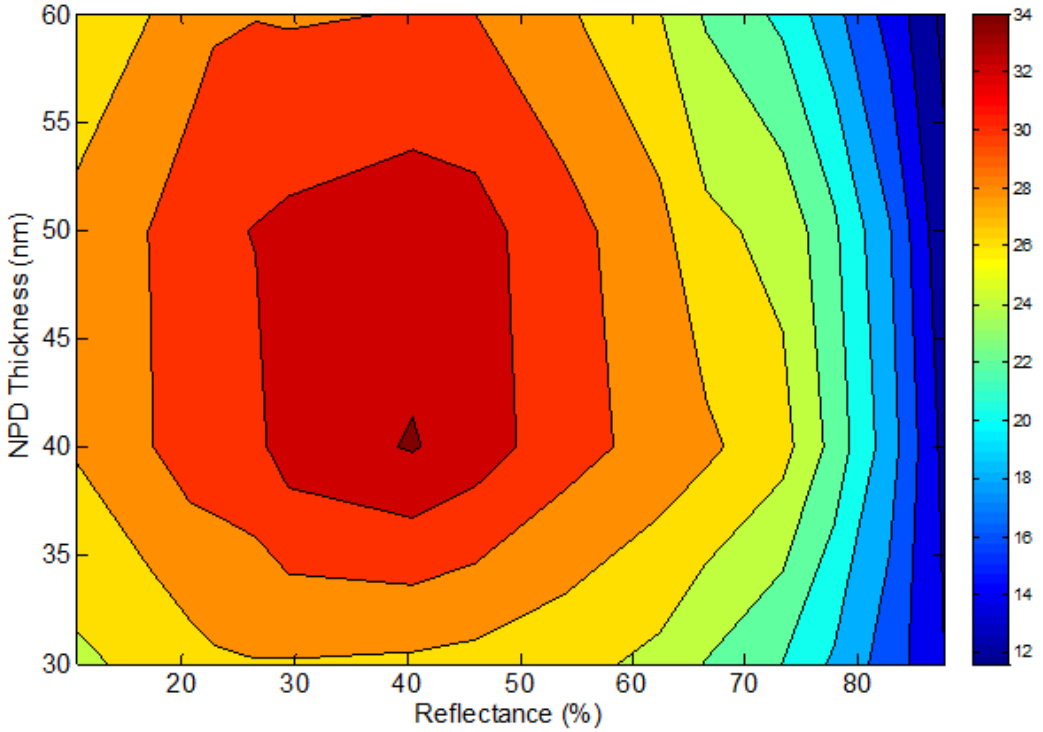

Figure 51. A summary of the light extraction efficiency or light out-coupling efficiency for select DBR configurations containing the low index low index dielectric MgF_2 with a high index dielectric MgO, Y_2O_3, ZnO, ZrO_2, TeO_2, and TiO_2 and the low index dielectric SiO2 with a high index dielectric MgO, Y_2O_3, ZnO, ZrO_2, TeO_2, and TiO_2 for NPD thickness 30nm, 40nm, 50nm, and 60nm.

6.8.3 Conclusion

A design of experiment was conducted implementing the narrow band emitter PtN1N into a second order MOLED architecture (m_c=2) consisting of a DBR out-coupling mirror and metal aluminum cathode. The out-coupling reflectivity was tuned using a series of dielectric materials including MgF_2, SiO_2, MgO, Y_2O_3, ZnO, ZrO_2, TeO_2, and TiO_2 with a quarter wave thickness ($\lambda/4n$) resulting in a large distribution in the out-coupling reflectance (10%-90%). The cavity length was tuned by adjusting the thickness of the hole transporting layer, NPD, in the structure of Glass/DBR(x)/ITO(60nm)/HATCN(10nm)/NPD(ynm)/TAPC(10nm)/8%:PtN1N

:26mCPy(25nm)/DPPS(10nm)/BmPyPB(45nm)/ LiF(1nm)/Al(100nm), where x is the DBR configuration and y is the NPD thickness (30nm, 40nm, 50nm, and 60nm). A single DBR pair with a peak reflectivity of ~41% (at 496nm) consisting of the low index dielectric, SiO_2, and high index dielectric, TiO_2, (configuration 12) in the structure of Glass/TiO_2(46nm)/ SiO_2(100nm)/ITO(60nm)/HATCN(10nm)/NPD(40nm) /TAPC(10nm)/8%PtN1N:26mCPy(25nm)/DPPS(10nm)/BmPyPB(45nm)/LiF (1nm)/Al(100nm) achieved the highest light out-coupling efficiency of 34.3% resulting in a ~1.38 improvement compared to the conventional structure of Glass/ ITO(50nm)/HATCN(10nm)/NPD(40nm)/TAPC(10nm)/8%PtN1N:26mCPy(25nm)/ DPPS(10nm)/BmPyPB(45nm)/LiF(1nm)/Al(100nm) with a light out-coupling efficiency of 24.9%. The design of experiment suggests that the highest enhancement in the out-coupling efficiency is achieved for out-coupling mirror reflectance energy of ~40% and a moderately detuned cavity which is in agreement with the design rules defined in section 2.5.

7 GREEN MICROCAVITY ORGANIC LIGHT EMITTING DIODES (MOLEDS) WITH A NARROW BAND EMISSION SOURCE

7.1 Introduction

The results obtained in the design of experiment in Chapter 6 will now be used as a guide in fabricating highly efficient microcavity OLEDs. The theoretical model developed in the foregoing chapter suggests that a moderate out-coupling reflectivity (~35-45%) is ideal for enhancing light out-coupling efficiency in MOLEDs. By implementing the high index material, TiO_2 (n~2.7), and low index material, SiO_2, (n~1.5) into the structure of Glass/TiO_2(46nm)/SiO_2(100nm)/ ITO(60nm)/HATCN(10nm)/NPD(40nm)/TAPC(10nm)/8%PtN1N:26mCPy(25nm)/DPPS(10nm)/BmPyPB(45nm)/LiF(1nm)/Al(100nm) an improvement in the light out-coupling efficiency of ~1.38 was predicted. Although the DBR configuration using the high index dielectric, TiO_2, in the device structure previously described demonstrated the highest improvement in light out-coupling efficiency in the design of experiment outlined in the foregoing section, ion-beam assisted TiO_2 films fabricated in the deposition system used in this study were shown to exhibit poor stability with changes in surface quality over time. Thus, the high index dielectric, TiO_2, was replaced with the high index dielectric, Ta_2O_5, for the MOLEDs fabricated in this study. Replacing TiO_2 with Ta_2O_5 showed only a small reduction in the predicted light out-coupling enhancement based on theoretical calculations. By implementing the tetradentate, cyclometalated, platinum complex, PtN1N, into the optimized MOLED structure based on theoretical calculations employing the finite difference time domain method in the structure of Glass/Ta_2O_5(57nm)/SiO_2(100nm)/ ITO(53nm)/HATCN(10nm)/NPD(45nm)/TAPC(10nm)/8%PtN1N:26mCPy(25nm)/

DPPS(10nm)/BmPyPB(45nm)/LiF(1nm)/Al(100nm) a high forward viewing measured EQE of 34.2% was achieved compared with the reference bottom emitting OLED structure on a planar glass substrate which exhibited a peak EQE of 25.4%. Thus, with the only an addition of a SiO_2 spacer layer and Ta_2O_5 high index layer onto the original device structure, an enhancement in EQE of 1.35 was achieved. This enhancement in the light out-coupling compared well with theoretical predictions based on FDTD.

7.2 Theoretical

The optical performance of MOLEDs implementing PtN1N and a low index dielectric, SiO_2, and high index dielectric, Ta_2O_5, will now be explored based on the finite difference time domain method outlined in Chapter 6.

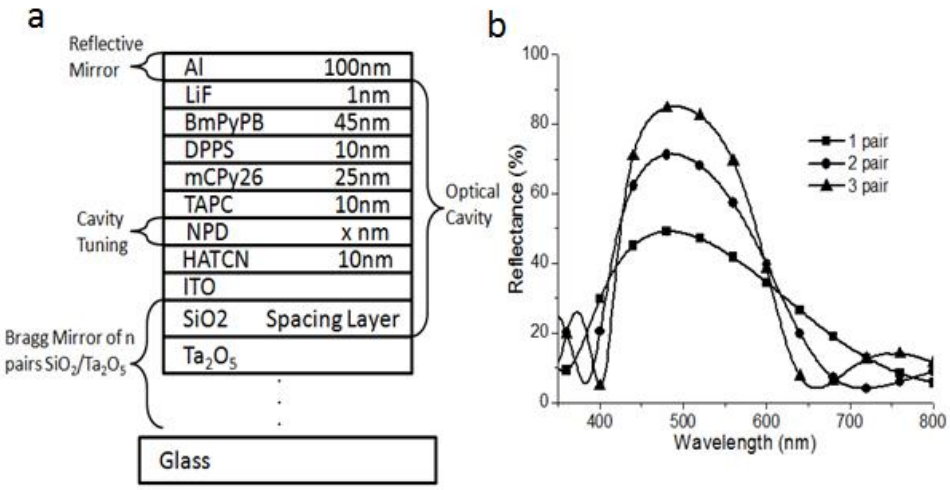

Figure 52. (a) Schematic diagram of the microcavity OLED. The optical cavity is defined between the reflective aluminum cathode mirror and the Bragg mirror, composed of alternating quarter-wavelength thick high index materials, Ta_2O_5, and low index materials, SiO_2. Cavity tuning was achieved by varying the NPD layer. The emitters in this study were co-deposited with the host, 26mCPy. (b) The measured reflectance spectra of glass/Ta_2O_5(57nm)/SiO_2(100nm)/ITO(53nm) (1 pair), glass/Ta_2O_5(57nm)/SiO_2(83nm)/ Ta_2O_5(57nm)/SiO_2(100nm)/ITO(53nm) (2 pair), and

glass/Ta_2O_5(57nm)/SiO_2(83nm)/ Ta_2O_5(57nm)/SiO_2(83nm)/Ta_2O_5(57nm)/SiO_2(100nm)/ ITO(53nm) (3 pair).

Figure 52 shows the schematic diagram of the microcavity OLED. The microcavity structure consists of a reflective aluminum cathode and a semi-reflective distributed Bragg reflector (DBR) or quarter wave stack (QWS) out-coupling mirror. The DBR consists of λ/4 optically thick repeat pairs of a high index of refraction material, Ta_2O_5 (n=2.2), and a low index of refraction material, SiO_2 (n=1.46). With a DBR design, reflectivity can be tuned by varying the number of DBR pairs..[128] Theoretical models conducted by Benisty et al. predict that a low out-coupling mirror reflectivity is ideal for enhancing the EQE of microcavity organic light emitting diodes since a large portion of the extractable Airy peaks can be squeezed reasonably well within the escape cone with little photon loss from the non-extractable Airy peaks.[53,144,145,145] In particular, for second order (m_c=2) MOLEDs wherein the optical cavity length (L) is equal to the peak wavelength (λ_s) of the source emission (L= m_c λ_s/2), it was predicted that an out-coupling mirror reflectivity on the order of 35-45% is ideal for light out-coupling enhancement. These values correlated well with the theoretical predictions in Chapter 6. In this study, we investigate a range out-coupling mirror reflectivities by varying the number of DBRs pairs in a second order MOLED design from one to three Ta_2O_5/SiO_2 pairs with a reflectivity centered on the peak intrinsic emission wavelength of PtN1N. The optical cavity length was altered by varying the thickness of the hole transporting layer, NPD, in the device structure of glass/DBR(z pairs)/ITO/HATCN(10nm)/NPD(xnm)/ TAPC(10nm)/ 8%PtN1N:26mCPy (25nm)/DPPS(10nm)/BmPyPB(45nm)/LiF(1nm)/Al (100nm), where x is the thickness of the NPD layer in nm, and z is the number of DBR pairs (0, 1, 2, or 3). A 100nm SiO_2 spacing layer was inserted between the ITO anode and

Ta_2O_5 to extend the optical cavity closer to the intrinsic emission wavelengths without significantly increasing the organic layer thickness to affect OLED performance. By implementing a spacing layer into the DBR design, coarse adjustments in the cavity length of the MOLED can be achieved without changing the electrical properties of the device. The NPD layer thickness range between 30nm to 60nm was chosen as to vary the optical cavity length from the lower band edge of the intrinsic spectral distribution of PtN1N (~490nm) to the upper band edge (~550nm).

A summary of the predicted peak external quantum efficiency versus NPD thickness for the reference structure (0 pair), 1 DBR pair, 2 DBR pairs, and 3 DBR pairs are shown in Figure 53. The single DBR pair had the highest calculated external quantum efficiency with a peak EQE of 32.1% for a 40nm NPD thickness. The peak EQE for a given NPD thickness decreases with increasing number of DBR pairs. In particular, for a 40nm NPD layer, the peak EQE is 32.1%, 31.2%, and 25.4% for 1 DBR pair, 2 DBR pairs, and 3 DBR pairs, respectively, compared to 24.9% for the reference structure (0 DBR pairs). Additionally, for a given DBR configuration, a maximum in EQE with respect to NPD thickness was observed. The source of these maxima will be described in more detail in a later section.

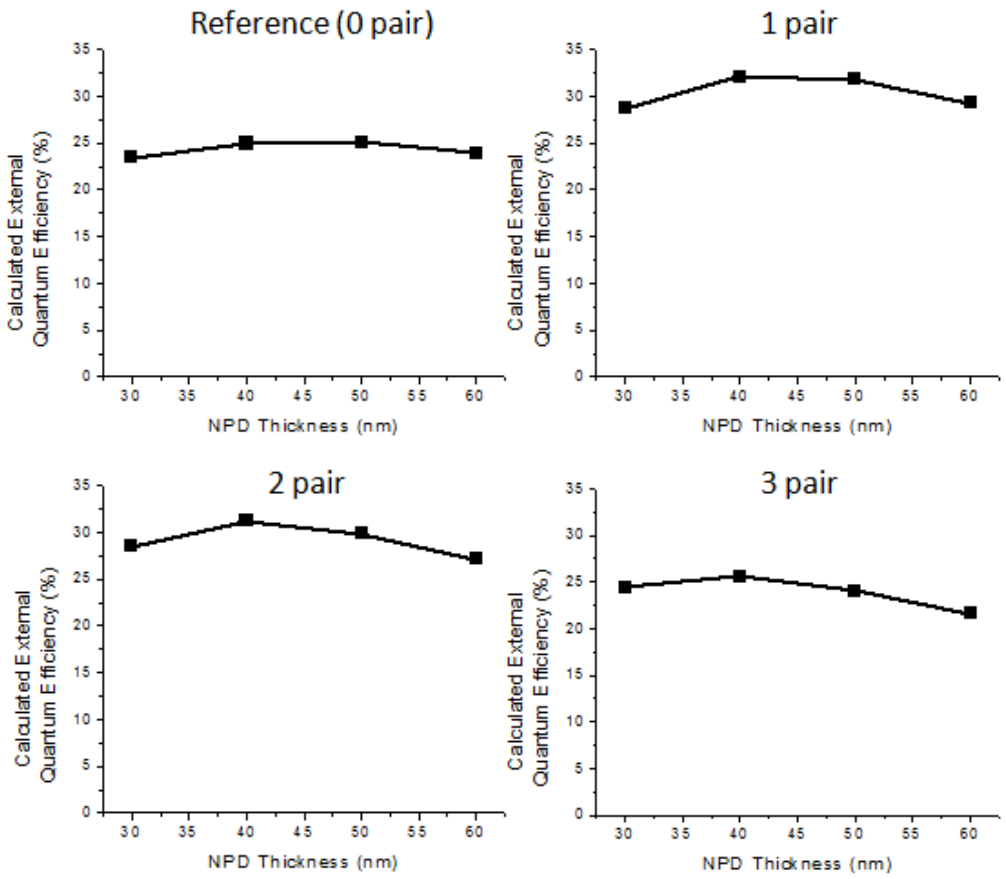

Figure 53. The calculated peak external quantum efficiency for the reference structure with 0 DBR pairs (top left), 1 DBR pair (top right), 2 DBR pairs (lower left), and 3 DBR pairs (lower right) based on the structure shown in Figure 52.

A summary of the calculated normalized electroluminescent spectra for 0 DBR pairs, 1 DBR pair, 2 DBR pairs, and 3 DBR pairs are shown in Figure 54. The high-finesse structure with 3 DBR pairs has a peak emission intensity of 504nm, 519nm, 533nm, and 544nm for 30nm, 40nm, 50nm, and 60nm, respectively. The red shifting in the electroluminescent spectra with increasing NPD thickness is a result of extending the cavity length with increasing NPD thickness. The resonant peaks, evident in regions of enhanced intensity relative to the non-cavity spectrum, at 504nm, 519nm, 533nm, and 544nm are directly proportional to the cavity length according to Equation 43 in Chapter 6 for normal incidence ($\theta=0°$). Spectral

narrowing is also observed with increasing DBR pairs which may be advantageous in some applications desiring high color purity with a specific emission wavelength. In particular, the spectra exhibit a FWHM of 23nm, 18nm, and 16nm for a MOLED with 1 DBR pair, 2 DBR pairs, and 3 DBR pairs, respectively, compared to the reference structure with FWHM of 22nm.

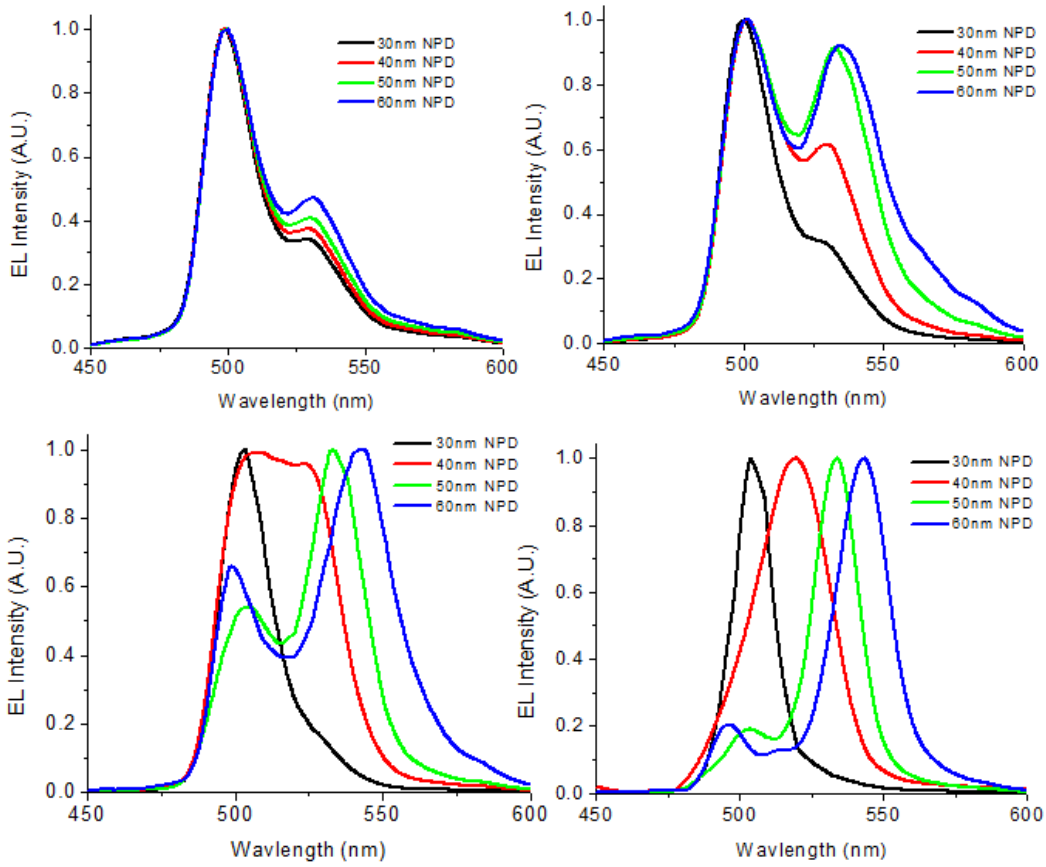

Figure 54. The calculated normalized electroluminescent spectra in the forward direction (0°) for the reference structure with 0 DBR pairs (top left), 1 DBR pair (top right), 2 DBR pairs (lower left), and 3 DBR pairs (lower right) based on the structure shown in Figure 52.

The angular intensity profile is an important metric in display and important to consider in the design of highly efficient microcavity OLEDs. A summary of the angular intensity profile for a 496nm wavelength (peak intrinsic emission

wavelength) is shown in Figure 55. The reference structure has a lambertian emission pattern, typical of conventional OLED structures, with a slight deviation in lambertian emission with increasing NPD thickness due to weak microcavity effects. The single DBR has a directional dependent angular intensity with a maxima in intensity at off-axis angles ($\theta>0$). In particular, the single DBR has a maximum intensity at 21°, 32°, 41°, and 54° for 30nm, 40nm, 50nm, and 60nm NPD thickness, respectively. This shift in the directionality with increasing cavity length is supported in Equation 43, which suggests that the cosine of the angle of incidence is inversely proportional to the cavity length.

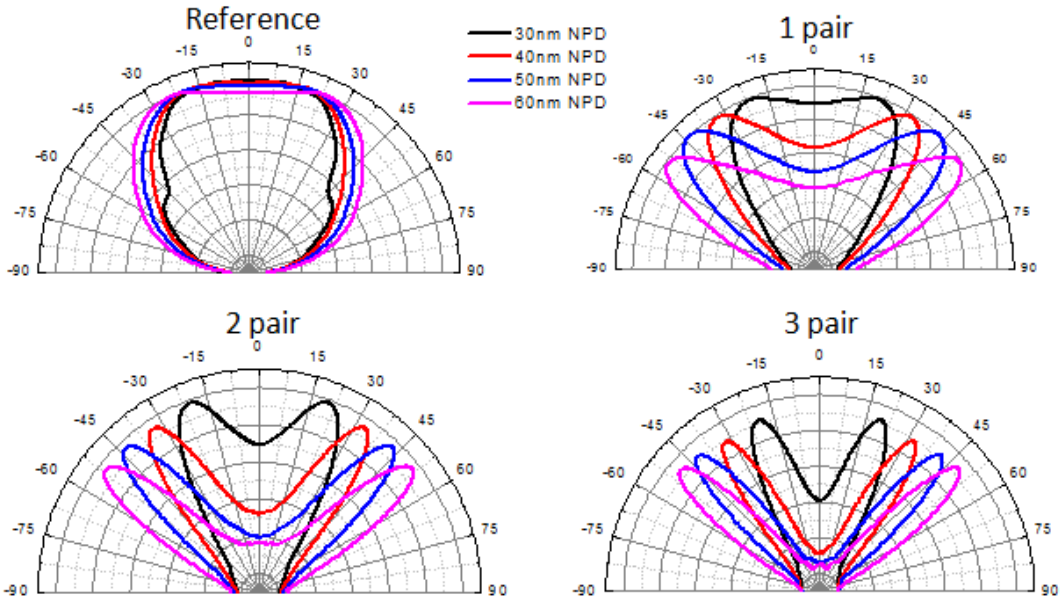

Figure 55. The calculated angular intensity profile for a wavelength of 496nm for the reference structure with 0 DBR pairs (top left), 1 DBR pair (top right), 2 DBR pairs (lower left), and 3 DBR pairs (lower right) based on the stru cture shown in Figure 52.

It is evident in Figure 55 that a 30nm NPD thickness is not tuned to the peak emission wavelength of 496nm as the intensity is not maximized in the forward direction, characteristic of a tuned MOLED. Thus, a 25nm NPD thickness was also calculated using the method outlined in Chapter 6 for the single DBR case. Additionally, the curve in Figure 55 suggests that the optimized detuned structure has a NPD thickness of 45nm. A summary of the tuned structure with a 25nm NPD thickness as well as the optimized detuned structure with a 45nm NPD thickness is shown in Figure 56.

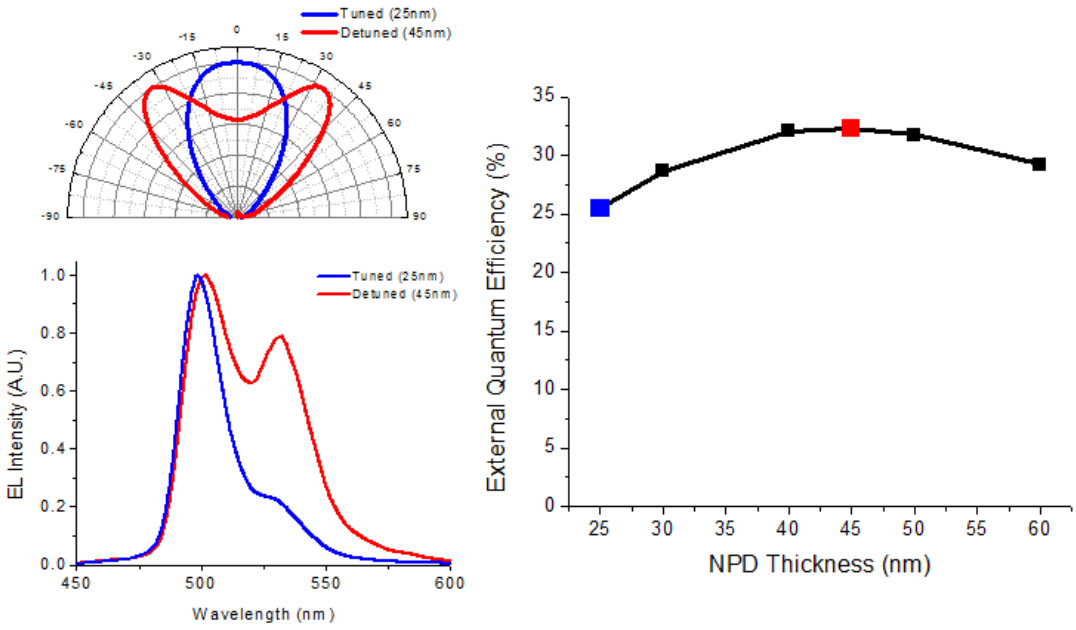

Figure 56. The calculated external quantum efficiency and EL characteristics for the tuned and detuned MOLED with a single DBR pair implementing 25nm and 45nm NPD layer thickness, respectively, based on the device structure shown in Figure 52.

A series of MOLEDs were fabricated based on the structures investigated in this section and will now be described.

7.3 Experimental

7.3.1 Materials

The hole injection material, 1,4,5,8,9,11-hexaazatriphenylene-hexacarbonitrile (HATCN), was purchased from Lumtec Corp., the hole transporting layer, N,N'-diphyenyl-N,N'-bis(1-naphthyl)-1,1'-biphenyl-4,4"-diamine (NPD), was purchased from Chemical Alta, and the materials di-[4-(N,N-di-toylyl-amino)-phyenyl]cyclohexane (TAPC),[71, 72] 2,6-bis(N-carbazolyl)pyridine (26mCPy),[79] diphenyl-bis[4-(pyridine-3-yl)phenyl]silane (DPPS),[41] 1,3-bis(3,5-dipyrid-3-yl-phenyl)benzene (BmPyPB),[177] platinum(II)-2'-(H-pyrazol-1-yl)-9-(pyridine-2-yl)-9H-2,9'-bicarbazole (PtN1N), and platinum(II)-2-(3-(3-(pyridine-2-yl)phenoxy)phenoxy)pyridine (PtOO3)[100] were prepared following previous literature reports.

7.3.2 Device Fabrication

Thin films implementing the high-index of refraction material, Ta_2O_5, and the low-index of refraction material, SiO_2, were deposited alternatively on glass substrates in a single chamber using an ion-beam sputtering technique. The last Ta_2O_5 layer was capped with a 100nm SiO_2 spacer layer.[54, 178] The DBR stack was then capped with an ITO layer deposited by ion assisted e-beam evaporation. The structures and naming convention that will be used in the remainder of the paper are as follows: glass/Ta_2O_5(57nm)/SiO_2(100nm)/ITO(53nm) (1 pair), glass/Ta_2O_5(57nm)/SiO_2(83nm)/Ta_2O_5(57nm)/SiO_2(100nm)/ITO(53nm) (2 pair), glass/Ta_2O_5(57nm)/ SiO_2(83nm)/Ta_2O_5(57nm)/SiO_2(83nm)/Ta_2O_5(57nm)/SiO_2(100nm)/ ITO (53nm) (3 pair) and the reference structure of ITO on glass will be referred to as

0 pair. All substrates described were patterned using photolithography. Prior to organic depositions, the substrates were cleaned by sonication in water, acetone, and isopropanol. Organic materials were thermally evaporated at deposition rates of 0.5 to 1.5 Å/s at a working pressure of less than 10^{-7} Torr. The deposition rates and thicknesses were monitored by quartz crystal microbalances. A thin 1 nm LiF layer was deposited at rates of <0.2 Å/s and aluminum cathodes were deposited at a rate of 1 Å/s through a shadow mask without breaking vacuum. Individual devices had areas of 0.04 cm^2.

7.3.3 Materials and Device Characterization

Steady state emission experiments of the sample at room temperature as well as electroluminescent spectra of the devices were performed on a Jobin Yvon Fluorolog spectrofluorometer. I-V characteristics were taken with a Keithley 2400 source-meter and the photocurrent was measured using an OSI optoelectronics 220DP Si photodiode with a large active area of 200mm^2 to effectively collect the emitted light from the device. All I-V-L measurements were done in a nitrogen-filled glove-box. Angular electroluminescent spectra (EL) were measured using a rotating stage measured in ten degree increments, driven at a low constant current (0.01 mA/cm^2 to 0.001 mA/cm^2) and measured with a constant slit width. Prior to EL spectra measurements, all devices were encapsulated in a nitrogen-filled glove-box and measured in air.

7.4 Results and Discussion

The photoluminescent spectrum and molecular structure of PtN1N are shown in Figure 57. The photoluminescent spectrum exhibits a narrow spectral bandwidth with a FWHM of 18nm.

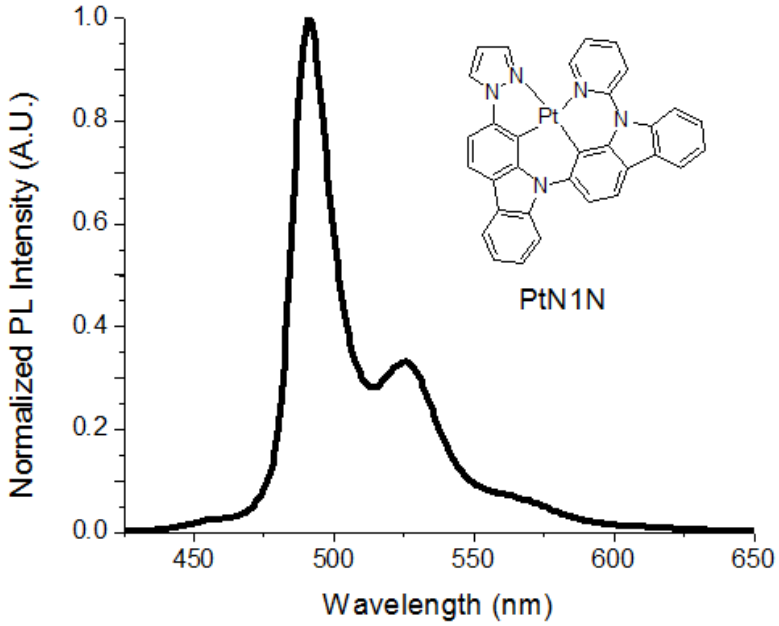

Figure 57. Room temperature photoluminescent emission spectrum of PtN1N. For room temperature measurements the solute, PtN1N, was dissolved in CH_2Cl_2. The molecular structure of PtN1N is shown in the inset.

The DOE in Chapter 6 assumed that the thickness of the NPD layer was independent on the device performance. The limits of this assumption will now be explored. We have chosen to tune the optical cavity length by varying the thickness of the hole transporting layer, NPD, due to its high hole mobility. Ideally, the electrical properties of the device should remain constant to simplify the analysis and directly correlate the light out-coupling efficiency to changes in the optical cavity length. Thus, the effect of NPD layer thickness on the device performance in the reference OLED structure of glass/ITO(50nm)/HATCN(10nm)/NPD(x

nm)/TAPC(10nm)/8%PtN1N: 26mCPy (25nm)/DPPS(10nm)/BmPyPB(45nm)/LiF (1nm)/Al(100nm) was explored. The structure chosen was based on a device structure previously reported to exhibit highly efficient OLEDs utilizing PtN1N. Figure 58 shows the J-V curves, the EL spectra in the forward direction, the external quantum efficiency versus current density, and the peak external quantum efficiencies vs NPD thickness in the range of 25-60nm. By implementing the effective hole blocker, DPPS, and electron blocker, TAPC, to confine excitons in the emissive layer, combined with the high hole mobility of NPD, good charge balance and a confined recombination zone are maintained. Consequently, similar J-V characteristics are achieved with a large range of NPD thicknesses (25nm-60nm).

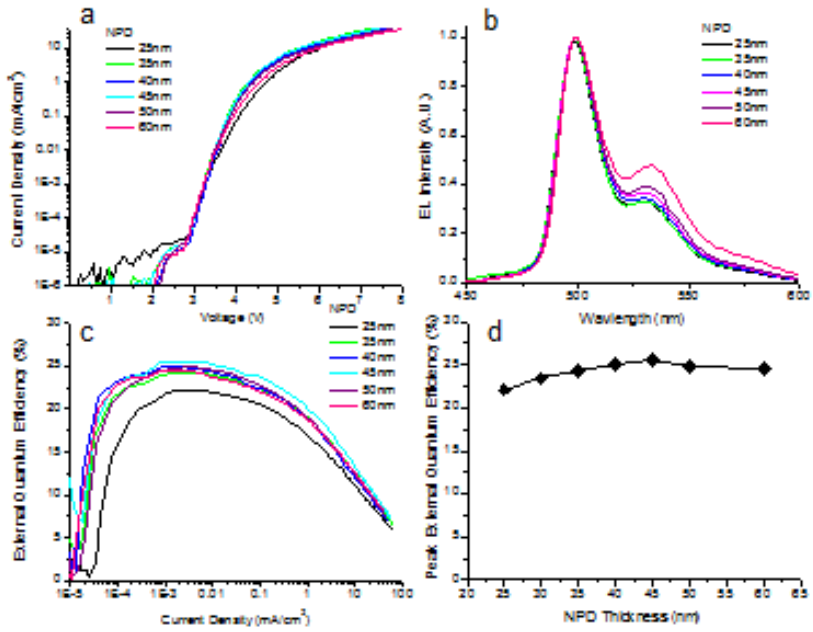

Figure 58. (a) The J-V curves, (b) the normalized electroluminescent spectra at a viewing angle of 0°, (c) the external quantum efficiency-versus current density, (d) and the peak EQE-versus NPD thickness for PtN1N in the reference OLED structure of glass/ITO(53nm)/HATCN(10nm)/NPD(x-nm)/TAPC(10nm)/ 8%PtN1N

:26mCPy(25nm)/DPPS(10nm)/BmPyPB(45nm)/LiF(1nm)/Al(100nm), where x=25nm, 30nm, 35nm, 40nm, 45nm, 50nm, 60nm.

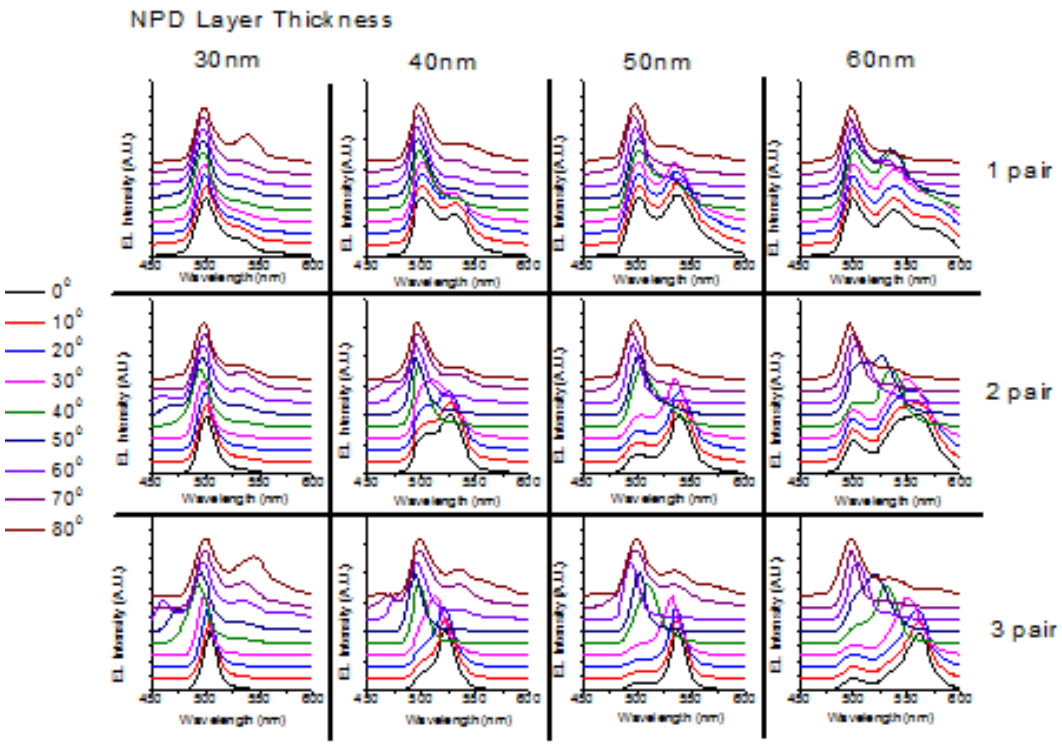

Figure 59. The normalized electroluminescent spectrum measured at different viewing angles between 0-80° in the device structure of glass/DBR(z pairs)/ITO(53nm)/HATCN(10nm)/NPD(x nm)/TAPC(10nm)/8%PtN1N:26mCPy(25nm)/DPPS(10nm)/BmPyPB(45nm)/ LiF(1nm)/Al(100nm).

A series of MOLEDs were fabricated in the structure of glass/DBR(z pairs)/ITO(53nm)/ HATCN(10nm)/NPD(x nm)/TAPC(10nm)/8%PtN1N:26mCPy (25nm)/DPPS(10nm)/ BmPyPB(45nm)/LiF(1nm)/Al(100nm), where x is the NPD thickness and z is the number of DBR pairs (0, 1, 2, or 3). Figure 59 shows the normalized electroluminescent spectra at viewing angles between 0-80° for MOLEDs with a 30nm, 40nm, 50nm, and 60nm NPD layer. For the MOLEDs in this study with a cavity order of 2 (m_c=2), the optical cavity length is directly proportional to the wavelength of resonance at normal incidence (0°).[46] The wavelength of resonance,

evident in regions of enhanced intensity in the electroluminescent spectrum relative to intrinsic emission of the source, is most pronounced for MOLEDs implementing 3 DBR pairs due to the high out-coupling mirror reflectivity.[65] MOLEDs consisting of 3 DBR pairs and a 30nm NPD layer resulted in an approximately tuned microcavity structure, wherein the optical cavity is equal to the peak emission wavelength, with a resonance peak of 504nm at normal incidence. For the approximately tuned structure, significant spectral narrowing in the EL spectra with increasing number of DBR pairs was observed with a FWHM of 24nm, 17nm, and 15nm for a single DBR pair, 2 DBR pairs, and 3 DBR pairs MOLED, respectively, at normal incidence (0°). The approximately tuned structure also exhibited a small color shift at varying viewing angles. By comparison, by increasing the NPD layer thickness a red-shift in the resonance peak was observed with a resonance peak of 522nm, 538nm, and 562nm for a 40nm, 50nm, and 60nm NPD layer, respectively, accompanied by large shifts in color at different viewing angles ($0\text{-}80^{o}$).

The external quantum efficiency versus current density for MOLEDs implementing a 40nm NPD layer thickness is shown in Figure 5(a). The series of devices were fabricated during the same deposition run to minimize variation in deposition thickness of the organic layers to minimize variation in cavity length between each case. A peak EQE of 33.6%, 32.8%, and 27.8% occur for MOLEDs with a single DBR pair, 2 DBR pairs, and 3 DBR pairs, respectively, compared to a peak EQE of 25% for the reference OLED without a DBR. The reduction in EQE with increasing number of DBR pairs or out-coupling mirror reflectivity is likely a result of increased photon absorption at the metallic cathode caused by additional round-trips inside of the optical cavity.[63]

A full summary of the peak EQE versus NPD thickness for the MOLEDs in this study is shown in Figure 60(a). MOLEDs implementing a 25nm NPD layer with a single DBR pair exhibited a peak EQE of 26.3%. Increasing the NPD layer thickness to 30nm resulted in an improvement in the peak EQE of 30.2%. Increasing the NPD layer thickness further to 45nm resulted in further improvement in EQE of 34.2%. Increasing the NPD thickness beyond 45nm to 50nm and 60nm resulted in a drop in EQE of 32.2% and 27.8%, respectively. The maximum in peak EQE with respect to NPD thickness is a result of positioning the resonant modes of the optical cavity such that the majority of emission of the source could out-couple from the cavity resonant modes.[44] This is supported in Figure 59, which identifies the degree of overlap of resonant modes of the optical cavity with the intrinsic spectral distribution of the source. For example, the resonant peaks for the MOLEDs consisting of 3 DBR pairs implementing a 50nm NPD layer occur at 538nm, 536nm, 510nm, and 494nm for 0°, 20°, 40°, and 60°, respectively, which are located well within the spectral distribution of the source and consequently a high EQE is achieved. On the other hand, for the MOLEDs consisting of 3 DBR pairs implementing a 30nm NPD layer exhibit resonant peaks at 504nm, 502nm, 494nm, and 460nm for 0°, 20°, 40°, 60°, respectively, which are located at the band edge of the intrinsic spectral distribution. Similarly, for a 60nm NPD thickness, resonant peaks at 562nm, 560nm, 532nm, and 504nm for 0°, 20°, 40°, 60°, respectively, are located at the band edge of the source and contribute weakly to the overall power output coupled from the cavity.

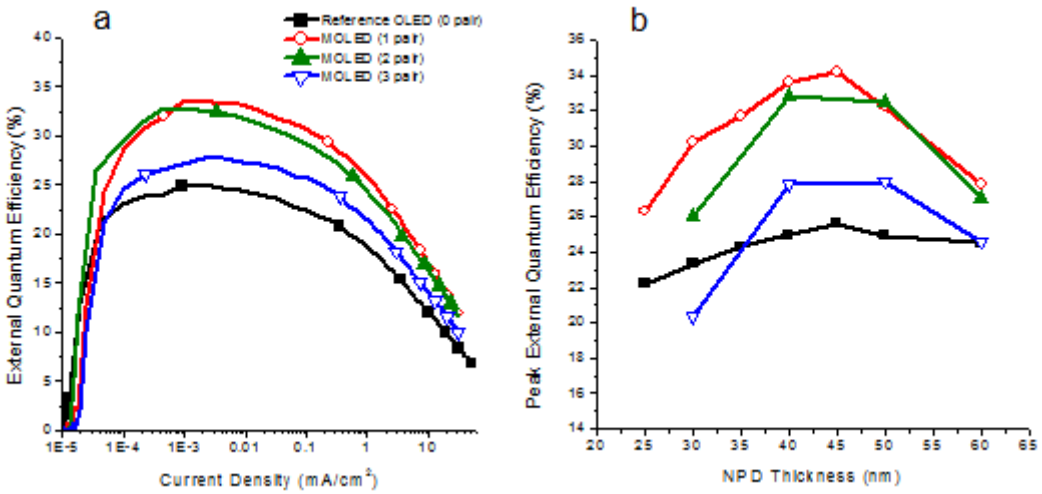

Figure 60. (a) The external quantum efficiency versus current density (mA/cm^2) for the structure of glass/DBR(z pair)/ITO(53nm)/HATCN(10nm)/NPD(40nm)/TAPC(10nm) /8%PtN1N:26mCPy(25nm)/DPPS(10nm)/BmPyPB(45nm)/LiF(1nm)/Al(100nm). (b) Peak External Quantum Efficiency versus NPD thickness for the reference OLED structure or 0 pair (black squares), 1 pair (red circles), 2 pair (green triangles), and 3 pair (blue triangles) in the general device structure of glass/DBR(z pairs)/ITO/HATCN(10nm)/NPD(x nm)/TAPC(10nm)/8%PtN1N:26mCPy(25nm) /DPPS(10nm)/BmPyPB(45nm)/ LiF(1nm)/Al(100nm)

To explore the differences associated with a tuned and detuned MOLED structure, the device characteristics of the optimized detuned MOLED and the tuned MOLED for the low-finesse single pair structure with a 45nm and 25nm NPD thickness, respectively, were compared (Figure 61) including the electroluminescent spectra, the angular intensity profile, and the external quantum efficiency versus current density.

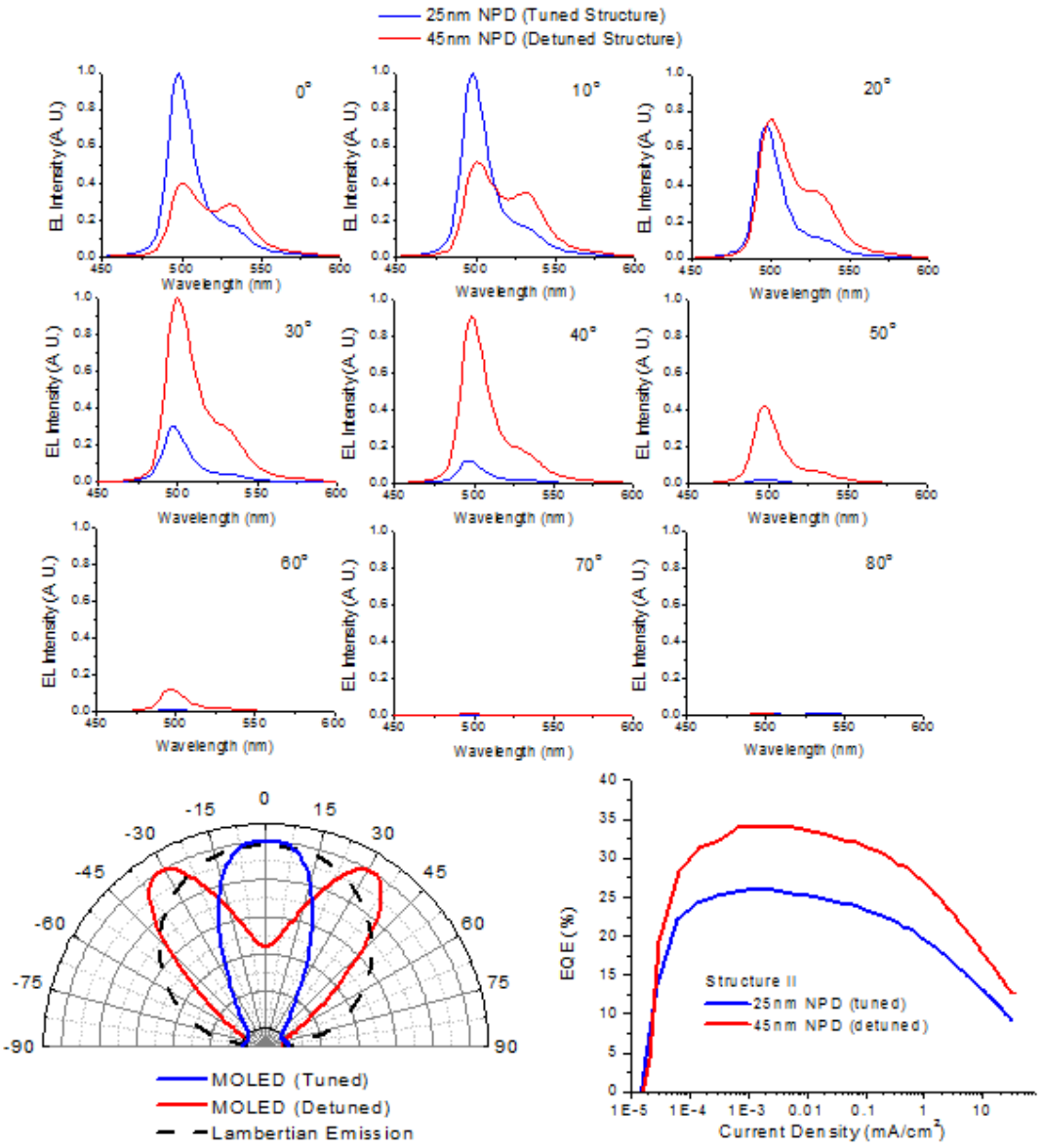

Figure 61. The electroluminescent spectrum (top) normalized to the max intensity within the angular series of measurements for 0°, 10°, 20°, 30°, 40°, 50°, 60°, 70°, and 80° viewing angles in the device structure of glass/Ta_2O_5(57nm)/SiO_2(100nm)/ITO(53nm)/HATCN(10nm)/NPD(25nm(blue),45nm(red))/TAPC(10nm)/8%PtN1N:26mCPy(25nm)/DPPS(10nm)/BmPyPB(45nm)/LiF(1nm)/Al(100nm). The angular emission profile (lower left) for the tuned structure with a 25nm NPD thickness (blue) and the detuned structure with a 45nm NPD thickness (red). Lambertian emission is shown as a reference (black dotted line). The external quantum efficiency-versus current density (lower right) for the tuned structure (blue) and detuned structure (red).

The electroluminescent spectra is shown in the top portion of Figure 61 for detection angles of 0°, 10°, 20°, 30°, 40°, 50°, 60°, 70°, and 80°. To compare the change in absolute intensity with angle for the tuned and detuned structure, the angular dependent series of spectra were normalized to its maximum intensity in the series of measurements. The moderately detuned cavity with a 45nm NPD thickness had an optimum intensity at an off-axis angle of 30°, compared to the tuned cavity which had an optimum intensity at the surface normal, 0°, for wavelengths near 498nm, the non-cavity emission peak. Thus, the angular intensity profile shown in the lower left portion of Figure 61 shows that the tuned cavity has preferential output in the forward direction and the detuned structure has preferential output at an off-axis angle, characteristic of detuned cavities.[53] Additionally, the spectral shape remains approximately uniform with increasing angle for the low-finesse tuned MOLED, whereas the detuned structure exhibits a strong angular dependent spectral shape as a result of strong long wavelength resonant contributions to the out-coupling of the cavity for small detection angles. The external quantum efficiency vs. current density (mA/cm^2) is shown in the lower right portion of Figure 61. The tuned structure with a 25nm NPD thickness exhibits a peak EQE of 26.3% compared to a peak EQE of 22.1% in the conventional OLED structure resulting in a 1.19 enhancement in EQE. The detuned structure with a 45nm NPD thickness exhibits a peak EQE of 34.2% compared to a peak EQE of 25.4% in the conventional OLED, resulting in a 1.35 enhancement in EQE. Thus, by extending the cavity beyond the tuned cavity length, higher light out-coupling improvement is achieved, however, significant changes to both the angular intensity profile and spectral shape result. Depending on the application, significant changes in spectral shape and intensity with angle may not be desirable and a balance

between out-coupling enhancement and spectral uniformity with angle is needed. Such a balance was achieved utilizing a single DBR pair MOLED with a 30nm NPD thickness which exhibited a high peak EQE of 30.2% compared to its conventional OLED with a peak EQE of 22.9% resulting in a light out-coupling enhancement of 1.3 and an angular intensity profile that preferentially emits in the forward direction with little change in the spectral shape. Such a preferential emission in the forward direction may prove useful for MOLEDs designed in conjunction with a microlens array or for a MOLED with a down converting phosphor for highly efficient white OLEDs.[126]

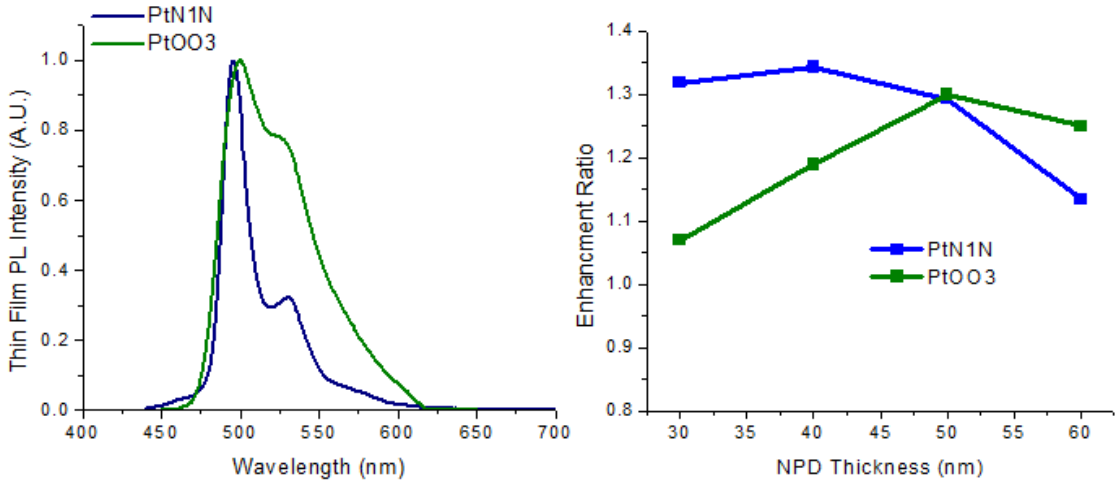

Figure 62. The thin film photoluminescent spectrum (left) of PtN1N (blue) and PtOO3 (green) in a thin film of 8%emitter:26mCPy. The enhancement ratio or fraction of EQE in the MOLED structure to EQE in the conventional OLED structure for PtOO3 and PtN1N in the structure of glass/Ta_2O_5(57nm)/ SiO_2(100nm)/ITO(53nm)/HATCN(10nm)/NPD(30nm,40nm,50nm,60nm)/TAPC(10nm)/8%PtN1N:26mCPy (25nm)/DPPS(10nm)/BmPyPB(45nm)/LiF(1nm)/Al(100nm).

It has been suggested that a narrow band emission source is ideal for EQE enhancement in a MOLED since a larger fraction of the emission profile has emission accelerated by the cavity.[35] However, to our knowledge there have been no

MOLED reports that have data to support this directly. In this study, the MOLED performance of the emitter, PtN1N (FWHM=18nm), with the emitter, PtOO3 (FWHM=72nm) were explored to compare the effects of the source spectral emission band on microcavity performance. Figure 62 (left) shows the thin film PL spectra for PtOO3 and PtN1N in thin films of 8%emitter:26mCPy. The intrinsic emission peak of PtN1N (496nm) is similar to the instrinsic emission peak of PtOO3 (500nm) and consequently were compared in identical MOLED structures. A series of devices implementing the emitter, PtOO3, were fabricated in the conventional OLED structure of glass/ITO(50nm)/HATCN(10nm)/NPD(xnm)/TAPC(10nm)/8%PtN1N :26mCPy(25nm)/DPPS(10nm)/BmPyPB(45nm)/LiF(1nm)/Al(100nm) and the low-finesse single DBR pair MOLED structure of glass/Ta2O5(57nm)/SiO2 (100nm)/ITO(53nm)/HATCN(10nm)/NPD(xnm)/TAPC(10nm)/8%PtN1N:26mCPy(25 nm)/DPPS(10nm)/BmPyPB(45nm)/LiF(1nm) /Al(100nm) with a NPD thickness (x) of 30nm, 40nm, 50nmm, and 60nm. Figure 62 (right) shows the enhancement in EQE for 30nm, 40nm, 50nm, and 60nm NPD thicknesses of MOLEDs implementing PtN1N and PtOO3. A summary of device data for all devices fabricated in this study is shown in Table 9. MOLEDs implementing the emitter PtOO3, have an EQE enhancement of 1.07, 1.18, 1.31, and 1.26 for 30nm, 40nm, 50nm, and 60nm NPD thicknesses, respectively, compared to PtN1N with an EQE enhancement of 1.32, 1.35, 1.29, and 1.13 for 30nm, 40nm, 50nm, and 60nm NPD thicknesses, respectively. Thus, MOLEDs implementing the emitter PtOO3, required more detuning to achieve optimum EQE enhancement and resulted in a lower overall EQE enhancement relative to MOLEDs implementing PtN1N. Additionally, PtN1N based MOLEDs implementing 30nm NPD had EQE enhancements as high as 1.3 with little change to the angular dependent EL spectral shape, whereas, PtOO3

based MOLEDs with a 30nm NPD thickness showed no improvement in EQE and experienced more significant change to the angular dependent EL spectral shape. Thus, a MOLED implementing a narrow spectral emission band has the potential of achieving significant enhancement with little detuning and consequently little change to the angular dependent spectral shape which can be advantageous for display applications.

The normalized EL spectra for PtOO3 and PtN1N in the structure of glass/Ta2O5(57nm)/SiO2(100nm)/ITO(53nm)/HATCN(10nm)/NPD(xnm)/TAPC(10nm)/8%Emitter:26mCPy(25nm)/DPPS(10nm)/BmPyPB(45nm)/LiF(1nm)/Al(100nm), where x is equal to 30nm, 40nm, 50nm, and 60nm, is shown in Figure 63. For a 30nm NPD thickness, smaller changes in the electroluminescent characteristics are observed with increasing angle of incidence compared to 40nm, 50nm, and 60nm NPD thicknesses. In particular, for MOLEDs implementing PtN1N and a 30nm NPD layer, the normal incident color coordinates were CIE(x=0.14,y=0.59) compared to a 60^{o} viewing angle for which the color coordinates were CIE(x=0.1,y=0.60). By comparison, for MOLEDs implementing PtN1N and a 50nm NPD layer, the normal incident color coordinates were CIE(x=0.21,y=0.67) compared to a 60^{o} viewing angle for which the color coordinates were CIE(x=0.09,y=0.53). Thus, larger changes in the color coordinates with increasing detection angle are observed with a larger NPD thickness. A full summary of the CIE coordinates at different viewing angles for a given NPD thickness of 30nm, 40nm, 50nm, and 60nm in the structures outlined in Figure 63 and is summarized in Figure 64. Figure 64 suggests that a 30nm NPD thickness has the smallest spread in CIE coordinates compared to 40nm, 50nm, and 60nm NPD thicknesses for MOLEDs implementing PtN1N and PtOO3.

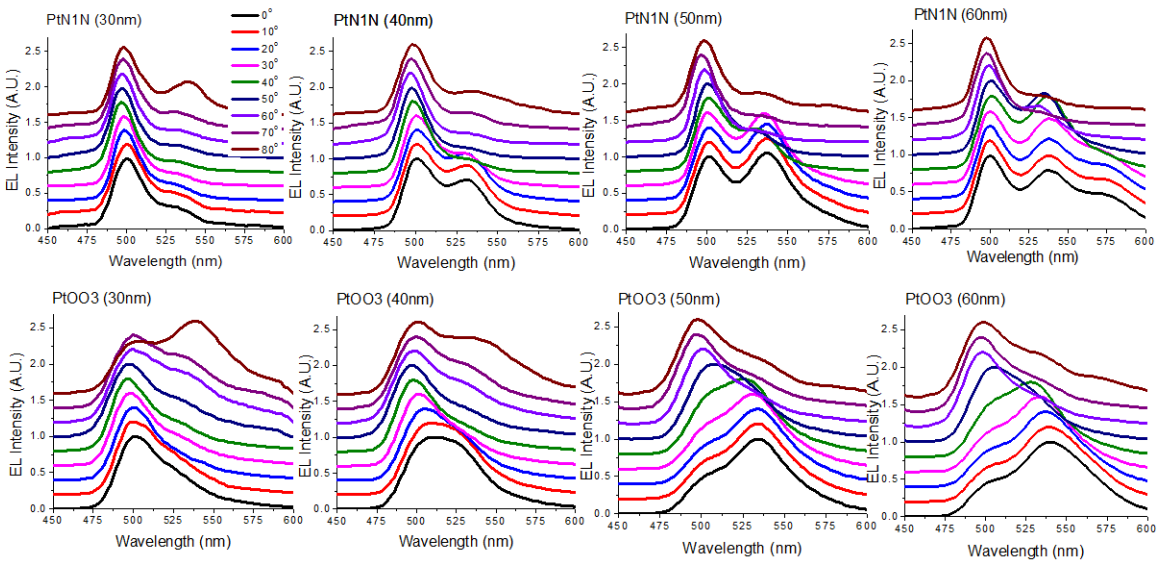

Figure 63. The normalized EL spectra for PtN1N (top) and PtOO3 (bottom) in the structure of glass/Ta2O5(57nm)/SiO2(100nm)/ITO(53nm)/HATCN(10nm)/NPD (xnm)/TAPC(10nm)/8%Emitter:26mCPy(25nm)/DPPS(10nm)/BmPyPB(45nm)/LiF (1nm)/Al(100nm), where x is the NPD thickness from left to right of 30nm, 40nm, 50nm, and 60nm.

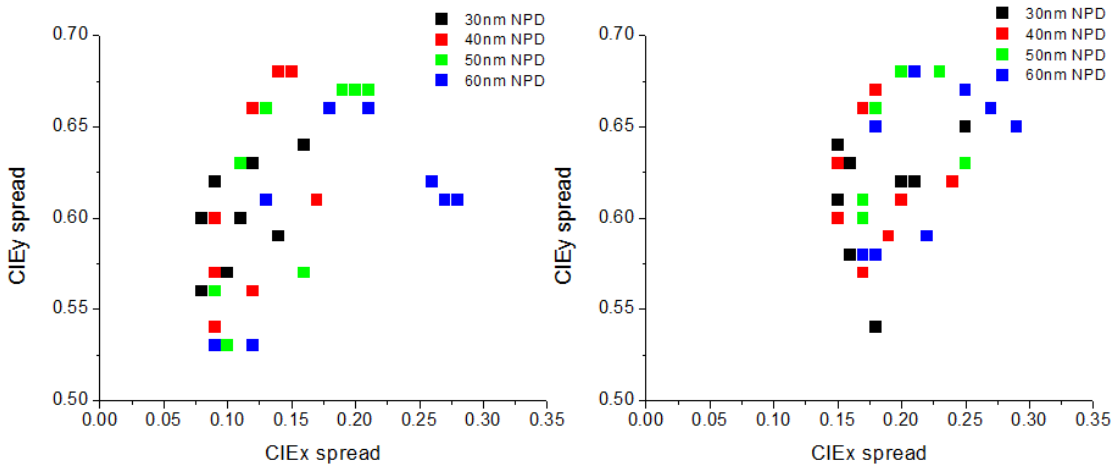

Figure 64. The CIE color coordinate spread of PtN1N (left) and PtOO3 (right) in the structure of glass/Ta2O5(57nm)/SiO2(100nm)/ITO(53nm)/HATCN(10nm)/NPD (30,40,50,60nm)/TAPC(10nm)/8%Emitter:26mCPy(25nm)/DPPS(10nm)/BmPyPB(45 nm)/LiF (1nm)/Al(100nm) at different viewing angles (0°, 10°, 20°, 30°, 40°, 50°, 60°, 70°, and 80°).

Table 9. A summary of device characteristics of PtN1N and PtOO3 in the devices fabricated from substrates with 0 DBR pair (I), 1 DBR pair (II), 2 DBR pair (III), 3 DBR pair (IV) and implementing various NPD thicknesses in the structure of glass/DBR(z-pairs)/ITO(53nm)/ HATCN(10nm)/NPD(xnm)/TAPC(10nm)/8%Emitter :26mCPy(25nm)/DPPS(10nm)/ BmPyPB(45nm)/LiF(1nm)/Al(100nm), where x is the NPD thickness and z is number of pairs (0, 1, 2, or 3). Device data in parenthesis represents the performance in the reference OLED structure without a DBR (0 pair).

			EQE (%)			
Structure	Emitter	NPD Thickness (nm)	Peak	100 cd/m^2	1000 cd/m^2	Enhancement
I	PtN1N	25	22.1	20.1	15.9	NA
I	PtN1N	30	22.9	19.7	14.8	NA
I	PtN1N	40	25	21.9	16.8	NA
I	PtN1N	45	25.4	23.3	18.2	NA
I	PtN1N	50	24.9	22.2	16.9	NA
I	PtN1N	60	24.5	21.6	16.9	NA
II	PtN1N	25	26.3	22.9	17.6	1.19
II	PtN1N	30	30.2	28	22.5	1.32
II	PtN1N	40	33.6	30.8	24.4	1.34
II	PtN1N	45	34.2	31.1	26.5	1.35
II	PtN1N	50	32.2	30.3	25.1	1.29
II	PtN1N	60	27.8	25.5	21.5	1.13
III	PtN1N	30	26.1	22.9	17.7	1.14
III	PtN1N	40	32.8	30.2	24.4	1.31
III	PtN1N	50	32.5	30.7	25.3	1.31
III	PtN1N	60	27	25	20.9	1.10
IV	PtN1N	30	20.4	17.5	13	0.89
IV	PtN1N	40	27.8	23.8	19.1	1.11
IV	PtN1N	50	28	26.2	21.7	1.12
IV	PtN1N	60	24.6	23.7	20.1	1
I	PtOO3	30	20.8	18.3	16.3	NA
I	PtOO3	40	21.6	20.01	17.4	NA
I	PtOO3	50	21.8	20.6	18.2	NA
I	PtOO3	60	23.3	21.6	19.1	NA
II	PtOO3	30	22.2	18.9	16.7	1.07
II	PtOO3	40	25.5	24	21.3	1.18
II	PtOO3	50	28.5	26.8	23.9	1.31
II	PtOO3	60	29.3	27.6	25	1.26

The wavelength dependence of the out-coupled power emitted from the MOLED can be calculated from the series of electroluminescent spectra measured at different detection angles. The total photon flux for a given wavelength can be

determined from its angular intensity profile, where the three-dimensional surface area of the angular intensity profile, I(θ,φ), for a given wavelength is equal to the photon flux according to the following relationship $P = \iint_S I(\theta,\phi)\sin\theta d\theta d\phi$. An example of the angular dependent EL spectra and angular intensity profile, used in the calculation described previously, for the emitter, PtN1N, in the structure of glass/Ta2O5(57nm)/SiO2(100nm)/ITO(53nm)/HATCN(10nm)/NPD(40nm)/TAPC(10 nm)/8%PtN1N:26mCPy(25nm)/DPPS(10nm)/BmPyPB(45nm)/LiF(1nm)/Al(100nm) is shown in Figure 65 and 66.

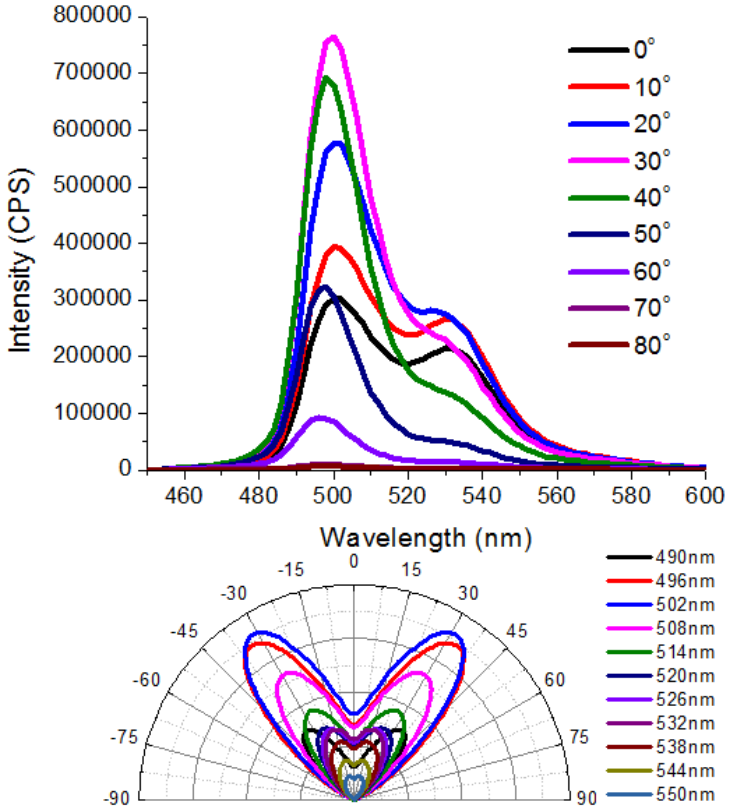

Figure 65. The EL spectra (photon counts per second) for PtN1N in the structure of glass/Ta2O5(57nm)/SiO2(100nm)/ITO(53nm)/HATCN(10nm)/NPD(40nm)/TAPC(10nm)/8%PtN1N:26mCPy(25nm)/DPPS(10nm)/BmPyPB(45nm)/LiF(1nm)/Al(100nm) at different detection angles (top). A polar plot (bottom) of the total intensity versus angle for a given wavelength (490nm, 496nm, 502nm, 508nm, 514nm, 520nm,

526nm, 532nm, 538nm, 544nm, and 550nm) derived from the angular dependent EL spectra and is also in units of photon counts per second.

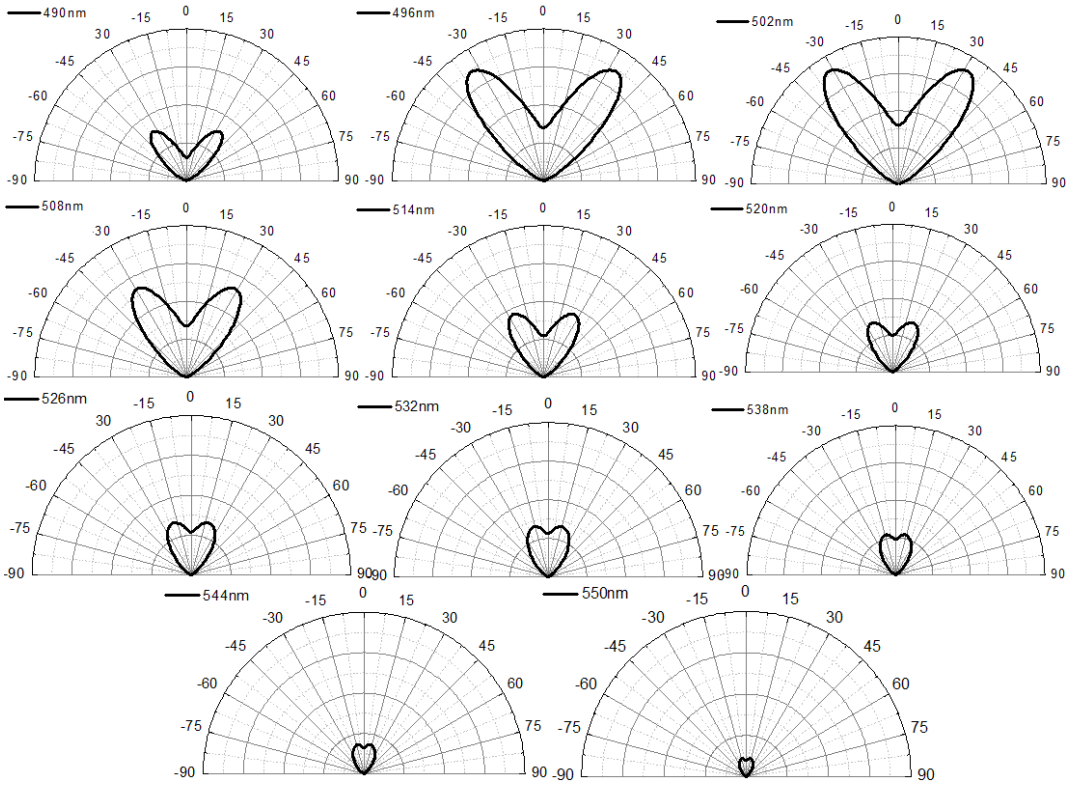

Figure 66. The angular intensity profile for 490nm, 496nm, 502nm, 508nm, 514nm, 520nm, 526nm, 532nm, 538nm, 544nm, and 550nm in the structure of glass/Ta2O5(57nm)/SiO2(100nm)/ITO(53nm)/HATCN(10nm)/NPD(40nm)/TAPC(10nm)/8%PtN1N:26mCPy(25nm)/DPPS(10nm)/BmPyPB(45nm)/LiF(1nm)/Al(100nm). Each profile has azimuthal symmetry and the three dimensional profile can be generated by setting the intensity for a given θ constant for all azimuthal angles, φ. The total photon flux for a given wavelength is the surface area of the three dimensional profile emission characteristics.

In order to define the true wavelength dependence on the total emitted power, the total photon flux must be normalized to the intrinsic emission spectrum. Unfortunately, the emitter, PtN1N, exhibits narrow band emission characteristics, introducing significant noise into the normalization on account of variation in the measurements implemented in this study. For this reason, the broader band emitter, PtOO3, is more suitable in defining the wavelength dependence on the total emitted power compared to the emitter, PtN1N. The total photon flux for PtOO3 in

the structure of glass/Ta2O5(57nm)/SiO2(100nm)/ITO(53nm)/HATCN(10nm)/ NPD(30,40,50,60nm)/TAPC(10nm)/8%PtOO3:26mCPy(25nm)/DPPS(10nm)/BmPyPB (45nm)/LiF(1nm)/Al(100nm) is shown in Figure 67. The normalized total photon flux exhibits peaks at 502nm, 514nm, 531nm, and 537nm for 30nm, 40nm, 50nm, and 60nm, respectively. The red-shifting in the peak wavelength is in agreement with the discussions previously with regards to the effect of cavity detuning on the out-coupling enhancement in MOLEDs.

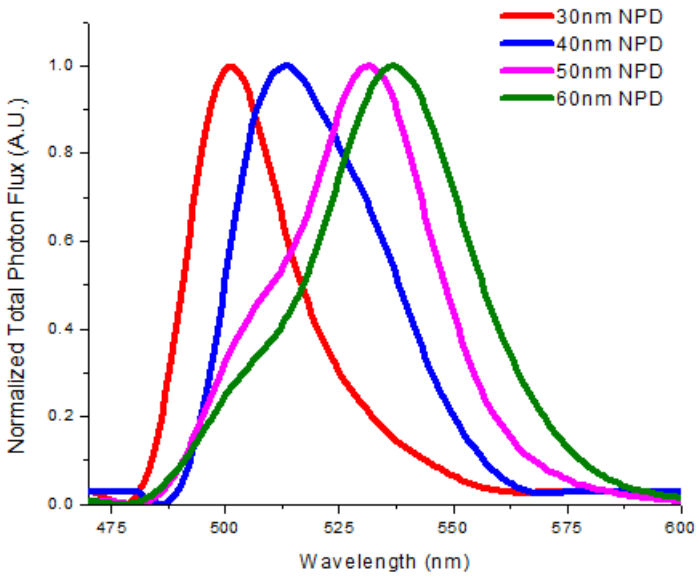

Figure 67. The total photon flux for the emitter, PtOO3, in the structure of glass/Ta2O5(57nm)/SiO2(100nm)/ITO(53nm)/HATCN(10nm)/NPD(30,40,50,60nm)/ TAPC(10nm)/8%PtOO3:26mCPy(25nm)/DPPS(10nm)/BmPyPB(45nm)/LiF(1nm)/Al (100nm).

The total photon flux normalized to the intrinsic emission spectrum is shown in Figure 68. From this point forward, the total photon flux normalized to the intrinsic emission spectrum will be properly referred to as the relative enhancement ratio as it defines the potential out-coupled power of a given wavelength relative to other emission wavelengths. In the structure of glass/Ta2O5(57nm)/SiO2(100nm)

/ITO(53nm)/HATCN(10nm)/NPD(30,40,50,60nm)/TAPC(10nm)/8%PtOO3:26mCPy (25nm)/DPPS(10nm)/BmPyPB(45nm)/LiF(1nm)/Al(100nm) the enhancement ratio exhibits peaks at 502nm, 511nm, 534nm, and 545nm for a 30nm, 40nm, 50nm, and 60nm NPD thickness, respectively. For a 30nm thick NPD layer, the enhancement ratio drops off rapidly for wavelengths greater than 502nm, however, there remains significant overlap in the enhancement ratio curve with the intrinsic emission spectrum of PtN1N on account of the narrow band emission characteristics of PtN1N. Conversely, the significant side band in the intrinsic emission spectrum of PtOO3 results in poor overlap in the enhancement ratio curve with the intrinsic emission spectrum of PtOO3 for a 30nm thick NPD layer and consequently less enhancement in the out-coupling efficiency. For this reason, significant detuning is required for MOLEDs implementing PtOO3 to achieve out-coupling enhancement, whereas, MOLEDs implementing PtN1N exhibited significant out-coupling enhancement with a 30nm NPD layer.

The enhancement ratio characteristics outlined in Figure 68 correlates well with the methods described in section 7.3.3 for measuring the external quantum efficiency of the MOLEDs in this study. Both results suggest that an optimum enhancement in light out-coupling occur for a ~30-40nm thick NPD layer in MOLEDs implementing PtN1N, and a ~50nm thick NPD layer in MOLEDs implementing PtOO3. Thus, the intrinsic emission characteristics of the source in a MOLED has a significant impact on MOLED performance and a narrow band source in a MOLED is ideal for achieving large enhancements in the light out-coupling efficiency without the need of significant detuning.

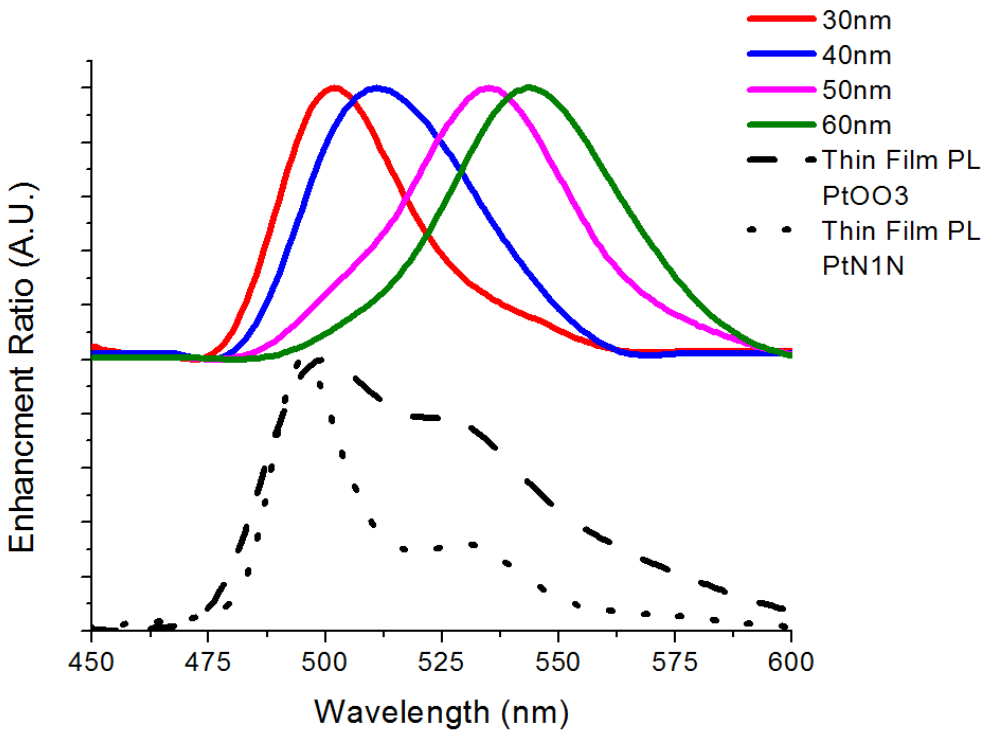

Figure 68. The total photon flux normalized to the intrinsic emission spectrum of the emitter, PtOO3, for the structure of glass/Ta2O5(57nm)/SiO2(100nm)/ITO(53nm)/ HATCN(10nm)/ NPD(30,40,50,60nm)/TAPC(10nm)/8%PtOO3:26mCPy(25nm)/DPPS (10nm)/BmPyPB(45nm)/LiF(1nm)/Al (100nm). The thin film PL of PtOO3 (dashed) and PtN1N (dotted) in a film of 8%dopant:26mCPy are also included in the Figure (bottom).

7.5 Conclusion

A systematic and comprehensive study of the microcavity effects in MOLEDs implementing a narrow band emission source was conducted. The phosphorescent emitter, PtN1N (FWHM=18nm), was implemented into a series of low-finesse, moderate-finesse, and high-finesse MOLEDs with different cavity tuning. Optimum EQE enhancement was achieved with a moderately detuned, low-finesse MOLED structure with a single DBR pair of quarter-wavelength thick high index material, Ta_2O_5, and low index material, SiO_2, which exhibited a peak EQE of 34.2% and a 1.35 enhancement in EQE compared to PtN1N in conventional device architectures.

Additionally, the effect of the source spectral emission band on MOLED performance was investigated by implementing two phosphorescent molecules, PtN1N (FWHM=18nm) and PtOO3 (FWHM=72nm), with similar non-cavity peak emission energies and different spectral emission bands into identical MOLED structures and found that a greater enhancement in light out-coupling is possible with MOLEDs containing PtN1N with enhancements in light out-coupling efficiency as high as 1.3 with detuning as low as $\Delta\lambda$~9nm, compared to MOLEDs containing PtOO3 for which little enhancement occurred for the same amount of detuning. This work suggests the potential for narrow band emission sources in MOLEDs and demonstrates that significant out-coupling enhancement can be achieved with a MOLED design.

8 FUTURE ROLE OF OLEDS

8.1 Summary

8.1.1 Motivation

Organic light emitting diodes (OLEDs) are strong candidates for next generation displays and solid state lighting. In order to further the development of OLEDs in display, efficient and stable phosphorescent emitters are desired. The work conducted in this thesis demonstrates the potential of platinum based complexes for use in highly efficient and stable OLEDs.

8.1.2 Highly Efficient White OLEDs and a Route towards Stable Blue OLEDs

In addition to being a promising route for stable and efficient OLEDs, platinum complexes have unique photophysical properties. For select cases, the planar geometry facilitates Pt---Pt interactions within the doped thin organic film resulting in excimer emission combined with parent monomer emission, enabling emission over the entire visible range for high quality white light. Typically, white light emission in OLEDs is achieved by simultaneous emission of multiple emissive materials, which need to be employed in either a single emissive layer with multiple molecular emitters or multiple emissive layers. The use of these multi-layered or multi-dopant device architectures not only results in increased fabrication difficulty and costs but also yields several possible operational problems making them a less attractive approach for generating white light. In Chapter 3, a highly efficient white OLED using the platinum complex platinum(II) bis(N-methyl-imidazolyl)-*benzene* chloride (Pt-16) was demonstrated which exhibited a maximum external quantum

efficiency (EQE) of 20.1%, a peak power efficiency of over 50 lm/W on a planar glass substrate and high quality white light with color coordinates of CIE(x=0.33, y=0.33) and a CRI of 80. To our knowledge, this was the first demonstration of a single doped white OLED with an EQE greater than 20%. Although Pt-16 based devices demonstrated high quality white light emission with high external quantum efficiency's, Pt-16 is electrochemically unstable which may be attributed to the highly electronegative halogen atom, chlorine. In Chapter 4, a route towards electrochemically stable platinum complexes with blue-green emission by utilizing a tetradentate, cyclometalated design was demonstrated. In particular, an OLED implementing the halogen free complex platinum(II) phenyl-methylimidazole (PtOO2) with a high external quantum efficiency of 23.1% and color coordinates of CIE(x=0.16,y=0.34) was demonstrated.

8.1.3 A Stable Red PhOLED

In Chapter 5, a stable and efficient red OLED based on the tetradentate cyclometalated platinum complex, PtON11-Me with an operational stability close to or exceeding its Iridium analog was demonstrated. Devices employing PtON11-Me in a stable structure exhibited a maximum EQE of 8.3%, color coordinates CIE(x=0.61,y=0.36) and an estimated operational lifetime $T_{0.97}$ ~ 1560 h at 100 cd/m^2, higher than its iridium analog, tris(1-phenylquinoline) iridium(III) (PQIr), using a similar device architecture. Additionally, it was found that the operational lifetime could be improved further by implementing a mCBP:BAlq cohost structure which exhibited an estimated operational lifetime $T_{0.97}$ = 3112 at 100 cd/m^2. Furthermore, by using more effective electron, hole, and exciton blocking materials, efficiencies as high as 12.5% were achieved, demonstrating the potential for both

stable and highly efficient red OLEDs utilizing PtON11-Me. Thus, this work suggests that platinum complexes can act as efficient and stable emitters with efficiencies and operational lifetimes close to or exceeding those of their iridium analogs. The demonstration of a stable and efficient red OLED based on a platinum complex debunks previous notions that platinum complexes are less stable than their iridium analogs.

8.1.4 Microcavity OLEDs using a Narrow Band Emitter

In addition to the need for improvements in the availability of efficient and stable phosphorescent emitters in OLEDs, improvements in device architectures are also needed. Using conventional device architectures limits the external quantum device efficiency to 20-30%, as most of the photons generated do not contribute to the out-coupled power as a result of optical losses inside of the device. These optical losses include surface plasmon polaritions (SPPs), absorption at the metal electrode surface, and modes trapped by total internal reflection due to the mismatch of the refractive indices between the organic layers (n~1.6-1.8)/ITO anode (n~1.9) and glass (n~1.5) (waveguide modes) and the mismatch of refractive indices between glass and air (n~1) (substrate modes). Thus, device architectures that improve out-coupling efficiency are highly desired and provide the greatest potential for improvements in OLED efficiency and methods that improve the light out-coupling efficiency, or fraction of light emitted from the device to total generated light, need to be considered. There have been a number of methods reported that enhance the external quantum efficiency (EQE) of OLEDs and overcome the light out-coupling limitation by releasing the light rays trapped by total internal reflection.[49] These include creating surface roughness on the top of the substrate to allow more light to

scatter out of the substrate,[50, 121-123] implementing an ordered microlens array at the top of the substrate to eliminate the critical angle condition at the substrate/air interface,[124] growing a periodic two-dimensional (2D) photonic crystal to couple the guided waves to the radiation mode in the direction normal to the device surface,[52, 125] or through the design of a microcavity OLED (MOLED). [53, 126-134] MOLEDs are of particular interest due to their simple fabrication and their ability to be used in conjunction with the other aforementioned strategies.[126, 135] It has been found in this study that MOLEDs, in particular, are a more suitable design for narrow band emitters. It has been found that platinum complexes exhibit narrow band emission for a cyclometalated, tetradentate design with a high degree of rigidity. Such narrow emission bands are more suitable for a MOLED design than typical organic phosphors with broad spectral widths (FWHM>50nm) since a larger fraction of the emission is accelerated by the cavity. A MOLED based on a tetradentate, cyclometalated, platinum complex, platinum(II)-2'-(H-pyrazol-1-yl)-9-(pyridine-2-yl)-9H-2,9'-bicarbazole (PtN1N), with a narrow spectral emission band exhibiting a FWHM of 18nm in a solution of DCM was demonstrated. By extending the spectral position of the optical mode beyond the peak intrinsic emission wavelength to form a so called over-tuned or detuned optical cavity, a high forward viewing EQE of 34.2% was achieved compared with the non-cavity structure which exhibited a peak EQE of 25.4%. Thus, with only an addition of a SiO2 spacer layer and Ta2O5 high index layer onto the original device structure, an enhancement in EQE of 1.35 was achieved with the detuned structure.

8.2 Outlook

A highly efficient and stable blue OLED with the ability to form excimer emission combined with monomer emission to generate high quality white light is the holy grail of organic light emitting diodes from platinum complexes. While several reporting's of stable and efficient phosphorescent complexes with red and green emission have been reported, there have been few reports of stable and efficient blue-emitting phosphorescent complexes. Thus, a blue-emitting platinum complex with the ability of generating a broad white emission will be a significant step forward in the field and the development of such emitters may provide a viable route to both energy efficient OLED displays as well as organic solid state lighting.

WOLEDs fabricated in this thesis utilizing platinum(II) bis(methyl-imidazolyl)benzene chloride (Pt-16), demonstrated excellent CIE color coordinates of (0.33,0.33), a high CRI of 80, and a high external quantum efficiency of 20.1%. However, the photoluminscent quantum yield (PLQY) measurements of Pt-16 doped in thin films of mCPy26 indicated that the Pt-16 monomer is inefficient requiring a tradeoff between color quality and high efficiency. Thus, square planar platinum complexes exhibiting both highly efficient monomer and excimer emission are highly desired. Additionally, a new molecular design motif is needed since excimer emitting materials employing N^C^N cyclometalating ligands and their analogs, typically utilize potentially unstable functional groups (i.e. halogens) as a fourth coordinating ligand bonded to the platinum metal ion to achieve deep blue emission. The need for a new molecular motif was alluded to in Chapter 4 and demonstrated a highly efficient halogen free platinum complex, PtOO2, with blue-green emission. However, the complex, PtOO2, did not exhibit excimer emission. The lack of an

excimer component from PtOO2 is likely a result of considerable distortion from planarity created by the oxygen linking atoms, which inhibits intermolecular interactions necessary for excimer formations.[100] Thus, further work is needed to achieve electrochemically stable, deep blue emission with excimer emission capability.

In addition to improvements in the availability of highly efficient and stable phosphorescent complexes, improvements in the light out-coupling efficiency are needed. Some of the benefits of a narrow band emitter in a microcavity organic light emitting diode for improved light out-coupling efficiency were outlined in Chapter 7. Further improvements in the light out-coupling efficiency utilizing a narrow band emitter in conjunction with a microcavity OLED design may be achieved by employing an exciplex forming co-host system. Kim et. al demonstrated an external quantum efficiency over 30% implementing an exciplex forming co-host system of 4,4',4"-tri (N-carbazolyl) tri-phenylamine (TCTA) and bis-4,6-(3,5-di-3-pyridylphenyl)-2-methylpyrimidine (B3PYMPM).[184] Optical analysis of the phosphorescent emitter $Ir(ppy)_2(acac)$ in device suggested a preferred non-isotropic orientation with a horizontal to vertical dipole ratio of 0.77:0.23 is achieved compared to 0.66:0.33 for isotropic emission. Thus, a MOLED implementing a narrow band emitting source doped in an exciplex forming co-host system may result in even further improvements in the external quantum efficiency. Such a structure combined with a microlens array, capable of releasing substrate modes, may result in record external quantum efficiencies of OLEDs.

REFERENCES

1. Internet Connected Devices Approaching 10 Billion, to exceed 28 Billion by 2020 http://imsresearch.com/press-release/Internet_Connected_Devices_Approaching_10_Billion_to_exceed_28_Billion_by_2020&cat_id=210&type=LatestResearch.

2. 24 Electronic Products Per Household -- Got Recycling? [http://www.forbes.com/sites/tjmccue/2013/01/02/24-electronic-products-per-household-got-recycling/.

3. The Future According to Freescale: 1,000 Embedded Devices Per Person http://www.eetimes.com/document.asp?doc_id=1168780.

4. Hazzardous Substances in e-Waste http://ewasteguide.info/node/219.

5. Forrest SR. Ultrathin organic films grown by organic molecular beam deposition and related techniques. Chem Rev 1997;97(6):1793-896.

6. Deaton R, Garzon M, Murphy R, Rose J, Franceschetti D, Stevens Jr SE. Reliability and efficiency of a DNA-based computation. Phys Rev Lett 1998;80(2):417.

7. Pope M, Swenberg CE. Electronic processes in organic crystals Clarendon: Oxford; 1982. .

8. Silinsh EA. Organic molecular crystals Berlin: Springer; 1980.

9. Sze SM. Physics of semiconductor devices New York: John Wiley; 1981.

10. Forrest SR, Kaplan ML, Schmidt PH. Organic-on-inorganic semiconductor contact barrier diodes. II. dependence on organic film and metal contact properties. J. Appl. Phys. 1984;56:543-51.

11. Warta W, Stehle R, Karl N. Ultrapure, high mobility organic photoconductors Appl. Phys. 1985;36:163-70.

12. Karl N. Studies of organic semiconductors for 40 years Mol. Cryst. Liq. Cryst. 1989;171:31-51.

13. Sirringhaus H. Mobility enhancement in conjugated polymer field-effect transistors through chain alignment in a liquid-crystalline phase Appl. Phys. Lett. 2000;77:406-8.

14. Forrest SR. Ultrathin organic films grown by organic molecular beam deposition and related techniques Chem. Rev. 1997;97:1793-896.

15. Bolotin KI, Sikes K, Jiang Z, Klima M, Fudenberg G, Hone J, Kim P, Stormer H. Ultrahigh electron mobility in suspended graphene. Solid State Commun

2008;146(9):351-5.

16. (a) Tang C, VanSlyke S. Organic electroluminescent diodes. Appl Phys Lett 1987;51:913. (b) Reineke, S, White Organic Light-Emitting Diodes: Status and Perspective. Reviews of Modern Physics JULY 13;85(1245).

17. Tang CW. Two-layer organic photovoltaic cell. Appl Phys Lett 1986;48:183.

18. Chiba Y, Islam A, Watanabe Y, Komiya R, Koide N, Han L. Dye-sensitized solar cells with conversion efficiency of 11.1%. Japanese Journal of Applied Physics Part 2 Letters 2006;45(24/28):L638.

19. Gundlach D, Lin Y. IEEE electron dev. lett. 18, 87 (1997); YY lin, DJ gundlach, SF nelson and TN jackson. IEEE Trans Electron Dev 1997;44:1325.

20. Gundlach DJ, Lin Y, Jackson TN, Nelson S, Schlom D. Pentacene organic thin-film transistors-molecular ordering and mobility. Electron Device Letters, IEEE 1997;18(3):87-9.

21. Schön J, Kloc C, Dodabalapur A, Batlogg B. An organic solid state injection laser. Science 2000;289(5479):599-601.

22. VG Kozlov VB, PE Burrows S. Laser action in organic semiconductor waveguide and double-heterostructure devices. Nature 1997;389(6649):362-4.

23. Crone B, Dodabalapur A, Sarpeshkar R, Gelperin A, Katz H, Bao Z. Organic oscillator and adaptive amplifier circuits for chemical vapor sensing. J Appl Phys 2002;91(12):10140-6.

24. Crone B, Dodabalapur A, Gelperin A, Torsi L, Katz H, Lovinger A, Bao Z. Electronic sensing of vapors with organic transistors. Appl Phys Lett 2001;78(15):2229-31.

25. Zhu Z, Mason JT, Dieckmann R, Malliaras GG. Humidity sensors based on pentacene thin-film transistors. Appl Phys Lett 2002;81(24):4643-5.

26. Ma D, Aguiar M, Freire JA, Hümmelgen IA. Organic reversible switching devices for memory applications. Adv Mater 2000;12(14):1063-6.

27. Tondelier D, Lmimouni K, Vuillaume D, Fery C, Haas G. Metal/organic/metal bistable memory devices. Appl Phys Lett 2004;85(23):5763-5.

28. [Internet]. Available from: http://www.oled-info.com/history.

29. Galaxy S3 Sold 50 Million Units, Demand for Galaxy S4 Deemed "Explosive" http://www.androidauthority.com/galaxy-s4-demand-galaxy-s3-sales-197892/.

30. Levy GB, Evans W, Ebner J, Farrell P, Hufford M, Allison BH, Wheeler D, Lin H, Prache O, Naviasky E. An 852× 600 pixel OLED-on-silicon color microdisplay using CMOS subthreshold-voltage-scaling current drivers. Solid-State Circuits, IEEE Journal of 2002;37(12):1879-89.

31. [Internet]. Available from: www.prweb.com.

32. Department of Energy. 2010 U.S. lighting market. 2010;Energy Efficiency and Renewable Energy.

33. So F, Kido J, Burrows P. Organic light-emitting devices for solid-state lighting. MRS Bull 2008;33(07):663-9.

34. Reineke S, Lindner F, Schwartz G, Seidler N, Walzer K, Luessem B, Leo K. White organic light-emitting diodes with fluorescent tube efficiency. Nature 2009 MAY 14;459(7244):234-U116.

35. Adachi C, Baldo MA, Thompson ME, Forrest SR. Nearly 100% internal phosphorescence efficiency in an organic light-emitting device. J Appl Phys 2001;90(10):5048-51.

36. Baldo M, O'brien D, You Y, Shoustikov A, Sibley S, Thompson M, Forrest S. Highly efficient phosphorescent emission from organic electroluminescent devices. Nature 1998;395(6698):151-4.

37. Lamansky S, Djurovich P, Murphy D, Abdel-Razzaq F, Lee H, Adachi C, Burrows P, Forrest S, Thompson M. Highly phosphorescent bis-cyclometalated iridium complexes: Synthesis, photophysical characterization, and use in organic light emitting diodes. J Am Chem Soc 2001 MAY 9;123(18):4304-12.

38. Schwartz G, Reineke S, Rosenow TC, Walzer K, Leo K. Triplet harvesting in hybrid white organic Light-Emitting diodes. Advanced Functional Materials 2009;19(9):1319-33.

39. 11.1: Invited paper: Advances in blue phosphorescent organic Light-Emitting devices. SID symposium digest of technical papersWiley Online Library; 2006.

40. Xiao L, Xing X, Chen Z, Qu B, Lan H, Gong Q, Kido J. Highly efficient Electron-Transporting/Injecting and thermally stable naphthyridines for organic electrophosphorescent devices. Advanced Functional Materials 2013;23(10):1323-30.

41. Xiao L, Su S, Agata Y, Lan H, Kido J. Nearly 100% internal quantum efficiency in an organic Blue-Light electrophosphorescent device using a weak electron transporting material with a wide energy gap. Adv Mater 2009;21(12):1271-4.

42. Eom S, Zheng Y, Wrzesniewski E, Lee J, Chopra N, So F, Xue J. White phosphorescent organic light-emitting devices with dual triple-doped emissive

layers. Appl Phys Lett 2009 APR 13;94(15):153303.

43. Hobson P, Wasey J, Sage I, Barnes W. The role of surface plasmons in organic light-emitting diodes. Ieee Journal of Selected Topics in Quantum Electronics 2002 MAR-APR;8(2):378-86.

44. Hobson P, Wedge S, Wasey J, Sage I, Barnes W. Surface plasmon mediated emission from organic light-emitting diodes (vol 14, pg 1393, 2002). Adv Mater 2002 NOV 18;14(22):1600.

45. Lin C, Lin H, Wu C. Examining microcavity organic light-emitting devices having two metal mirrors. Appl Phys Lett 2005 JUL 11;87(2):021101.

46. Krummacher BC, Nowy S, Frischeisen J, Klein M, Bruetting W. Efficiency analysis of organic light-emitting diodes based on optical simulation. Organic Electronics 2009 MAY;10(3):478-85.

47. Nowy S, Krummacher BC, Frischeisen J, Reinke NA, Brütting W. Light extraction and optical loss mechanisms in organic light-emitting diodes: Influence of the emitter quantum efficiency. J Appl Phys 2008;104(12):123109.

48. Nowy S, Krummacher BC, Frischeisen J, Reinke NA, Bruetting W. Light extraction and optical loss mechanisms in organic light-emitting diodes: Influence of the emitter quantum efficiency. J Appl Phys 2008 DEC 15;104(12):123109.

49. Hong K, Lee J. Review paper: Recent developments in light extraction technologies of organic light emitting diodes. Electronic Materials Letters 2011;7(2):77-91.

50. Schnitzer I, Yablonovitch E, Caneau C, Gmitter T, Scherer A. 30% external quantum efficiency from surface textured, thin-film light-emitting diodes. Appl Phys Lett 1993;63(16):2174-6.

51. Moller S, Forrest S. Improved light out-coupling in organic light emitting diodes employing ordered microlens arrays. J Appl Phys 2002 MAR 1;91(5):3324-7.

52. Do Y, Kim YC, Song Y, Cho C, Jeon H, Lee Y, Kim S, Lee Y. Enhanced light extraction from organic Light-Emitting diodes with 2D SiO2/SiNx photonic crystals. Adv Mater 2003;15(14):1214-8.

53. Jordan R, Rothberg L, Dodabalapur A, Slusher R. Efficiency enhancement of microcavity organic light emitting diodes. Appl Phys Lett 1996 SEP 30;69(14):1997-9.

54. Dodabalapur A, Rothberg L, Jordan R, Miller T, Slusher R, Phillips JM. Physics and applications of organic microcavity light emitting diodes. J Appl Phys 1996;80(12):6954-64.

55. Coren S, Girgus JS. Density of human lens pigmentation:< i> in vivo</i> measures over an extended age range. Vision Res 1972;12(2):343-6.

56. LIghting handbook. 8th ed. New York: IESNA; 1993.

57. Forrest S, Bradley D, Thompson M. Measuring the efficiency of organic light-emitting devices. Adv Mater 2003 JUL 4;15(13):1043-8.

58. van Mensfoort SLM, Carvelli M, Megens M, Wehenkel D, Bartyzel M, Greiner H, Janssen RAJ, Coehoorn R. Measuring the light emission profile in organic light-emitting diodes with nanometre spatial resolution. Nature Photonics 2010 MAY;4(5):329-35.

59. Ganzorig C, Fujihira M. A possible mechanism for enhanced electrofluorescence emission through triplet-triplet annihilation in organic electroluminescent devices. Appl Phys Lett 2002 OCT 21;81(17):3137-9.

60. Huang J, Li G, Wu E, Xu Q, Yang Y. Achieving high-efficiency polymer white-light-emitting devices. Adv Mater 2006 JAN 5;18(1):114-7.

61. Probst M, Haight R. Unoccupied molecular orbital states of tris (8-hydroxy quinoline) aluminum: Observation and dynamics. Appl Phys Lett 1997 JUL 14;71(2):202-4.

62. Kawamura Y, Goushi K, Brooks J, Brown J, Sasabe H, Adachi C. 100% phosphorescence quantum efficiency of ir(III) complexes in organic semiconductor films. Appl Phys Lett 2005 FEB 14;86(7):071104.

63. Huang J, Hou W, Li J, Li G, Yang Y. Improving the power efficiency of white light-emitting diode by doping electron transport material. Appl Phys Lett 2006 SEP 25;89(13):133509.

64. Bulovic V, Khalfin V, Gu G, Burrows P, Garbuzov D, Forrest S. Weak microcavity effects in organic light-emitting devices. Physical Review B 1998 AUG 15;58(7):3730-40.

65. W. L. Wolfe. Introduction to radiometry: Tutorial texts in optical engineering. TT29 ed. Bellingham, WA: SPIE Optical Engineering Press; 1998.

66. Chang C, Chen C, Wu C, Chang S, Hung J, Chi Y. High-color-rendering pure-white phosphorescent organic light-emitting devices employing only two complementary colors. Organic Electronics 2010;11(2):266-72.

67. Xiao L, Chen Z, Qu B, Luo J, Kong S, Gong Q, Kido J. Recent progresses on materials for electrophosphorescent organic light-emitting devices. Adv Mater 2011 FEB 22 2011;23(8):926-52.

68. Sun Y, Giebink N, Kanno H, Ma B, Thompson M, Forrest S. Management of singlet and triplet excitons for efficient white organic light-emitting devices. Nature

2006 APR 13;440(7086):908-12.

69. Gordon M. The exciplex. New York: Academic Press; 1975.

70. Kim D, Brédas J. Triplet excimer formation in platinum-based phosphors: A theoretical study of the roles of pt– pt bimetallic interactions and interligand π– π interactions. J Am Chem Soc 2009;131(32):11371-80.

71. Adamovich V, Brooks J, Tamayo A, Alexander A, Djurovich P, D'Andrade B, Adachi C, Forrest S, Thompson M. High efficiency single dopant white electrophosphorescent light emitting diodes. New Journal of Chemistry 2002;26(9):1171-8.

72. Williams EL, Haavisto K, Li J, Jabbour GE. Excimer-based white phosphorescent organic light emitting diodes with nearly 100 % internal quantum efficiency. Adv Mater 2007 JAN 20;19(2):197.

73. Bakken N, Wang Z, Li J. Highly efficient white organic light-emitting device using a single emitter. Journal of Photonics for Energy 2012;2(1):021203,1-021203-7.

74. D'Andrade B, Forrest S. White organic light-emitting devices for solid-state lighting. Adv Mater 2004 SEP 16;16(18):1585-95.

75. Turro NJ. Modern molecular photochemistry. Sausalito, CA: University Science Books; 1991. .

76. Ma B, Djurovich PI, Thompson ME. Excimer and electron transfer quenching studies of a cyclometalated platinum complex. Coord Chem Rev 2005;249(13):1501-10.

77. Ma B, Li J, Djurovich PI, Yousufuddin M, Bau R, Thompson ME. Synthetic control of pt⊙⊙⊙ pt separation and photophysics of binuclear platinum complexes. J Am Chem Soc 2005;127(1):28-9.

78. Develay S, Blackburn O, Thompson AL, Williams JG. Cyclometalated platinum (II) complexes of pyrazole-based, N∧ C∧ N-coordinating, terdentate ligands: The contrasting influence of pyrazolyl and pyridyl rings on luminescence. Inorg Chem 2008;47(23):11129-42.

79. Sajoto T, Djurovich PI, Tamayo AB, Oxgaard J, Goddard III WA, Thompson ME. Temperature dependence of blue phosphorescent cyclometalated ir (III) complexes. J Am Chem Soc 2009;131(28):9813-22.

80. Divayana Y, Sun X. Observation of excitonic quenching by long-range dipole-dipole interaction in sequentially doped organic phosphorescent host-guest system. Phys Rev Lett 2007;99(14):143003.

81. Giebink N, D'Andrade B, Weaver M, Mackenzie P, Brown J, Thompson M, Forrest S. Intrinsic luminance loss in phosphorescent small-molecule organic light emitting devices due to bimolecular annihilation reactions. J Appl Phys 2008;103(4):044509.

82. Chopra N, Swensen JS, Polikarpov E, Cosimbescu L, So F, Padmaperuma AB. High efficiency and low roll-off blue phosphorescent organic light-emitting devices using mixed host architecture. Appl Phys Lett 2010;97(3):033304.

83. Su S, Gonmori E, Sasabe H, Kido J. Highly efficient organic blue-and white-light-emitting devices having a carrier-and exciton-confining structure for reduced efficiency roll-off. Adv Mater 2008;20(21):4189-94.

84. Baldo M, Lamansky S, Burrows P, Thompson M, Forrest S. Very high-efficiency green organic light-emitting devices based on electrophosphorescence. Appl Phys Lett 1999;75(1):4-6.

85. Gather MC, Koehnen A, Meerholz K. White organic light-emitting diodes. Adv Mater 2011 JAN 11;23(2):233-48.

86. D'Andrade BW, Forrest SR. White organic light-emitting devices for solid-state lighting. Adv Mater 2004;16(18):1585-95.

87. Tokito S, Iijima T, Suzuri Y, Kita H, Tsuzuki T, Sato F. Confinement of triplet energy on phosphorescent molecules for highly-efficient organic blue-light-emitting devices. Appl Phys Lett 2003;83(3):569-71.

88. Yeh S, Wu M, Chen C, Song Y, Chi Y, Ho M, Hsu S, Chen CH. New dopant and host materials for Blue-Light-Emitting phosphorescent organic electroluminescent devices. Adv Mater 2005;17(3):285-9.

89. Jeon SO, Jang SE, Son HS, Lee JY. External quantum efficiency above 20% in deep blue phosphorescent organic Light-Emitting diodes. Adv Mater 2011;23(12):1436-41.

90. Wang Z, Turner E, Mahoney V, Madakuni S, Groy T, Li J. Facile synthesis and characterization of phosphorescent pt (N^ C^ N) X complexes. Inorg Chem 2010;49(24):11276-86.

91. Yang X, Wang Z, Madakuni S, Li J, Jabbour GE. Efficient blue- and white-emitting electrophosphorescent devices based on platinum(II) [1,3-difluoro-4,6-di(2-pyridinyl)benzene] chloride. Adv Mater 2008 JUN 18;20(12):2405.

92. Sivasubramaniam V, Brodkorb F, Hanning S, Loebl HP, van Elsbergen V, Boerner H, Scherf U, Kreyenschmidt M. Fluorine cleavage of the light blue heteroleptic triplet emitter FIrpic. J Fluorine Chem 2009;130(7):640-9.

93. Fleetham T, Wang Z, Li J. Efficient deep blue electrophosphorescent devices based on platinum (II) bis (n-methyl-imidazolyl) benzene chloride. Organic Electronics 2012;13(8):1430-5.

94. Kui SC, Chow PK, Cheng G, Kwok CC, Kwong CL, Low KH, Che CM. Robust phosphorescent platinum(II) complexes with tetradentate O^N^C^N ligands: High efficiency OLEDs with excellent efficiency stability. Chem Commun (Camb) 2013 Feb 21;49(15):1497-9.

95. Kalinowski J, Fattori V, Cocchi M, Williams J. Light-emitting devices based on organometallic platinum complexes as emitters. Coord Chem Rev 2011;255(21):2401-25.

96. Vezzu DA, Deaton JC, Jones JS, Bartolotti L, Harris CF, Marchetti AP, Kondakova M, Pike RD, Huo S. Highly luminescent tetradentate bis-cyclometalated platinum complexes: Design, synthesis, structure, photophysics, and electroluminescence application⊥. Inorg Chem 2010;49(11):5107-19.

97. Jones G, Jackson WR, Choi CY, Bergmark WR. Solvent effects on emission yield and lifetime for coumarin laser dyes. requirements for a rotatory decay mechanism. J Phys Chem 1985;89(2):294-300.

98. DePriest J, Zheng GY, Goswami N, Eichhorn DM, Woods C, Rillema DP. Structure, physical, and photophysical properties of platinum (II) complexes containing bidentate aromatic and bis (diphenylphosphino) methane as ligands. Inorg Chem 2000;39(9):1955-63.

99. Connelly NG, Geiger WE. Chemical redox agents for organometallic chemistry. Chem Rev 1996;96(2):877-910.

100. Turner E, Bakken N, Li J. Cyclometalated platinum complexes with luminescent quantum yields approaching 100%. Inorg Chem 2013;52(13):7344-51.

101. Hang X, Fleetham T, Turner E, Brooks J, Li J. Highly efficient Blue-Emitting cyclometalated platinum (II) complexes by judicious molecular design. Angewandte Chemie International Edition 2013;52(26):6753-6.

102. Schneidenbach D, Ammermann S, Debeaux M, Freund A, Zöllner M, Daniliuc C, Jones PG, Kowalsky W, Johannes H. Efficient and long-time stable red iridium (III) complexes for organic light-emitting diodes based on quinoxaline ligands. Inorg Chem 2009;49(2):397-406.

103. Li C, Su Y, Tao Y, Chou P, Chien C, Cheng C, Liu R. Yellow and red electrophosphors based on linkage isomers of phenylisoquinolinyliridium complexes: Distinct differences in photophysical and electroluminescence properties. Advanced Functional Materials 2005;15(3):387-95.

104. Yang C, Tai C, Sun I. Synthesis of a high-efficiency red phosphorescent emitter for organic light-emitting diodes. Journal of Materials Chemistry 2004;14(6):947-50.

105. Tsuboyama A, Iwawaki H, Furugori M, Mukaide T, Kamatani J, Igawa S, Moriyama T, Miura S, Takiguchi T, Okada S. Homoleptic cyclometalated iridium complexes with highly efficient red phosphorescence and application to organic light-emitting diode. J Am Chem Soc 2003;125(42):12971-9.

106. Duan J, Sun P, Cheng C. New iridium complexes as highly efficient Orange–Red emitters in organic Light-Emitting diodes. Adv Mater 2003;15(3):224-8.

107. Meerheim R, Walzer K, Pfeiffer M, Leo K. Ultrastable and efficient red organic light emitting diodes with doped transport layers. Appl Phys Lett 2006;89(6):061111,061111-3.

108. Li G, Fleetham T, Li J. Efficient and stable white organic Light-Emitting diodes employing a single emitter. Adv Mater 2014.

109. Kwong RC, Nugent MR, Michalski L, Ngo T, Rajan K, Tung Y, Weaver MS, Zhou TX, Hack M, Thompson ME. High operational stability of electrophosphorescent devices. Appl Phys Lett 2002;81(1):162-4.

110. Lee J, Chopra N, Eom S, Zheng Y, Xue J, So F, Shi J. Effects of triplet energies and transporting properties of carrier transporting materials on blue phosphorescent organic light emitting devices. Appl Phys Lett 2008;93(12):123306.

111. Tanaka I, Tabata Y, Tokito S. Förster and dexter energy-transfer processes in fluorescent BAlq thin films doped with phosphorescent ir (ppy) 3 molecules. J Appl Phys 2006;99(7):073501,073501-5.

112. Adamovich VI, Cordero SR, Djurovich PI, Tamayo A, Thompson ME, D'Andrade BW, Forrest SR. New charge-carrier blocking materials for high efficiency OLEDs. Organic Electronics 2003;4(2):77-87.

113. Ye S, Liu Y, Di C, Xi H, Wu W, Wen Y, Lu K, Du C, Liu Y, Yu G. Wide-energy-gap host materials for blue phosphorescent organic light-emitting diodes. Chemistry of Materials 2009;21(7):1333-42.

114. Lee YG, Lee H, Kang SK, Oh TS, Lee S, Koh KH. Fabrication of highly efficient and stable doped red organic light-emitting device using 2-methyl-9, 10-di (2-napthyl) anthracene and tris (8-hydroxyquinolinato) aluminum as cohost materials. Appl Phys Lett 2006;89(18):183515.

115. Forrest SR. The path to ubiquitous and low-cost organic electronic appliances on plastic. Nature 2004;428(6986):911-8.

116. Watanabe S, Ide N, Kido J. High-efficiency green phosphorescent organic light-emitting devices with chemically doped layers. Japanese Journal of Applied Physics

2007;46(3R):1186.

117. Bulovic V, Khalfin V, Gu G, Burrows P, Garbuzov D, Forrest S. Weak microcavity effects in organic light-emitting devices. Physical Review B 1998 AUG 15;58(7):3730-40.

118. Worthing P, Barnes W. Efficient coupling of surface plasmon polaritons to radiation using a bi-grating. Appl Phys Lett 2001 NOV 5;79(19):3035-7.

119. Madigan C, Lu M, Sturm J. Improvement of output coupling efficiency of organic light-emitting diodes by backside substrate modification. Appl Phys Lett 2000 MAR 27;76(13):1650-2.

120. Meerheim R, Furno M, Hofmann S, Lüssem B, Leo K. Quantification of energy loss mechanisms in organic light-emitting diodes. Appl Phys Lett 2010;97(25):253305.

121. Windisch R, Heremans P, Knobloch A, Kiesel P, Döhler G, Dutta B, Borghs G. Light-emitting diodes with 31% external quantum efficiency by outcoupling of lateral waveguide modes. Appl Phys Lett 1999;74(16):2256-8.

122. Fujii T, Gao Y, Sharma R, Hu E, DenBaars S, Nakamura S. Increase in the extraction efficiency of GaN-based light-emitting diodes via surface roughening. Appl Phys Lett 2004;84(6):855-7.

123. Madigan C, Lu M, Sturm J. Improvement of output coupling efficiency of organic light-emitting diodes by backside substrate modification. Appl Phys Lett 2000;76(13):1650-2.

124. Möller S, Forrest S. Improved light out-coupling in organic light emitting diodes employing ordered microlens arrays. J Appl Phys 2002;91(5):3324-7.

125. Fujita M, Ueno T, Asano T, Noda S, Ohhata H, Tsuji T, Nakada H, Shimoji N. Organic light-emitting diode with ITO/organic photonic crystal. Electron Lett 2003;39(24):1750-2.

126. Lee J, Chopra N, Bera D, Maslov S, Eom S, Zheng Y, Holloway P, Xue J, So F. Down-conversion white organic light-emitting diodes using microcavity structure. Advanced Energy Materials 2011 MAR 18 2011;1(2):174-8.

127. Yang Yang, Chen Shu-Fen, Xie Jun, Chen Chun-Yan, Shao Ming, Guo Xu, Huang Wei. Light out-coupling progress in organic light emitting device. Acta Phys Sinica 2011 APR;60(4):047809.

128. Kim HK, Cho S, Oh JR, Lee Y, Lee J, Lee J, Ki S, Park Y, Park J, Do YR. Deep blue, efficient, moderate microcavity organic light-emitting diodes. Organic Electronics 2010 JAN 2010;11(1):137-45.

129. Adawi A, Connolly L, Whittaker D, Lidzey D, Smith E, Roberts M, Qureshi F, Foden C, Athanassopoulou N. Improving the light extraction efficiency of red-emitting conjugated polymer light emitting diodes. J Appl Phys 2006 MAR 1;99(5):054505.

130. Lu M, Sturm J. Optimization of external coupling and light emission in organic light-emitting devices: Modeling and experiment. J Appl Phys 2002 JAN 15;91(2):595-604.

131. Benisty H, De Neve H, Weisbuch C. Impact of planar microcavity effects on light extraction - part I: Basic concepts and analytical trends. IEEE J Quant Electron 1998 SEP;34(9):1612-31.

132. Blondelle J., Neve H, Borghs G, Baets R. High efficiency (>20%) microcavity LEDs. The Institution of Electrical Engineers 1996.

133. Deneve H, Blondelle J, Baets R, Demeester P, Vandele P, Borghs G. High-efficiency planar microcavity leds - comparison of design and experiment. Ieee Photonics Technology Letters 1995 MAR;7(3):287-9.

134. Schubert E, Hunt N. Highly efficient light-emitting-diodes with microcavities. Compound Semiconductors 1994 1995(141):489-96.

135. Wang, Z.B., Helander, M.G., Puzzo DP, Wang S, Liu ZW, Lu ZH. Unlocking the full potential of organic light-emitting diodes on flexible plastic. Nature Photonics 2011;259.

136. Suzuki M, Yokoyama H, Brorson S, Ippen E. Observation of spontaneous emission lifetime change of dye-containing Langmuir–Blodgett films in optical microcavities. Appl Phys Lett 1991;58(10):998-1000.

137. Delbeke D, Bockstaele R, Bienstman P, Baets R, Benisty H. High-efficiency semiconductor resonant-cavity light-emitting diodes: A review. Ieee Journal of Selected Topics in Quantum Electronics 2002 MAR-APR;8(2):189-206.

138. Purcell E. Spontaneous emission probabilities at radio frequencies. Physical Review 1946;69(11-1):681.

139. Yokoyama H. Physics and device applications of optical microcavities. Science 1992 APR 3;256(5053):66-70.

140. Abram I, Robert I, Kuszelewicz R. Spontaneous emission control in semiconductor microcavities with metallic or bragg mirrors. IEEE J Quant Electron 1998 JAN;34(1):71-6.

141. Bjork G, Machida S, Yamamato Y, Igeta K. Modification of spontaneous emission rate in planar dielectric microcavity structures. Physical Review a 1991

JUL 1;44(1):669-81.

142. Baets R. Resonant-cavity light-emitting diodes: A review. Proceedings of SPIE 2003;4996:74-86.

143. Gerard J, Gayral B. Strong purcell effect for InAs quantum boxes in three-dimensional solid-state microcavities. J Lightwave Technol 1999 NOV;17(11):2089-95.

144. Dirr S, Wiese S, Johannes H, Ammermann D, Böhler A, Grahn W, Kowalsky W. Luminescence enhancement in microcavity organic multilayer structures. Synth Met 1997;91(1):53-6.

145. Jean F, Mulot J, Geffroy B, Denis C, Cambon P. Microcavity organic light-emitting diodes on silicon. Appl Phys Lett 2002;81(9):1717-9.

146. Fletcher R, Lidzey D, Bradley D, Bernius M, Walker S. Spectral properties of resonant-cavity, polyfluorene light-emitting diodes. Appl Phys Lett 2000;77(9):1262-4.

147. Grüner J, Cacialli F, Friend R. Emission enhancement in single-layer conjugated polymer microcavities. J Appl Phys 1996;80(1):207-15.

148. Fisher T, Lidzey D, Pate M, Weaver M, Whittaker D, Skolnick M, Bradley D. Electroluminescence from a conjugated polymer microcavity structure. Appl Phys Lett 1995;67(10):1355-7.

149. Nakayama T, Itoh Y, Kakuta A. Organic photo-and electroluminescent devices with double mirrors. Appl Phys Lett 1993;63(5):594-5.

150. Slusher R, Weisbuch C. Optical microcavities in condensed matter systems. Solid State Commun 1994;92(1):149-58.

151. Barnes W, Murray W, Dintinger J, Devaux E, Ebbesen T. Surface plasmon polaritons and their role in the enhanced transmission of light through periodic arrays of subwavelength holes in a metal film. Phys Rev Lett 2004 MAR 12;92(10):107401.

152. Moreland J, Adams A, Hansma P. Efficiency of light-emission from surface-plasmons. Physical Review B 1982;25(4):2297-300.

153. Barnes W. Electromagnetic crystals for surface plasmon polaritons and the extraction of light from emissive devices. J Lightwave Technol 1999 NOV;17(11):2170-82.

154. Sharply directed and spectral narrowing emission in organic light emiting diodes with a microcavity structure. Extended abstracts on solid state devices and

materials; 2001.

155. Juang F, Laih L, Lin C, Hsu Y. Angular dependence of the sharply directed emission in organic light emitting diodes with a microcavity structure. Japanese Journal of Applied Physics 2002;41(4S):2787.

156. Dirr S, Böhler A, Wiese S, Johannes H, Kowalsky W. Organic light emitting diodes with reduced spectral and spacial halfwidths. Japanese Journal of Applied Physics 1998;37(part 1):1457-61.

157. Wolter H. Born,m - principles of optics electromagnetic theory of propagation interference and diffraction of light. ; 1966. PT: B; UT: WOS:A19668562300046.

158. Lukosz W. Light-emission by magnetic and electric dipoles close to a plane dielectric interface .3. radiation-patterns of dipoles with arbitrary orientation. J Opt Soc Am 1979 1979;69(11):1495-503.

159. Lukosz W, Kunz R. Light-emission by magnetic and electric dipoles close to a plane interface .1. total radiated power. J Opt Soc Am 1977;67(12):1607-15.

160. Benisty H, Stanley R, Mayer M. Method of source terms for dipole emission modification in modes of arbitrary planar structures. Journal of the Optical Society of America A-Optics Image Science and Vision 1998 MAY;15(5):1192-201.

161. Zhang H, Shi J, Wang W, Guo S, Liu M, You H, Ma D. Tunability of resonant wavelength by fabry-perot microcavity in organic light-emitting diodes. J Lumin 2007 JAN-APR;122:652-5.

162. Delbeke D, Bockstaele R, Bienstman P, Baets R, Benisty H. High-efficiency semiconductor resonant-cavity light-emitting diodes: A review. Selected Topics in Quantum Electronics, IEEE Journal of 2002;8(2):189-206.

163. Baets R. Micro-cavity light emitting diodes. In: A. Miller, M. Ebrahimzadeh, D.M. Finlayson, editor. Semiconductor quantum optoelectronics: From quantum physics to smart devices. Philadelphia, PA: SUSSP Publications; 1998.

164. Vanderzeil J, Ilegems M. Multilayer gaas-Al0.3ga0.7as dielectric quarter wave stacks grown by molecular-beam epitaxy. Appl Opt 1975;14(11):2627-30.

165. Babic D, Corzine S. Analytic expressions for the reflection delay, penetration depth, and absorptance of quarter-wave dielectric mirrors. IEEE J Quant Electron 1992 FEB;28(2):514-24.

166. H. A. Macleod, editor. Thin-film optical filters. 2nd ed. Adam Hilger Ltd; 1986.

167. Yeh P. Optical waves in layered media. New York: Wiley Series in Pure and Applied Optics; 1988.

168. Peumans P, Yakimov A, Forrest SR. Small molecular weight organic thin-film photodetectors and solar cells. J Appl Phys 2003;93(7):3693-723.

169. YEE K. Numerical solution of initial boundary value problems involving maxwells equations in isotropic media. Ieee Transactions on Antennas and Propagation 1966;AP14(3):302.

170. Gedney DS, editor. Introduction to the finite-difference time-domain (FDTD) method for electromagnetics. Morgan and Claypool Publishers; 2011.

171. Chutinan A, Ishihara K, Asano T, Fujita M, Noda S. Theoretical analysis on light-extraction efficiency of organic light-emitting diodes using FDTD and mode-expansion methods. Organic Electronics 2005 FEB;6(1):3-9.

172. Barnes W. Fluorescence near interfaces: The role of photonic mode density. Journal of Modern Optics 1998 APR;45(4):661-99.

173. Kim J, Ho P, Greenham N, Friend R. Electroluminescence emission pattern of organic light-emitting diodes: Implications for device efficiency calculations. J Appl Phys 2000 JUL 15;88(2):1073-81.

174. Schmidt TD, Setz DS, Flämmich M, Frischeisen J, Michaelis D, Krummacher BC, Danz N, Brütting W. Evidence for non-isotropic emitter orientation in a red phosphorescent organic light-emitting diode and its implications for determining the emitter's radiative quantum efficiency. Appl Phys Lett 2011;99(16):163302.

175. Flämmich M, Frischeisen J, Setz DS, Michaelis D, Krummacher BC, Schmidt TD, Brütting W, Danz N. Oriented phosphorescent emitters boost OLED efficiency. Organic Electronics 2011;12(10):1663-8.

176. Tokito S, Tsutsui T, Taga Y. Microcavity organic light-emitting diodes for strongly directed pure red, green, and blue emissions. J Appl Phys 1999;86(5):2407-11.

177. Sasabe H, Gonmori E, Chiba T, Li Y, Tanaka D, Su S, Takeda T, Pu Y, Nakayama K, Kido J. Wide-energy-gap electron-transport materials containing 3, 5-dipyridylphenyl moieties for an ultra high efficiency blue organic light-emitting device. Chemistry of Materials 2008;20(19):5951-3.

178. Lu AW, Chan J, Rakić A, Ng AMC, Djurišić A. Optimization of microcavity OLED by varying the thickness of multi-layered mirror. Opt Quant Electron 2006;38(12-14):1091-9.

179. Tokito S, Tsutsui T, Taga Y. Microcavity organic light-emitting diodes for strongly directed pure red, green, and blue emissions. J Appl Phys 1999;86(5):2407-11.

180. Sun X, Li W, Hong Z, Wei H, Zang F, Chen L, Shi Z, Bi D, Li B, Zhang Z. Investigation of dye-doped red emitting organic electroluminescent devices with

metal-mirror microcavity structure. J Appl Phys 2005;97(10):103112.

181. Mladenovski S, Neyts K, Pavicic D, Werner A, Rothe C. Exceptionally efficient organic light emitting devices using high refractive index substrates. Optics Express 2009 APR 27 2009;17(9):7562-70.

182. Ochoa D, Houdré R, Ilegems M, Hanke C, Borchert B. Microcavity light emitting diodes as efficient planar light emitters for telecommunication applications. Comptes Rendus Physique 2002;3(1):3-14.

183. Wasey J, Barnes W. Efficiency of spontaneous emission from planar microcavities. Journal of Modern Optics 2000;47(4):725-41.

184. Kim S, Jeong W, Mayr C, Park Y, Kim K, Lee J, Moon C, Brütting W, Kim J. Organic Light-Emitting diodes with 30% external quantum efficiency based on a horizontally oriented emitter. Advanced Functional Materials 2013;23(31):3896-900.

APPENDIX I

CALCULATING THE REFLECTANCE OF A MULTILAYER STACK:

MATRIX METHOD CODEING IN MATLAB

```
%Matrix Method of a Multi-layer Stack
clear all
%define optical constants
%%%%%%%%%%%%%%%%%%%%%%%%%%%%%%%%%%%%%%%%%%%%%%%%
%%%%
angs=0; %angle start
anginc=2; %angle increments
ange=90; %angle end
lams=300; %Starting lamda
laminc=2; %lamda increments
lame=850; %Ending lamda
lamda=[lams:laminc:lame];
next=1;
ns=1.7; %Emission Medium Index
n0=1.7; %Incident Medium: Organic Layers (ns)
load ITO_CP.m
load SiO2_CP.m
load TA2O5_CP.m
load Glass_CP.m
%define thickness of each layer
ds=[65,0]
%%%%%%%%%%%%%%%%%%%%%%%%%%%%%%%%%%%%%%%%%%%%%%%%
%%%%
%Define range of wavelength and angles and configuration of stack
lamda=[lams:laminc:lame];
B=length(ds);
M=length(lamda);
for j=1:M
n(1,j)=ITO_CP(j,2)+ITO_CP(j,3)*i;
n(2,j)=SiO2_CP(j,2)+SiO2_CP(j,3)*i;
n(3,j)=TA2O5_CP(j,2)+TA2O5_CP(j,3)*i;
n(4,j)=SiO2_CP(j,2)+SiO2_CP(j,3)*i;
n(5,j)=TA2O5_CP(j,2)+TA2O5_CP(j,3)*i;
n(6,j)=SiO2_CP(j,2)+SiO2_CP(j,3)*i;
n(7,j)=TA2O5_CP(j,2)+TA2O5_CP(j,3)*i;
nB(B+1,j)=Glass_CP(j,2);
end
%define angle of incidence in polar units (tip)
tip=[angs:anginc:ange];
V=length(tip);
%convert polar to radians for ti
for p=1:V
   tir(p,1)=(tip(p)/180)*3.14;
end
%%%%%%%%%%%%%%%%%%%%%%%%%%%%%%%%%%%%%%%%%%%%%%%%
%%%%
%Matrix Method
```

```
%determine the fresnel r and t coefficients
for j=1:M
   for k=2:B
      for p=1:V

%use snells law to determine the transmitted angle within multistack (at each layer)
and final transmitted angle (B/B+1)
for z=1:V
   for b=2:B
ttr(z,1)=asin((n0*sin(tir(z,1)))/n(1,j)); %0/1 (1)
ttr(z,b)=asin((n(b-1,j)*sin(ttr(z,b-1)))/n(b,j)); %1/2 (2) ,2/3 (3), ...B/B+1 (B+1)
   end
ttr(z,B+1)=asin((n(B,j)*sin(ttr(z,B)))/nB(B+1,j)); %B+1/B (final refracted angle)
end
%n0/1
ti=tir(p,1);
tt=ttr(p,1);
ni=n0;
nt=n(1,j);
aa=ni*cos(ti);
bb=nt*cos(tt);
cc=nt*cos(ti);
dd=ni*cos(tt);
rpar(1,j,p)=(cc-dd)/(dd+cc);
rperp(1,j,p)=(aa-bb)/(aa+bb);
tpar(1,j,p)=(2*aa)/(dd+cc);
tperp(1,j,p)=(2*aa)/(aa+bb);
%1/2,3/4,4/5....B-1/B
ti=ttr(p,k-1);
tt=ttr(p,k);
ni=n(k-1,j);
nt=n(k,j);
aa=ni*cos(ti);
bb=nt*cos(tt);
cc=nt*cos(ti);
dd=ni*cos(tt);
rpar(k,j,p)=(cc-dd)/(dd+cc);
rperp(k,j,p)=(aa-bb)/(aa+bb);
tpar(k,j,p)=(2*aa)/(dd+cc);
tperp(k,j,p)=(2*aa)/(aa+bb);
%B/nB
ti=ttr(p,B);
tt=ttr(p,B+1);
ni=n(B,j);
nt=nB(B+1,j);
aa=ni*cos(ti);
bb=nt*cos(tt);
cc=nt*cos(ti);
dd=ni*cos(tt);
```

```
rpar(B+1,j,p)=(cc-dd)/(dd+cc);
rperp(B+1,j,p)=(aa-bb)/(aa+bb);
tpar(B+1,j,p)=(2*aa)/(dd+cc);
tperp(B+1,j,p)=(2*aa)/(aa+bb);
      end
   end
end
for j=1:M
   for k=1:B+1
      for p=1:V
Iperp(1,1,j,k,p)=1/tperp(k,j,p);
Iperp(1,2,j,k,p)=rperp(k,j,p)/tperp(k,j,p);
Iperp(2,1,j,k,p)=rperp(k,j,p)/tperp(k,j,p);
Iperp(2,2,j,k,p)=1/tperp(k,j,p);
Ipar(1,1,j,k,p)=1/tpar(k,j,p);
Ipar(1,2,j,k,p)=rpar(k,j,p)/tpar(k,j,p);
Ipar(2,1,j,k,p)=rpar(k,j,p)/tpar(k,j,p);
Ipar(2,2,j,k,p)=1/tpar(k,j,p);
      end
   end
end
for j=1:M
   for k=1:B
epp(k,j)=((2*3.14)/(lamda(j)))*n(k,j);
   end
end
for j=1:M
   for k=1:B
         for p=1:V
   L(1,1,j,k,p)=exp(-i*epp(k,j)*(ds(k)/cos(ttr(p,k))));
   L(1,2,j,k,p)=0;
   L(2,1,j,k,p)=0;
   L(2,2,j,k,p)=exp(i*epp(k,j)*(ds(k)/cos(ttr(p,k))));
         end
   end
end
Spar=ones(2,2,M,B+1,V);
PRODpar=ones(2,2,M,B+1,V);
for j=1:M
   for p=1:V
   PRODpar(:,:,j,1,p)=Ipar(:,:,j,1,p)*L(:,:,j,1,p);
   for k=1:B-1
PRODpar(:,:,j,k+1,p)=PRODpar(:,:,j,k,p)*Ipar(:,:,j,k+1,p)*L(:,:,j,k+1,p);
   end
   Spar(:,:,j,B,p)=PRODpar(:,:,j,B,p)*Ipar(:,:,j,B+1,p);
   end
end
Sperp=ones(2,2,M,B+1,V);
PRODperp=ones(2,2,M,B+1,V);
```

```
for j=1:M
   for p=1:V
   PRODperp(:,:,j,1,p)=Iperp(:,:,j,1,p)*L(:,:,j,1,p);
   for k=1:B-1
PRODperp(:,:,j,k+1,p)=PRODperp(:,:,j,k,p)*Iperp(:,:,j,k+1,p)*L(:,:,j,k+1,p);
   end
   Sperp(:,:,j,B,p)=PRODperp(:,:,j,B,p)*Iperp(:,:,j,B+1,p);
   end
end
for j=1:M
   for p=1:V
rp1(j,p)=Spar(2,1,j,B,p)/Spar(1,1,j,B,p);
Rp1(j,p)=abs(rp1(j,p)*rp1(j,p));
   end
end
for j=1:M
   for p=1:V
argrp1(j,p)=atan2(imag(rp1(j,p)),real(rp1(j,p)));
   end
end
for j=1:M
   for p=1:V
rs1(j,p)=Sperp(2,1,j,B,p)/Sperp(1,1,j,B,p);
Rs1(j,p)=abs(rs1(j,p)*rs1(j,p));
   end
end
for j=1:M
   for p=1:V
argrs1(j,p)=atan2(imag(rs1(j,p)),real(rs1(j,p)));
   end
end
for j=1:M
   for p=1:V
tp1(j,p)=1/Spar(1,1,j,B,p);
Tp1(j,p)=abs(tp1(j,p)*tp1(j,p))*((nB(B+1,j)*cos(ttr(p,B+1)))/(n0*cos(tir(p,1))));
   end
end
for j=1:M
   for p=1:V
ts1(j,p)=1/Sperp(1,1,j,B,p);
Ts1(j,p)=abs(ts1(j,p)*ts1(j,p))*((nB(B+1,j)*cos(ttr(p,B+1)))/(n0*cos(tir(p,1))));
   end
end
%Ignoring reflectance at glass/air surface
%plot reflectance spectra at normal incidence vs wavelength (nm)
figure
plot(lamda,Rs1(1,:))
```

APPENDIX II

FDTD SCRIPTS

FDTD SCRIPT

```
current_h = 0;
addrect;
set("name","cathode");
set("material",%cathode material%);
set("x span",%cathode span%);
set("y span",%cathode span%);
set("z min",current_h);
current_h = current_h + %cathode h%;
set("z max",current_h);

copy(0,0,0);
set("name","BMPYPB");
set("material",%BMPYPB material%);
set("x span",span);
set("y span",span);
set("z min",current_h);
current_h = current_h + %BMPYPB h%;
set("z max",current_h);

copy(0,0,0);
set("name","PO15");
set("material",%PO15 material%);
set("x span",span);
set("y span",span);
set("z min",current_h);
current_h = current_h + %PO15 h%;
set("z max",current_h);

copy(0,0,0);
set("name","ActiveLayerMCPY");
set("material",%activeorganics index%);
set("x span",span);
set("y span",span);
set("z min",current_h);
current_h = current_h + %activeorganics h%;
set("z max",current_h);

copy(0,0,0);
set("name","TAPC");
set("material",%TAPC material%);
set("x span",span);
set("y span",span);
set("z min",current_h);
current_h = current_h + %TAPC h%;
set("z max",current_h);

copy(0,0,0);
```

```
set("name","NPD");
set("material",%NPD material%);
set("x span",span);
set("y span",span);
set("z min",current_h);
current_h = current_h + %NPD h%;
set("z max",current_h);

copy(0,0,0);
set("name","HATCN");
set("material",%HIL material%);
set("x span",span);
set("y span",span);
set("z min",current_h);
current_h = current_h + %HIL h%;
set("z max",current_h);

copy(0,0,0);
set("name","anode");
set("material",%anode material%);
set("z min",current_h);
current_h = current_h + %anode h%;
set("z max",current_h);

copy(0,0,0);
set("name","SiO2");
set("material",%SiO2 material%);
set("z min",current_h);
current_h = current_h + %SiO2 h%;
set("z max",current_h);

copy(0,0,0);
set("name","Ta2O5");
set("material",%Ta2O5 material%);
set("z min",current_h);
current_h = current_h + %Ta2O5 h%;
set("z max",current_h);

copy(0,0,0);
set("name","SiO2_2");
set("material",%SiO2 material%);
set("z min",current_h);
current_h = current_h + %SiO2_2 h%;
set("z max",current_h);

copy(0,0,0);
set("name","Ta2O5_2");
set("material",%Ta2O5 material%);
set("z min",current_h);
```

```
current_h = current_h + %Ta2O5_2 h%;
set("z max",current_h);

copy(0,0,0);
set("name","SiO2_3");
set("material",%SiO2 material%);
set("z min",current_h);
current_h = current_h + %SiO2_3 h%;
set("z max",current_h);

copy(0,0,0);
set("name","Ta2O5_3");
set("material",%Ta2O5 material%);
set("z min",current_h);
current_h = current_h + %Ta2O5_3 h%;
set("z max",current_h);

copy(0,0,0);
set("name","backfill");
set("material",%backfill material%);
set("alpha",0.6);
set("z min",current_h);
current_h = current_h + %backfill h%;
set("z max",current_h);
pc_top_height = current_h;

copy(0,0,0);
set("name","glass");
set("material","<Object defined dielectric>");
set("index",%glass index%);
set("alpha",0.2);
set("z min",current_h);
current_h = current_h + %glass h%;
set("z max",current_h);
```

SCRIPT-LIGHT OUT-COUPLING EFFICIENCY, EL SPECTRA, ANGULAR

INTENSITY PLOTS

```
runsweep;
#####################################################################
# User inputs
res = 101;
project_in_air = 1;
#farfieldfilter(0.1);
plot_all_wavelengths = 0;
mname = "substrate";
#####################################################################
```

```
np_source_power = getsweepdata("nopattern_dipole_orientation","sourcepower");
np_dipole_power = getsweepdata("nopattern_dipole_orientation","dipolepower");
np_dipole_box_power = getsweepdata("nopattern_dipole_orientation","dipoleboxpower");
select("source1");
f = linspace(get("frequency start"),get("frequency stop"),length(np_source_power));
lambda=(c/f)*1e9;
p1=1;
p2=length(f);
theta=linspace(-90,90,1001);
phi=0;
result0_x = matrix(res,res,length(f));
result0_y = matrix(res,res,length(f));
result0_z = matrix(res,res,length(f));
result0_xg = matrix(res,res,length(f));
result0_yg = matrix(res,res,length(f));
result0_zg = matrix(res,res,length(f));
ffx = matrix(length(theta),length(f));
ffy = matrix(length(theta),length(f));
ffz = matrix(length(theta),length(f));
ffxg = matrix(length(theta),length(f));
ffyg = matrix(length(theta),length(f));
ffzg = matrix(length(theta),length(f));
load("Run 1_nopattern_dipole_orientation/nopattern_dipole_orientation_1");
for(fpoint=p1:p2) {
temp = farfield3d(mname,fpoint,res,res,1,1,1,1.0);
result0_x(1:res,1:res,fpoint) = pinch(result0_x,3,fpoint) + temp;
result0_y(1:res,1:res,fpoint) = pinch(result0_y,3,fpoint) + transpose(temp);
tempg = farfield3d(mname,fpoint,res,res,1,1,1,1.5);
result0_xg(1:res,1:res,fpoint) = pinch(result0_xg,3,fpoint) + tempg;
result0_yg(1:res,1:res,fpoint) = pinch(result0_yg,3,fpoint) + transpose(tempg);
uxang = farfieldux(mname,fpoint,res,res);
uyang = farfieldux(mname,fpoint,res,res);
ffx(1:length(theta),fpoint)=farfieldspherical(pinch(result0_x,3,fpoint),uxang,uyang,theta,
phi);
ffy(1:length(theta),fpoint)=farfieldspherical(pinch(result0_y,3,fpoint),uxang,uyang,theta,
phi);
uxangglass = farfieldux(mname,fpoint,res,res,1.5);
uyangglass = farfieldux(mname,fpoint,res,res,1.5);
ffxg(1:length(theta),fpoint)=farfieldspherical(pinch(result0_xg,3,fpoint),uxangglass,uyan
gglass,theta,phi);
ffyg(1:length(theta),fpoint)=farfieldspherical(pinch(result0_yg,3,fpoint),uxangglass,uyan
gglass,theta,phi);
}
load("nopattern_dipole_orientation_2");
for(fpoint=p1:p2) {
result0_z(1:res,1:res,fpoint) = pinch(result0_z,3,fpoint) +
farfield3d(mname,fpoint,res,res,1,1,1,1.0);
result0_zg(1:res,1:res,fpoint) = pinch(result0_zg,3,fpoint) +
farfield3d(mname,fpoint,res,res,1,1,1,1.5);
ffz(1:length(theta),fpoint)=farfieldspherical(pinch(result0_z,3,fpoint),uxang,uyang,theta,
phi);
```

```
ffzg(1:length(theta),fpoint)=farfieldspherical(pinch(result0_zg,3,fpoint),uxangglass,uyan
gglass,theta,phi);
}
result0 = (1/3)*(result0_x+result0_y+result0_z);
result0g = (1/3)*(result0_xg+result0_yg+result0_zg);
ff = (1/3)*(ffx+ffy+ffz);
ffg = (1/3)*(ffxg+ffyg+ffzg);
# calculate extraction efficiency at each wavelength
power_radiated0 = matrix(length(f));
EEair1= matrix(length(f));
EEair2= matrix(length(f));
EE1deg= matrix(length(f));
EE10deg= matrix(length(f));
EE20deg= matrix(length(f));
EE30deg= matrix(length(f));
EE40deg= matrix(length(f));
EE50deg= matrix(length(f));
EE60deg= matrix(length(f));
EE70deg= matrix(length(f));
EE80deg= matrix(length(f));
EEgm= matrix(length(f));
EEother= matrix(length(f));
for(fpoint=1:length(f)) {
ux = farfieldux(mname,fpoint,res,res,1.0);
uy = farfieldux(mname,fpoint,res,res,1.0);
uxg = farfieldux(mname,fpoint,res,res,1.5);
uyg = farfieldux(mname,fpoint,res,res,1.5);
}
for(fpoint=1:length(f)) {
power_radiated0(fpoint) =
0.5*sqrt(eps0/mu0)*farfield3dintegrate(pinch(result0,3,fpoint),ux,uy);
EEair2(fpoint)=((0.5*sqrt(eps0/mu0)*farfield3dintegrate(pinch(result0g,3,fpoint),uxg,uy
g,42,0,0))/np_source_power(fpoint))*100;
EE1deg(fpoint)=((0.5*sqrt(eps0/mu0)*farfield3dintegrate(pinch(result0g,3,fpoint),uxg,uy
g,1,0,0))/np_source_power(fpoint))*100;
EE10deg(fpoint)=((0.5*sqrt(eps0/mu0)*farfield3dintegrate(pinch(result0g,3,fpoint),uxg,u
yg,7,6,0))/np_source_power(fpoint))*100;
EE20deg(fpoint)=((0.5*sqrt(eps0/mu0)*farfield3dintegrate(pinch(result0g,3,fpoint),uxg,u
yg,13,12,0))/np_source_power(fpoint))*100;
EE30deg(fpoint)=((0.5*sqrt(eps0/mu0)*farfield3dintegrate(pinch(result0g,3,fpoint),uxg,u
yg,20,19,0))/np_source_power(fpoint))*100;
EE40deg(fpoint)=((0.5*sqrt(eps0/mu0)*farfield3dintegrate(pinch(result0g,3,fpoint),uxg,u
yg,25,24,0))/np_source_power(fpoint))*100;
EE50deg(fpoint)=((0.5*sqrt(eps0/mu0)*farfield3dintegrate(pinch(result0g,3,fpoint),uxg,u
yg,31,30,0))/np_source_power(fpoint))*100;
EE60deg(fpoint)=((0.5*sqrt(eps0/mu0)*farfield3dintegrate(pinch(result0g,3,fpoint),uxg,u
yg,35,34,0))/np_source_power(fpoint))*100;
EE70deg(fpoint)=((0.5*sqrt(eps0/mu0)*farfield3dintegrate(pinch(result0g,3,fpoint),uxg,u
yg,39,38,0))/np_source_power(fpoint))*100;
EE80deg(fpoint)=((0.5*sqrt(eps0/mu0)*farfield3dintegrate(pinch(result0g,3,fpoint),uxg,u
yg,41,40,0))/np_source_power(fpoint))*100;
```

```
EEgm(fpoint)=((0.5*sqrt(eps0/mu0)*farfield3dintegrate(pinch(result0g,3,fpoint),uxg,uyg,
90,0,0)-
0.5*sqrt(eps0/mu0)*farfield3dintegrate(pinch(result0g,3,fpoint),uxg,uyg,42,0,0))/np_sour
ce_power(fpoint))*100;
EEother(fpoint)=100-EEgm(fpoint)-EEair2(fpoint);
}
# calculate E2 vs position x and y
EExy=matrix(res,res,length(f));
for(fpoint=1:length(f)) {
for(n1=1:res) {
for(n2=1:res) {
EExy(n1,n2,fpoint)=result0g(n1,n2,fpoint);
}
}
}
# Summary Plots
plot(c/f*1e9,EEair2,"wavelength (nm)","Extraction efficiency");
plot(c/f*1e9,EE1deg,"wavelength (nm)","Extraction efficiency");
plot(c/f*1e9,EE20deg,"wavelength (nm)","Extraction efficiency");
plot(c/f*1e9,EEgm,"wavelength (nm)","Extraction efficiency");
plot(theta,ff(1:length(theta),28),"Angle","Intentisy at 500nm");
matlabsave("Run
1",power_radiated0,EEair2,EE1deg,EE10deg,EE20deg,EE30deg,EE40deg,EE50deg,EE6
0deg,EE70deg,EE80deg,EEgm,EEother,f,lambda,EExy,theta,ff,ffx,ffy,ffz,ffg,ffxg,ffyg,ffzg
);
```

MATLAB CODE – DATA ANALYSIS OF FDTD CALCULATIONS

```
%Angular Emission Profile
WAVE=490;
ng=1.5;
nair=1;
crit=43;
for j=1:length(lambda)
   PIN(j)=abs(lambda(j)-WAVE);
end
for j=1:length(theta)
   P490(j)=ff(j,find(PIN==min(PIN)));
   thetagrad(j)=(theta(j))*(3.14/180);
end
for j=1:length(theta)
PINstart(j)=abs(0-theta(j));
PINend(j)=abs(90-theta(j));
end
for j=find(PINstart==min(PINstart)):find(PINend==min(PINend))
   TT(j-find(PINstart==min(PINstart))+1)=theta(j);
   PP490(j-find(PINstart==min(PINstart))+1)=P490(j);
```

```
end
WAVE=496;
ng=1.5;
nair=1;
crit=43;
for j=1:length(lambda)
   PIN(j)=abs(lambda(j)-WAVE);
end
for j=1:length(theta)
   P496(j)=ff(j,find(PIN==min(PIN)));
   thetagrad(j)=(theta(j))*(3.14/180);
end
for j=1:length(theta)
PINstart(j)=abs(0-theta(j));
PINend(j)=abs(90-theta(j));
end
for j=find(PINstart==min(PINstart)):find(PINend==min(PINend))
   TT(j-find(PINstart==min(PINstart))+1)=theta(j);
   PP496(j-find(PINstart==min(PINstart))+1)=P496(j);
end
WAVE=502;
ng=1.5;
nair=1;
crit=43;
for j=1:length(lambda)
   PIN(j)=abs(lambda(j)-WAVE);
end
for j=1:length(theta)
   P502(j)=ff(j,find(PIN==min(PIN)));
   thetagrad(j)=(theta(j))*(3.14/180);
end
for j=1:length(theta)
PINstart(j)=abs(0-theta(j));
PINend(j)=abs(90-theta(j));
end
for j=find(PINstart==min(PINstart)):find(PINend==min(PINend))
   TT(j-find(PINstart==min(PINstart))+1)=theta(j);
   PP502(j-find(PINstart==min(PINstart))+1)=P502(j);
end
WAVE=508;
ng=1.5;
nair=1;
crit=43;
for j=1:length(lambda)
   PIN(j)=abs(lambda(j)-WAVE);
end
for j=1:length(theta)
   P508(j)=ff(j,find(PIN==min(PIN)));
   thetagrad(j)=(theta(j))*(3.14/180);
```

```
end
for j=1:length(theta)
PINstart(j)=abs(0-theta(j));
PINend(j)=abs(90-theta(j));
end
for j=find(PINstart==min(PINstart)):find(PINend==min(PINend))
   TT(j-find(PINstart==min(PINstart))+1)=theta(j);
   PP508(j-find(PINstart==min(PINstart))+1)=P508(j);
end
WAVE=514;
ng=1.5;
nair=1;
crit=43;
for j=1:length(lambda)
   PIN(j)=abs(lambda(j)-WAVE);
end
for j=1:length(theta)
   P514(j)=ff(j,find(PIN==min(PIN)));
   thetagrad(j)=(theta(j))*(3.14/180);
end
for j=1:length(theta)
PINstart(j)=abs(0-theta(j));
PINend(j)=abs(90-theta(j));
end
for j=find(PINstart==min(PINstart)):find(PINend==min(PINend))
   TT(j-find(PINstart==min(PINstart))+1)=theta(j);
   PP514(j-find(PINstart==min(PINstart))+1)=P514(j);
end
WAVE=520;
ng=1.5;
nair=1;
crit=43;
for j=1:length(lambda)
   PIN(j)=abs(lambda(j)-WAVE);
end
for j=1:length(theta)
   P520(j)=ff(j,find(PIN==min(PIN)));
   thetagrad(j)=(theta(j))*(3.14/180);
end
for j=1:length(theta)
PINstart(j)=abs(0-theta(j));
PINend(j)=abs(90-theta(j));
end
for j=find(PINstart==min(PINstart)):find(PINend==min(PINend))
   TT(j-find(PINstart==min(PINstart))+1)=theta(j);
   PP520(j-find(PINstart==min(PINstart))+1)=P520(j);
end
WAVE=526;
ng=1.5;
```

```
nair=1;
crit=43;
for j=1:length(lambda)
   PIN(j)=abs(lambda(j)-WAVE);
end
for j=1:length(theta)
   P526(j)=ff(j,find(PIN==min(PIN)));
   thetagrad(j)=(theta(j))*(3.14/180);
end
for j=1:length(theta)
PINstart(j)=abs(0-theta(j));
PINend(j)=abs(90-theta(j));
end
for j=find(PINstart==min(PINstart)):find(PINend==min(PINend))
   TT(j-find(PINstart==min(PINstart))+1)=theta(j);
   PP526(j-find(PINstart==min(PINstart))+1)=P526(j);
end
WAVE=532;
ng=1.5;
nair=1;
crit=43;
for j=1:length(lambda)
   PIN(j)=abs(lambda(j)-WAVE);
end
for j=1:length(theta)
   P532(j)=ff(j,find(PIN==min(PIN)));
   thetagrad(j)=(theta(j))*(3.14/180);
end
for j=1:length(theta)
PINstart(j)=abs(0-theta(j));
PINend(j)=abs(90-theta(j));
end
for j=find(PINstart==min(PINstart)):find(PINend==min(PINend))
   TT(j-find(PINstart==min(PINstart))+1)=theta(j);
   PP532(j-find(PINstart==min(PINstart))+1)=P532(j);
end
WAVE=538;
ng=1.5;
nair=1;
crit=43;
for j=1:length(lambda)
   PIN(j)=abs(lambda(j)-WAVE);
end
for j=1:length(theta)
   P538(j)=ff(j,find(PIN==min(PIN)));
   thetagrad(j)=(theta(j))*(3.14/180);
end
for j=1:length(theta)
PINstart(j)=abs(0-theta(j));
```

```
PINend(j)=abs(90-theta(j));
end
for j=find(PINstart==min(PINstart)):find(PINend==min(PINend))
   TT(j-find(PINstart==min(PINstart))+1)=theta(j);
   PP538(j-find(PINstart==min(PINstart))+1)=P538(j);
end
WAVE=544;
ng=1.5;
nair=1;
crit=43;
for j=1:length(lambda)
   PIN(j)=abs(lambda(j)-WAVE);
end
for j=1:length(theta)
   P544(j)=ff(j,find(PIN==min(PIN)));
   thetagrad(j)=(theta(j))*(3.14/180);
end
for j=1:length(theta)
PINstart(j)=abs(0-theta(j));
PINend(j)=abs(90-theta(j));
end
for j=find(PINstart==min(PINstart)):find(PINend==min(PINend))
   TT(j-find(PINstart==min(PINstart))+1)=theta(j);
   PP544(j-find(PINstart==min(PINstart))+1)=P544(j);
end
WAVE=550;
ng=1.5;
nair=1;
crit=43;
for j=1:length(lambda)
   PIN(j)=abs(lambda(j)-WAVE);
end
for j=1:length(theta)
   P550(j)=ff(j,find(PIN==min(PIN)));
   thetagrad(j)=(theta(j))*(3.14/180);
end
for j=1:length(theta)
PINstart(j)=abs(0-theta(j));
PINend(j)=abs(90-theta(j));
end
for j=find(PINstart==min(PINstart)):find(PINend==min(PINend))
   TT(j-find(PINstart==min(PINstart))+1)=theta(j);
   PP550(j-find(PINstart==min(PINstart))+1)=P550(j);
end
%Extraction Efficiency plots
%find pl for ptn1n and load it using
load PtN1N_PL_RT.m %PL spectrum of PtN1N
RTx=PtN1N_PL_RT(:,1);
RTy=PtN1N_PL_RT(:,2);
```

```
LTx=PtN1N_PL_LT(:,1);
LTy=PtN1N_PL_LT(:,2);
TFx=PtN1N_PL_TF(:,1);
TFy=PtN1N_PL_TF(:,2);
%interpolate data
A=[450:.1:650];
Z=length(A);
for j=1:Z
   x1(j)=A(j);
end
PLRT=interp1(RTx,RTy,x1);
PLLT=interp1(LTx,LTy,x1);
PLTF=interp1(TFx,TFy,x1);
EEa=interp1(lambda,EEair2,x1);
EEgm=interp1(lambda,EEgm,x1);
EEo=interp1(lambda,EEother,x1);
EEfor1=interp1(lambda,EE1deg,x1);
for j=1:Z
   PL(j)=PLRT(j);
end
%Extraction Efficiency calculations
%Product of Spectrum and EEair2
for j=1:Z
   AIRRT(j)=EEa(j)*PLRT(j);
   GLASSRT(j)=EEgm(j)*PLRT(j);
   OTHERRT(j)=EEo(j)*PLRT(j);
   AIRLT(j)=EEa(j)*PLLT(j);
   GLASSLT(j)=EEgm(j)*PLLT(j);
   OTHERLT(j)=EEo(j)*PLLT(j);
   AIRTF(j)=EEa(j)*PLTF(j);
   GLASSTF(j)=EEgm(j)*PLTF(j);
   OTHERTF(j)=EEo(j)*PLTF(j);
end
%Integrate product and spectrum
TOPAIRRT=trapz(x1,AIRRT);
TOPGLASSRT=trapz(x1,GLASSRT);
TOPOTHERRT=trapz(x1,OTHERRT);
BOTRT=trapz(x1,PLRT);
EERT=(TOPAIRRT/BOTRT);
EEGMRT=(TOPGLASSRT/BOTRT);
EEOTHERRT=(TOPOTHERRT/BOTRT);
TOPAIRLT=trapz(x1,AIRLT);
TOPGLASSLT=trapz(x1,GLASSLT);
TOPOTHERLT=trapz(x1,OTHERLT);
BOTLT=trapz(x1,PLLT);
EELT=(TOPAIRLT/BOTLT);
EEGMLT=(TOPGLASSLT/BOTLT);
EEOTHERLT=(TOPOTHERLT/BOTLT);
TOPAIRTF=trapz(x1,AIRTF);
```

```
TOPGLASSTF=trapz(x1,GLASSTF);
TOPOTHERTF=trapz(x1,OTHERTF);
BOTTF=trapz(x1,PLTF);
EETF=(TOPAIRTF/BOTTF);
EEGMTF=(TOPGLASSTF/BOTTF);
EEOTHERTF=(TOPOTHERTF/BOTTF);
%STRING=int2str(EE);
%STRING2=int2str(EEGM);
%STRING3=int2str(EEOTHER);
%Modified PL at normal, 10, 20, etc.
EE10=interp1(lambda,EE10deg,x1);
EE20=interp1(lambda,EE20deg,x1);
EE30=interp1(lambda,EE30deg,x1);
EE40=interp1(lambda,EE40deg,x1);
EE50=interp1(lambda,EE50deg,x1);
EE60=interp1(lambda,EE60deg,x1);
EE70=interp1(lambda,EE70deg,x1);
EE80=interp1(lambda,EE80deg,x1);
for j=1:Z
ZERO(j)=PL(j)*EEfor1(j);
TEN(j)=PL(j)*EE10(j);
TWENTY(j)=PL(j)*EE20(j);
THIRTY(j)=PL(j)*EE30(j);
FORTY(j)=PL(j)*EE40(j);
FIFTY(j)=PL(j)*EE50(j);
SIXTY(j)=PL(j)*EE60(j);
SEVENTY(j)=PL(j)*EE70(j);
EIGHTY(j)=PL(j)*EE80(j);
end
G1=max(ZERO);
G2=max(TEN);
G3=max(TWENTY);
G4=max(THIRTY);
G5=max(FORTY);
G6=max(FIFTY);
G7=max(SIXTY);
G8=max(SEVENTY);
G9=max(EIGHTY);
for j=1:Z
ZEROn(j)=ZERO(j)/G1;
TENn(j)=TEN(j)/G2;
TWENTYn(j)=TWENTY(j)/G3;
THIRTYn(j)=THIRTY(j)/G4;
FORTYn(j)=FORTY(j)/G5;
FIFTYn(j)=FIFTY(j)/G6;
SIXTYn(j)=SIXTY(j)/G7;
SEVENTYn(j)=SEVENTY(j)/G8;
EIGHTYn(j)=EIGHTY(j)/G9;
end
```

```
SOS=zeros(length(x1),39);
for j=1:length(x1)
SOS(j,1)=x1(j);
SOS(j,2)=ZEROn(j);
SOS(j,3)=TENn(j);
SOS(j,4)=TWENTYn(j);
SOS(j,5)=THIRTYn(j);
SOS(j,6)=FORTYn(j);
SOS(j,7)=FIFTYn(j);
SOS(j,8)=SIXTYn(j);
SOS(j,9)=SEVENTYn(j);
SOS(j,10)=EIGHTYn(j);
end
for j=1:length(TT)-1
SOS(j,11)=TT(j)-90;
SOS(j,12)=PP490(length(TT)-j);
SOS(j,13)=PP496(length(TT)-j);
SOS(j,14)=PP502(length(TT)-j);
SOS(j,15)=PP508(length(TT)-j);
SOS(j,16)=PP514(length(TT)-j);
SOS(j,17)=PP520(length(TT)-j);
SOS(j,18)=PP526(length(TT)-j);
SOS(j,19)=PP532(length(TT)-j);
SOS(j,20)=PP538(length(TT)-j);
SOS(j,21)=PP544(length(TT)-j);
SOS(j,22)=PP550(length(TT)-j);
end
for j=length(TT):length(TT)+length(TT)-1
SOS(j,11)=TT(j-length(TT)+1);
SOS(j,12)=PP490(j-length(TT)+1);
SOS(j,13)=PP496(j-length(TT)+1);
SOS(j,14)=PP502(j-length(TT)+1);
SOS(j,15)=PP508(j-length(TT)+1);
SOS(j,16)=PP514(j-length(TT)+1);
SOS(j,17)=PP520(j-length(TT)+1);
SOS(j,18)=PP526(j-length(TT)+1);
SOS(j,19)=PP532(j-length(TT)+1);
SOS(j,20)=PP538(j-length(TT)+1);
SOS(j,21)=PP544(j-length(TT)+1);
SOS(j,22)=PP550(j-length(TT)+1);
end
for j=1:length(x1)
SOS(j,23)=x1(j);
SOS(j,24)=EEa(j);
SOS(j,25)=EEgm(j);
SOS(j,26)=EEo(j);
end
SOS(1,27)=EERT;
SOS(1,28)=EEGMRT;
```

```
SOS(1,29)=EELT;
SOS(1,30)=EEGMLT;
SOS(1,31)=EETF;
SOS(1,32)=EEGMTF;
SOS(1,33)=max(EEa(:));
SOS(1,34)=x1(find(EEa==max(EEa(:))));
%find EE at a specific wavelength value - WAVE
WAVE=498;
for j=1:length(x1)
   PIN(j)=abs(x1(j)-WAVE);
end
SOS(1,35)=EEa(find(PIN==min(PIN)));
WAVE=480;
for j=1:length(x1)
   PIN(j)=abs(x1(j)-WAVE);
end
SOS(1,36)=EEa(find(PIN==min(PIN)));
WAVE=490;
for j=1:length(x1)
   PIN(j)=abs(x1(j)-WAVE);
end
SOS(1,37)=EEa(find(PIN==min(PIN)));
WAVE=510;
for j=1:length(x1)
   PIN(j)=abs(x1(j)-WAVE);
end
SOS(1,38)=EEa(find(PIN==min(PIN)));
WAVE=520;
for j=1:length(x1)
   PIN(j)=abs(x1(j)-WAVE);
end
SOS(1,39)=EEa(find(PIN==min(PIN)));
```

APPENDIX III

DESIGN OF EXPERIMENT DETAILS

HIGH AND LOW INDEX OPTICAL PROPERTIES

REFLECTANCE SPECTRA OF DBR STRUCTURES

TABULATED REFLECTANCE

RUN SCHEME

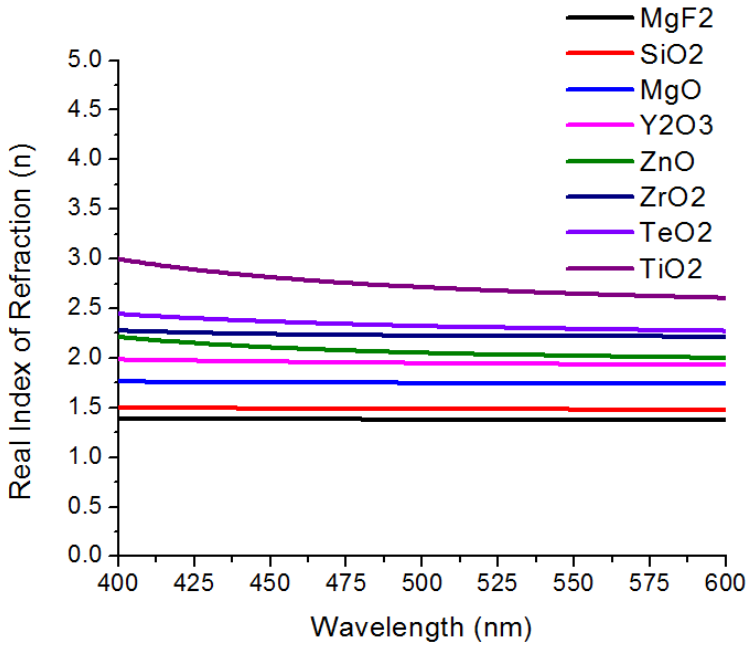
MgF2
SiO2
MgO
Y2O3
ZnO
ZrO2
TeO2
TiO2
Real Index of Refraction (n)
Wavelength (nm)

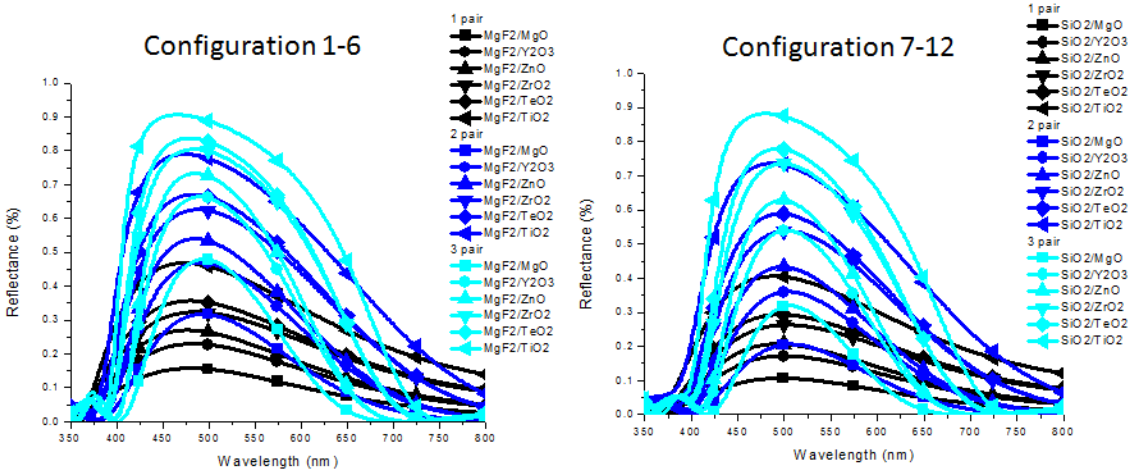
Configuration 1-6
Reflectance (%)
Wavelength (nm)
1 pair
MgF2/MgO
MgF2/Y2O3
MgF2/ZnO
MgF2/ZrO2
MgF2/TeO2
MgF2/TiO2
2 pair
3 pair
Configuration 7-12
SiO2/MgO
SiO2/Y2O3
SiO2/ZnO
SiO2/ZrO2
SiO2/TeO2
SiO2/TiO2

Configuration	Number of pairs	Peak Reflectivity	R {500nm}	R {495nm}	R {505nm}	LI/HI	Low Index (n)	High Index (n)
7	1	11	11	11	11	SiO2/MgO	1.49	1.75
1	1	16	16	16	15	MgF2/MgO	1.38	1.75
8	1	17	17	17	17	SiO2/Y2O3	1.49	1.95
7	2	21	20	20	21	SiO2/MgO	1.49	1.75
9	1	21	21	21	21	SiO2/ZnO	1.49	2.05
2	1	23	23	23	23	MgF2/Y2O3	1.38	1.95
10	1	26	26	26	26	SiO2/ZrO2	1.49	2.22
3	1	27	26	27	26	MgF2/ZnO	1.38	2.05
11	1	29	29	29	29	SiO2/TeO2	1.49	2.32
1	2	32	32	32	31	MgF2/MgO	1.38	1.75
7	3	32	32	31	32	SiO2/MgO	1.49	1.75
4	1	32	32	32	32	MgF2/ZrO2	1.38	2.22
5	1	36	35	35	35	MgF2/TeO2	1.38	2.32
8	2	36	36	36	36	SiO2/Y2O3	1.49	1.95
12	1	41	40	41	40	SiO2/TiO2	1.49	2.71
9	2	43	43	43	43	SiO2/ZnO	1.49	2.05
6	1	47	46	46	46	MgF2/TiO2	1.38	2.71
2	2	47	47	47	46	MgF2/Y2O3	1.38	1.95
1	3	48	48	48	47	MgF2/MgO	1.38	1.75
10	2	54	54	54	54	SiO2/ZrO2	1.49	2.22
3	2	54	54	54	53	MgF2/ZnO	1.38	2.05
8	3	54	54	54	54	SiO2/Y2O3	1.49	1.95
11	2	59	59	59	59	SiO2/TeO2	1.49	2.32
4	2	63	62	63	62	MgF2/ZrO2	1.38	2.22
9	3	63	63	63	63	SiO2/ZnO	1.49	2.05
2	3	66	66	66	66	MgF2/Y2O3	1.38	1.95
5	2	67	67	67	66	MgF2/TeO2	1.38	2.32
3	3	73	73	73	72	MgF2/ZnO	1.38	2.05
10	3	73	73	73	73	SiO2/ZrO2	1.49	2.22
12	2	74	73	73	73	SiO2/TiO2	1.49	2.71
11	3	78	78	78	77	SiO2/TeO2	1.49	2.32
6	2	79	78	78	77	MgF2/TiO2	1.38	2.71
4	3	80	80	80	79	MgF2/ZrO2	1.38	2.22
5	3	84	83	83	82	MgF2/TeO2	1.38	2.32
12	3	88	88	88	87	SiO2/TiO2	1.49	2.71
6	3	91	89	89	88	MgF2/TiO2	1.38	2.71

Run Number	Configuration	L/H	NPD thickness	Pairs
1	1	MgF2/MgO	30	1
2	1	MgF2/MgO	40	1
3	1	MgF2/MgO	50	1
4	1	MgF2/MgO	60	1
5	1	MgF2/MgO	30	2
6	1	MgF2/MgO	40	2
7	1	MgF2/MgO	50	2
8	1	MgF2/MgO	60	2
9	1	MgF2/MgO	30	3
10	1	MgF2/MgO	40	3
11	1	MgF2/MgO	50	3
12	1	MgF2/MgO	60	3
13	2	MgF2/Y2O3	30	1
14	2	MgF2/Y2O3	40	1
15	2	MgF2/Y2O3	50	1
16	2	MgF2/Y2O3	60	1
17	2	MgF2/Y2O3	30	2
18	2	MgF2/Y2O3	40	2
19	2	MgF2/Y2O3	50	2
20	2	MgF2/Y2O3	60	2
21	2	MgF2/Y2O3	30	3
22	2	MgF2/Y2O3	40	3
23	2	MgF2/Y2O3	50	3
24	2	MgF2/Y2O3	60	3
25	3	MgF2/ZnO	30	1
26	3	MgF2/ZnO	40	1
27	3	MgF2/ZnO	50	1
28	3	MgF2/ZnO	60	1
29	3	MgF2/ZnO	30	2
30	3	MgF2/ZnO	40	2
31	3	MgF2/ZnO	50	2
32	3	MgF2/ZnO	60	2
33	3	MgF2/ZnO	30	3
34	3	MgF2/ZnO	40	3
35	3	MgF2/ZnO	50	3
36	3	MgF2/ZnO	60	3
37	4	MgF2/ZrO2	30	1
38	4	MgF2/ZrO2	40	1
39	4	MgF2/ZrO2	50	1
40	4	MgF2/ZrO2	60	1
41	4	MgF2/ZrO2	30	2
42	4	MgF2/ZrO2	40	2
43	4	MgF2/ZrO2	50	2
44	4	MgF2/ZrO2	60	2
45	4	MgF2/ZrO2	30	3
46	4	MgF2/ZrO2	40	3
47	4	MgF2/ZrO2	50	3
48	4	MgF2/ZrO2	60	3
49	5	MgF2/TeO2	30	1
50	5	MgF2/TeO2	40	1
51	5	MgF2/TeO2	50	1
52	5	MgF2/TeO2	60	1
53	5	MgF2/TeO2	30	2
54	5	MgF2/TeO2	40	2
55	5	MgF2/TeO2	50	2
56	5	MgF2/TeO2	60	2
57	5	MgF2/TeO2	30	3
58	5	MgF2/TeO2	40	3
59	5	MgF2/TeO2	50	3
60	5	MgF2/TeO2	60	3
61	6	MgF2/TiO2	30	1
62	6	MgF2/TiO2	40	1
63	6	MgF2/TiO2	50	1
64	6	MgF2/TiO2	60	1
65	6	MgF2/TiO2	30	2
66	6	MgF2/TiO2	40	2
67	6	MgF2/TiO2	50	2
68	6	MgF2/TiO2	60	2
69	6	MgF2/TiO2	30	3
70	6	MgF2/TiO2	40	3
71	6	MgF2/TiO2	50	3
72	6	MgF2/TiO2	60	3
73	7	SiO2/MgO	30	1
74	7	SiO2/MgO	40	1
75	7	SiO2/MgO	50	1
76	7	SiO2/MgO	60	1
77	7	SiO2/MgO	30	2
78	7	SiO2/MgO	40	2
79	7	SiO2/MgO	50	2
80	7	SiO2/MgO	60	2
81	7	SiO2/MgO	30	3
82	7	SiO2/MgO	40	3
83	7	SiO2/MgO	50	3
84	7	SiO2/MgO	60	3
85	8	SiO2/Y2O3	30	1
86	8	SiO2/Y2O3	40	1
87	8	SiO2/Y2O3	50	1
88	8	SiO2/Y2O3	60	1
89	8	SiO2/Y2O3	30	2
90	8	SiO2/Y2O3	40	2
91	8	SiO2/Y2O3	50	2
92	8	SiO2/Y2O3	60	2
93	8	SiO2/Y2O3	30	3
94	8	SiO2/Y2O3	40	3
95	8	SiO2/Y2O3	50	3
96	8	SiO2/Y2O3	60	3
97	9	SiO2/ZnO	30	1
98	9	SiO2/ZnO	40	1
99	9	SiO2/ZnO	50	1
100	9	SiO2/ZnO	60	1
101	9	SiO2/ZnO	30	2
102	9	SiO2/ZnO	40	2
103	9	SiO2/ZnO	50	2
104	9	SiO2/ZnO	60	2
105	9	SiO2/ZnO	30	3
106	9	SiO2/ZnO	40	3
107	9	SiO2/ZnO	50	3
108	9	SiO2/ZnO	60	3
109	10	SiO2/ZrO2	30	1
110	10	SiO2/ZrO2	40	1
111	10	SiO2/ZrO2	50	1
112	10	SiO2/ZrO2	60	1
113	10	SiO2/ZrO2	30	2
114	10	SiO2/ZrO2	40	2
115	10	SiO2/ZrO2	50	2
116	10	SiO2/ZrO2	60	2
117	10	SiO2/ZrO2	30	3
118	10	SiO2/ZrO2	40	3
119	10	SiO2/ZrO2	50	3
120	10	SiO2/ZrO2	60	3
121	11	SiO2/TeO2	30	1
122	11	SiO2/TeO2	40	1
123	11	SiO2/TeO2	50	1
124	11	SiO2/TeO2	60	1
125	11	SiO2/TeO2	30	2
126	11	SiO2/TeO2	40	2
127	11	SiO2/TeO2	50	2
128	11	SiO2/TeO2	60	2
129	11	SiO2/TeO2	30	3
130	11	SiO2/TeO2	40	3
131	11	SiO2/TeO2	50	3
132	11	SiO2/TeO2	60	3
133	12	SiO2/TiO2	30	1
134	12	SiO2/TiO2	40	1
135	12	SiO2/TiO2	50	1
136	12	SiO2/TiO2	60	1
137	12	SiO2/TiO2	30	2
138	12	SiO2/TiO2	40	2
139	12	SiO2/TiO2	50	2
140	12	SiO2/TiO2	60	2
141	12	SiO2/TiO2	30	3
142	12	SiO2/TiO2	40	3
143	12	SiO2/TiO2	50	3
144	12	SiO2/TiO2	60	3